Stabilization of sulfates and molybdenum by using alternative binders

Laura Diaz Caselles

▶ To cite this version:

HAL Id: tel-03209902

https://theses.hal.science/tel-03209902

Submitted on 27 Apr 2021

THÈSE

En vue de l'obtention du
DOCTORAT DE L'UNIVERSITÉ DE TOULOUSE

Délivré par l'Université Toulouse 3 - Paul Sabatier

Présentée et soutenue par
LAURA DIAZ CASELLES

Le 11 décembre 2020

Stabilisation des sulfates et du molybdène par des liants alternatifs

Ecole doctorale : **MEGEP - Mécanique, Energétique, Génie civil, Procédés**

Spécialité : **Génie civil**

Unité de recherche :
LMDC - Laboratoire Matériaux et Durabilité des Constructions de Toulouse

Thèse dirigée par
Martin CYR et Julie HOT

Jury
Mme Céline CAU-DIT-COUMES, Rapporteure
M. Gwenn LE-SAOUT, Rapporteur
M. Laurent DE WINDT, Examinateur
M. Cédric ROOSZ, Examinateur
M. Martin CYR, Directeur de thèse
Mme Julie HOT, Co-directrice de thèse
M. Carl Redon, Invité

ABSTRACT

Abstract

Excavation operations produce several tons of soil generally contaminated by the presence of pollutants. Excavated soil is considered as waste and it can be either sent to landfill or destined for reuse depending on the level of pollution. In any case, soil should be properly treated in order to: (i) decrease the release of pollutants into the environment, and (ii) minimize the problems involved in civil engineering applications due to the reactions between cementitious phases and pollutants. In the context of this thesis, we focused on sulfates and molybdenum (Mo). Concerning sulfates, we considered two main issues: (i) external sulfate attack of concrete structures, which are in direct contact with sulfate-rich soil (e.g. dams, foundations), and (ii) the release of sulfates into solution in addition to the swelling and mechanical strength loss in sulfate-rich soil intended for valorization (e.g. reuse in road construction). In the case of Mo, its release into solution is also a serious concern as it can lead to significant risks for the environment. Therefore, in this thesis, we investigated the reaction of concrete in contact with sulfates, and the stabilization of sulfates by using alternative binders for pollution reduction and for reuse of soil. Additionally, we studied the interaction of Mo with alternative binders and their capacity to stabilize Mo.

First, we studied the capacity of seven different concretes to resist external sulfate attack under similar experimental conditions. It was found that ordinary Portland cement had high expansions (>0.1%) due to the formation of ettringite in excess caused by the reaction between aluminates and sulfates. Portland cement without C_3A presented lower expansions but gypsum was found to be responsible of cracking at later ages. Meanwhile, alternative binders had low expansions in the range of 0.01-0.03% explained by the absence of C_3A and portlandite, in addition to the formation of ettringite during hydration (case of ettringite binders) and the absence of calcium (case of the geopolymer-based metakaolin).

Second, we compared the capacity of four different binders to stabilize sulfates in a sulfate-spiked soil. Binders having high C_3A content led to high volume expansions (>5%) caused by the formation of ettringite in excess. These binders also released heavy metals into solution due to their high clinker content. In contrast, binders containing ground granulated blast furnace slag (GGBS) led to low expansions (<2%), sulfate retention was about 89% and lower heavy metals contents were detected in solution. Sulfate solubility was controlled by ettringite, which did not lead to expansion probably due to the low kinetics of precipitation in addition to the absence of portlandite, which is often related to expansive ettringite.

Finally, we studied the interaction of Mo with three different binders and their capacity to stabilize Mo. Mo retention varied from one binder to another and also depended on the initial Mo concentration. At high Mo concentrations (>500 mg/kg of binder), the precipitation of powellite ($CaMoO_4$) was found to be the dominant mechanism controlling Mo solubility. Mo was also found with calcium and sulfates probably due to the interaction of Mo with sulfate-bearing phases (e.g. substitution or adsorption). Moreover, Mo interacted with calcium silicate hydrates (C-S-H), probably due to the adsorption onto C-S-H surface. The synthesis of C-S-H using 5 different Mo concentrations were then performed. Mo was largely immobilized (>95%) in all the synthetic C-S-H phases. The main mechanism of Mo stabilization was attributed to the coprecipitation of powellite. The adsorption of Mo onto the surface of C-S-H was assumed to be a secondary mechanism of Mo stabilization. Finally, modeling performed with PHREEQC showed that powellite only precipitated for Mo concentrations superior to 90 mg/kg of solid.

Keywords: immobilization, alternative binders, stabilization mechanisms, concrete, soil, sulfates, molybdenum, modeling.

Résumé

Les opérations d'excavation produisent plusieurs tonnes de sols généralement contaminés par la présence de polluants. Les sols excavés sont considérés comme des déchets et sont soit envoyés en décharge, soit destinés à être réutilisés en fonction du niveau de pollution. Dans tous les cas, les sols doivent être correctement traités afin de : (i) diminuer le relargage de polluants dans l'environnement, et (ii) minimiser les problèmes entrainés dans les projets de génie civil liés aux réactions entre les phases cimentaires et les polluants. Dans cette thèse, nous nous sommes concentrés sur les sulfates et le molybdène (Mo). Concernant les sulfates, nous avons considéré deux problématiques principales : (i) l'attaque sulfatique externe des structures en béton qui sont en contact direct avec des sols sulfatés (ex : barrages, fondations), et (ii) le relargage de sulfates en solution, en plus du gonflement et de la perte de résistance mécanique dans des sols sulfatés destinés à la valorisation (ex : réutilisation dans la construction de routes). Dans le cas du Mo, il peut se retrouver en solution, entraînant alors des risques importants pour l'environnement. Par conséquent, dans cette thèse, nous avons étudié la réaction du béton au contact des sulfates et la stabilisation des sulfates dans les sols en utilisant des liants alternatifs afin de réduire leur pollution et envisager leur réutilisation. De plus, nous nous sommes intéressés à l'interaction du Mo avec des liants alternatifs et leur capacité à stabiliser le Mo.

Dans un premier temps, nous avons étudié la capacité de sept bétons différents à résister à l'attaque sulfatique externe dans des conditions expérimentales similaires. Le ciment Portland ordinaire a présenté des expansions élevées (>0,1%) en raison de la formation d'ettringite en excès provoquée par la réaction entre les aluminates et les sulfates. Pour le ciment Portland sans C_3A, des expansions plus faibles ont été mesurées, mais l'apparition de fissures à plus long terme a été attribuée à la formation de gypse. Par ailleurs, les liants alternatifs ont présenté de faibles expansions, de l'ordre de 0,01 à 0,03%, expliquées par l'absence de C_3A et de portlandite, en plus de la formation d'ettringite lors de l'hydratation (cas des liants ettringitiques) et de l'absence de calcium (cas du géopolymère à base de métakaolin).

Dans un deuxième temps, nous avons comparé la capacité de quatre liants à stabiliser les sulfates dans des sols sulfatés. Les liants ayant une teneur élevée en C_3A ont entrainé des expansions élevées (>5%) à cause de la formation d'ettringite en excès. Ces liants ont également rélargué des métaux lourds en solution du fait de leur teneur élevée en clinker. En revanche, les liants contenant du laitier ont conduit à de faibles expansions (<2%), la rétention des sulfates a été d'environ 89%, et avec un relargage limité de métaux lourds. La solubilité des sulfates a été contrôlée par l'ettringite, qui n'a pas conduit à une expansion, peut-être en raison de la faible cinétique de précipitation et de l'absence de portlandite, souvent liée à l'ettringite expansive.

Enfin, nous avons étudié l'interaction du Mo avec trois liants différents et leur capacité à stabiliser le Mo. La rétention du Mo variait d'un liant à l'autre et dépendait également de la concentration initiale en Mo. À des concentrations élevées de Mo (>500 mg/kg de liant), la précipitation de powellite ($CaMoO_4$) s'est avérée être le principal mécanisme de stabilisation du Mo. Le Mo a également été trouvé avec le calcium et les sulfates probablement en raison de l'interaction (substitution ou adsorption) du Mo avec des phases sulfatées (ex : ettringite/monosulfoaluminate). De plus, le Mo a été aussi mélangé avec des silicates de calcium hydratés (C-S-H), probablement en raison de l'adsorption du Mo dans la surface de C-S-H. La synthèse de 5 différents C-S-H avec du Mo a été réalisée et le Mo a été largement immobilisé (>95%) dans toutes les phases. Le principal mécanisme de stabilisation du Mo a été attribué à la coprécipitation de la powellite et l'adsorption de Mo sur la surface de C-S-H a été considérée le mécanisme secondaire de stabilisation. Enfin, la modélisation réalisée avec PHREEQC a montré que le powellite a précipité uniquement pour des concentrations de Mo supérieures à 90 mg/kg de solide.

Mots clés : immobilisation, mécanismes de stabilisation, béton, sol, métaux lourds, sulfates, molybdène, modélisation.

Acknowledgment

Table of Contents

Notations

AAM: Alkali-activated materials

AAS: Alkali-activated ground granulated blast furnace slag cement

AFt: Ettringite

C-S-H: Calcium silicate hydrate

$C\bar{S}$:   Calcium sulfate or anhydrite ($CaSO_4$)

C_2S: Calcium silicate or belite (Ca_2SiO_4)

C_3A: Tricalcium aluminate or celite (Ca_3Al_2O6)

C_3S: Tricalcium silicate or alite (Ca_3SiO_5)

C_4AF: Tetracalcium alumonoferrite or brownmillerite

CEM-SR: Sulfate-resisting Portland cement

CEM I: Ordinary Portland cement of type I

CEM III/C: Blast furnace slag CEM III/C cement

CH: Portlandite

CSA: Calcium sulfoaluminate-belite cement

E: Young modulus

ESA: External sulfate attack

FT-IR: Fourier transform infrared spectroscopy

GGBS: Ground granulated blast furnace slag

GP: Metakaolin geopolymer cement

Gv: Volume expansion

ICP-AES: Inductively Coupled Plasma Atomic Emission Spectrometry

L/S: Liquid to solid ratio

MK: Metakaolin

Mo: Molybdenum

Ms: Calcium monosulfoaluminate

ND: Not determined

NG: Negligible

Rc: Compressive strength

Rit or Rtb: Indirect tensile strength

SEM/EDS: Scanning Electron Microscopy with Energy Dispersive Spectroscopy

$SS\bar{C}$:   Supersulfated GGBS cement

TGA: Thermogravimetric analysis

TOC: Total organic carbon

v%:   Percentage by volume

VBS: Soil methylene blue value

w/c: Water to cement ratio

w/s: Water to solid ratio

wt%:   Percentage by weight

XA2:   Moderately aggressive chemical environment exposure class

XRD: X-ray diffraction

GENERAL INTRODUCTION

General introduction

Excavation operations produce several tons of soil generally contaminated by the presence of pollutants. The source of pollutants in soil can be either from natural origin (i.e. soil parent materials) or from anthropogenic activities (e.g. mining, oil and agriculture industries). Excavated soil is considered as waste and it can be either sent to landfill (disposal in conditioned areas) or destined for reuse depending on the level of pollution. In any case, soil should be properly treated in order to: (i) decrease the release of pollutants into the environment, and (ii) minimize the problems involved in civil engineering applications due to the interaction between cementitious binders and pollutants. In the context of this thesis, we focused on sulfates and molybdenum (Mo).

Concerning sulfates, we considered two main issues: (i) external sulfate attack of concrete structures, which are in direct contact with sulfate-rich soil (e.g. dams, foundations), and (ii) the release of sulfates into solution, in addition to the swelling and mechanical strength loss in sulfate-rich soil intended for valorization (e.g. reuse in road construction). In the case of Mo, its release into solution is also a serious concern as it can lead to significant risks for both human health and for the local environment. Therefore, in this study, we investigated the reaction of concrete in contact with sulfates, and the stabilization of sulfates by using alternative binders for pollution reduction and for reuse of soil. Additionally, we studied the interaction of Mo with alternative binders in order to better understand the stabilization of Mo-contaminated materials.

Figure 1.1 outlines the context of this thesis. For ease of reading, all the objectives were summarized after the introduction.
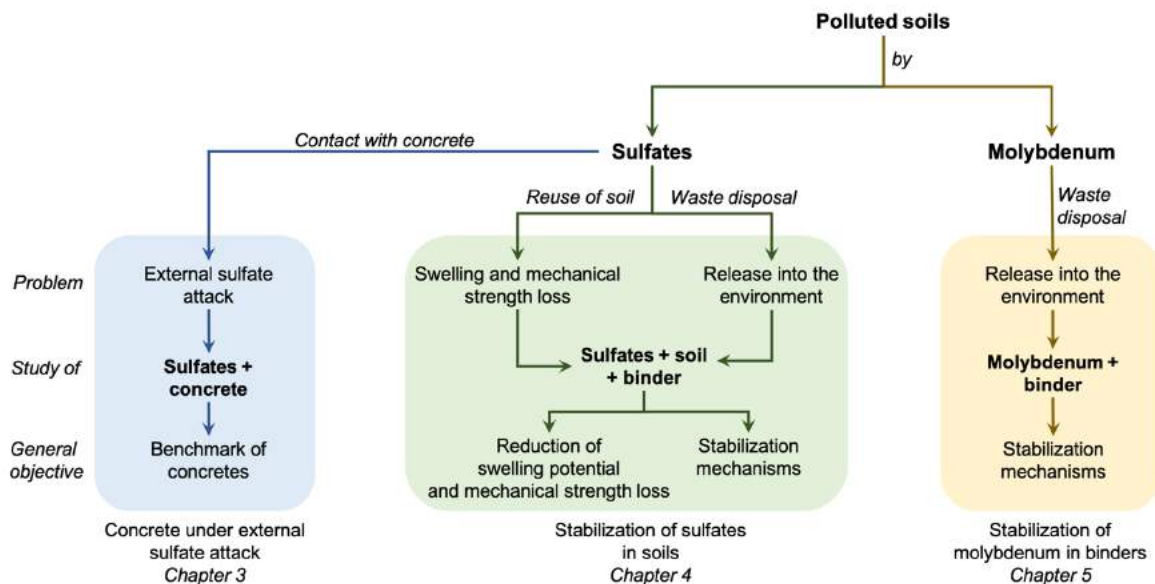

Figure 1.1 – Concept mapping presenting the context of the present thesis "stabilization of sulfates and molybdenum by using alternative binders".

First, we present in **Chapter 1** the literature review of this study. The first part focuses on the presence of sulfates in soil, their sources and concentrations. As sulfate-rich soils are an external source of sulfates for concrete leading to durability issues, we also discuss the behavior of ordinary Portland cement (OPC) and alternative binders under external sulfate attack (ESA). The second part of this chapter presents a general overview of the treatment of sulfate-rich soils by using cementitious binders. The last part of this chapter focuses on the presence of heavy metals in soil, and especially on Mo. This section describes the main immobilization mechanisms of heavy metals by using cementitious binders and refers to previous research works in this field. In addition, we explain the main characteristics of the geochemical model used in this investigation.

Chapter 2 describes all the materials and methods used in this study. The first part of this chapter presents all the materials (composition, preparation and curing conditions) and the second part focuses on the methods used to accomplish the objectives of this research.

Since sulfate-rich soils represent an external source of sulfates for concretes, we study in **Chapter 3** the capacity of seven concretes to resist ESA under similar experimental conditions. Three different Portland cements and four alternative binders were used to fabricate the concretes. The alternative binders were grouped into two categories: (i) alkali-activated binders with or without calcium oxides, and (ii) ettringite binders (supersulfated ground granulated blast furnace slag (GGBS) cement and calcium sulfoaluminate cement). Therefore, the first part of this chapter describes the compressive strength results obtained in the hardened state of all the concretes tested. The second part presents the results obtained from the longitudinal expansion and mass variations. Finally, we present the microstructural observations, chemical and mineralogical analyses and thermodynamic calculations performed in concretes before and after ESA.

On the other hand, sulfate-rich soils can represent an important durability issue when they are treated for reuse. Therefore, **Chapter 4** deals with the study of stabilization of sulfates. In the literature, preliminary work in this field focused mainly on the evaluation of swelling in sulfate-rich soils. However, not much is known about the decrease in the sulfate concentration in solution and about the underlying sulfate stabilization mechanisms after treatment with cementitious and alternative binders. Hence, we studied the sulfate immobilization, swelling and mechanical properties of different treatments. To this end, a sulfate-spiked soil was treated with four different binders: one OPC, one alternative clinker (composed of ye'elimite and belite), one blast furnace slag Portland cement (CEM III), and one experimental binder (90% GGBS and 10% OPC). The first part of this chapter describes the results obtained from leaching tests and the results of swelling and splitting tests carried out for all the treatments. The third part of this chapter focuses on one specific treatment, which seemed to give the best results in terms of sulfate immobilization and swelling. Therefore, we present the analyses in the medium and long-term (leaching, geotechnical properties and modeling) and the numerical results obtained by modeling using the code PHREEQC.

Finally, the release of Mo into solution results in negative impact on the environment. Therefore, the understanding of Mo stabilization becomes necessary in order to decrease the potential risk of Mo-contaminated materials. To this end, **Chapter 5** focuses on the stabilization of Mo by using cementitious binders. In this part, we studied the interaction of Mo with three different binders and their capacity to immobilize Mo. Thus, the binders (one OPC, one experimental binder (90% GGBS and 10% OPC) and one supersulfated cement) were

artificially spiked with different Mo concentrations. First, we present the results obtained from leaching tests of Mo-spiked binders, their mineralogical characterization and modeling carried out with PHREEQC. The Mo stabilization mechanisms were also studied by the synthesis of calcium silicate hydrate (C-S-H); therefore, the results obtained from the synthetic C-S-H phases with Mo are presented. This includes the Mo concentration in solution after filtration of C-S-H as well as the microstructure and mineralogical characterization of all the synthetic phases, followed by the numerical calculations obtained in the modeling of C-S-H with Mo.

Summary of objectives

The objectives of this research were grouped in three main parts:

1. Concrete under external sulfate attack

This part of the project aims to: (i) realize a benchmark of several binders by testing their capacity to resist external sulfate attack under similar experimental conditions, and (ii) contribute to the understanding of the mechanisms associated with the expansion or non-expansion of the binders by using microstructural and mineralogical analyses and thermodynamic calculations.

2. Stabilization of sulfates

This part of the research aims to (i) compare the capacity of several alternative binders to immobilize sulfates in a sulfate-spiked soil, (ii) contribute to the understanding of the sulfate stabilization mechanisms, and (iii) evaluate the swelling potential and the mechanical properties of all the treatments.

3. Stabilization of molybdenum

This part of the work aims to (i) compare the capacity of several binders to immobilize molybdenum, and (ii) contribute to the understanding of the mechanisms associated with the molybdenum stabilization.

Introduction générale

Les opérations d'excavation produisent plusieurs tonnes de sols généralement contaminés par la présence de polluants. La source des polluants dans le sol peut être d'origine naturelle (c'est-à-dire provenant de la dégradation de la roche-mère) ou anthropique (par exemple les industries minière, pétrolière et agricole). Les sols excavés sont considérés comme des déchets et sont soit envoyés en décharge, soit destinés à être réutilisés en fonction du niveau de pollution. Dans tous les cas, les sols doivent être correctement traités afin de : (i) diminuer le relargage de polluants dans l'environnement, et (ii) minimiser les problèmes entrainés dans les projets de génie civil liés aux réactions entre les phases des liants et les polluants. Dans cette thèse, nous nous sommes concentrés sur les sulfates et le molybdène (Mo).

Concernant les sulfates, nous avons considéré deux problématiques principales : (i) l'attaque sulfatique externe des structures en béton qui sont en contact direct avec des sols sulfatés (ex : barrages, fondations), et (ii) le relargage de sulfates en solution, en plus du gonflement et de la perte de résistance mécanique dans des sols sulfatés destinés à la valorisation (ex : réutilisation dans la construction de routes). Dans le cas du Mo, il peut se retrouver en solution entraînant des risques importants pour l'environnement.

Par conséquent, dans cette thèse, nous avons étudié la réaction du béton au contact des sulfates et la stabilisation des sulfates dans les sols en utilisant des liants alternatifs afin de réduire leur pollution et envisager leur réutilisation. De plus, nous nous sommes intéressés à l'interaction du Mo avec des liants alternatifs et leur capacité à stabiliser le Mo. Une représentation schématique de ce projet de thèse est proposée en Figure 1.1. Les objectifs sont précisés à la fin de cette introduction.

Pour commencer, nous présentons au Chapitre 1 l'état de l'art de cette étude. La première partie se concentre sur la présence de sulfates dans les sols, leurs sources et leurs concentrations. Étant donné que les sols sulfatés sont une source externe de sulfates entrainant des problèmes de durabilité dans les bétons, nous traitons le comportement du ciment Portland ordinaire (OPC) et des liants alternatifs vis-à-vis de l'attaque sulfatique externe. La deuxième partie présente un état de l'art général sur le traitement des sols sulfatés à l'aide de liants cimentaires. Enfin, la troisième partie s'intéresse à la présence de métaux lourds dans les sols, et notamment à celle du Mo. Cette section décrit les principaux mécanismes d'immobilisation des métaux lourds et fait référence aux recherches antérieures dans ce domaine. De plus, nous présentons une explication succincte et des exemples du modèle géochimique utilisé dans cette recherche.

Le Chapitre 2 décrit les matériaux et les méthodes utilisés dans cette étude. La première partie se concentre sur les matériaux, leur description, leur composition, leur préparation et les conditions de stockage. La deuxième partie porte sur les méthodes utilisées pour atteindre les objectifs de cette recherche.

Puisque les sols sulfatés représentent une source externe de sulfates pour les bétons, nous avons étudié, dans le Chapitre 3, la capacité de sept bétons à résister à l'attaque sulfatique externe dans les mêmes conditions expérimentales. Trois ciments Portland et quatre liants alternatifs ont été utilisés pour fabriquer ces bétons. Les liants alternatifs ont été regroupés en deux catégories : (i) liants alcali-activés avec ou sans oxydes de calcium et (ii) liants ettringitiques (ciment sursulfaté et ciment sulfoalumineux). La première partie de ce chapitre décrit les résultats de résistance à la compression obtenus à l'état durci des bétons. La deuxième partie présente les résultats obtenus à partir des analyses effectuées dans les bétons avant et après attaque. Premièrement, les résultats de l'expansion longitudinale et de la variation de masse sont présentés. Finalement, nous présentons les analyses minéralogiques et microstructurales et des calculs thermodynamiques avant et après attaque réalisés afin de mettre en évidence les mécanismes d'expansion et de non-expansion des liants.

Le Chapitre 4 est dédié à l'étude de la stabilisation des sulfates dans les sols. Dans la littérature, les travaux de recherche se concentrent principalement sur l'évaluation du gonflement des sols sulfatés. Dans ce projet, nous

avons donc étudié l'immobilisation des sulfates, le gonflement et les propriétés mécaniques de différents traitements. Un sol sulfaté artificiellement a été traité par quatre liants différents : un OPC, un clinker alternatif (composé de ye'elimite et de bélite), un ciment au laitier de haut fourneau (de type CEM III) et un liant expérimental (90% laitier et 10% OPC). La première partie de ce chapitre se concentre sur la justification des formulations utilisées pour les traitements du sol sulfaté. Ensuite, il présente les résultats obtenus lors des essais de lixiviation pour évaluer l'immobilisation des sulfates ainsi que les résultats des essais d'aptitude des traitements (gonflement et résistance mécanique). La troisième partie présente l'étude approfondie faite sur un traitement particulier du sol sulfaté. Ici, l'immobilisation des sulfates ainsi que les propriétés géotechniques du traitement ont été évaluées à court, moyen et long termes. De plus, tous les résultats expérimentaux obtenus lors des essais de lixiviation ont été comparés avec des calculs numériques obtenus à partir d'un modèle géochimique développé avec le logiciel PHREEQC. Ce travail de modélisation a été effectué afin de mieux comprendre les mécanismes de stabilisation des sulfates pour ce traitement en particulier.

Enfin, le Chapitre 5 est dédié à l'étude de la stabilisation du molybdène (Mo). Nous nous sommes concentrés sur l'interaction du Mo avec trois liants différents (un OPC, un liant expérimental (90% laitier et 10% OPC) et un ciment sursulfaté) et sur leur capacité à immobiliser le Mo. Ainsi, ces trois liants ont été artificiellement dopés avec différentes concentrations de Mo. La stabilisation du Mo a été aussi étudiée par la synthèse du silicate de calcium hydraté (C-S-H). La première partie de ce chapitre présente tous les résultats expérimentaux obtenus sur les pates dopées en Mo. Dans un premier temps, nous présentons les résultats des tests de lixiviation réalisés sur pâte et leur caractérisation minéralogique suivie de la modélisation développée avec le logiciel PHREEQC. Deuxièmement, les résultats obtenus à partir des phases synthétiques de C-S-H avec Mo sont présentés. Cela comprend la concentration en Mo en solution après filtration du C-S-H ainsi que leur caractérisation minéralogique et microstructurale et les calculs numériques obtenus dans la modélisation sur le C-S-H avec Mo.

Résumé des objectifs

Les objectifs de ce travail de recherche ont été regroupés par parties :

1. Béton sous attaque sulfatique externe

Cette partie vise à : (i) réaliser un « benchmark » ou une étude comparative de plusieurs liants vis-à-vis de leur capacité à résister à l'attaque sulfatique externe dans des conditions expérimentales similaires, et (ii) contribuer à la compréhension des mécanismes associés à l'expansion ou non-expansion des liants en utilisant des analyses microstructurales et minéralogiques ainsi que des calculs thermodynamiques.

2. Stabilisation des sulfates

Cette partie vise à : (i) comparer la capacité de plusieurs liants alternatifs à immobiliser les sulfates dans un sol sulfaté, (ii) comprendre les mécanismes d'immobilisation des sulfates, et (iii) évaluer le potentiel de gonflement et les propriétés mécaniques des traitements du sol sulfaté.

3. Stabilisation du molybdène

Cette partie vise à : (i) comparer la capacité de plusieurs liants à immobiliser du molybdène, et (ii) contribuer à la compréhension des mécanismes associés à sa stabilisation.

CHAPTER 1 - LITERATURE REVIEW

Table of Contents

1. Chapter 1 – Literature review

Résumé

Ce premier chapitre présente l'état de l'art sur la pollution des sols et leur valorisation ou mise en décharge après les opérations d'excavation. De plus, nous présentons l'état de l'art sur la présence des sulfates dans les sols et les problèmes de durabilité qu'il entraine sur les projets de génie civil. Par conséquent, nous traitons l'attaque sulfatique externe sur les bétons. De plus, comme les sulfates représentent aussi un problème de durabilité après traitement pour leur valorisation, ce chapitre présente l'état de l'art sur le traitement des sols par de ciment Portland et les désavantages vis-à-vis du gonflement. Enfin, comme le molybdène (Mo) dans les sols peut se relarguer en solution polluant l'environnement, la dernière partie de ce chapitre présente l'état de l'art sur la présence des métaux lourds dans les sols et les mécanismes de stabilisation par des liants cimentaires. Cette partie se focalise notamment sur la stabilisation de molybdène (Mo). La Table 1.11 présente un bilan de l'état de l'art fait dans cette thèse.

Les sulfates :

L'anion sulfate SO_4^{2-} est trouvé dans des sols provenant des diverses sources dont on peut citer des sources directes ou primaires de sulfate dans son état pur, telles que les roches contenant du gypse ($CaSO_4 \cdot 2H_2O$) (forme de sulfate la plus répandue à l'échelle mondiale), l'anhydrite ($CaSO_4$), le sulfate de sodium (Na_2SO_4) et le sulfate de magnésium ($MgSO_4$). Parmi les sources secondaires de sulfate, on trouve les eaux interstitielles qui transportent les ions sulfate, ainsi que les minéraux riches en sulfure comme les pyrites (FeS_2) lors des réactions d'oxydation.

Les sols sulfatés représentent une source externe de sulfates qui, en contact avec des bétons, peuvent entrainer des expansions et fissurations. Ce phénomène est connu sous le nom d'attaque sulfatique externe, terme utilisé pour décrire les réactions chimiques entre les ions sulfate et les composants du béton (notamment à base de ciment Portland). L'action de sulfates sur le béton produit divers phénomènes physico-chimiques qui dépendent de nombreux paramètres, tels que l'origine des ions sulfate, le cation associé et sa concentration, la formulation du béton, etc., et conduiront à des dégradations plus ou moins importantes. Il existe des ciments Portland avec une chimie modifiée connus sous le nom « ciments résistants aux sulfates » ayant une expansion limitée (e.g. CEM I-SR0 ou ciments de type CEM III/C en accord avec la norme EN 197-1). Cependant, ces matériaux ont aussi présenté des dégradations dans le temps (e.g. fissuration et décohésion). De ce fait, des liants alternatifs comme les liants ettringitiques (e.g. ciments sur-sulfaté et sulfo-alumineux) et les liants alcali-activés (e.g. laitiers alcali-activés et géopolymères) ont été aussi testés vis-à-vis des attaques sulfatiques externes et ont montré des résistances supérieures à celles des ciments Portland vis-à-vis des expansions.

Bien que les liants alternatifs soient reconnus comme étant résistants aux sulfates externes, les résultats disponibles dans la littérature sont difficilement comparables, notamment à cause des conditions expérimentales variables d'une étude à l'autre (e.g. la fabrication d'éprouvettes, le cation associé à la solution sulfatique, la concentration de sulfate, le temps de l'essai). Il est alors nécessaire de pouvoir comparer ces liants vis-à-vis de l'attaque sulfatique externe en évaluant leurs gonflements sous les mêmes conditions expérimentales.

L'immobilisation des sulfates :

Concernant la mise en décharge des sols en France, l'arrêté du 12 décembre 2014 avec la décision n°2003[1] établissent les valeurs limites de concentrations des sulfates en matière de lixiviation (en termes de relargage cumulé). En fonction de ces limites de concentration, il y a trois catégories de déchets : les déchets non dangereux inertes, les déchets non dangereux non inertes et les déchets dangereux (cf. Chapitre 1 - Table 1.6). L'impact économique de la mise en décharge des sols sulfatés est plus important dans le cas de fortes teneurs en polluants, d'où l'importance de réduire le relargage des sulfates en solution. L'immobilisation des sulfates peut se faire via l'utilisation de liants cimentaires ; on parle alors de la stabilisation. Cette technique regroupe des procédés chimiques permettant de réduire le potentiel dangereux d'un déchet car les polluants deviennent moins solubles, moins mobiles ou moins toxiques. Ce processus permet donc de transformer un déchet dangereux en un matériau acceptable d'un point de vue environnemental.

La valorisation des sols sulfatés :

L'utilisation des liants pour le traitement des sols permet d'obtenir une amélioration de leurs propriétés mécaniques à court et long termes. D'après Le Roux et Orsetti [1], la chaux est communément utilisée pour le traitement des sols grâce à l'amélioration des propriétés mécaniques (e.g. augmentation de la portance, amélioration de la consistance). Cependant, le traitement des sols sulfatés à la chaux ou aux liants similaires comme le ciment Portland, entrainent des réactions sulfatiques expansives. Ces réactions sulfatiques se produisent lors de l'interaction entre les oxydes de calcium, aluminium et silicium (provenant soit des sols notamment argileux, soit des liants) et les sulfates formant alors des minéraux expansifs tels que l'ettringite et la thaumasite (cette dernière phase n'est pas étudiée dans la présente étude). Ces minéraux expansifs entrainent des gonflements dans les sols, réduisant alors la résistance mécanique acquise et pouvant conduire à l'effondrement de la structure. Ce processus décrit dans ce chapitre dans les équations : Equation 6, Equation 7, Equation 8 et Equation 9. De plus, un schéma explicatif des réactions conduisant l'expansion du sol est présenté en Figure 1.10.

D'après la littérature, les liants pouvant être utilisés dans le traitement des sols sulfatés limitant la formation des phases expansives sont les liants hydrauliques qui consomment de la chaux pendant leur processus d'hydratation (e.g. ciments à base de laitier de haut-fourneau, des fumées de silice et des cendres volantes). Ils peuvent aussi avoir des teneurs limitées en aluminates tricalciques (C_3A), car en réduisant la teneur en aluminium on réduit sa disponibilité à réagir avec les sulfates et donc à former de l'ettringite.

La stabilisation du molybdène (Mo) :

Concernant la mise en décharge des sols en France, l'arrêté du 12 décembre 2014 avec la décision n°2003 établissent les valeurs limites de concentrations en métaux lourds en matière de lixiviation (en termes de relargage cumulé). Concernant le molybdène (Mo), il y a trois catégories de déchets en fonction des limites de concentration du Mo : les déchets non dangereux inertes, les déchets non dangereux non inertes et les déchets dangereux (cf. Chapitre 1 - Table 1.6). L'impact économique de la mise en décharge des sols contaminés en Mo est plus important dans le cas de fortes teneurs en polluants, d'où l'importance de réduire le relargage des Mo en solution.

Plusieurs métaux lourds sont des micronutriments essentiels pour les plantes, les animaux et l'Homme. Néanmoins, si les concentrations dépassent certains seuils, ils deviennent toxiques. C'est le cas du Mo, qui en excès peut entrainer une sévère toxicité dont la maladie associée est la « molybdénose ». Ce métal est trouvé naturellement dans les sols mais est aussi produit par des activités anthropiques (e.g. industrielles agricoles, métallurgiques et pétrolières). Dans le sol, le Mo se présente notamment sous la forme de molybdate (MoO_4^{2-}), qui est un anion avec le Mo en état d'oxydation +6.

---

[1] Annexe des critères et procédures d'admission des déchets en décharge.

D'après la littérature, les métaux lourds sous forme d'anions (ions de charge négative) ou de cations (ions de charge positive) présentent des différences importantes dans leur comportement d'adsorption ou de précipitation en fonction du pH (cf. Figure 1.25 and Figure 1.26). Ces réactions redox deviennent plus importantes quand les espèces peuvent changer son état d'oxydation. Cependant, le Mo est toujours présent sous la forme de molybdate pour les valeurs du pH au milieu cimentaire.

Il est important d'immobiliser les métaux lourds présents dans les sols afin de réduire leur solubilité dans l'eau. Il existe différentes techniques de stabilisation qui pourraient être employées, parmi lesquelles « la stabilisation par des liants cimentaires » fait l'objet de cette étude. Dans la littérature, les mécanismes d'immobilisation des métaux lourds par des liants cimentaires sont principalement : la sorption, la substitution et la précipitation. Quelques auteurs ont rapporté l'immobilisation partielle de Mo par le ciment Portland dont le mécanisme de stabilisation identifié était la précipitation d'un minéral de faible solubilité appelé powellite ($CaMoO_4$). D'autres ont montré une immobilisation partielle du Mo par substitution des anions comme le sulfate dans l'ettringite. Une compréhension plus approfondie des mécanismes de stabilisation du Mo par des liants cimentaires apparait nécessaire afin d'envisager, dans le futur, un traitement des matériaux pollués en Mo.

Introduction

This chapter presents the literature review related to polluted soils and their reuse or disposal after excavation operations. Therefore, we present a general background on the presence of sulfates in soil and its effect in concrete. First, we deal with the external sulfate attack (ESA) and the reaction of several binders under this phenomenon. Second, since the presence of sulfates in soil can also lead to important durability issues when soil is treated for reuse, this chapter presents an overview of the treatment of sulfate-rich soil by using cementitious binders. In this part, we explain why the treatment of this type of soil by using Portland cement or lime is not suitable compared with the use of alternative binders.

Furthermore, as molybdenum (Mo) in contaminated materials can release into solution polluting the environment, we present an overview of the stabilization of heavy metals by using cementitious binders and give details about the immobilization of Mo. Therefore, this section describes the main immobilization mechanisms of heavy metal-stabilization and refers to previous research in this field.

Finally, the last part of this chapter provides a background on the modeling used to predict the behavior of pollutants in aqueous systems and presents some examples that inspired the modeling carried out in the current investigation.

At the end of this chapter, Table 1.11 presents a summary of the literature review.

1.1 Soil containing sulfates: a durability issue for concrete

As mentioned previously, the presence of sulfates leads to serious concerns in civil engineering projects. In this part, we deal with the external sulfate attack (ESA) of concrete structures in direct contact with sulfate-rich soil.

Sulfate (SO_4^{2-}) is an anion found in soil due to the dissolution of minerals such as gypsum ($CaSO_4 \cdot 2H_2O$), anhydrite ($CaSO_4$), sodium sulfate (Na_2SO_4), barite ($BaSO_4$) and magnesium sulfate ($MgSO_4$). Among these minerals, gypsum ($CaSO_4 \cdot 2H_2O$) is the main form of sulfate found in soil [2]–[4]. Other sources of sulfates in soil are the groundwater, which transports the sulfate ions, and some minerals containing sulfurs such as pyrite (FeS_2) after oxidation reactions [2].

In France, sulfates are generally found in sedimentary rocks in the form of gypsum or anhydrite. The principal mines of gypsum are located in the Paris Basin where the production of gypsum

reaches about 68% of the national production [5]. The Paris Basin consists of three or four layers of gypsum alternating with sedimentary rocks, mainly marlstone, which contains lime and clay and therefore protect gypsum from dissolution [5]. Table 1.1 presents the water solubility values of different sulfate species commonly found in soils.

Table 1.1 – Solubility in water at 20°C of different species of sulfates found in soils [3], [6], [7].

Sulfate specie	Solubility (g/L)	Sulfate specie	Solubility (g/L)
$MgSO_4.6H_2O$	440	Na_2SO_4	58
$FeSO_4.7H_2O$	260	$CaSO_4.2H_2O$	2.4 [7]
$Na_2SO_4.10H_2O$	194	$CaSO_4$	2 [7]
K_2SO_4	111		

In the following sections, we first present an overview of the behavior of ordinary Portland cement (OPC)-based concretes and alternative binders under ESA. Second, we present the literature review related to the treatment of sulfate-rich soils with OPC or lime and with alternative binders.

1.1.1 Ordinary Portland Cement-based binders under external sulfate attack

External sulfate attack (ESA) is the process of degradation where expansive reactions are involved between sulfate ions coming from an external source and the phases in hardened matrices [8], [9]. Currently, the chemistry behind the degradation of Ordinary Portland Cement (OPC) under ESA has been widely studied and significant progress has been made towards its understanding in the last few years. In the literature, OPC is defined as a mixture of clinker (initially about 80% limestone and 20% clay) and calcium sulfate, which is generally added in the form of gypsum or semi-hydrate ($CaSO_4 \cdot 2H_2O$ or $CaSO_4 \cdot 1/2H_2O$) and to slow the setting of the cement.

The clinker is primarily composed of calcium oxide (CaO), silica (SiO_2), alumina (Al_2O_3), and ferric oxide (Fe_2O_3). These oxides combine with each other to form four principal crystalline phases: tricalcium silicate or alite (C_3S), bicalcium silicate or belite (C_2S), tricalcium aluminate or celite (C_3A) and tetracalcium aluminoferrite (C_4AF) [10], [11]. An addition of water is necessary to hydrate the anhydrous cement. The hydrated OPC is typically composed of four

minerals—calcium silicate hydrate (C-S-H), portlandite (CH), ettringite (AFt), and calcium monosulfoaluminate (Ms). C-S-H is amorphous while the other three minerals are crystalline.

In the following sections, we present an overview of the mechanisms of degradation of OPC under ESA and we describe the main parameters influencing its resistance to this type of attack.

1.1.1.1 Mechanisms of degradation

ESA is characterized by the ingress of sulfate ions from the environment into the concrete matrix. The matrix can initially present the leaching of portlandite (CH) and the decalcification of C-S-H [8], [12]. Subsequently, sulfate ions chemically react in the matrix with anhydrous calcium aluminate phases (C_3A and C_4AF) to form ettringite ($3CaO \cdot Al_2O_3 \cdot 3CaSO_4 \cdot 32H_2O$). It has also been reported that the ingress of sulfate ions into OPC materials can cause the transformation of Ms into AFt [12]–[14]. All of these chemical reactions lead to concrete expansion and cracking, which seem to appear when tensile stress due to restrained expansion exceeds the tensile strength of the matrix (theory of crystallization pressure) [15]–[17]. Eventually, this damage can lead to softening and decohesion of OPC-based concretes [8], [9], [18].

According to the literature, two types of ESA have been identified in Portland cement-based materials: (i) an attack characterized by the formation of ettringite in hardened matrices containing high C_3A content, and (ii) an attack characterized by the formation of gypsum in materials with low C_3A content [14]. Therefore, several parameters should be taken into account in the formulation of concretes destined to be in contact with sulfates. According to Escadeillas and Hornin [3], the main parameters are:

Environmental parameters: The European Standard NF EN 206-1 defines different exposure classes to formulate a concrete when exposed to chemical attacks. The exposure class is selected depending on the sulfate concentration present in either groundwater or natural soil. Hence, three different exposure classes are defined, and they are presented in Table 1.2: XA1 "slightly aggressive chemical environment", XA2 "moderately aggressive chemical environment" and XA3 "highly aggressive chemical environment". This classification allows for improved selection of parameters for the formulation of durable concrete, such as the minimum cement content and the water to cement (w/c) ratio [3].

Table 1.2 – Ranges of sulfate concentrations given in mg/L depending on the exposure classes of concretes under chemical attacks according to EN 206-1.

	Concentration of sulfate (SO_4^{2-}) in mg/L		
Exposure class	XA1	XA2	XA3
Groundwater	≥200 and ≤600	>600 and ≤ 3000	>3000 and ≤ 6000
Natural soils	≥2000 and ≤3000	>3000 and ≤ 12000	>12000 and ≤ 24000

<u>Chemical parameters</u>: The alumina content in the form of anhydrous aluminates (mainly C_3A) seems to be the most important chemical parameter to influence the resistance of OPC materials to ESA. C_3A reacts with sulfate ions at a late stage to form ettringite ($3CaO·Al_2O_3·3CaSO_4·32H_2O$) causing expansion and degradation in the material [3], [19], [20]. Ettringite forms following the reaction presented in Equation 1 [3]:

Equation 1. $3CaO·Al_2O_3 + 3CaSO_4·2H_2O + 26H_2O \rightarrow 3CaO·Al_2O_3·3CaSO_4·32H_2O$
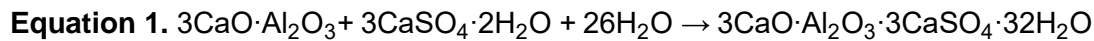
As a result, the French Standard NF P15-317 proposes 10% as the upper limit in C_3A content for Portland cement clinker under sulfate environments, these cements are referred to as cements "PM". The French Standard NF P 15-319 refers to the cements destined for being in contact with water at high sulfate concentrations as cements "ES" and proposed 5% as the upper limit in C_3A content for Portland cement [3]. Similarly, the European Standard EN 197-1 proposes that the amount of C_3A should not exceed 5% when Portland cement clinker is used to make sulfate-resisting Portland cements. As an example, Ouyang et al. [20] studied ESA in four OPC-based mortars batched with a w/c ratio of 0.6 and with four different amounts of C_3A (12%, 8.8%, 7% and 4.3%). Mortars were immersed in a sulfate solution containing 4.3% magnesium sulfate and 2.5% sodium sulfate. They showed that expansions in mortars increased with increasing the C_3A content. Moreover, they also verified that mortars with low C_3A content (4.3% and 7%) presented a lower rate of expansion in time compared to the ones with high C_3A content (8.8% and 12%). Figure 1.1 illustrates the results obtained by Ouyang et al. In this figure, x and y-axes represent the time given in months and the expansion given in percentage, respectively.

Figure 1.1 – Expansion in percentage as a function of time in months of OPC mortars immersed in a sulfate solution (4.3% magnesium sulfate and 2.5% sodium sulfate). W/c ratio = 0.6, C_3A amounts: 12%, 8.8%, 7% and 4.3%. Taken from Ouyang et al. [20].

Physical parameters: The water to cement (w/c) ratio usually defines the porosity in OPC-based materials. This parameter also influences their permeability and their mechanical strength. Several authors showed that the rate of degradation of OPC-based concretes under ESA increased with increasing the w/c ratio [3], [20]. Figure 1.2 shows the results of the influence of w/c ratio in the expansion of OPC under ESA obtained by Ouyang et al. [20], who studied OPC mortars immersed in a solution containing 4.3% magnesium sulfate and 2.5% sodium sulfate. Mortars were batched with three different w/c ratios (0.45, 0.6 and 0.8) and with a 12% C_3A content. The authors showed that the rate of expansion in mortars increased with increasing the w/c ratio.
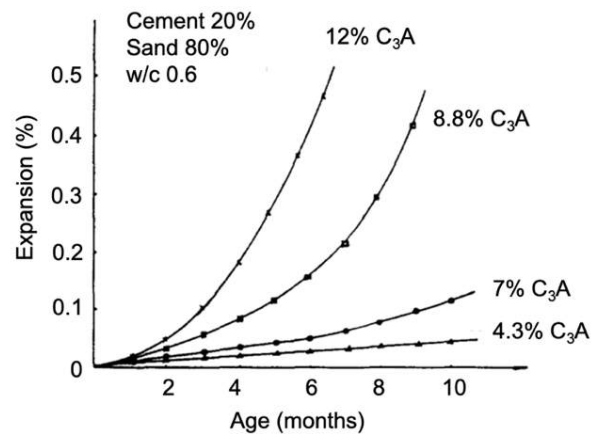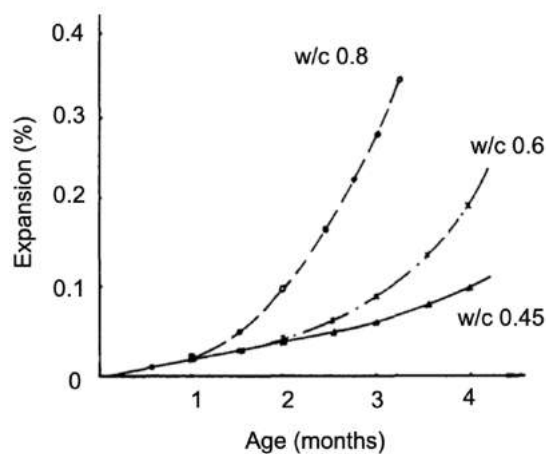

Figure 1.2 – Expansion in percentage as a function of time in months of OPC mortars immersed in a sulfate solution (4.3% magnesium sulfate and 2.5% sodium sulfate). W/c ratios: 0.45, 0.6 and 0.8 and C_3A content of 12%. Taken from Ouyang et al. [20].

1.1.1.2   Sulfate-resisting Portland cements

Some modifications in the chemical compositions of classical OPCs have been made by varying the C_3A content in order to improve their durability under ESA. These cements are referred to as sulfate-resisting Portland cements (SR-Cements) because of the low C_3A content [21]–[23]. Some of these materials do not contain C_3A (e.g. CEM I-SR0 in accordance with EN 197-1). Instead, they have high amounts of tetracalcium alumino-ferrite (C_4AF), which reacts with lower kinetics compared to C_3A [21]–[23]. However, the hydration process of both phases C_3A and C_4AF are similar: first, the formation of ettringite and then, when gypsum is consumed, its conversion into calcium monosulfoaluminate (Ms) [23]. Tragardh and Bellmann [24] explained that C_4AF is less reactive at low Al/Fe ratios and thus, SR-cements are made with raw materials containing low amounts of alumina in order to ensure the low rate of C_4AF reaction. As a result, ettringite forms at a very slow rate and in a minor extent in these materials compared to the ones containing high amounts of C_3A.

The main hydration products of SR-cements are CH and C-S-H. Table 1.3 presents the three types of SR-cements according to the European Standard EN 197-1.

Table 1.3 – Types of sulfate-resisting Portland cements according to EN 197-1.

Type	Amount of C_3A in the clinker
CEM I-SR 0	0%
CEM I-SR 3	≤3%
CEM I-SR 5	≤5%

Several authors have shown that SR-Portland cement-based materials presented lower expansions than those in OPC materials when exposed to ESA [21]–[24]. Despite this, these materials have also presented damages. In some cases, SR-Portland cement-based materials showed delayed expansions and micro cracking, which have been attributed to the formation of gypsum. According to the literature, in these types of cement under ESA, gypsum might form besides ettringite, leading to the decohesion of the materials [12]–[14], [21]–[24].

1.1.1.3   Blast furnace cements

Blast furnace cements are blended cements mainly composed of ground granulated blast furnace slag (GGBS) and Portland cement or Portland clinker. GGBS is a product from the ferrous metallurgy industry, and it is mainly composed of four oxides: lime (CaO) (30-50%),

silica (SiO_2) (28-38%), alumina (Al_2O_3) (8-24%) and magnesia (MgO) (1-18%). There are also some minor elements such as sulfur (S), manganese oxide (MnO), iron oxide (Fe_2O_3), titanium oxide (TiO_2) and alkalines (Na_2O and K_2O) [10], [25].

When the liquid slag, coming out of the furnace, is rapidly cooled down, it forms a glassy structure which has latent hydraulic properties. This means that it is necessary to activate it in order to initiate its reaction with water. To this end, the pH of the system has to be high enough (pH 11 – 12); therefore, clinker or Portland cement is generally added to the mixture [10]. In these types of cement, the clinker provides the ions calcium (Ca^{2+}), the hydroxides (OH^-) NaOH and KOH, which activate the dissolution of the slag and the formation of C-(A)-S-H, which is the main hydration product of these types of cement.

The reaction between the slag and the lime is represented in the theoretical Equation 2 (C-S-H with an Ca/Si ratio of 1.5) [25].

Equation 2. $C_5S_3A + 2\ C + 16H \rightarrow C_4AH_{13} + 3\ CSH$
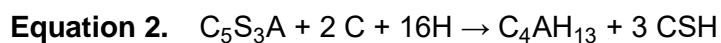
Slag + lime + water → calcium silicate hydrate

When the slag contains high amounts of magnesium and it is activated by clinker or Portland cement, the phase hydrotalcite may also precipitate.

Table 1.4 presents the three types of blast furnace slag cement depending on their proportions in GGBS and Portland clinker according to the European Standard EN 197-1.

Table 1.4 – Types of blast furnace slag cement according to EN 197-1.

Type	Blast furnace slag	Portland clinker
CEM III/A	36-65%	35-64%
CEM III/B	66-80%	20-34%
CEM III/C	81-95%	5-19%

Several studies have shown that blended cements generally improve the durability of concrete exposed to ESA [17], [24], [26]–[28]. In addition to the decrease in the C_3A content due to the dilution effect [24], the addition of pozzolans to OPC produces positive impacts on sulfate attack because of the consumption of portlandite (CH) to produce C-(A)-S-H and reduce the formation of gypsum [27]. Since blended cements consume a significant proportion of CH, the hydration of these types of cement decreases the pH and subsequently, minor quantities of ettringite are formed [17], [27]. Additionally, the incorporation of GGBS densifies the

microstructure and decreases the porosity of concretes reducing the capillary pore size and therefore, the ingress of sulfate ions from the environment into the matrix [24], [26].

Blanc [28] showed that CEM I-based mortars presented significant expansions (0.5%) compared to those measured in CEM III/C-based mortars (< 0.1%) after 56 weeks of exposure in a sulfate solution at 50 g/L. He explained that the low expansion of CEM III/C-based mortars was a result of the low C_3A content. Similarly, Al-Amoudi [27] showed that blended cements exposed to sulfate environments were highly resistant to sodium sulfate attack compared to classic cements. They saw that blended cements-based specimens, especially those containing silica fume and blast furnace slag, presented low expansions and minor strength loss after attack. They explained that the reduction of CH and the densification of the microstructure diminished the production of deleterious ettringite.

Colas [29] studied the expansion of mortars batched with CEM I and CEM III/C cements and with sulfate-rich aggregates and immersed in water at 20 ºC. Figure 1.3 presents the expansion results obtained by Colas. From this figure, it can be observed that CEM I mortar expansions increased linearly in time and reached about 0.5%. In the contrary, CEM III/C mortars presented lower expansions and reached about 0.1% of expansion at the end of the tests.
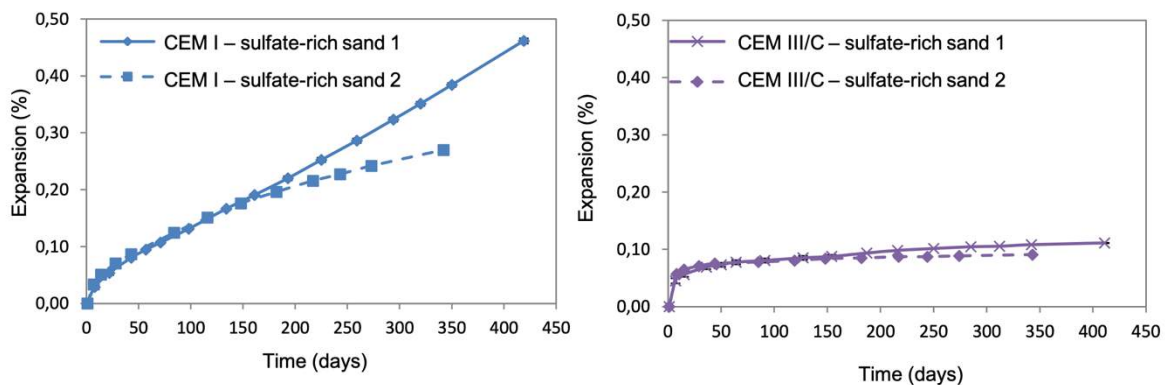
Figure 1.3 – Expansion of CEM I and CEM III/C-based mortars batched with two different sulfate-rich aggregates and immersed in water at 20 ºC. Taken from Colas [29].

It should be noted that some studies have shown that slag blended cements can also suffer some degradations under ESA in a long-time period due to the gradual loss of surface (e.g. delamination, dusting, scaling) [30].

1.1.2 Alternative binders under external sulfate attack

Other binders have also been reported as efficient alternatives to classical Portland cements under ESA [9], [20], [31]–[35]. This section describes the main chemical characteristics of two groups of alternative binders (alkali-activated and ettringite binders) and their behavior under ESA.

1.1.2.1 Alkali-activated materials

Alkali-activated materials (AAM) are made by mixing an alkaline activating solution with solid powders, sources of aluminosilicates (e.g. ground granulated blast furnace slag (GGBS), metakaolin (calcinated clay) or fly ash) [19], [36]. The chemistry of AAM depends on the nature of both the source of aluminosilicates and the alkali activator. The common activating solutions are alkali silicate-based and alkali hydroxide-based such as sodium or potassium activators [37].

Some sources of aluminosilicates can contain high calcium contents (e.g. GGBS); therefore, the main reaction product is C-(A)-S-H. When the raw material is GGBS, the alkali-activated material is referred to as alkali-activated slag (AAS). On the other hand, the reaction produced between a source of aluminosilicates without calcium and activated by an alkali hydroxide or silicate solution is referred as to "geopolymerization". This process involves the dissolution of alumina and silica in the alkaline solution and the chemical reaction produces a synthetic material with a network of three dimensions Si-O-Al-O. This structure is similar to the structures of organic polymers and consequently the name "geopolymers" [19], [38], [39].

Several studies have shown that AAM may resist better to ESA than OPCs and this resistance may vary depending on the raw material composition and the activator used [9], [26], [31], [32], [40]–[45]. For example, Allahverdi et al. [41] studied the sulfate resistance of sodium silicate alkali-activated slag (AAS)-based mortars and two types of Portland cement-based mortars immersed in a solution containing 5% of sodium sulfate. After 360 days of exposure, the authors observed a reduction in the compressive strength of 45% and 71% in AAS and Portland cement mortars, respectively. Visual inspection allowed for detection of few surface scaling in AAS mortars explained by the crystallization of sodium sulfate in the surface. Meanwhile, OPC mortars presented large damages due to cracks and scaling in the corners. Additionally, longitudinal expansions in AAS mortars were between 12 and 8 times lower than that resulted in Portland cement mortars. Figure 1.4 presents the results of longitudinal

expansions obtained by Allahverdi et al. This figure presents the length change in percentage as a function of exposure time in days.
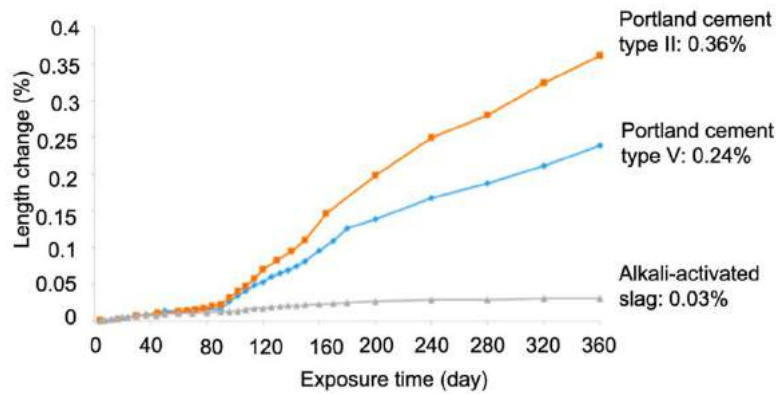
Figure 1.4 – Length change in percentage versus exposure time in days of alkali-activated slag mortars and Portland cement-based mortars immersed in a solution containing 5% of sodium sulfate. Taken and modified from Allahverdi et al. [41].

Similarly, Komljenović et al. [40] showed that a sodium silicate AAS did not present expansion after immersion in a 5% Na_2SO_4 solution. The authors explained that AAS resisted better to ESA than OPC due to the absence of CH and the unavailability of aluminum for reaction with sulfates due to the formation of calcium aluminosilicate hydrate (C-A-S-H) and hydrotalcite (M_5AH_{13}) during hydration. On the other hand, Ye et al. [42] and Ismail et al. [43] showed that an AAS presented higher sulfate resistance in Na_2SO_4 solutions than that in $MgSO_4$, which produced high decalcification of C-A-S-H. It means that degradation mechanisms of AAM under ESA are related with the nature of the cation associated with the sulfate ions.

The durability of AAM under ESA has also been linked to its calcium content, in other words, the sulfate resistance of AAM decreases with increasing calcium content because of the formation of secondary phases such as ettringite and gypsum [32], [44], [45]. For example, Duan et al. [32] studied the influence of partial replacement of calcareous fly ash by metakaolin (MK) in a calcareous fly ash geopolymer under ESA. They measured the compressive strength before and after sulfate exposure and estimated the compressive strength loss ratio. They verified that the compressive strength loss of the geopolymer decreased with increasing replacement of MK. This was explained by the reduction of the calcium content and thus, the formation of expansive products which led to the degradation of the material. Figure 1.5 illustrates the results obtained by Duan et al. where x-axis and y-axis represent the compressive strength loss ratio in percentage and the exposure ages in days.
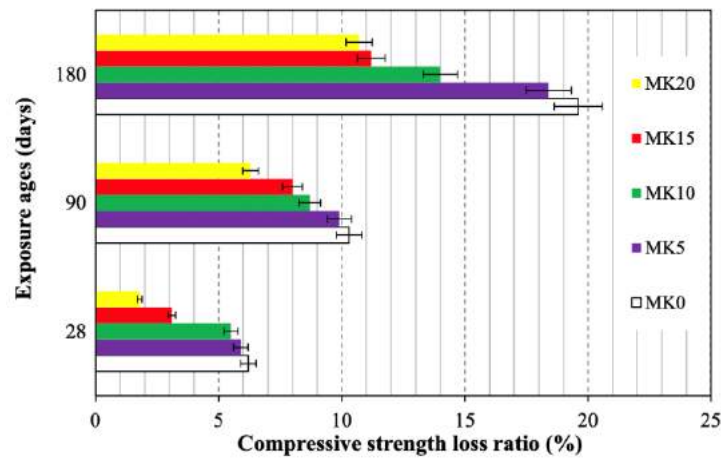
Figure 1.5 – Compressive strength loss ratio given in percentage of a calcareous fly ash geopolymer with partial replacement of calcareous fly ash by metakaolin. Materials immersed in a sulfate solution containing 5% sodium sulfate. Taken from Duan et al. [32].

1.1.2.2 Ettringite binders

Ettringite binders, such as supersulfated (SSC) and calcium sulfoaluminate (CSA) cements have also been studied under ESA showing good resistance to this phenomenon [19], [46]–[54].

Calcium sulfoaluminate belite cements (CSA)

CSA cements contain ye'elimite or tetracalcium trialuminate sulfate ($C_4A_3\bar{S}$), gypsum ($C\bar{S}H_2$) or anhydrite ($C\bar{S}$) and belite (C_2S) as major constituents [51]. In the case of CSA-belite cements, ye'elimite ($C_4A_3\bar{S}$) is used instead of alite (C_3S) to develop early-age strength, and belite (C_2S) is used to gain additional long-term strength [46]. Some CSA cements also contain ferrialuminate phases such as C_4AF [55], [56]. Unlike OPC, the content of C_3S and C_3A phases are very low or absent in CSA cements [51]. With water alone, $C_4A_3\bar{S}$ reacts to form calcium monosulfoaluminate (Ms) and aluminum hydroxide according to the reaction presented in Equation 3 [25], [55], [57].

Equation 3. $C_4A_3\bar{S} + 18H \rightarrow C_3A \cdot C\bar{S} \cdot 12H + 2AH_3$

Ye'elimite + water → mosulfoaluminate + aluminum hydroxide

The kinetics of CSA reaction is accelerated by the addition of calcium sulfate. In this case, ettringite is formed together with aluminum hydroxide as shown in Equation 4 [55]:

Equation 4. $C_4A_3\bar{S} + 2C\bar{S}H_2 + 34H \rightarrow C_3A\cdot3C\bar{S}\cdot32H + 2AH_3$
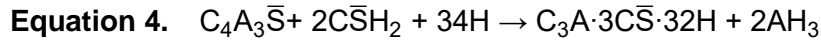
Ye'elimite + calcium sulfate (gypsum) + water → ettringite + aluminum hydroxide

Other hydration products such as C-S-H, monocarboaluminate or hydrogarnet may also form depending on the other minor constituents present in CSA cements. In the presence of belite (C_2S), the phase straetlingite (C_4ASH_8) may also precipitate [55].

Many studies [46]–[48] have been focused on the dimensional stability of CSA-belite cements; even though, the mechanisms of expansion of this binder is still a topic of discussion since there is a large variability of the composition of CSA cements. Some authors suggested that the expansions in this binder, during and after hydration, depend on diverse factors such as the contents of ye'elimite, calcium sulfate (dissolution rate varies as a function of the calcium sulfate source), free lime (CaO), and calcium hydroxide (CH) as well as the pore structure, the water to cement (w/c) ratio and the curing conditions [46]–[49], [58], [59].

Various studies have shown that high ye'elimite content (>50 wt%) produce expansion and cracking because the crystallization pressure of ettringite increases [49], [58]. However, others studies suggested that CSA cements would not be expansive if the most of this ettringite forms before hardening [46], [48]. On the other hand, Hargis et al. [47] explained that not only the crystallization pressure of ettringite contributes to expansion, but also the crystallization pressure of the other hydrates present in CSA cements such as aluminum hydroxide (AH_3), calcium aluminate decahydrate (CAH_{10}), monosulfoaluminate ($C_4A\bar{S}H_{12}$) and straetlingite (C_4ASH_8).

Other studies showed that the expansion in CSA may increase with increasing the amounts of calcium sulfate due to an accelerated reaction of ye'elimite to form ettringite causing a more rapid expansion [46], [47], [51]. Furthermore, the microstructure of ettringite formed in CSA cements seems to vary depending on the presence of calcium hydroxide (CH). According to Trauchessec [56], in the absence of lime (cf. Equation 4), the ettringite produced has no expansive effects and generates high early strength in the matrix. In contrast, ettringite produces expansion in the presence of lime. Similarly, Ndiaye et al. [59] showed that the addition of calcium hydroxide (CH) to a CSA binder led to a high volume expansions of the matrix during a few days of hydration. Some authors explained that when free lime (CaO) is available, the materials expand because the rate of ettringite formation is higher than those with no-free CaO content [46], [50].

Moreover, it has been reported that low w/c ratios in CSA cements may lead to large amounts of unhydrated cement after setting. This may represent a risk of durability if the material is later

in contact with water coming from the environment because of the formation of secondary ettringite, and thus the expansion of the material [46], [49]. Chen et al. [46] suggested that the interdependency of all the mentioned factors above (calcium hydroxide content, w/c ratio, ye'elimite content, calcium sulfate content, among others) should be verified in order to control the expansion in CSA cements.

As presented above, several studies have been concentrated on the dimensional stability of CSA cements rather than the understanding of their resistance under sulfate attack. Therefore, there are many unsolved questions and some information reported in the literature with respect to their expansion mechanisms under ESA is contradictory. For the reasons explained above, Chen et al. [46] suggested that CSA-belite cements should avoid contact with sulfate solutions in order to reduce their risk of expansion. On the contrary, other authors suggested that CSA-belite cements may resist better to ESA than classic Portland cements [19], [51], [52]. As example, Bescher et al. [52] observed that after two years of sulfate exposure, CSA-based mortars did not show signs of deterioration while different Portland cement-based mortars were highly affected. The authors pointed out that the absence of C_3A content in CSA mortars may be one of the reasons explaining the low expansions produced during the exposure to sulfates. As a reminder, in CSA cements, ye'elimite ($C_4A_3\bar{S}$) is the alumina source instead of C_3A, which is related with the formation of expansive ettringite. Bescher et al. [52] explained that $C_4A_3\bar{S}$ reacts during hydration to form ettringite; therefore, a later exposure to sulfates will cause no further reactions. In addition to this, they indicated that the formation of low amounts of C-S-H may favor the good resistance of CSA cements to magnesium sulfate attacks since C-S-H is the most affected phase in this type of attack.

Figure 1.6 shows the results obtained by Bescher et al. in terms of weight change. X-axis and y-axis represent the age of exposure in months and the weight change in percentage, respectively.
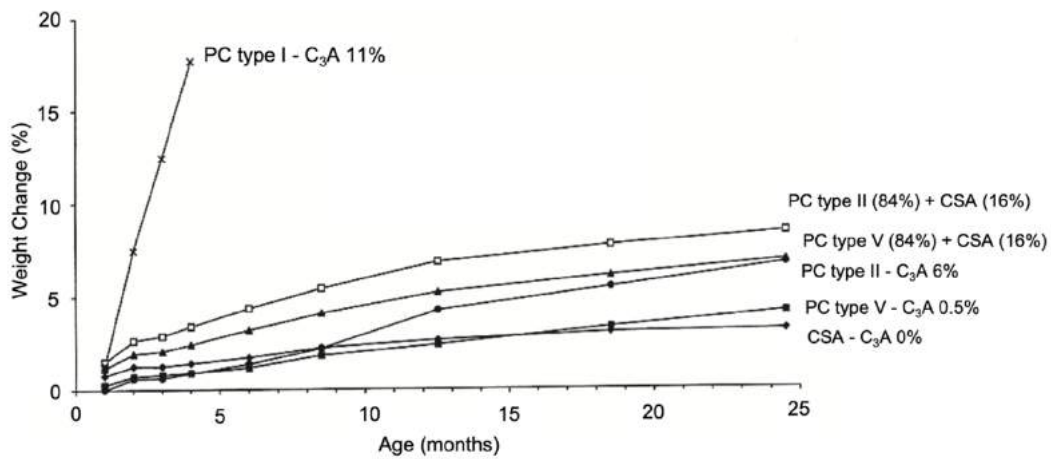
Figure 1.6 – Weight change in percentage versus age of exposure in months of mortars immersed in a sulfate solution containing 10% sodium sulfate. PC: Portland cement. Taken and modified from Bescher et al. [52].

Supersulfated cements (SSC)

According to the literature, supersulfated cements (SSC) are generally composed of blast furnace slag (70-90%), calcium sulfate (10-20%) (mainly gypsum or anhydrite), and an alkali activator [47], which is often Portland cement in small quantities (<5%) [19], [60]. The typical chemical composition of supersulfated cements is presented in Table 1.5.

Table 1.5 – Typical chemical composition of a supersulfated cements [60]

Oxyde	Proportion (%)	Oxyde	Proportion (%)
CaO	41 – 45	MgO	2.6 – 7
SiO_2	24 – 30	Na_2O	0.3 – 0.7
Al_2O_3	11 – 14	K_2O	0.52 – 1.1
Fe_2O_3	0.5 – 1	SO_3	5 – 9
Mn_2O_3	0.7 – 1.2	S	< 2
TiO_2	0.4 – 0.8	P_2O_5	< 0.3

The hydration of SSC consists of the dissolution of the slag due to the alkaline environment of the pore solution. The reaction of dissolved aluminum, calcium and silicon ions with the added calcium sulfate leads to the formation of the main hydration products C-(A)-S-H and ettringite (AFt). These products are formed following the Equation 5 [29].

Equation 5. $C_5S_3A + C + 3C\bar{S}H_x + yH \rightarrow C_3A \cdot 3C\bar{S} \cdot 32H + 3CSH$

Slag + lime + calcium sulfate (gypsum) → ettringite + calcium silicate hydrate

The ettringite formed during hydration is not associated with destructive swelling of the matrix due to the precipitation of the ettringite crystals particularly in large pores [19], [25], [61]. Minor hydration products such as calcium monosulfoaluminate (Ms) ($C_3A \cdot CaSO_4 \cdot 12H_2O$) and hydrotalcite may also occur [61].

SSC cements have been reported in the literature as sulfate-resisting binders because their durability in sulfate attack is higher than that of OPCs [19], [25], [53], [54], [60], [62]–[64]. Such sulfate resistance has been mainly attributed to (i) the low content or absence of calcium hydroxide (CH), and (ii) the consumption of most of the free alumina, coming from the slag, to form ettringite during hydration without producing expansion [60].

Grounds et al. [53] studied the sulfate resistance of SSC-based mortars cured at different conditions and exposed to sodium sulfate, magnesium sulfate and saturated calcium sulfate. The authors showed that SSC mortars, cured at 100% relative humidity (RH), did not present expansion or visible signs of attack after 9 months of immersion in calcium or sodium sulfate solutions. Meanwhile, samples cured at low RH (11%) presented expansion due to the rehydration of the binder; however, these mortars did not present cracking. In contrast, all SSC mortars exposed to magnesium sulfate presented an extensive surface damage and high linear expansions (about 4%) regardless of the RH. The authors explained that the main degradation mechanism of SSC samples exposed to magnesium sulfate consisted of the C-S-H attack in addition to the precipitation of gypsum in large amounts.

Niu et al. [54] also studied the resistance of SSC-based mortars immersed in a sodium sulfate solution. They indicated that SSC mortars presented an expansion of about 7 times lower (0.06%) than that in OPC (about 0.4%). The authors also attributed the low expansion of SSC mortars to the very small content of clinker and thus, a very low amount of CH, which was consumed by the pozzolanic reaction to form ettringite and C-S-H. Therefore, free CaO coming from the clinker was insufficient to react with the sulfate ions coming from the sodium sulfate solution. Figure 1.7 presents the results of expansion obtained by Niu et al. where x-axis and y-axis represent the time exposure in weeks and the ratio of expansion of mortars in percentage, respectively.
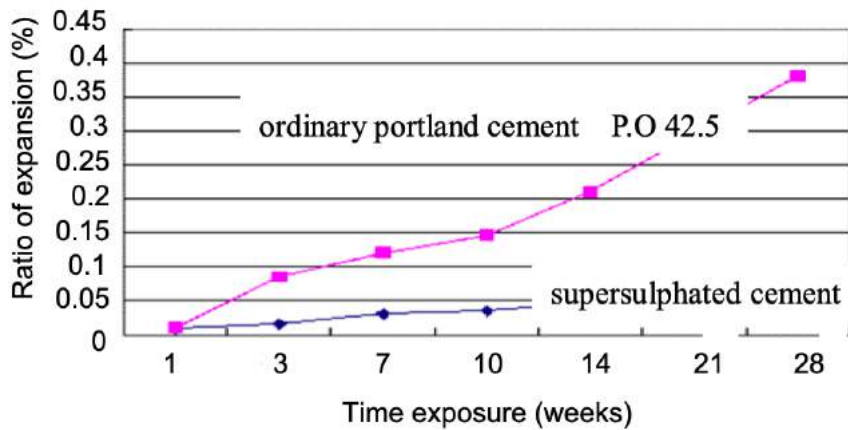
Figure 1.7 – Ratio of expansion in percentage versus time of exposure in weeks of supersulfated cement and OPC mortars immersed in a solution of 5% sodium sulfate. Taken and modified from Niu et al. [54].

Colas [29] studied the expansion of mortars batched with CEM I and SSC cements by using sulfate-rich aggregates and immersed in water at 20 °C. Figure 1.3 presents the expansion results obtained by Colas. From this figure, it can be observed that expansion of CEM I mortars increased linearly in time and reached about 0.5% of expansion. In the contrary, SSC mortars presented very low expansions reaching about 0.02% at 407 days of tests. According to Colas, the low expansion of SSC mortars was explained by the low content of portlandite, which in CEM I-mortars led to the formation of expansive ettringite. In SSC binders, well crystallized ettringite forms in the interstitials; therefore, this type of ettringite is considered non-expansive.
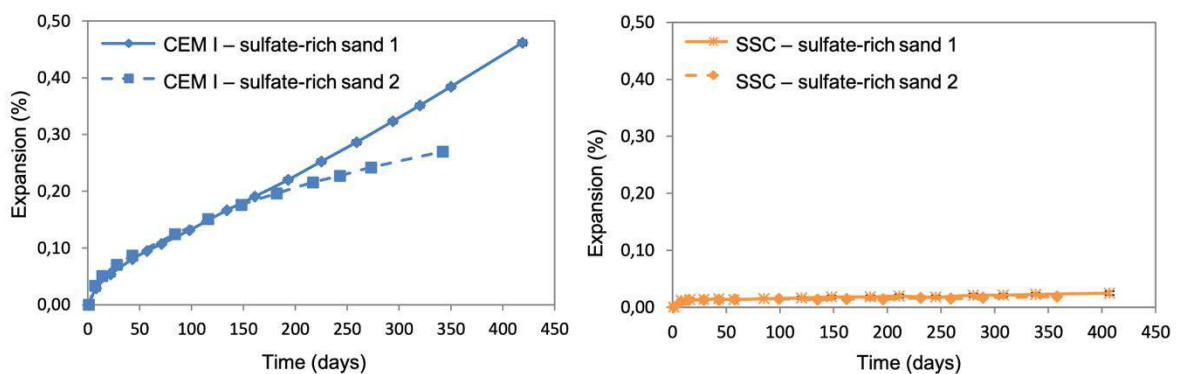
Figure 1.8 – Expansion of CEM I and SSC-based mortars batched with two different sulfate-rich aggregates and immersed in water at 20 °C. Taken from Colas [29].

In this previous section, we presented the reaction of different binders in contact with external sulfates. It was shown that Portland cement-based materials do not present good characteristics to resist ESA. Meanwhile alternative binders present better performance to ESA (low expansion and low degradation). Nonetheless, comparisons between these binders are difficult due to the difference in the experimental conditions.

In the next sections, we deal with the durability problem of sulfate-rich soil treated with cementitious binders.

1.2 Valorization of sulfate-rich soil for reuse

In this study, we use the term "reuse" to refers to the operation by which the soil, that is not considered as waste, is used again for civil engineering purposes. Soil containing sulfates can be reused after treatment. The use of cementitious binders may allow for the valorization or reuse of sulfate-rich soil for civil engineering applications (e.g. subgrades and backfills).

According to the French Technical Guide GTR (*Guide technique pour la réalisation des remblais et des couches de forme*) [65] when treated soil (by lime or hydraulic binder) is destined to the realization of subgrades, it has to be assessed in accordance with the French Standard NF P 94-100 [66]. This standard proposes geotechnical experiments to verify the volume expansion and the indirect tensile strength of compacted soil. The performance of a treated soil is suitable when volume expansions are inferior to 5% and when indirect tensile strengths are superior to 0.2 MPa. Furthermore, the treated soil has to be evaluated in terms of workability and mechanical performances.

The French technical guide GTS (*Traitement des Sols à la chaux et/ou aux liants hydrauliques*) [66] published by the Laboratoire Central des Ponts et Chaussées (LCPC) and the Service d'Études Techniques des Routes et Autoroutes (SETRA) explains that the mechanical properties of soils (e.g. workability, impermeability, stability, bearing capacity) are improved by adding lime (quicklime or hydrated lime), hydraulic cements (e.g. Portland cement) or other binders such as blast furnace slag cement, fly ash, among others. Several benefits can be cited when soils are treated by lime: swell and plasticity reduction, improved stability, drying [67]. The addition of lime increases the pH of the system (above 10) and consequently, clay dissolves and releases aluminates and silicates. Then, pozzolanic reaction takes place in the soil when pH is superior to 12. In this reaction, the calcium from the lime reacts with the

aluminates and silicates (coming from the clay) and leads to the production of calcium silicate hydrates (C-S-H) and calcium aluminate hydrates and thus, a long-term strength in the soil [66]. However, when a soil containing sulfates is treated by lime or Portland cement, the treatment represents a potential risk to the stability and durability of the material application due to expansive reactions induced in the treated soil [67], [68].

In the following sections, we explain in detail the reactions that take place in a sulfate-rich soil treated with Portland cement or lime. We also present the benefits reported in the literature when sulfate-rich soil is treated with alternative binders.

1.2.1 Swelling of sulfate-rich soil treated with lime or ordinary Portland cement

Several studies have highlighted that sulfate-rich soil treated with either ordinary Portland cement (OPC) or lime led to volume expansions [2], [29], [68]–[74]. Moreover, it has been shown that soil containing clay (>10 wt%, % by weight of dry soil) and sulfate concentrations greater than 1 wt% produced swelling after treatment with lime or Portland cement [68], [75]. As mentioned previously, at high pH values (pH>10.5), clay releases alumina, which reacts with calcium ions (coming from OPC or lime) and the sulfates ions in the soil, and also the water available in the soil to form expansive products (e.g. ettringite) [68], [70], [75], [76]. As example, Wang et al. [74] investigated the expansion of a soil treated with Portland cement of type I. Figure 1.9 presents the expansion of the soil treated by different proportions of Portland cement. From this figure, it can be observed that expansion started immediately at the beginning of the curing. Additionally, the expansion was directly proportional to the amount of Portland cement added to the soil. The maximum expansion in the soil (6%) was obtained when 20% of cement was added to the soil.
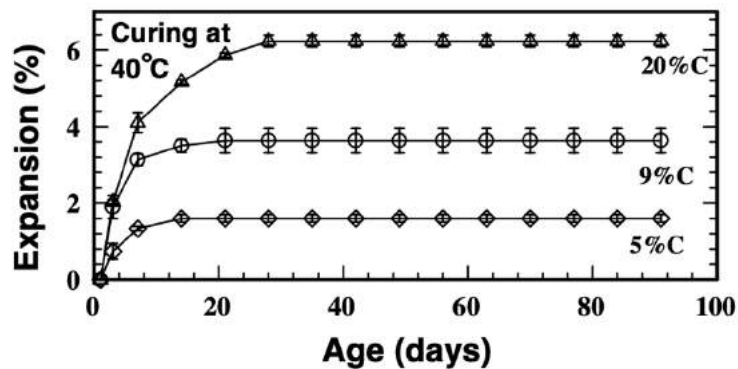
Figure 1.9 – Expansion of a sulfate-rich soil treated by Portland cement and cured in water at 40ºC. C: Portland cement. Taken from Wang et al. [74].

Hunter [68] proposed a simplified geochemical system to explain the reactions of expansion in sulfate-rich soils treated with lime or OPC. This system is divided into four steps presented in Equation 6, Equation 7, Equation 8 and Equation 9. Moreover, Figure 1.10 presents a diagram explaining the reaction of sulfate-rich soil treated by OPC or lime.

Equation 6. $CaO + H_2O \rightarrow Ca(OH)_2$ – *lime hydration*

Equation 7. $Ca(OH)_2 \rightarrow Ca^{2+} + 2(OH)^-$ – *portlandite dissolution*

Equation 8. $Al_2Si_2O_{10}(OH)_2 \cdot nH_2O + 2(OH)^- + 10H_2O \rightarrow 2Al(OH)_4^- + 4H_4SiO_4 + nH_2O$
   Dissolution of clay minerals because of pH > 10.5.

The dissolution of clay minerals provides to the soil dissolved silica and alumina, which can react with calcium ions. In this example, the clay mineral presented by Hunter [68] is the montmorillonite. As long as the source of aluminum exists, this reaction can be applied to any soil (OPC is also a source of aluminum).

Equation 9. $6Ca^{2+} + 2Al(OH)_4^- + 4OH^- + 3SO_4^{2-} + 26H_2O \rightarrow Ca_6[Al(OH)_6]_2 \cdot (SO_4)_3 \cdot 26H_2O$
   Long-term precipitation of expansive phases: sulfate chemically reacts with calcium and aluminum ions and the water available in the soil to form ettringite.

It should be noted that at low temperatures (<15°C), ettringite transforms into thaumasite due to the substitution of alumina by silica and the substitution of sulfate by carbonate. However, this phenomenon was not studied in the present work.

Present in the binder for treatment

Present in the soil

Water ➕ Sulfates ➕ Alumina ➕ Calcium ions ➕ = Ettringite

- Gypsum or anhydrite

- Coming from the dissolution of clays present in the soil due to the reaction with lime

- Coming from ordinary Portland cement

- Coming from the lime or the ordinary Portland cement

$$20H_2O \; + \; 3(CaSO_4 \cdot 2H_2O) \; + \; 3[CaO,Al_2O_3,6H_2O] \; \rightarrow \; 3CaO,Al_2O_3,3CaSO_4,32H_2O$$
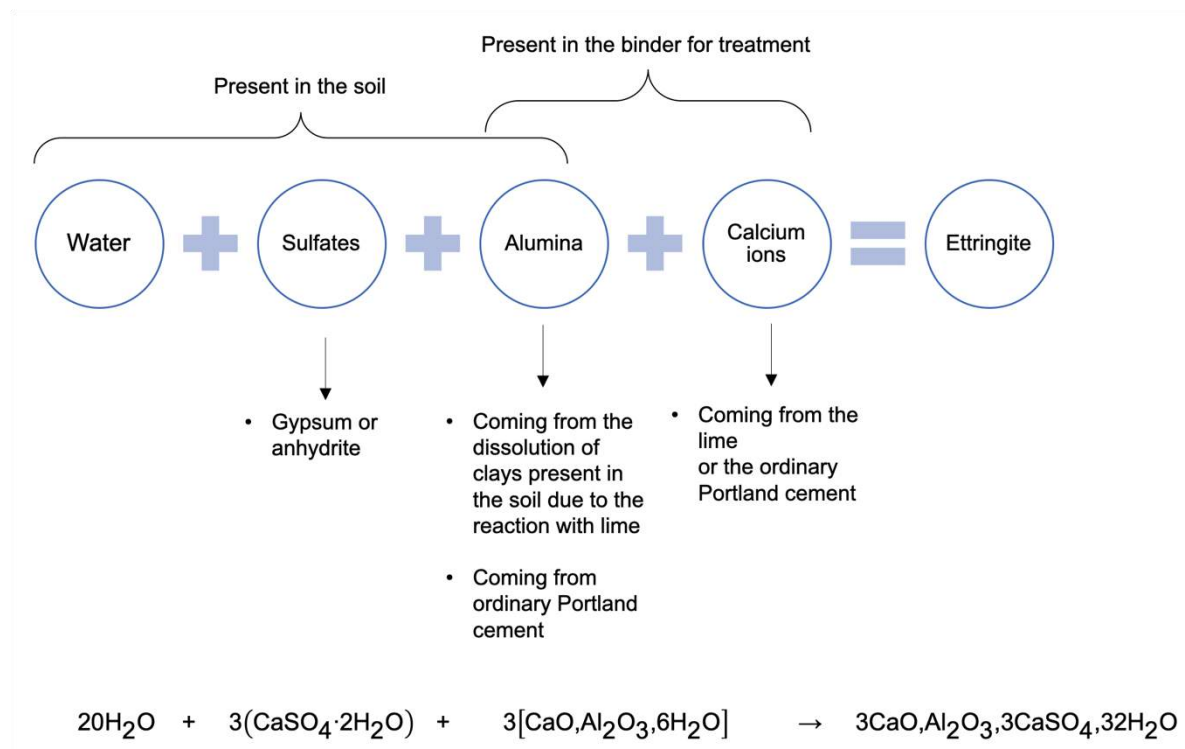
Figure 1.10 – Schema explaining the reaction of sulfate-rich soil treated by OPC and lime. Equation taken from Le Roux et Orsetti [1].

1.2.2 Treatment of sulfate-rich soil by using alternative binders

It has been reported that the swelling potential of sulfate-rich soil decreased when they are treated with binders other than lime or OPC [2], [70], [71], [73], [74], [76]–[78]. Several researchers have focused on the use of ground granulated blast furnace slag (GGBS) to treat sulfate-rich soil. It has been reported that GGBS is effective because of the decrease in expansion while improving the mechanical properties of the soil [71], [79]–[83]. As explained previously, GGBS is activated by a small amount of clinker and the mixture with sulfates leads to the formation of small quantities of non-expansive ettringite [29], [71]. Furthermore, it is known that the shape, size and rate of crystallization of ettringite depend on the raw composition of the binder used in each treatment [84].

Wang et al. [74] investigated the expansion of an anhydrite soil by replacing a part of OPC by GGBS as a function of different curing conditions. Figure 1.11 shows the results obtained by Wang et al., in which the expansion in expressed in percentage as a function of the age in days. From this figure, it can be observed that the treatment of the anhydrite soil with 100% OPC led to high expansions (>4%). Moreover, it can be observed that the replacement of 50% of OPC by GGBS decreased the amount of expansion in the soil (<0.4%). When more than

50% of OPC was replaced by GGBS, the expansion was near 0.1% and did not depend on the curing conditions.
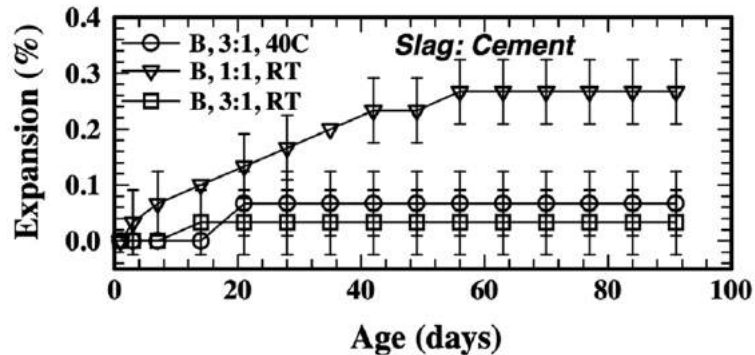
Figure 1.11 – Expansion of an anhydrite soil treated by different mixtures of Portland cement and GGBS at different curing conditions. 40C: in water at 40ºC, RT: room temperature (23 ºC) C: Portland cement. Taken from Wang et al. [74].

Similarly, Celik and Nalbantoglu [70] showed the effectiveness of slag in the treatment of soils containing different concentrations of sulfate. They found that a soil containing 10000 mg/kg of dry mass of sulfates and treated with only lime presented swelling of about 8% with respect to the initial volume of the sample. However, when slag was added, the swelling was reduced to 1%. These results are presented in Figure 1.12 where three different conditions are presented: untreated soil without sulfates (CS), treatment of sulfate-rich soil by using 5% lime (CS+5L), and treatment of sulfate-rich soil by using 5% lime and 6% slag (CS+5L+6S). It can be observed that (i) swelling increased with increasing the sulfate concentration in the soil, and (ii) treatment with slag was effective for decreasing the potential swelling of sulfate-rich soils.
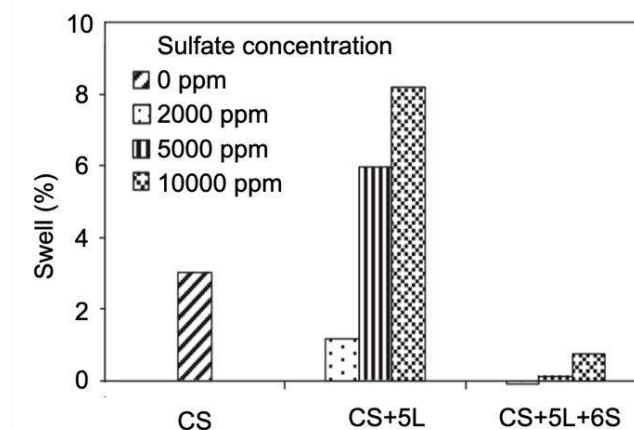
Figure 1.12 – Swelling in percentage of a soil containing sulfates (sulfate concentrations: 0, 2000, 5000 and 10000 ppm). CS = natural soil without sulfates. Treatments: CS+5L = 5 wt% lime, CS+5L+6S = 5 wt% lime + 6 wt% slag. Taken from Celik and Nalbantoglu [70].

Likewise, Wild and Tasong [81] and Tasong et al. [82] studied the expansion of a clay soil treated by different mixtures composed of GGBS and lime and exposed to a sodium sulfate solution. They showed that the treatment of the soil with 6 wt% of a binder, composed of 83% GGBS and 17% lime, presented expansions were inferior to 2%; while treatments with 100% lime led to expansions superior to 10%. The authors explained the decrease in swelling with the slag treatment due to the limited supply of calcium ions, and thus, the limitation of the growth in size of ettringite to produce expansion.

Wild et al. [83] also demonstrated that the proportion of GGBS influenced the magnitude of expansion in a soil treated with a mixture of GGBS and lime. They showed that the expansions in the sulfate-rich soil decreased with increasing the GGBS content. The decrease in expansion was explained by the consumption of lime by the GGBS to be activated [83]. In this case, the dissolution of GGBS became the dominant reaction and the amount of lime was considered insufficient to enable the precipitation of large amounts of expansive phases [83]. Similarly, Puppala et al. [73] studied the treatment of sulfate-rich soils (sulfate concentration superior to 4000 mg/kg of dry mass) by using four different binders: sulfate-resisting cement, a binder composed of lime and fibers, GGBS and class F fly ash. All the binders were added in the range of 0 to 20 wt%. The authors observed a decrease in the free swelling for all the treatments. For example, when 10% of GGBS was used for the treatment, the swelling in the soil decreased 4 times with respect to the initial swelling of the soil.

In the previous section, we presented information about the treatment of sulfate-rich soil by using cementitious binders. We saw that treatment of sulfate-rich soil by using lime or OPC can lead to durability issues due to the swelling of the soil. We also saw that treatment with binders, especially those containing GGBS binders may allow for the decrease of swelling.

In the following sections, we deal with the stabilization (immobilization) of sulfates by using cementitious binders.

1.2.3 Stabilization of sulfates by using cementitious binders

Stabilization is the chemical process allowing for the decrease of the potential harm of a waste because the pollutants become less soluble, less mobile or less toxic. This process is usually

completed with a mechanical process called "solidification" or encapsulation of waste. In this case, the transfer of pollutants into solution decreases with decreasing the exposed surface. These chemical and physical processes allow for the transformation of harmful wastes into acceptable materials from an environmental viewpoint [85], [86].

According to the literature, from an environmental viewpoint, the existing data do not identify a level of sulfate in drinking-water that can cause risks in human health. However, high concentrations of sulfates in drinking-waters (1000 mg/l to 1200 mg/l) can produce laxative effects when sulfates are combined with calcium and magnesium [87]. Other studies reported that sulfates can be detected by taste when mean concentrations in drinking-waters are greater than 237 mg/l, 370 mg/l and 419 mg/l for sodium sulfate, calcium sulfate and magnesium sulfate salts, respectively. Unpleasant taste was indicated in drinking-waters when calcium sulfate and magnesium sulfate concentrations were of about 1000 mg/l and 850 mg/l, respectively [87]. As a result, some organizations have defined the upper limits for sulfate concentration in water intended for consumption: the World Health Organization (WHO) set 500 mg/l [87] and the European Union in the Council Directive 98/89/ZC in 1998 set 250 mg/l.

In France, soil is classified in three categories depending on the leachable sulfate concentrations according to the French Ministerial decree on waste classification for disposal (*Arrêté du 12 décembre 2014*) [88]. It should be noted that the definitions of inert waste, non-hazardous and hazardous of the French Environmental code follow the European definitions (Directive 2008/98/EC, decision 2000/532/EC and decision 2001/573/EC).

Table 1.6 presents the different categories of wastes in France as a function of the limits of leachable sulfate concentrations.

Table 1.6 – Categories of waste as a function of the legal limits values of the leachable sulfate concentrations required by the French decree [88], [89]. Concentrations are given in mg/kg of dry soil and in percentage by weight of dry soil.

Waste category	Sulfate concentration		
Inert and non-hazardous	1000 mg/kg	10000 mg/L*	0.1%
Non-inert and non-hazardous	20000 mg/kg	200000 mg/L*	2%
Hazardous	50000 mg/kg	500000 mg/L*	5%

* Concentrations in mg/L were estimated by assuming 100 g of dry mass and a liquid to solid (L/S) ratio of 10.

The treatment of soil by using binders may be a solution to meet the sulfate limit concentration of 1000 mg/kg established by the French decree [88] for the "inert and non-hazardous waste" category. In the literature, preliminary work in this field focused mainly on the evaluation of the swelling phenomena in sulfate-contaminated soil (as reported in the last sections). However,

a few studies have deal with the decrease of leachable sulfate concentration after binder treatment and the sulfate stabilization mechanisms. As example, Trincal et al. [84] studied the effectiveness of several experimental binders to decrease sulfate leaching from gypsum-rich soils (maximum content of gypsum: 34 wt%). They observed that sulfates were partially immobilized by the formation of ettringite. Among all the formulations tested, the best result was obtained by adding about 5 wt% of a hydraulic binder mainly composed of ye'elimite ($C_4A_3\bar{S}$) and belite (C_2S). Leaching tests carried out with this formulation showed a decrease of 50% in the sulfate leachable concentration. Another study about the stabilization of sulfates was conducted by Bergmans et al. [90] who investigated the decrease of sulfate leaching in recycled aggregates. They showed that the sulfate concentration increased in solution with decreasing the leachate pH. Some authors explained that the pH dependency of sulfate leaching is in agreement with the ettringite solubility [90], [91]. In contrast, Colas observed that sulfate concentration increased in solution with increasing pH values. They showed that 55% of sulfates were in solution when pH leachate was 5; meanwhile 92% of sulfates were in solution when pH leachate was 13.5. Moreover, Colas [29] carried out leaching tests in excavation materials containing calcium sulfate in order to predict the behavior of sulfate-rich aggregates destined for the fabrication of concretes. They observed that sulfate concentration in solution increases with increasing the agitation rate of leaching tests. They explained that the kinetics of sulfate dissolution increased at high rates of agitation because the aggregates grains were less surrounded by other aggregates and therefore, they were in higher contact with the leaching solution. Figure 1.13 illustrates the results obtained by Colas for leaching tests of sulfate-rich aggregates with an agitation rate of 4 rpm. In this figure, x-axis and y-axis represent the agitation time in hours and the ratio of sulfate concentration in solution, respectively. As shown, sulfate concentrations (expressed in terms of SO_3) increased with the agitation time and with the pH of the leachate solution.

Colas [29] also indicated that sulfate concentration in solution increased with decreasing the grain size of aggregates. Figure 1.14 illustrates the leaching tests results carried out in sulfate-rich aggregates by using five different grain sizes. As shown, for a pH leachate of 13.5, sulfate concentrations in solution were about 90%, 85%, 80%, 40% and 20% for the grain sizes of 0/0.315 mm, 0.315/1 mm, 1/4 mm, 4/8 mm and 8/16 mm, respectively.
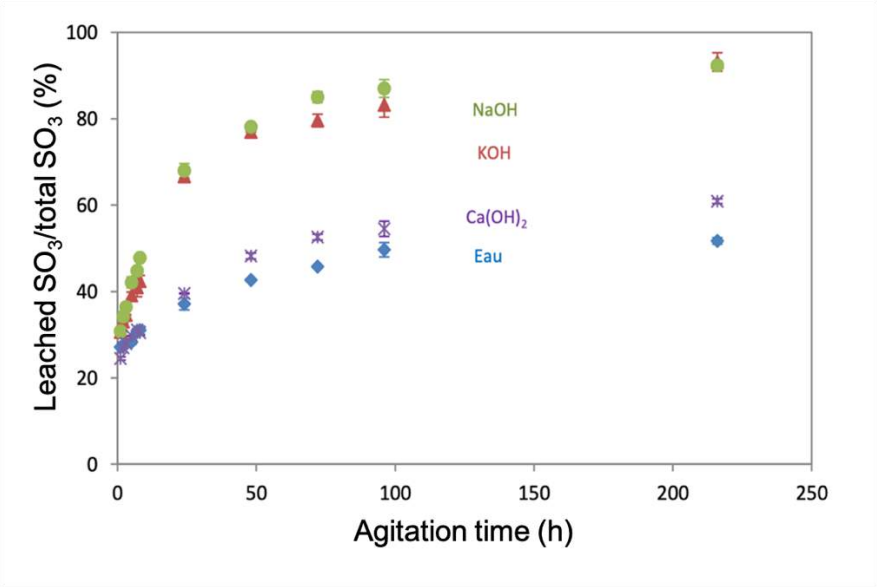
Figure 1.13 – Sulfate leaching from excavated sulfate-rich aggregates as a function of the leachate solution and the agitation time. pH values of NaOH: 13.5, KOH: 13.5, Ca(OH)$_2$: 12.6, Eau=Water: 5. Taken from Colas [29].
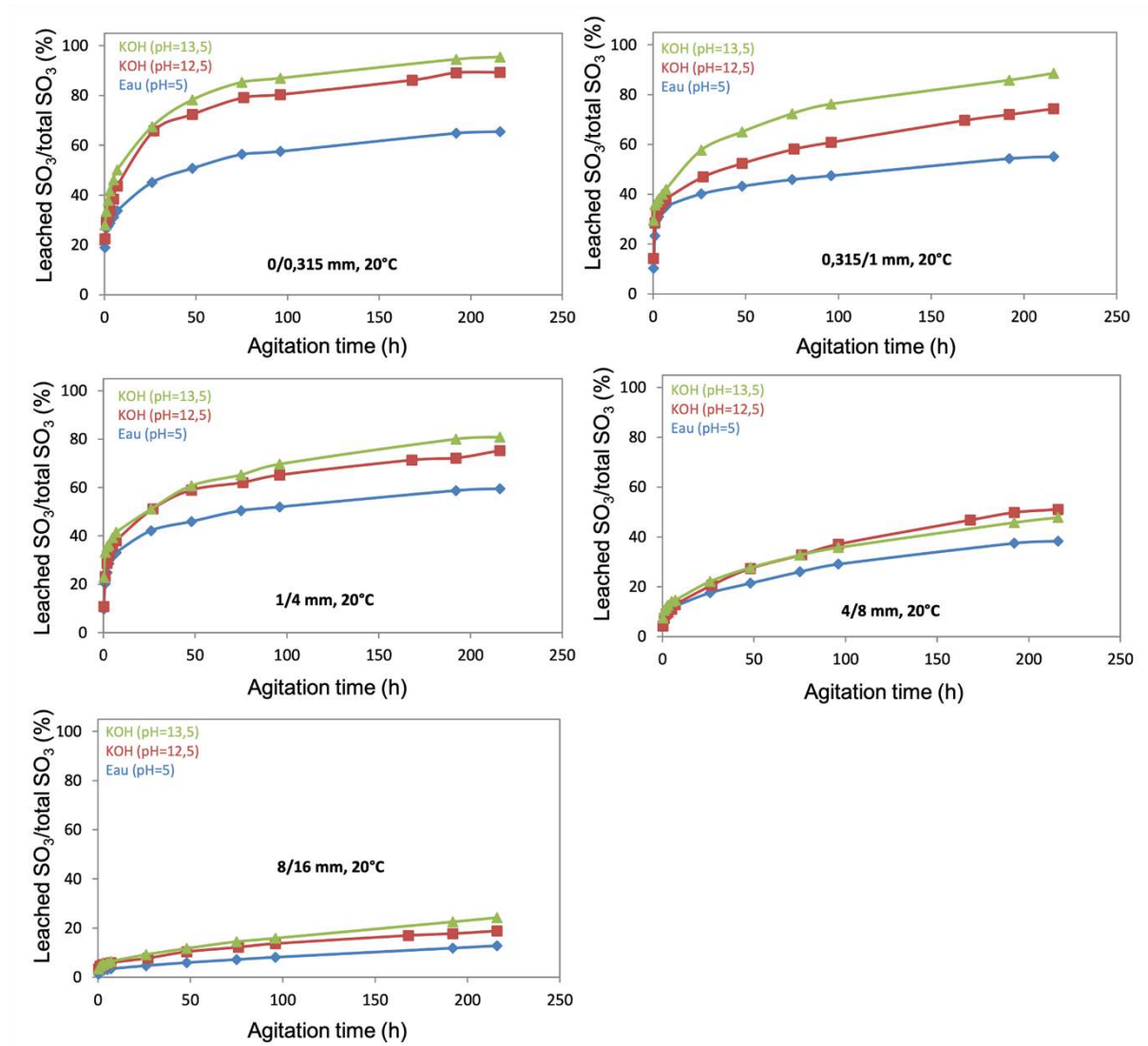
Figure 1.14 – Sulfate leaching from excavated sulfate-rich aggregates as a function of the leachate solution, grain size and time of agitation. Eau=Water. Taken and modified from Colas [29].

1.3 Stabilization of molybdenum

Molybdenum (Mo) is a heavy metal placed in the group VI of the periodic table. In this section, we first define the term of heavy metal and then, we describe their different sources and species in soil. Second, we present a more detailed overview of Mo. Finally, the different mechanisms of stabilization of heavy metals by using cementitious binders are addressed and some examples reported in the literature are cited by type of mechanism.

1.3.1 Heavy metals in soil

Heavy metals are metallic elements, which have an atomic weight greater than the atomic weight of iron (55.85 g/mol). However, two non-metallic elements – arsenic and selenium – are also included in this group because they have physical characteristics like metallic elements even if chemically they do not behave in the same way [92]–[94]. Additionally, heavy metals refer to the group of elements – metallic, metalloids and non-metallic – that have toxic properties in large amounts [94]. Heavy metals also include "traces elements" because they are found in nature in low concentrations (< 1000 mg/kg of dry mass of soil) [94], [95].

Some heavy metals are essential nutrients for plants, animals and humans. However, they are also toxic above specific quantities depending on each element [92], [95], [96]. Therefore, the release of heavy metals is a serious concern as it can lead to significant risks for both human health and for the local environment [94].

The source of heavy metals in soil can be either from natural origin (mineral alteration) or from anthropogenic activities (e.g. lawn fertilization and urbanization) [92]–[94], [96]. In France, the geographical distribution of some heavy metals can be related to nonpoint source pollution meaning that it can derive from many different activities as industrial agriculture, lawn fertilization, use of pesticides or construction [97]. The French Environment and Energy Management Agency (ADEME from its French initials) identified and quantified the fingerprint of some trace heavy metals at national and departmental levels in 2007. From a quantitative viewpoint, the main anthropogenic sources of heavy metals in the soils in France are: animal excreta, mineral fertilizers, phytosanitary treatment and atmospheric deposition [97], [98]. Figure 1.15 presents six different anthropogenic sources of contamination of ten trace heavy metals: arsenic (As), cadmium (Cd), chrome (Cr), cooper (Cu), mercury (Hg), molybdenum (Mo), nickel (Ni), lead (Pb), selenium (Se) and zinc (Zn). It should be noted that animal excreta represent the main source of these heavy metals in the soils in France followed by mineral fertilizers [98].
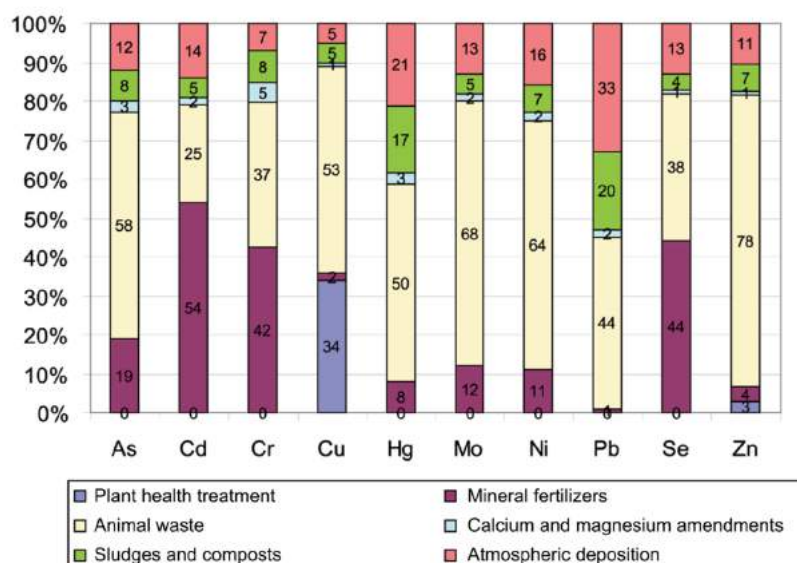
Figure 1.15 – Different sources of trace heavy metals in the soils in France. Source: Sogreah-ADEME, 2007 [97], [98].

1.3.2 Molybdenum in soil: origin and concentration

Molybdenum (Mo) is considered as an essential nutriment for plants and animals. It is naturally found in granite rocks [99], volcanic rocks, limestone [97] and in sedimentary rocks with high content of organic matter (e.g. black shale), in which the concentration of Mo can reach of about 570 mg/kg of dry mass of soil [94]. On the other hand, Mo can be artificially found in soil as a result of anthropogenic activities such as industrial agriculture, in metallurgy for the production of alloys and in oil operations [97].

Concentration of Mo in soil

According to the literature, Mo concentration is generally low in soil (in the order of a few ppm). Different average Mo concentrations in soil have been established: 1.8 mg/kg [94], 1 to 2.3 mg/kg [99], 0.2 to 5 mg/kg [94], [100] (concentrations are given in mg of Mo/kg of dry mass of soil). The variation of Mo concentrations in soil is explained by the large Mo concentrations detected in a few places such as United States ($Mo=30$ mg_{Mo}/kg_{soil}), Canada ($Mo=24$ mg_{Mo}/kg_{soil}) and Baltic region ($Mo=74$ mg_{Mo}/kg_{soil}). In these places, Mo sources are either natural or anthropogenic [94], [100].

In soil with high Mo concentrations, Mo is often associated to organic matter and to iron hydroxides [5]. At low Mo concentrations (in the order of a few ppm), Mo is generally present as a substituent in certain compounds. According to the literature, Mo can replace Fe(II), Ti and Al and possibly Si in some mineralogical structures [94], [99], [100]. Figure 1.16 shows

two models representing the substitution of an iron atom by an atom of Mo in the structure of iron sulfide [101], [102].
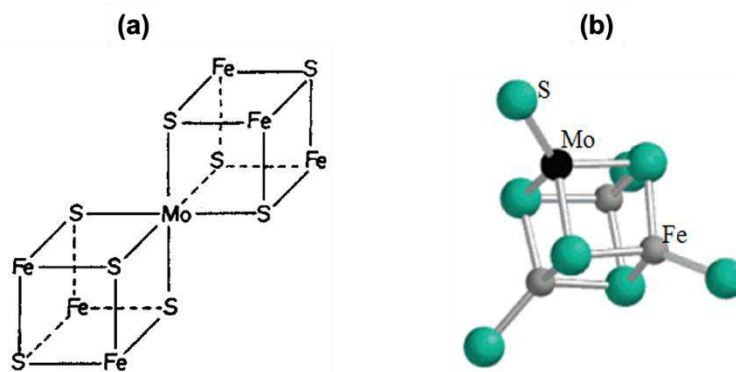
Figure 1.16 – Models of Mo-Fe-S taken from **(a)** Averill [101], and **(b)** Bostick et al. [102].

In France, Mo is naturally found in volcanic rocks and in some limestone. According to the database of the Soil Quality Monitoring Network (RMQS for its French initials), the concentrations of Mo in French soils are inferior to 0.6 mg_{Mo}/kg_{soil} [97]. Exceptionally, higher concentrations of Mo (> 2 mg_{Mo}/kg_{soil}) have been reported in some soils containing clays in the North of France (Region of Lorraine) and in the Central Massif, especially in the Chaîne des Puys [97]. Figure 1.17 shows a chart of France with the distribution of Mo concentrations detected in the surface layer (0 to 30 cm deep) of the soil.
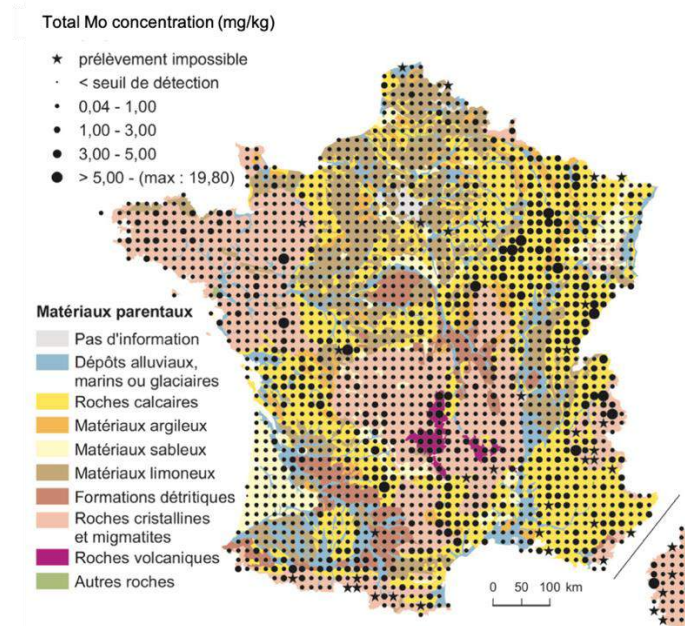
Figure 1.17 – Total molybdenum (Mo) concentrations given in mg/kg of dry mass found in the surface layer (0 to 30 cm) in the soils in France. Source: Gis Sol, RMQS, 2011; Inra, BDGSF, 1998 [97].

Guideline limit of Mo concentrations in soil

Large amounts of this metal can be toxic and produce an illness known as "molybdenosis", which is characterized by several symptoms such as weight loss, skin depigmentation and osteoporosis [94], [99], [103], [104]. Mo generally occurs at low concentration in drinking-waters and the World Health Organization (WHO) set a health-based value of 0.07 mg/l [87], which is derived on the basis of toxicological results and essential daily requirement for Mo.

In France, soils are classified in three categories depending on their leachable Mo concentrations according to the French Ministerial decree on waste classification for disposal (*Arrêté du 12 décembre 2014*) [88]. Table 1.7 presents the different categories of wastes in France as a function of the limits of leachable Mo concentrations.

Table 1.7 – Categories of waste as a function of the legal limits values of the leachable Mo concentrations required by the French decree [88], [89]. Mo concentrations are given in mg/kg of dry soil and in percentage by weight of soil.

Waste category	Mo concentration		
Inert and non-hazardous	0.5 mg/kg	0.05 mg/L*	0.05‰
Non-inert and non-hazardous	10 mg/kg	1 mg/L*	1‰
Hazardous	30 mg/kg	3 mg/L*	3‰

* Concentrations in mg/L were estimated by assuming 100 g of dry mass and a liquid to solid (L/S) ratio of 10.

Chemical species of Mo in soil

Mo is not found in nature as a free metal, but it is chemically combined with other elements. Mo can be present in a large range of oxidation states -2, 0, +1, +2, +3, +4, +5 and +6. At the lowest oxidation states (-2, 0, +1), Mo is usually found with organometallics complexes such as the monoxide of carbon or the nitric oxides. At the oxidation state +2, Mo is present in the ion $Mo_6Cl_8^{4+}$.

Mo is present in soil in the form of oxyanion with the oxidation states +4 and +6. The main Mo oxyanions in soil are: MoO_4^{2-}, MoO^{4+}, MoO_2^{2+}, MoO_3, $Mo_2O_5^{2+}$, MoO^{3+}, $Mo_2O_3^{4+}$, $Mo_2O_4^{2+}$ [99], [105]. Among these species, molybdate (MoO_4^{2-}) is the most common oxyanion of Mo found in soil. Molybdate is mostly adsorbed onto mineral surfaces under pH < 7 [94], [99], [100], [105]. Smedley and Kinniburgh [106] presented the dominant species of Mo in a Mo-H_2O system as a function of the Mo concentration and the pH values. These diagrams are presented in Figure 1.18 and they were calculated by using different databases. Aside from the variations observed in Figure 1.18, all the diagrams agreed that molybdate (MoO_4^{2-}) dominates above pH values 5-6.
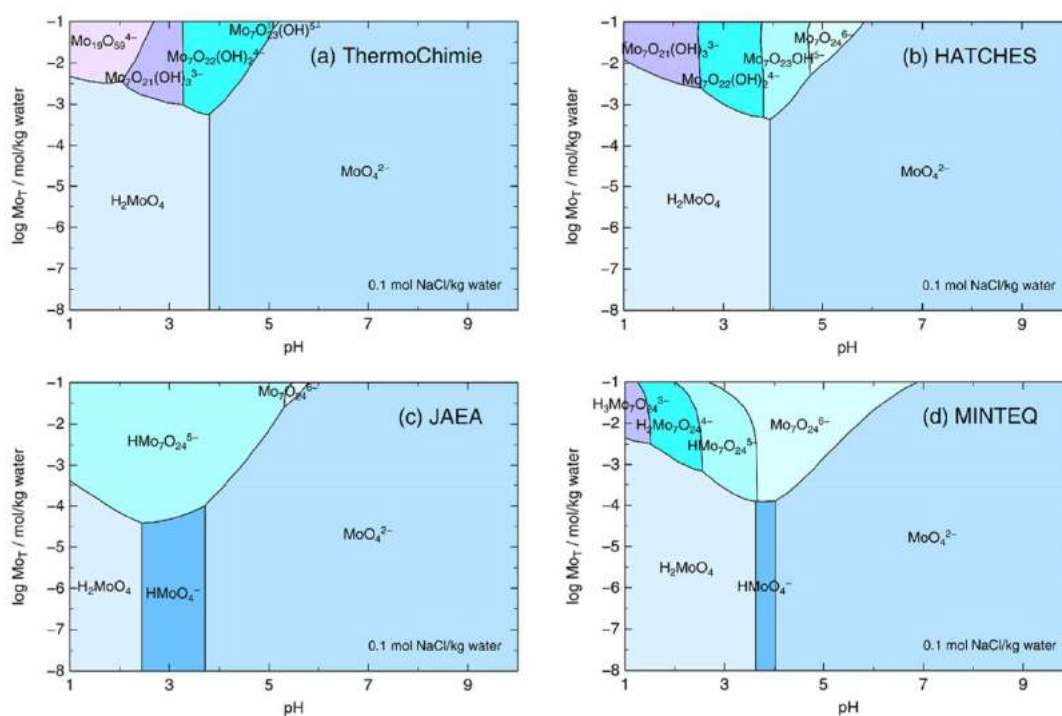
Figure 1.18 – Predominance diagrams showing the dominant species of Mo in a Mo-H$_2$O system calculated using four different databases. Taken from Smedley and Kinniburgh [106].

In soil, Mo is also found in solid forms in which molybdenite (MoS$_2$) is the main specie specially found in soil containing granite [99]. Other species are: ammonium molybdate ((NH$_4$)$_6$Mo$_7$O$_{24}$·4H$_2$O), sodium molybdate dihydrate (Na$_2$MoO$_4$·2H$_2$O) and sodium molybdate (Na$_2$MoO$_4$), which are used as lawn fertilizers when soils have Mo deficiency [94]. Table 1.8 presents the common solid forms of Mo found in soils [94], [99], [100].

Cabrerizo et al. [107] investigated a soil from Paris (France) containing Mo at very low concentrations (leachable Mo concentrations using water resulted in 1.5 ppm). They determined the oxidation state of Mo and its potential mobility in this soil by carrying out chemical sequential extractions and synchrotron analyses. The authors estimated that about 70% of Mo was present with the oxidation state +4 and about 30% of Mo was present with the oxidation state +6. They explained that Mo+4 was probably in the form of molybdenite (MoS$_2$) and that Mo+6 was in the form of molybdate (MoO$_4^{2-}$) coming probably from the dissolution of powellite (CaMoO$_4$) or MgMoO$_4$. However, it should be noted that molybdenite is insoluble.

In this project, we decided to study the stabilization of Mo by using sodium molybdate (Na$_2$MoO$_4$) in which Mo is found in the form of molybdate (MoO$_4^{2-}$) with the most common Mo oxidation state +6. A more detailed justification will be presented in later chapters.

Table 1.8 – Common solid forms of Mo found in soil [94], [99], [100].

Specie		Water solubility at 20ºC (g/100 ml)	Mo oxidation state
Molybdenite	MoS_2	insoluble	-2, +2, +4
Powellite	$CaMoO_4$	4.1×10^{-3}	+6
Ferrimolybdite	$Fe_2(MoO_4)_3$	insoluble	+6
Wulfenite	$PbMoO_4$	1.16×10^{-5}	+6
Ilsemannite	Mo_3O_8	insoluble	+1
Sodium molybdate*	Na_2MoO_4	65	+6
Sodium molybdate dihydrate*	$Na_2MoO_4 \cdot 2H_2O$	85	+6
Ammonium molybdate*	$(NH_4)_6Mo_7O_{24} \cdot 4H_2O$	0.4	+6

*Used as fertilizers in soils.

1.3.3 Stabilization of heavy metals by using cementitious binders

Unlike organic pollutants, heavy metals cannot be destroyed by biochemical processes. Therefore, several techniques *in-situ* and *ex-situ* have been tested in order to decrease heavy metal contamination in soil. Among the most known techniques, it can be cited: incineration, separation process, electrokinetic remediation, bioleaching and phytoremediation [86], [108]–[110]. Although some techniques are economic and ecologically interesting (e.g. bioleaching and phytoremediation), they require large time of treatment (in the order of several years) due to the high amounts of soil to treat [108]. Additionally, some of these techniques are not ecologically sustainable (e.g. incineration and waste disposal). As a result, in this project, the technique of stabilization by using cementitious binders was chosen to study the immobilization of Mo [86], [111].

The stabilization of heavy metals by using cementitious binders includes various phenomena such as the interactions between the pollutants and the hydration products and the physical encapsulation of pollutants (this last phenomenon decreases the permeability and the surface exposed of waste materials) [86], [112]. In this present project, we focused on the first phenomenon. The interactions between the pollutants and the cementitious products may include adsorption, precipitation or redox reactions that can affect the cement hydration process [113]. However, these interactions can also control the solubility of heavy metals and decrease their release into solution. The main mechanisms of heavy metal immobilization are presented as follow:

1.3.3.1 Oxidation-reduction (redox)

Oxidation-reduction reactions (redox) are chemical reactions leading the change of the oxidation number (gain or loss of an electron) of a molecule, atom or ion. An atom is reduced when it gains electrons, it means that the oxidation number decreases.

<div align="center">Gain of electrons (e⁻) → reduction</div>

While the loss of electrons leads to the oxidation of the atom and thus, the number oxidation increases.

<div align="center">Loss of electrons (e⁻) → oxidation</div>

Batchelor [114] explained that oxidation-reduction reactions are important immobilization mechanisms for those pollutants that exist in various redox states and have different behaviors (e.g. chemical or toxicological) in each of these states. Generally, reduced species are less soluble than oxidized ones (e.g. Cr+6 is more soluble and toxic than Cr+3). In order to reduce species in a system, it should exist "reducing agents", which are species able to transfer or donate electrons.

Mancini et al. [115] investigated the immobilization of molybdenum (Mo) contained in bottom and fly ashes from a hazardous waste by using a ferrous sulfate-based additive. They explained that this additive presented reducing conditions, which could reduce Mo and therefore, decrease its solubility. The authors explained the Mo could be immobilized by the formation of insoluble Mo oxides such as ilsemite (Mo_3O_8). The redox reaction of Mo in the ferrous sulfate-based additive would follow the Equation 10 [115]:

Equation 10.

$$Fe^{2+} \rightarrow Fe^{3+} + e^-$$

$$MoO_4^{2-} + e^- \rightarrow Mo_3O_8, MoO_2$$
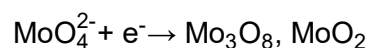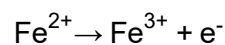
Mancini et al. [115] showed that treatment of the Mo-rich waste with the ferrous sulfate-based additive was effective to immobilize Mo. They indicated that Mo concentrations in solution decreased with increasing the proportion of the additive used for stabilization. Additionally, they suggested that Mo concentration in solution decreased with increasing the reducing conditions of the system because Mo was highly immobilized at pH values lower than 6.

Therefore, the use of cementitious binders may represent an issue for the reduction of species if such reducing conditions should be guaranteed. Ordinary Portland cement (OPC) with or without pozzolanic additions (fly ash, silica fume, etc.) is the most common binder used to

immobilize heavy metals due to its low cost and its simplicity in terms of implementation [112]. However, the high pH (12.5 to 13.5 [112]) and electrochemical potential Eh (+100 mV to +200 mV [85], -100mV to +100 mV [116]) of the OPC pore solution represent an oxidizing internal environment and therefore, a disadvantage to the reduction of species [86], [117], [118]. Other binders containing GGBS have reducing internal environments due to the presence of sulfur in a reduced state [119], [116]. The reducing nature of the binder depends on the amount of GGBS and the degree of hydration [116]. This type of binder may allow the reduction of species and thus, their immobilization. Additionally, GGBS binders would allow the precipitation of some metals in the form of sulfides, which have lower water solubility than hydroxides [85], [112], [120]. Figure 1.19 presents the internal redox conditions of different cementitious materials.
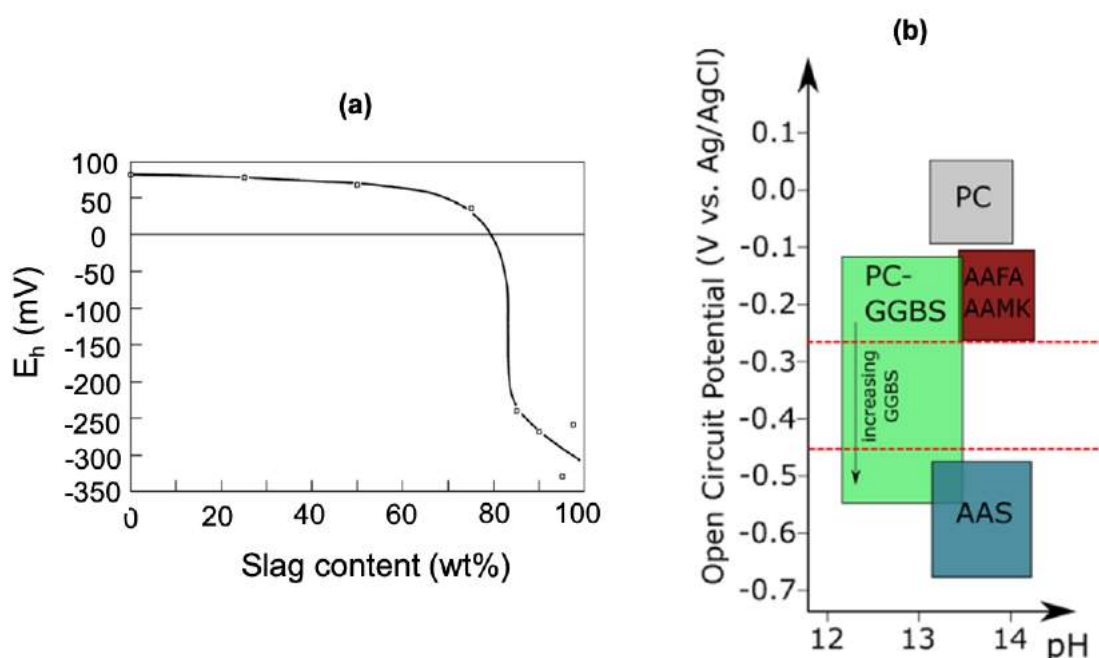
Figure 1.19 – Internal redox conditions of different cementitious materials **(a)** variation of electrochemical potential (Eh) expressed in mV as a function of the slag content taken from Bai et al. [119]. **(b)** Eh given in V for a PC: Portland cement, PC-GGBS: Portland cement and ground granulated blast furnace slag, AAFA: alkali-activated fly ashes AAMK: alkali-activated metakaolin, plotted as a function of pH values, taken from Mundra et al. [116].

Kogbara et al. [121] showed that the leachable concentrations of several heavy metals (Cd, Ni, Zn, Cu et Pb) decreased in contaminated soil after treatment with GGBS binders. Similarly, Giergiczny et al. [122] showed that Pb, Cu, Zn, Cd and Mn were highly immobilized (85% - 93%) in the solid fractions of polluted mortars composed of 85% GGBS and 15% OPC. Allan et al. [123] studied the immobilization of Cr(III) and Cr(VI) in soils by adding different proportions of OPC, bentonite and GGBS. Results obtained by Allan et al. [123] are presented

in Figure 1.20, in which Cr concentrations in solution are presented as a function of different soil/cement ratios. From this figure, it can be observed that the Cr concentration in solution decreased with increasing the proportion of slag in the treated soil.

Deja [120] studied the immobilization of Cr(VI), Cd(II), Zn(II) et Pb(II) in spiked alkali-activated slag (AAS) mortars. They observed that the retention of all heavy metals by the binders were of about 99%. The presence of these heavy metals was not observed in the hydration products; therefore, their immobilization was explained by the change of oxidation state (reduction) of the species due to the pH and Eh of the AAS.
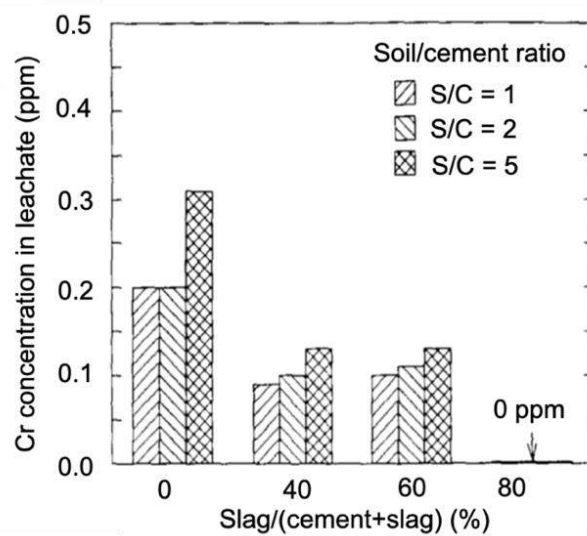
Figure 1.20 – Leaching results of a contaminated soil containing 200 ppm of Cr(III) and treated with a mixture composed of Portland cement and GGBS. Taken from Allan et al. [123].

Concerning molybdenum (Mo); however, it is mostly present as molybdate (MoO_4^{2-}) for the pH values characteristic of cementitious binders (cf. Figure 1.18). Figure 1.21 presents the redox (Eh-pH) diagrams calculated for Mo species in which the redox conditions of slag and OPC are presented in Figure 1.21(a) and (b).
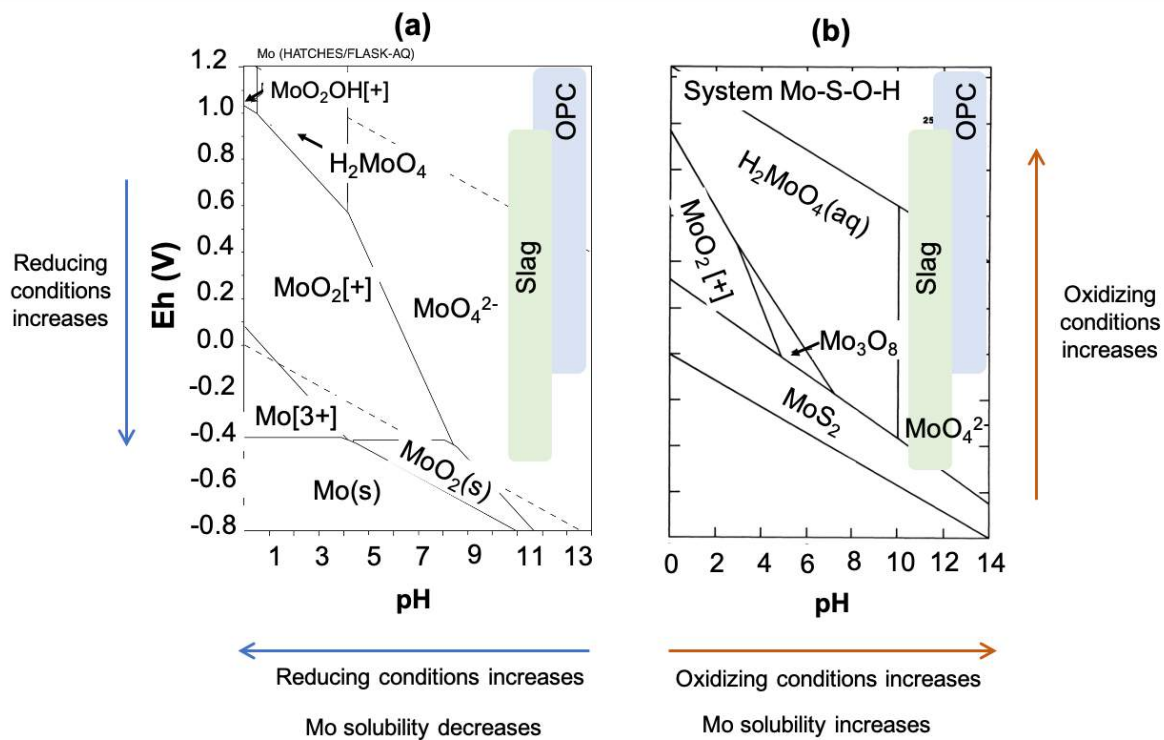
Figure 1.21 – Eh-pH diagrams for molybdenum species **(a)** in the system Mo-O-H with Mo: 10^{-10} mol/L from [124], and **(b)** in the system Mo-S-O-H (Mo=10^{-8}, S=10^{-3}) from [125]. Eh>0: oxidizing conditions (loss of electrons), Eh<0: reducing conditions (gain of electrons). Green and blue stripes show the redox internal conditions of slag and OPC binders, respectively.

From Figure 1.21, it can be observed that at pH 11 to 13.5, the dominant specie of Mo remains in the form of molybdate (MoO_4^{2-}). Only extreme reducing internal environment would be able to reduce Mo species. Therefore, the immobilization of Mo by reducing molybdate (gain of electrons) seems a difficult task. Consequently, other immobilization mechanisms should be studied, and they are presented in the following sections.

1.3.3.2 Precipitation

Precipitation consists of the subtraction of ions present in solution in order to form a solid product or a solid compound with lower water solubility than the original specie. According to the literature, heavy metals can be immobilized by cementitious binders when they form species with low water solubility in the form of hydroxides, carbonates, sulfates or silicates [86], [126]. Even though the redox conditions of OPC (high pH and high Eh), various studies have reported significant immobilization of anionic heavy metals by Portland cement due to the precipitation of new species [86], [109], [112], [127]–[129].

Palomo et al. [130] studied the immobilization of Cr and Pb in a matrix composed of fly ash of type F activated by a NaOH solution. They verified that Pb was immobilized in the matrix due to the precipitation of Pb_3SiO_5, which has a low water solubility. In contrast, Cr was released into solution due to the precipitation of $Na_2CrO_4 \cdot 4H_2O$, which has a very high-water solubility. Likewise, Minocha and Goyal [131] studied the immobilization of Mo in a Na_2MoO_4-spiked OPC at different Mo concentrations varying from 1 to 5000 ppm. After the leaching tests of Mo-spiked OPCs, containing Mo concentrations of 1000, 1500 and 2000 ppm, Mo was found in solutions at concentrations of 2.5, 3 and 11 ppm, respectively. By X-ray diffraction (XRD) analyses, the authors observed that Mo precipitated with calcium ions to form the mineral powellite ($CaMoO_4$). Similarly, Kindness et al. [132] studied the immobilization of Mo in $Na_2MoO_4 \cdot 2H_2O$-spiked OPC pastes. Initial Mo concentration was 2000 ppm and after leaching tests carried out at 12 days of curing, the leachable Mo concentration was 40 times lower than the initial Mo concentration. Mo immobilization was explained by the precipitation of $CaMoO_4$ and by the substitution of sulfate (SO_4^{2-}) by molybdate (MoO_4^{2-}) in the calcium monosulfoaluminate phase resulting in $Ca_3Al_2O_6CaMoO_4 \cdot 10\text{-}14H_2O$.

1.3.3.3 Substitution and incorporation

Substitution occurs when an atom or a molecule is replaced by another atom or molecule in a particular phase. This phenomenon takes place when several conditions are met, such as concentration, similarity in the atomic radius and in the electric charge compensation [133]. The incorporation of metallic species into mineral structures is also considered as a mechanism of immobilization. In this case, the incorporation can or not alter the original structure of the hosted mineral and decreases the solubility of the metallic specie [86], [134]. Several studies have reported that phases such as ettringite and calcium monosulfoaluminate allow for the substitution of constituents by cationic and anionic heavy metals [85].

According to the literature, ettringite ($3CaO \cdot Al_2O_3 \cdot 3CaSO_4 \cdot 32H_2O$) and calcium monosulfoaluminate ($3CaO \cdot Al_2O_3 \cdot CaSO_4 \cdot 12H_2O$) are the main phases synthetized to study heavy metal immobilization by hydration products [135]–[137]. These phases allow for substitution of cationic and anionic constituents. The anion sulfate (SO_4^{2-}) can be substituted by a few oxyanions such as chromate (CrO_4^{3-}), arsenate (AsO_4^{3-}), vanadate (VO_4^{3-}), borate $B(OH)_4^-$ and selenate (SeO_4^{2-}) due to the similar electric charge and similar structure [86], [126], [127], [138], [139]. For example, Figure 1.22 presents a model of arsenate incorporation

in ettringite by the substitution of sulfate. Moreover, Table 1.9 presents some trivalent cations and oxyanions that can replace the constituents of ettringite (Ca^{2+}, Al^{3+}, SO_4^{2-}) [86], [127].
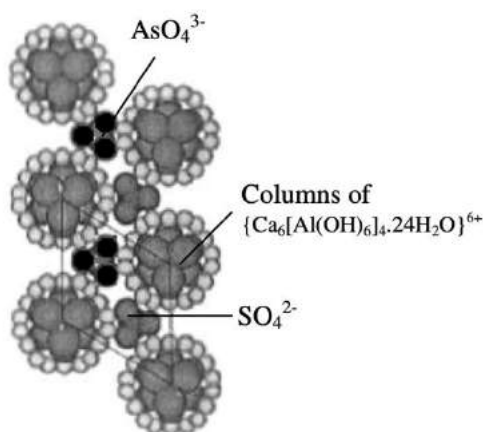
Figure 1.22 – Model of the incorporation of arsenate in ettringite by the substitution of sulfate. Taken from and cited by Cornelis et al. [138]. Original source: Myneni et al. [140].

Table 1.9 – Possible ion substitutions in ettringite [86], [113], [127].

Ettringite constituents	Ionic substitutions
Ca^{2+}	Sr^{2+}, Ba^{2+}, Pb^{2+}, Cd^{2+}, Co^{2+}, Ni^{2+}, Zn^{2+}
Al^{3+}	Cr^{3+}, Si^{4+}, Fe^{3+}, Mn^{3+}, Ni^{3+}, Co^{3+}, Ti^{3+}
SO_4^{2-}	CO_3^{2-}, OH^-, CrO_4^{2-}, AsO_4^{3-}, NO_3^-, SO_3^{2-}, SeO_4^{2-}, VO_4^{3-}, BrO_3^{1-}, MoO_4^{2-}, ClO_3^{1-}, IO_3^{1-}, $B(OH)_4^-$

Hasset et al. [141] showed that sulfate (SO_4^{2-}) was substituted by selenate (SeO_4^{2-}) in the structure of ettringite by using XRD analyses. Figure 1.23 presents the XRD patterns obtained by Hasset et al. from the synthetic ettringite with selenium. From this figure, it can be observed that the peaks of ettringite shifted towards lower degrees with increasing the retention of selenate. The final phase formed was called "ettringite-selenate" ($Ca_6Al_2(SeO_4)_3 \cdot (OH)_{12} \cdot 26H_2O$). Similarly, McCarthy et al. [142] studied the immobilization of Se, Cr and B by ettringite. They showed that the peaks of synthetic ettringite shifted from its original position and that was attributed to the modification of the ettringite structure because of the substitution of sulfate by these oxyanions which have a different molecular size.
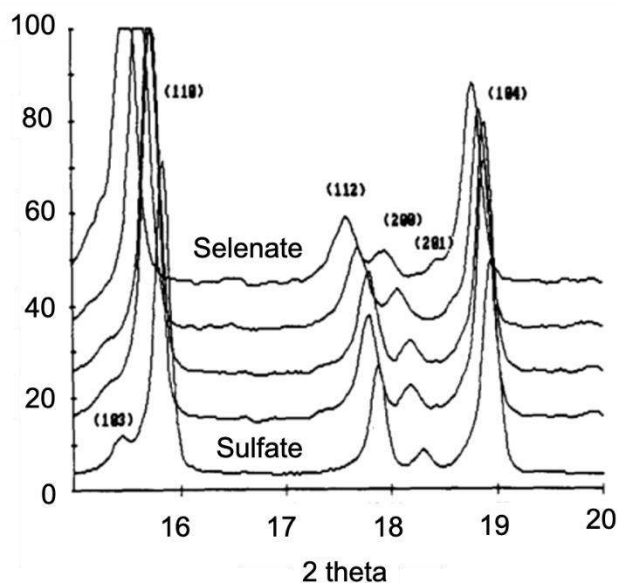
Figure 1.23 – XRD patterns of ettringite sulfate-selenate. Intensity normalized at 100%. Cu Kα radiation. Taken from D.J. Hasset et al. [141].

Likewise, Zhang et al. [143] studied the immobilization of B, Cr, Se and Mo by synthetic ettringite. They found that ettringite was able to partially immobilize all of these oxyanions. The authors explained that ettringite presented the following order of preference: $B(OH)_4^- > SeO_4^{2-} > CrO_4^{2-} > MoO_4^{2-}$. In the case of Mo, only 53% of the initial Mo concentration was immobilized. Molybdate (MoO_4^{2-}) was the last oxyanion preferred by ettringite due to the important difference in size with sulfate. In contrast, Mo preferred to co-precipitate with Ca^{2+} to form powellite ($CaMoO_4$). Figure 1.24 presents the bond length of sulfate, chromate, vanadate and molybdate. From this figure, it can be observed that molybdate presents the biggest different in size with sulfate.
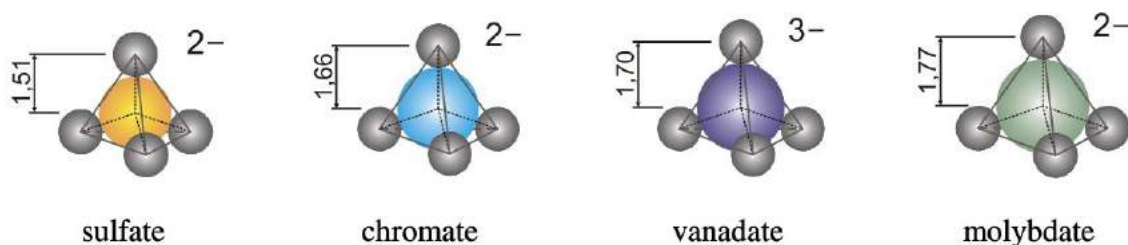
Figure 1.24 – Bond length in angstrom (Å) of sulfate, chromate, vanadate and molybdate. Taken from and cited by Vollpracht and Brameshuber [144]. Original source: [145]

58

Similarly, Zhang et al. [143] also studied the immobilization of B, Cr, Se and Mo by synthetic hydrocalumite ($Ca_4Al_2(OH)_{12}(OH)_2 \cdot 6H_2O$). They observed that hydrocalumite had a great capacity to immobilize all of these heavy metals. After XRD analyses, it was observed that Mo precipitated with Ca^{2+} to form powellite and molybdate-hydrocalumite. Zhang et al. proposed three different mechanisms of heavy metal immobilization by using synthetic ettringite and hydrocalumite: (i) adsorption onto their surfaces, (ii) substitution of the OH^- anion in hydrocalumite, and (iii) substitution of SO_4^{2-} in ettringite.

Therefore, ettringite binders such as calcium sulfoaluminate cements (CSA) and supersulfated cements are of interest in the field of hazardous waste immobilization [55], [113], [139]. In addition, these cements also produce C-S-H phases than can adsorb heavy metals onto their surface. As an example, Peysson [85] studied the immobilization of Cr and Cd by using a calcium sulfo-aluminate (CSA) cement. They showed that Cr and Cd were immobilized in the solid fractions in percentages of 20% and 30%, respectively. They observed that the morphology of ettringite crystals was modified when these heavy metals were added to the cement; however, the chemical composition of ettringite remained the same. Similarly, Berger [135] studied the immobilization of Zn(II) in CSA. The author observed that Zn was partially immobilized in the solid fraction by the adsorption onto AH_3 and C-S-H phases.

1.3.3.4 Sorption

Sorption mechanism refers to the phenomena of physical and chemical adsorption of heavy metals [86]. Physical adsorption occurs when metallic elements are attracted by the surface of another element or compound due to the electrical charge difference, while chemical adsorption refers to the chemical interaction between elements or compounds. Therefore, chemical adsorption is usually stronger than physical adsorption [86].

All heavy metals behave differently as a function of pH (depending on different parameters such as the adsorbent, temperature, concentration, nature of the metal, etc.). Heavy metals are adsorbed up to a specific limit (depending on each specie) from which they start again to pass into solution [10]. However, two general behaviors can be observed in cationic (ions with positive charge) and anionic (ions with a negative charge) heavy metals. Cationic heavy metals tend to dissolve at low pH values while anionic heavy metals tend to dissolve at high pH values [95], [134], [146]. This behavior is presented in Figure 1.25, in which x and y-axes represent the pH value and the fraction of anion/cation not soluble, respectively.
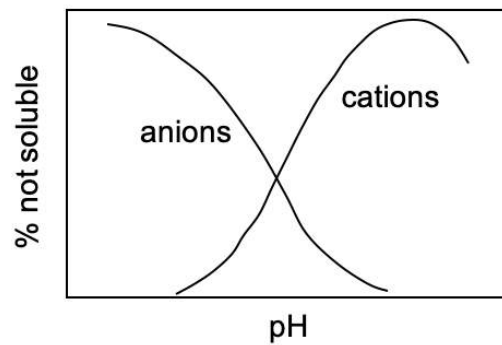
Figure 1.25 – Typical behavior of adsorption and desorption of heavy metals in the form of cations and anions in an aqueous system as a function of pH (modified graph and taken from Bourg [134]).

In order to better illustrate the behavior mentioned above, Figure 1.26 presents examples of different heavy metals adsorbed by iron hydroxide (in the form of goethite αFeOOH) as a function of pH. Figure 1.26(a) presents the adsorption of AsO_4^{3-}, SeO_3^{2-}, PO_4^{3-}, MoO_4^{2-}, et CrO_4^{2-} (anionic species) in the pH range 2 to 12. Meanwhile, Figure 1.26(b) presents the adsorption of some cationic species in the pH range 2 to 8. From Figure 1.26, it can be observed that the adsorption of the anionic species decreased with increasing pH values. In the contrary, the adsorption of cationic heavy metals increased with increasing pH.
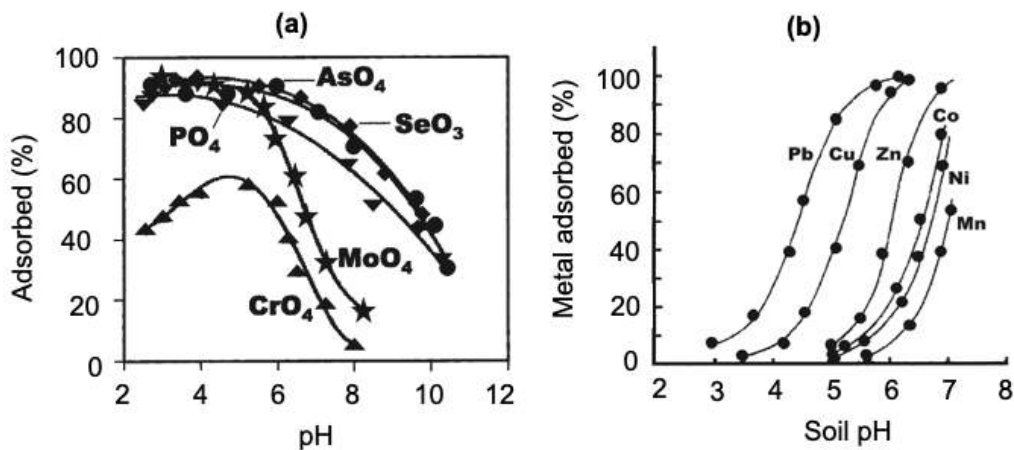
Figure 1.26 – Heavy metal adsorbed by iron hydroxide as a function of pH **(a)** Anionic heavy metals, and **(b)** cationic heavy metals. Figures were taken from Basta et al. [95].

The immobilization of heavy metals has been attributed in several studies to their physical adsorption in the hydration products of the binders. The adsorption capacity of a compound is correlated to its specific surface. Compounds with large specific surfaces (> 600 m²/g) seem to have a high capacity to immobilize heavy metals by physical adsorption [94], [147]. It is the

case of iron, manganese and aluminum oxides and colloidal particles [94], [95], [99], [134], [146]. Also, the phase C-S-H presents high sorption capacity due to its micro-porosity which creates a high surface area controlling the sorption properties [86], [127], [118].

Park [118] represented the mechanisms of immobilization of Pb, Cr and Cd by portlandite (CH) and C-S-H formed in OPC. Figure 1.27 illustrates the co-precipitation of Pb in the surface of C-S-H, the incorporation of Cr into the C-S-H structure and the partial substitution of Cd by calcium in the CH forming a new compound (CdCa(OH)$_4$) [118].
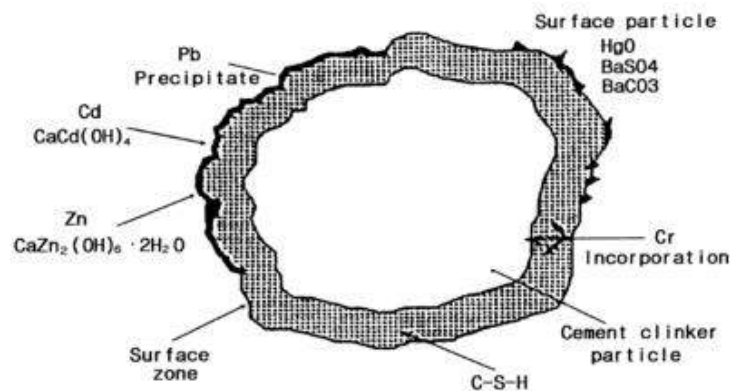
Figure 1.27 – Immobilization of Pd, Cd and Cr by the hydration products (C-S-H and CH) of Portland cement [118].

Gougar et al. [127] presented a review of the ion immobilization of heavy metals by C-S-H. They gave several examples of ion immobilization by C-S-H and we cite some of them as follow:

- Iodine (I) was adsorbed in the form of I^{-1} by a C-S-H having a Ca/Si ratio of 1.7.

- Nickel (Ni) was present in the form of $Ni(OH)_2$ and it was intermixed with C-S-H.

- Uranium (U) was immobilized by sorption and co-precipitation in C-S-H forming a phase referred to as "uranyl silicate hydrate-urophane".

- Ni and cooper (Co) were immobilized in the surface of C-S-H, probably because of the substitution of calcium ions.

- Immobilization of chromium (Cr) in poorly crystalline C-S-H explained by the substitution of Si.

- Cadmium (Cd) in the form of $Cd(OH)_2$ was incorporated into the layer structure of C-S-H.

Duchesne and Laforest [148] studied the immobilization of Cr(+6) by using GGBS. They showed that Cr concentration decreased in solution when 100% of slag was used (Cr was completely immobilized at 50 days of curing). They observed the presence of Cr in C-S-H by SEM observations. In addition, they studied the effect of Mo in the immobilization of Cr in contact with 100% slag. They showed that Cr did not compete with Mo and that Mo was partially immobilized (60% retention) after 80 days of hydration. However, the authors did not give a clear explanation of the mechanism of Mo immobilization. The results of this study are presented in Figure 1.28, where x-axis and y-axis represent the metal concentration in solution (given in ppm) and the time in days, respectively.
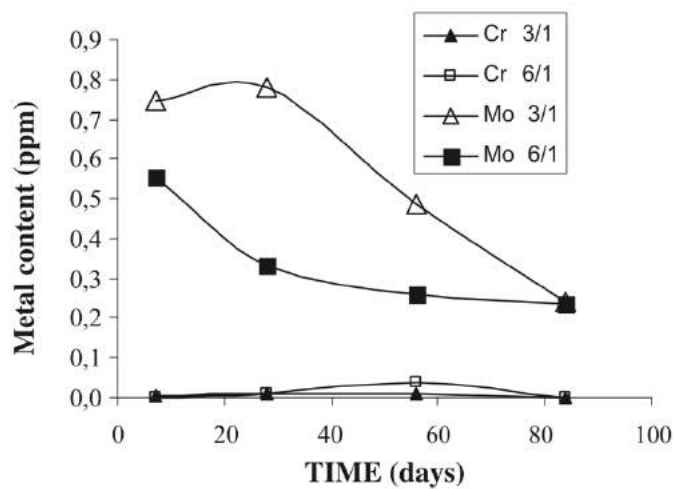
Figure 1.28 – Concentrations of Cr or Mo in solution given in ppm for samples containing 100% slag. Initial Cr and Mo concentrations: 20 ppm. Ratios refers to water to solid ratios. Taken from Duchesne and Laforest [148].

As presented in the past section, several mechanisms may be responsible for the immobilization of heavy metals by using cementitious binders. It was shown that Mo was present in the form of molybdate (MoO_4^{2-}) in the pH range of cementitious binders (pH 11 - 13). It was also shown that precipitation of powellite is likely to be the main phase controlling Mo solubility in binders containing high content of calcium. Other stabilization mechanisms as sorption and substitution also contribute to the immobilization of Mo. Therefore, it is necessary to evaluate the capacity of several binders to immobilize Mo and to contribute to the understanding of the mechanisms of Mo stabilization.

1.4 Understanding the immobilization of pollutants by using modeling

Modeling is an useful tool in simulating the interactions between different elements or compounds in a solution [149]. Therefore, modeling is useful to better understand the dissolution/precipitation of elements such as sulfates and molybdenum in a defined system. Additionally, modeling helps to better understand the phenomena that are difficult to analyze experimentally. In this thesis, we focus on one specific type of models called "speciation-solubility geochemical models". Thus, in this section, we present the principle of this type of model, and we give some examples of modeling related with the topic of this thesis.

1.4.1 How does the model work?

The speciation-solubility geochemical models give information about the concentrations and activities of ionic and molecular species in an aqueous solution at the equilibrium. They also provide the Saturation Indices (SI) about different minerals in the system and the reactions that might happen at the equilibrium [149]. As explained by Zhu and Anderson [149], a system is at equilibrium if none of its properties change with time. This means that these models do not contain spatial or temporal information (kinetic rates are not taken into account). Figure 1.29 shows the main components of a speciation-solubility geochemical model according to Zhu and Anderson [149].
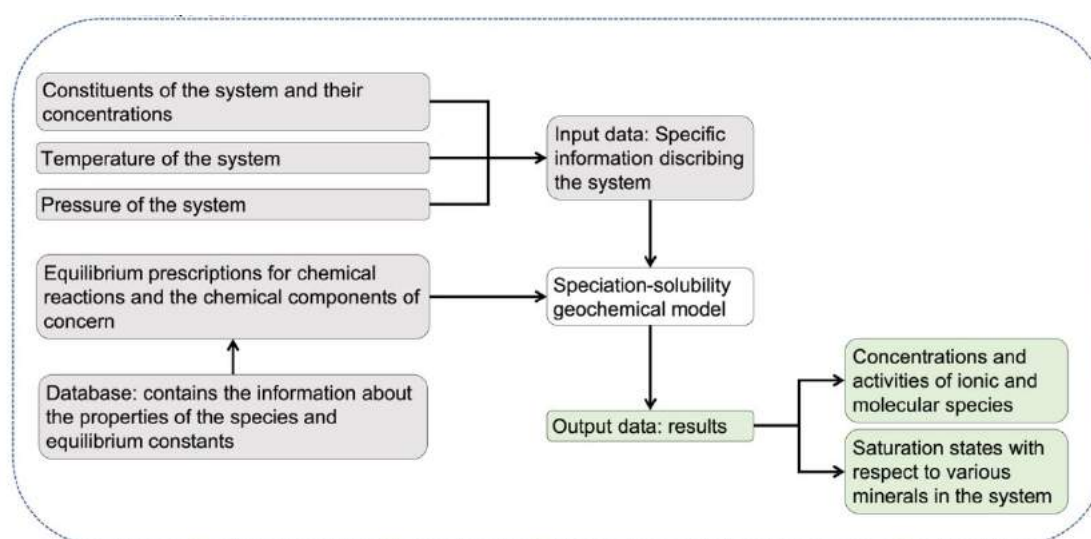
Figure 1.29 – Description of a speciation-solubility geochemical model.

Output obtained in the model

As mentioned above, the speciation-solubility geochemical model provides information about concentrations and activities of ionic and molecular species as well as the Saturation Indices (SI) of different minerals. This permits to know if a mineral may dissolve or precipitate at the equilibrium of the system. Table 1.10 presents the relations between the Ion Activity Product (IAP), the solubility product or equilibrium constant (Ksp), and the Saturation Index (SI). The equilibrium constant (Ksp) is given by the law of the mass action, which is represented in the Equation 11.

Equation 11. $aA + bB \leftrightarrow cC + dD$

The distribution at equilibrium of the species at the left and right side of the reaction given in Equation 11 is then the constant Ksp. Equation 12 presents the constant Ksp. In this equation, the quantities in brackets mean activities or "effective concentrations" [150].

Equation 12.

$$Ksp = \frac{[C]^c\ [D]^d}{[A]^a\ [B]^b}$$

The IAP is the analogue product of the activities [150], and the SI is the logarithm of the saturation state (Ω) expressed as the ratio between IAP and Ksp. As presented in Table 1.10, when SI>0 the mineral can precipitate (supersaturation), when SI<0 the mineral dissolves (subsaturation), and S=0 means equilibrium between the mineral and the solution [149], [150].

Table 1.10 – Relations between IAP, Ksp, and SI taken from Zhu and Anderson [149].

IAP, Ksp	Ω	SI	Result
IAP< Ksp	< 1	Negative	Mineral dissolves
IAP > Ksp	> 1	Positive	Mineral can precipitate
IAP = Ksp	1	0	equilibrium

Verification and validation of the model:

Among the codes to carried out the speciation-solubility geochemical models, we chose in this thesis to work with the computer code PHREEQC version 3.0 [151], a speciation and reaction path program produced by the US Geological Survey. This code allows to develop models that are built on the fundamental laws of thermodynamics. The type of model used in this study is a "speciation-solubility geochemical model".

Verification refers to the computer code (PHREEQC in our case) used to solve the problem of concern. According to Zhu and Anderson [149], codes that are generally available and extensively used have all been verified. This is the case of PHREEQC code which has been used for several applications (e.g. precipitation and dissolution reactions related to environmental issues, prediction of hydration reactions in cement-based systems). After Zhu and Anderson [149], PHREEQC has been verified against other codes or hand calculations for assure their mathematical functionality.

On the other hand, validation refers to the process of determining if the model produces realistic results and if it represents natural processes. This depends on the input (e.g. definition of the system and quality of the database) used in the model. It should also be remembered, that speciation-solubility geochemical models do not contain spatial or temporal information; therefore, these types of models will be inaccurate to some degree [149]. However, these models are approximations to the real situations and allow to predict and better understand the underlying phenomena at the equilibrium state.

1.4.2 Immobilization of pollutants

Sun and Selim [152] studied the retention and transport of molybdenum (Mo)-phosphate in soils. To this end, they calculated the speciation of an aqueous system and estimated the speciation of the solution for Mo in a pH range from 2 to 11. Figure 1.30 shows the results obtained from a model calculated with PHREEQC; from this figure, it can be observed that Mo was present in solution in the form of molybdate (MoO_4^{2-}) over the pH 5-11 and that $HMoO_4^-$ was also present but at minor concentrations.

Similarly, Carroll et al. [153] studied the transport of Mo in a biosolid-amended alkaline soil. The authors used a geochemical model to examine the Mo speciation and chemical reactions between the soil minerals and the groundwater solution. The calculations showed that about 76% of solution contained Mo in the form of MoO_4^{2-} and about 14% of Mo was present in the form of $CaMoO_4$ (over the pH range of 4-12). Other minor concentrations of Mo were calculated in the form of $MgMoO_4$, $NaMoO_4$ and negligible quantities of MoO_2^{2+}, $KMoO_4^{-1}$, $HMoO_4^{-1}$, H_2MoO_4, MoO_2OH^+, MoO_2^{+1} and MoO_3^+.
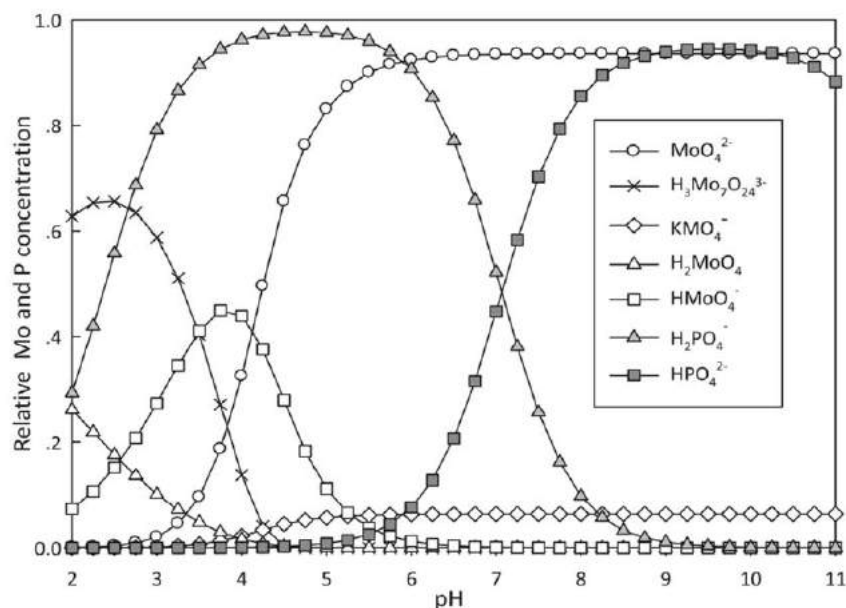
Figure 1.30 – Geochemical model results for the aqueous species distribution of Mo and P under the pH range 2-11. Taken from Sun and Selim [152].

Reddy and Gloss [154] investigated the chemical speciation of soil leachates, extracted at different depth of soil, in order to evaluate the mobility of F, Mo and Se in a calcareous soil. They used a model for chemical speciation and ion activity calculations known as GEOCHEM. Concerning to Mo, the chemical speciation indicated that Mo concentrations increased with depth and suggested that the dominated Mo species were: $MgMoO_4$ (41-70%), followed by $CaMoO_4$ (15-38%) and MoO_4^{2-} (7-16%). In a similar study, Wang et al. [155] suggested that wulfenite ($PbMoO_4$) was the solid phase controlling Mo concentrations in a soil near mine spoils. Modeling indicated that the dissolved Mo concentrations in the leachates of the soil were controlled by this phase, whose solubility increases with increasing pH values.

The estimation of the mineral assemblage in a system can also be predicted by using the concentration of several elements present in a solution and thus, the prediction of phases controlling the solubility of species. As an example, Hyks et al. [156] studied the long-term leaching of several elements (including Mo) from two different solid waste residues which were monitored for 24 months under column percolation experiment tests. Element concentrations in solution allowed for the estimation of phases controlling the solubility of numerous elements. In the case of Mo, it was suggested that it was present in the form of molybdate (MoO_4^{2-}) and it was not related to the precipitation/dissolution of ettringite. In contrast, the authors suggested that powellite was the possible phase controlling Mo solubility. In the case of sulfates, they

suggested that SO_4^{2-} solubility was controlled by the dissolution of gypsum. Furthermore, the decrease in sulfate concentration in solution was linked to the precipitation of ettringite.

As presented, modeling is a useful tool to predict the behavior of species in a specific system. Even though the kinetics of reaction are not taken into account, understanding the speciation in the equilibrium state allows for improving the understanding of different phenomena for which the experimental analyses are difficult (e.g. stabilization of pollutants at low molybdenum or sulfates concentrations).

1.5 Conclusions

The presence of sulfates and molybdenum in contaminated materials (e.g. excavated soil and by-products) is a serious concern in civil engineering projects. The aim of this chapter was to realize an overview of polluted soil and its reuse or disposal after excavation operations. We focused on (i) sulfate-rich soil in contact with concrete (external sulfate attack), (ii) stabilization of sulfates for reuse or disposal, and (ii) stabilization of molybdenum. Table 1.11 presents a summary of the main conclusions of this literature review.

Table 1.11 – Conclusions of the Chapter 1 - Literature review.

	What is known?	What is missing?
Concrete under external sulfate attack	- Classic Portland cements are not suitable binders against external sulfate attack (ESA) due to high C_3A and portlandite contents. - Portland cement exposed to ESA present expansion, cracking and softening. - Alternative binders have shown better performances (minor expansion and minor degradation) to ESA compared to Portland cements.	- Compare the capacity of several binders to resist ESA by using similar experimental conditions. - Better understand the mechanisms of expansion/non-expansion of binders under ESA.
Stabilization of sulfates	Sulfate-rich soil treated by: - OPC leads to swelling. - lime can lead to swelling if soil contains clay. - alternative binders containing GGBS can reduce the swelling potential of soil. A few studies deal with mechanisms of stabilization of sulfates by using cementitious binders.	- Compare the capacity of several binders to stabilize sulfates. - Evaluate the different treatments with respect to the swelling and mechanical properties. - Better understand the mechanisms of immobilization of sulfates.

Stabilization of molybdenum (Mo)	- Several studies focused on the study of heavy metals by using cementitious binders.
	- The main mechanisms of immobilization are:
	    ○ redox reactions,
	    ○ precipitation,
	    ○ adsorption,
	    ○ substitution.
	- A few studies focused on the stabilization of Mo by using cementitious binders.
		- Evaluate the capacity of several binders to immobilize Mo.
		- Contribute to the understanding of the mechanisms of Mo stabilization.
		- Study the capacity of calcium silicate hydrate (C-S-H) to immobilize Mo.

CHAPTER 2 – MATERIALS AND METHODS

Table of Contents

2. Chapter 2 – Materials and Methods

Résumé

Ce deuxième chapitre présente les matériaux et méthodes utilisés pour l'étude de (i) l'attaque sulfatique externe, (ii) la stabilisation des sulfates, et (iii) la stabilisation du molybdène. Ce chapitre est organisé en deux parties principales : Matériaux et Méthodes.

Pour faciliter la lecture, les données numériques utilisées pour la modélisation réalisée dans ce projet sont présentées à la fin du chapitre en annexes (cf. Annexe 1).

Matériaux :

La première partie de ce chapitre se concentre sur les matériaux utilisés, leur description, composition, fabrication et temps de cure. Les matériaux sont présentés selon trois sections distinctes :

(i)   Attaque sulfatique externe sur des bétons :

Dans cette partie de l'étude, sept liants différents ont été utilisés afin d'évaluer leur résistance vis-à-vis de l'attaque sulfatique externe. L'ensemble des liants utilisés et leur composition chimique et minéralogique sont présentés en Table 2.1 et Table 2.2. La Table 2.3 regroupe les formulations adoptées pour la fabrication des bétons. De plus, un schéma est présenté en Figure 2.8 représentant les produits hydratés de ces liants.

(ii)   Stabilisation des sols sulfatés :

Dans cette partie de l'étude, cinq formulations différentes ont été adoptées pour étudier la stabilisation des sulfates dans les sols. La composition des matériaux utilisés est présentée en Table 2.4. De plus, la description des formulations est présentée en Table 2.5 et en Figure 2.14.

(iii)   Stabilisation du molybdène :

Dans cette partie de l'étude, trois liants différents ont été choisis pour étudier leur capacité à immobiliser le molybdène (Mo). Ces liants ont été dopés en Mo en utilisant six concentrations différentes. La description des formulations utilisées est présentée en Table 2.6. De plus, la synthèse de la phase cimentaire silicate de calcium hydraté (C-S-H) a été aussi réalisée afin de vérifier sa capacité à immobiliser le Mo. La description des synthèses est présentée en Table 2.7.

Méthodes :

La deuxième partie de ce chapitre présente les méthodes employées lors des essais expérimentaux. De plus, la modélisation est aussi présentée dans la dernière partie de ce chapitre.

Les méthodes utilisées dans ce projet de thèse ont été regroupées en cinq parties différentes :

(i)   Caractérisation minéralogique :

Cette partie décrit les protocoles et caractéristiques des différentes techniques d'analyses utilisées, telles que la diffraction à rayons X, la microscopie électronique à balayage, la thermogravimétrie et la spectroscopie infrarouge à transformée de Fourier.

(ii)   Analyses chimiques :

Cette partie regroupe toutes les analyses réalisées en solution et présente les techniques suivantes : tests de lixiviation, chromatographie ionique et spectroscopie d'émission atomique avec plasma à couplage inductif.

      (iii)   Test réalisés sur béton :

Cette section présente les protocoles des essais employés pour tester les bétons fabriqués. Les techniques décrites sont : la résistance à la compression, le protocole de l'attaque sulfatique externe et l'extraction de la solution porale.

      (iv)   Essais géotechniques sur des sols traités :

Cette partie regroupe les essais réalisés sur les sols sulfatés traités par les différents liants. D'abord, les protocoles pour évaluer les propriétés géotechniques à court-terme sont présentés : gonflement et résistance à la traction indirecte (essais d'aptitude). Ensuite, le protocole de maniabilité est décrit, suivi des essais géotechniques pour évaluer les propriétés mécaniques à moyen et long-termes des matériaux traités : résistance en compression, détermination de la classe mécanique et détermination du gonflement.

      (v)   Modélisation :

Cette section est divisée en trois parties :

         a.   Explication des calculs réalisés pour estimer les indices de saturation sur l'étude de l'attaque sulfatique externe,
         b.   Modèle géochimique pour comprendre l'immobilisation des sulfates,
         c.   Modèle géochimique pour comprendre l'immobilisation du molybdène.

Introduction

This chapter gives information related to the materials and methods used in the study of (i) concrete under external sulfate attack, (ii) stabilization of sulfates, and (iii) stabilization of molybdenum. The first part of this chapter focuses on the materials, their description, composition, preparation and curing conditions. In addition, a comparison of all the materials is presented in several diagrams showing the main hydration products of the binders. The second part of this chapter focuses on the methods used to accomplish the objectives of this research including the description of the modeling carried out in each part of the study. For ease of reading, at the end of this chapter, the Annex 1 presents the input of the modeling used in this study.

2.1 Materials

2.1.1 Concrete under external sulfate attack

2.1.1.1 Binders

Seven binders grouped into three categories were tested under external sulfate attack (ESA). The summary of these binders is presented in Table 2.1. The chemical and mineralogical compositions of each of the anhydrous binders are listed in Table 2.2. Figure 2.8 represents in a schema the main hydration products per binder used in this part of the study. This representation shows the hydration products normalized to 100%; therefore, the remaining anhydrous phases are not represented in this figure.

Table 2.1 – Summary of binders used in the study of external sulfate attack.

Category	Portland cements	Ettringite binders	Alkali-activated binders
Binder ID	CEM I CEM-SR CEM III/C	SSC CSA	AAS GP

Table 2.2 – Chemical and mineralogical compositions of each of the anhydrous binders (% by weight). The GGBS(1) and GGBS(2) were used to fabricate the SSC and the AAS binder, respectively.

		CEM I[a]	CEM-SR[a]	CEM III/C[a]	GGBS(1)[b]	GGBS(2)[b]	Metakaolin[a]	CSA[a]
Oxides (% mass)	CaO	64.5	65.3	46.1	43.0	43.8	1.6	43.6
	SiO_2	20.2	21.7	31.3	36.0	37.4	65.9	8.2
	Al_2O_3	5.2	3.6	10.5	11.9	10.2	25.1	18.2
	Fe_2O_3	3.3	6.2	0.90	0.47	0.60	4.3	7.6
	MgO	0.80	0.90	5.8	7.0	6.4	0.37	ND
	Mn_2O_3	ND	0.10	ND	0.17	0.20	0.01	ND
	Na_2O	0.28	0.10	0.53	0.34	0.21	0.07	ND
	K_2O	0.76	0.60	0.65	0.45	0.28	0.35	ND
	SO_3	3.0	1.6	2.5	0.10	0.10	-	15.2
	Cl-	0.07	0.03	0.30	ND	ND	ND	0.05
Clinker composition (% mass)	C_3A	8.6	0.0	8.4	-	-	-	-
	C_3S	60.3	59.0	63.0	-	-	-	-
	C_2S	12.6	22.0	ND	-	-	-	29.1
	C_4AF	10.1	17.0	10.5	-	-	-	-
	$C_4A_3\bar{S}$	-	-	-	-	-	-	54.3
	C_3MS_2	-	-	-	-	-	-	4.5
	C_3FT	-	-	-	-	-	-	4.5
	$C\bar{S}$	5.1	2.6	3.4	-	-	-	0.40
	LOI	1.8	0.32	1.4	NG	NG	2.6	3.8

[a]: compositions were obtained from the technical data sheet of the binder

[b]: compositions were determined from ICP-AES analyses

ND: Not determined

NG: Negligible

LOI: loss on ignition

Description of the binders:

(i)   Portland cements:

Ordinary Portland cement (OPC): CEM I 52.5 N CE CP2 NF, with a C_3A content of 8.6% and a C_4AF content of 10.1%, referred to as "CEM I". It has a strength class of 52.5 N in accordance with the European Standard EN 197-1 and a cement fineness of 4400 cm^2/g. This cement was used to cast the control concrete. The X-ray diffraction (XRD) pattern of the anhydrous cement is presented in Figure 2.1. The main hydration products of this cement are portlandite (CH), calcium silicate hydrate (C-S-H) and ettringite (AFt) [3].
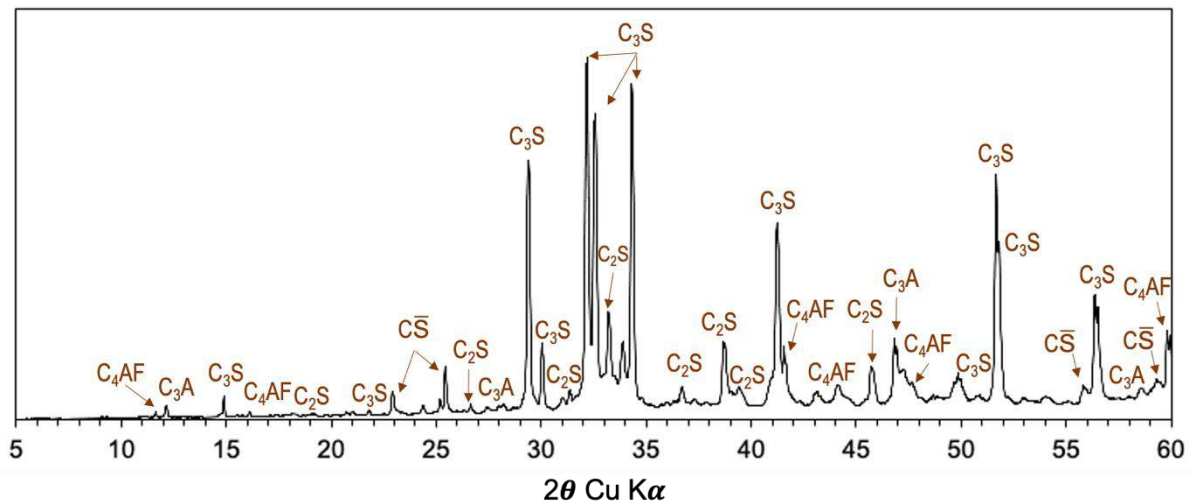
Figure 2.1 – XRD pattern of the anhydrous CEM I. **C$\bar{S}$:** anhydrite, **C$_2$S:** belite, **C$_3$S:** alite, **C$_3$A:** celite, **C$_4$AF:** brownmillerite.

Sulfate-resisting (SR) Portland cement: a commercial cement without C$_3$A and a C$_4$AF content of 17%, it is referred to as "CEM-SR". It has a strength class of 52.5 N in accordance with the European Standard EN 197-1 and a cement fineness of 4220 cm^2/g. The XRD pattern of the anhydrous cement is presented in Figure 2.2. The main hydration products of this cement are CH and C-S-H [23].
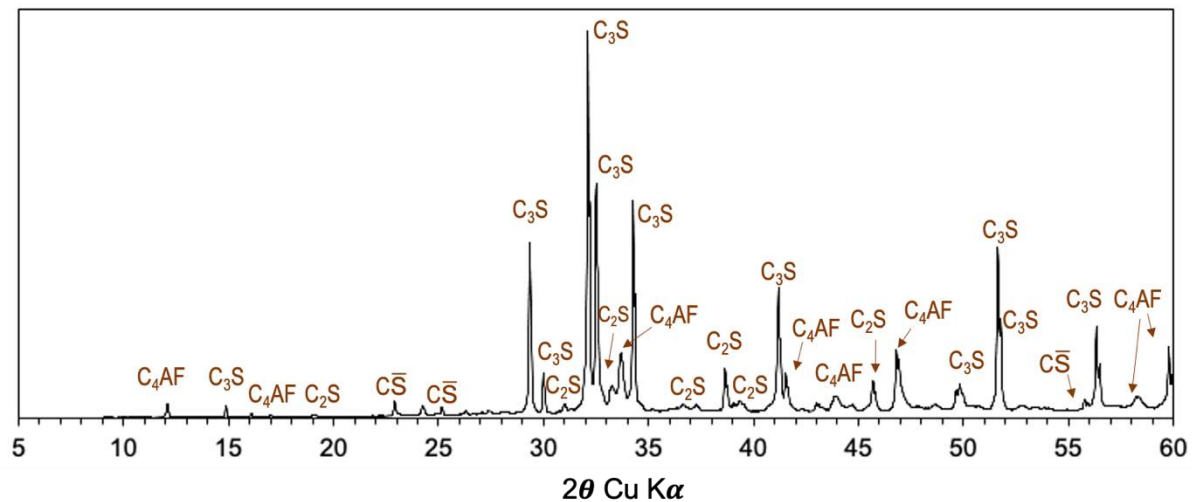
Figure 2.2 – XRD pattern of anhydrous the sulfate-resisting (SR) Portland cement. **C$\bar{S}$:** anhydrite, **C$_2$S:** belite, **C$_3$S:** alite, **C$_3$A:** celite, **C$_4$AF:** brownmillerite.

Blast furnace slag cement: CEM III/C 32,5 N–LH/SR PM (according to EN 197-1), referred to as "CEM III/C". This cement has a strength class of 32.5 N and a cement fineness of

4400 cm^2/g. It is composed of 82% ground granulated blast furnace slag (GGBS), 15% clinker and 3% of secondary constituents. The XRD pattern of the anhydrous cement is presented in Figure 2.3. The main hydration products in slag blended with clinker cements include C-(A)-S-H (with alumina replacing some silica), hydrotalcite (M_5AH_{13}) and AFm phases such as C_4AH_{13} [72], [157].
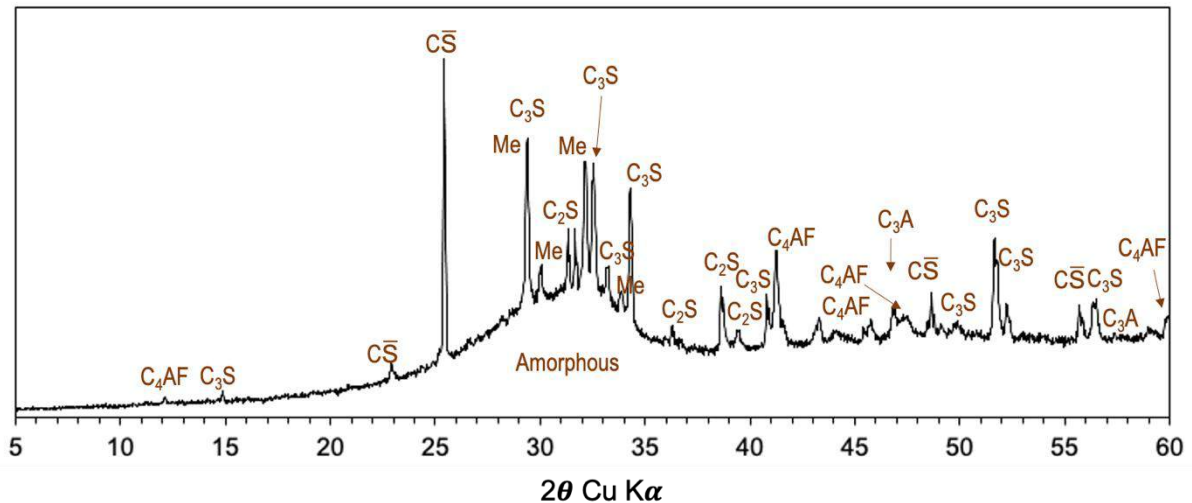
Figure 2.3 – XRD pattern of the anhydrous blast furnace slag Portland cement. **Me:** merwinite, **C$\bar{S}$:** anhydrite, **C$_2$S:** belite, **C$_3$S:** alite, **C$_3$A:** celite, **C$_4$AF:** brownmillerite.

(ii)   Ettringite binders:

<u>Supersulfated GGBS cement (SSC):</u> conforms to EN 15743. This experimental binder (prepared at the laboratory) is composed of about 75% GGBS (fineness of 5300 cm^2/g), 20% calcium sulfate (confidential) and 5% OPC. The XRD pattern of the anhydrous cement is presented in Figure 2.4. The main hydration products of this binder are AFt and C-(A)-S-H. M_5AH_{13} may also precipitate.

77
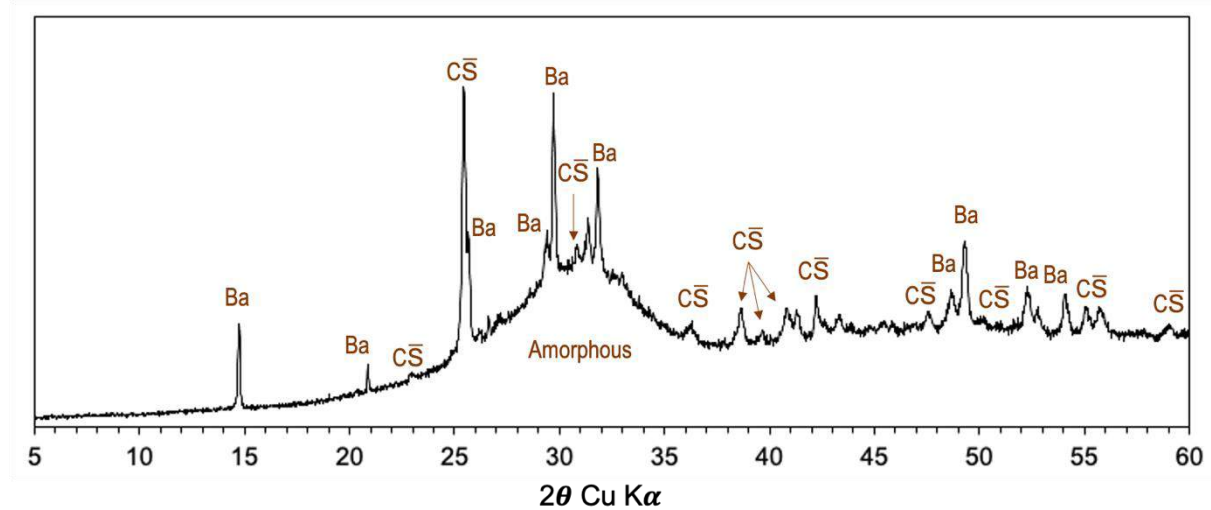
Figure 2.4 – XRD pattern of the anhydrous supersulfated GGBS cement. **Ba:** bassanite, **C$\bar{\text{S}}$:** anhydrite.

Calcium sulfoaluminate-belite cement (CSA): this commercial cement is mainly composed of 77% sulfoaluminate clinker, 18% anhydrite and 5% limestone filler. The cement fineness is 4500 cm^2/g and the XRD pattern of the anhydrous cement is presented in Figure 2.5. The main hydration products of this binder are AFt and Ms [55]. Other phases such as aluminum hydroxide (AH$_3$), straetlingite (C$_2$ASH$_8$) and calcium aluminate decahydrate (CAH$_{10}$) may also precipitate [47].
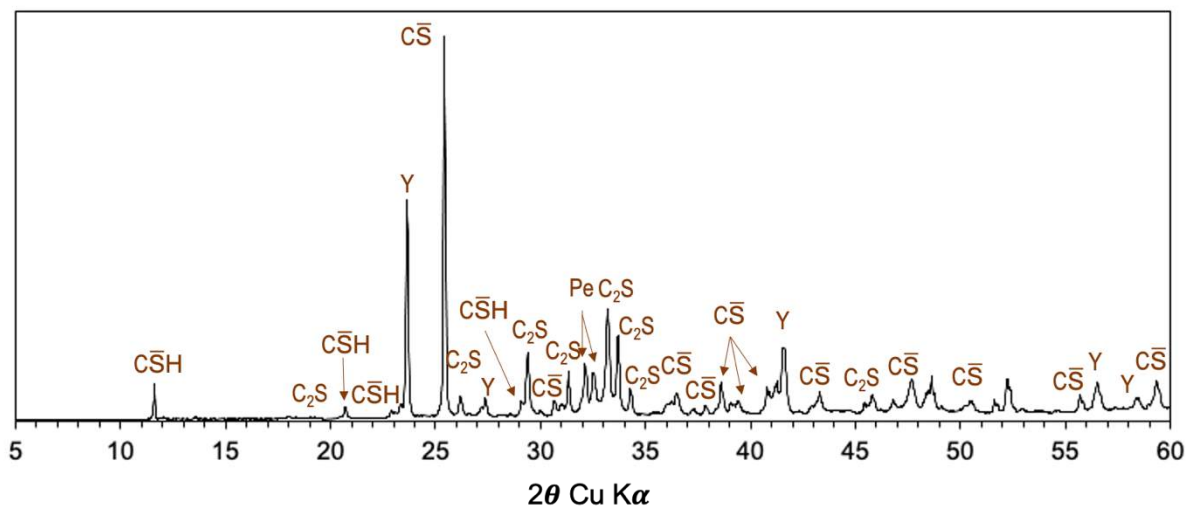
Figure 2.5 – XRD pattern of the anhydrous calcium sulfoaluminate-belite cement. **Y:** yeelimite, **C$\bar{\text{S}}$H:** gypsum, **C$\bar{\text{S}}$:** anhydrite, **Pe:** Perovskite, **C$_2$S:** belite.

(iii)   Alkali-activated binders:

Metakaolin-based geopolymer (GP): the formulation of this binder corresponds to the C7 formulation used by Pouhet et al. [158]. The XRD pattern of the anhydrous metakaolin is presented in Figure 2.6. The metakaolin was activated by adding 79.7 wt% sodium silicate solution (waterglass) (% by weight of metakaolin), which had a SiO_2/Na_2O molar ratio of 1.7 (27.5 wt% SiO_2, 16 wt% Na_2O and 55.5 wt% H_2O). The low calcium content of this binder (<2 wt%) leads to the formation of a N-A-S-H gel and a highly cross-linked aluminosilicate gel (Si-O-Al-O) [159].
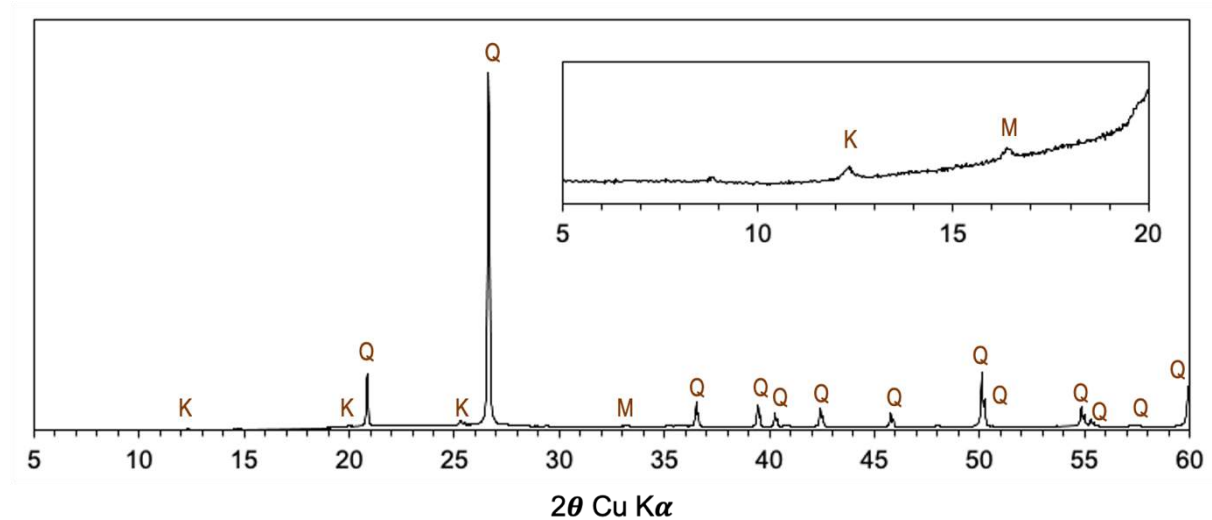
Figure 2.6 – XRD pattern of the anhydrous metakaolin. **K:** kaolinite, **M:** mullite, **Q:** quartz.

Alkali-activated GGBS cement (AAS): this binder was composed of 95% GGBS and 5% clinker. The cement fineness of the GGBS used is 4200 cm^2/g and the XRD pattern of the anhydrous GGBS is presented in Figure 2.7. In this case, the GGBS was activated by adding 8 wt% sodium carbonate (Na_2CO_3) and an experimental admixture (confidential). The main hydration products of this type of binder are C-A-S-H and M_5AH_{13} [19].
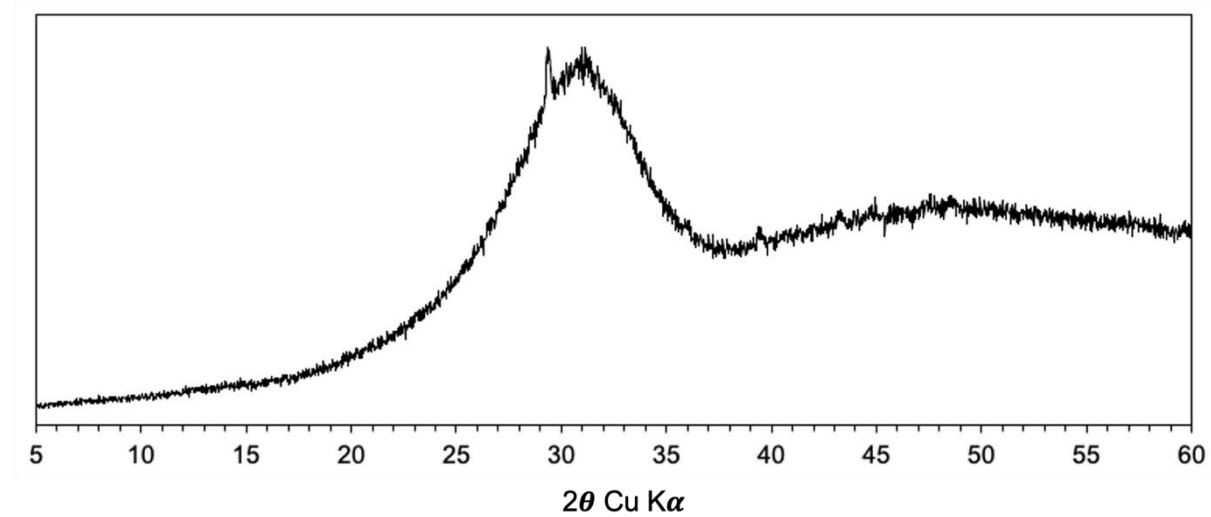
Figure 2.7 – XRD pattern of the anhydrous GGBS used for the alkali-activated GGBS cement.

(a) Portland cements

CEM I
Clinker 95-100%
C₃A~8%
C₄AF~12%
C₃S~60%
C₂S~18%
CS̄ 0-5%

C-S-H 60-75%
AFt 0-5%
AFm 0-5%
CH 20-30%

CEM-SR
Clinker 95-100%
C₄AF~12%
C₃S~60%
C₂S~18%
CS̄ 0-5%

C-S-H 60-75%
AFt 0-5%
AFm 0-5%
CH 20-30%

CEM III/C
Clinker 5-19%
C₃A~8%
C₄AF~12%
C₃S~60%
C₂S~18%
GGBS 81-95%
Secondary constituents 0-5%

C-(A)-S-H 84-96%
CH 1-6%
AFm/Hydrotalcite 3-10%

Binder
Anhydrous products
Reaction products

Expansion under external sulfate attack [a]
High (0.4%)   Low (0.07%)   Low (0.05-0.13%)

(b) Ettringite binders

SSC
GGBS 75-95%
Clinker 0-5%
C₃A~8%
C₄AF~12%
C₃S~60%
C₂S~18%
CS̄ 5-20%

C-(A)-S-H 55-70%
AFm/Hydrotalcite 5-10%
AFt 25-35%

CSA
C₂S 10-50%
CS̄ 10-20%
Ye'elimite 20-50%

C-S-H 20-30%
AFt 60-75%
Others* 5-10%

AFm, stratlingite, monocarboaluminate, gibbsite, hydrogarnet

Expansion under external sulfate attack [a]
Low (0.08%)   Low (0.03%)

(c) Alkali-activated binders

GP
Dry waterglass ~36wt%
Metakaolin

Si-O-Al-O

AAS
GGBS ~95%
Clinker ~5%
Na₂CO₃~8wt%

C-(A)-S-H 60-80%
Others* 10-20%

AFm, monocarboaluminate, hydrotalcite

Expansion under external sulfate attack [a]
Very low (0.015%)   Very low (0.021%)

Typical clinker compound composition from Lea's Chemistry 2019

[a] *Based on longitudinal expansions obtained in Chapter 3 – max. Guideline value: 0.1%*

Figure 2.8 – Anhydrous and reaction products per binder used to fabricate the concretes for ESA. Hydration products were normalized at 100% (the remaining anhydrous phases are not represented in this figure). Expansion under external sulfate attack based on expansion results presented in Chapter 3. This diagram is a representation of the distribution of the anhydrous and reaction products of each binder and it may vary as long as the composition of the binder change, which is mostly the case for CSA cements. Proportions are based on the literature.

2.1.1.2 Aggregates

The aggregates used —one coarse and one fine— were from southwest France. The coarse aggregate was an alluvial siliceous semi-rolled gravel having a particle size of $D_{max} \leq 10$ mm. The fine aggregate was a sand mainly composed of quartz having a particle size of $D_{max} \leq 4$ mm. Figure 2.9(a) and Figure 2.9(b) present the XRD patterns of the fine and coarse aggregates, respectively. Both aggregates present similar composition with small differences on the relative intensities. The aggregates were mainly composed of quartz (Q), feldspars (F) and micas (M). The peak observed between 2θ 10° and 11° was an unidentified mineral present in both aggregates. It should be noted that these aggregates did not have any soluble sulfates in their composition.
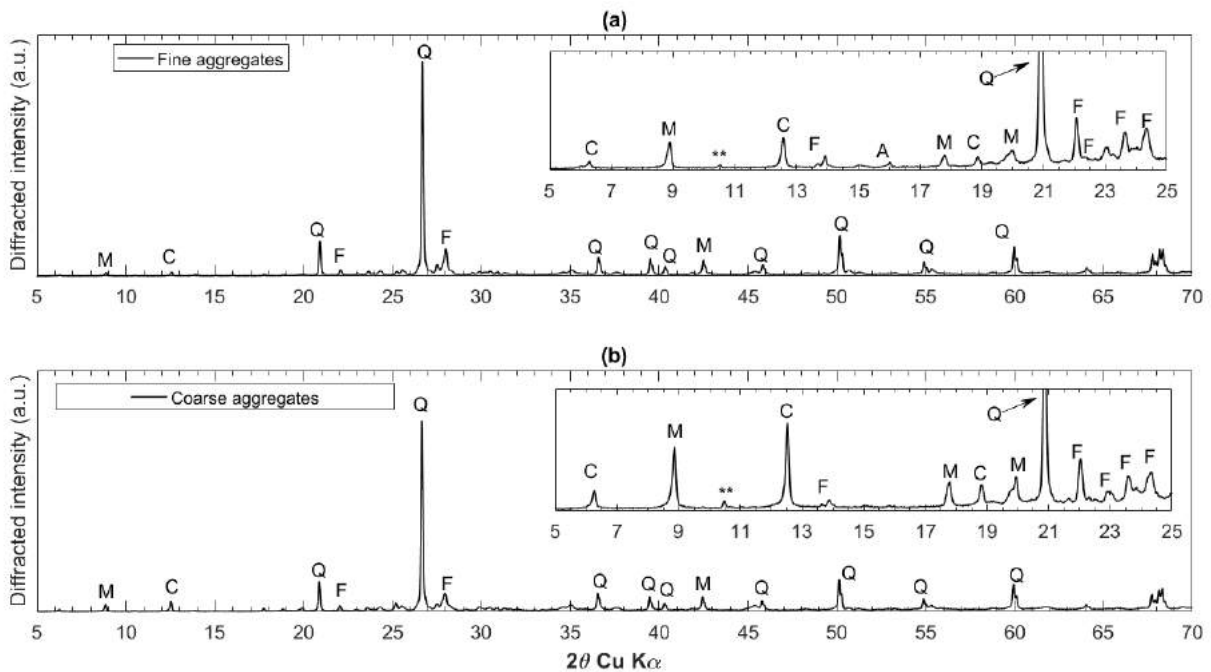
Figure 2.9 – XRD patterns obtained from the aggregates used to cast the concretes. All the patterns were plotted over the range from 2θ 5° to 70º and the selected range from 2θ 5° to 25°. **(a)** Fine aggregate, and **(b)** coarse aggregate. **C:** chlorite, **M:** mica, **Q:** quartz, **F:** feldspar, **A:** andalusite, ****:** unidentified mineral.

2.1.1.3 Specimen preparation and curing

Seven different concretes were batched using the recommended limiting values of the moderately aggressive chemical environment exposure class (XA2) proposed by the European Standard NF EN 206/CN. Therefore, the minimum binder content and the maximum water to binder (w/b) ratio were set to 350 kg/m^3 and 0.5, respectively. The coarse to fine aggregates

ratio was 1.1 and 25 L-batch of concrete was prepared per formulation using a concrete mixer, which is presented in Figure 2.10. The first layer of fresh mixture was vibrated for 30 s in a vibration table and then, the second layer was also vibrated for 30 s in order to expel air bubbles. Description and curing for all concretes are presented in Table 2.3.

Figure 2.10 – Concrete mixer "Collomix 25 L" used to fabricate the concretes.

Water to binder (w/b) ratio justification:

Concretes from the Portland cement (OPC) category (referred to as C-I, C-0 and C-III) were cast with a w/b ratio of 0.5 as recommended by NF EN 206/CN. Meanwhile, for the others binders' categories, the w/b ratio was adapted to the chemistry of each binder. In order to increase the strength of concrete with blended cement, it is recommended to decrease its w/b ratio [60]. Therefore, for SSC-based concretes (C-SSC) and CSA-based concretes (C-CSA), the w/b ratios were set to 0.38 and 0.45, respectively.

For the metakaolin-based geopolymer (C-GP) and the sodium carbonate AAS (C-AAS) concretes, the w/b ratios were set to 0.42 and 0.37, respectively. In the case of C-GP, the effective water content consisted of the water provided by the waterglass and the supplementary water added to the mixture to reach the target w/b. Therefore, the total amount of binder was the addition of the metakaolin and the dry waterglass. For the C-AAS, the total amount of binder consisted of GGBS, clinker and the alkali activator (Na_2CO_3) (proportions are given in Table 2.3).

Curing:

All concretes were cured for 28 days in a room at 20°C and 95% relative humidity (RH). Exceptionally, concretes containing GGBS (C-III, C-SSC and C-AAS) were cured for 90 days in order to ensure their hydration, which is known to be slower than OPCs.

Table 2.3 – Designation (ID), composition and curing of the concretes.

Category	Concrete	Binder (kg/m^3)	Gravel (kg/m^3)	Sand (kg/m^3)	Effective water content (kg/m^3)	w/b[a]	Activator (wt%)	Curing (d)
Portland cement	C-I	350	969	868	175	0.50	-	28
	C-0	350	974	903	175	0.50	-	28
	C-III	350	961	890	175	0.50	-	28/90
Ettringite binders	C-SSC	350	1020	946	131	0.38	-	90
	C-CSA	350	987	914	158	0.45	-	28
Alkali-activated binders	C-GP	350	1143	1059	197[b]	0.42[c]	35.7[d]	28
	C-AAS	350	1007	933	140	0.37[e]	8[f]	90

[a] Effective water content to binder ratio

[b] Total of water coming from waterglass and the supplementary water

[c] Total binder consisted of metakaolin powder and the dry waterglass

[d] Dry sodium silicate (dry waterglass)

[e] Total binder consisted of GGBS, clinker and Na_2CO_3

[f] Na_2CO_3

Cube molds of 150 mm length, 150 mm width and 150 mm height were used to cast the concretes. Cylinder samples of 150 mm height and 29 mm ± 1 mm diameter were cored from the cubes 3 days before starting ESA. Then, stainless steel nuts were positioned at the extremities of the core samples using a highly resistant glue, which does not present creep behavior. These steel nuts were adapted to the extensometer device used to measure length variations. Materials described here are presented in Figure 2.11 and Figure 2.12. Furthermore, cube molds of 100x100x100 mm^3 were used to cast the samples for the compressive strength tests.

Figure 2.11 – At left, core drill FLOTT type M5 S/N 320201TR used to core the cylinder samples. At right, concrete cubes.

Figure 2.12 – One series of cylinder samples of 150 mm height and 29 mm ± 1 mm diameter with stainless steel nuts positioned at the extremities.

2.1.2 Stabilization of sulfates

2.1.2.1 Soil and the source of sulfate

Since a natural sulfate-rich soil was not available, it was chosen to artificially contaminate a soil from the Paris region. This soil was classified as a "silt" using the Unified Soil Classification System (USCS). It had a total organic carbon (TOC) content of about 2450 mg/kg of dry mass of soil $\pm$ 6% and no heavy metal contamination was detected. Its chemical composition is presented in Table 2.4. In order to study sulfate stabilization, the soil was spiked with gypsum ($CaSO_4 \cdot 2H_2O$) at 1.8 wt% (% of weight of dry mass of soil) in order to obtain 1 wt% of sulfate (SO_4^{2-}) (10000 mg/kg of dry mass of soil). The sulfate dosage of 1 wt% is reported as the level where sulfate-rich soil usually presents swelling after cement treatment [160]. In addition, gypsum was selected as the sulfate source because sulfates are generally found in this form in the soils of France [5], [83]. Gypsum is reported to be the major source of sulfate that produces swelling in soils treated with lime [161] and it has a high water solubility (2.4 g/l at 25 °C) [3], [6], [7], [162]. Figure 2.13 presents the XRD patterns obtained from this soil before and after sulfate contamination. Figure 2.13(a) shows that the soil is mainly composed of quartz (Q) and calcite (C). Furthermore, the peaks observed before 2θ 10° showed some traces of clays. Finally, the pattern of natural soil did not show the presence of any crystalline mineral containing sulfates. On the other hand, Figure 2.13(b) shows the XRD pattern in a selected range from 2θ 10° to 15º. The sulfate-spiked soil pattern revealed the presence of gypsum (characteristic peaks between 2θ 11° and 12°).
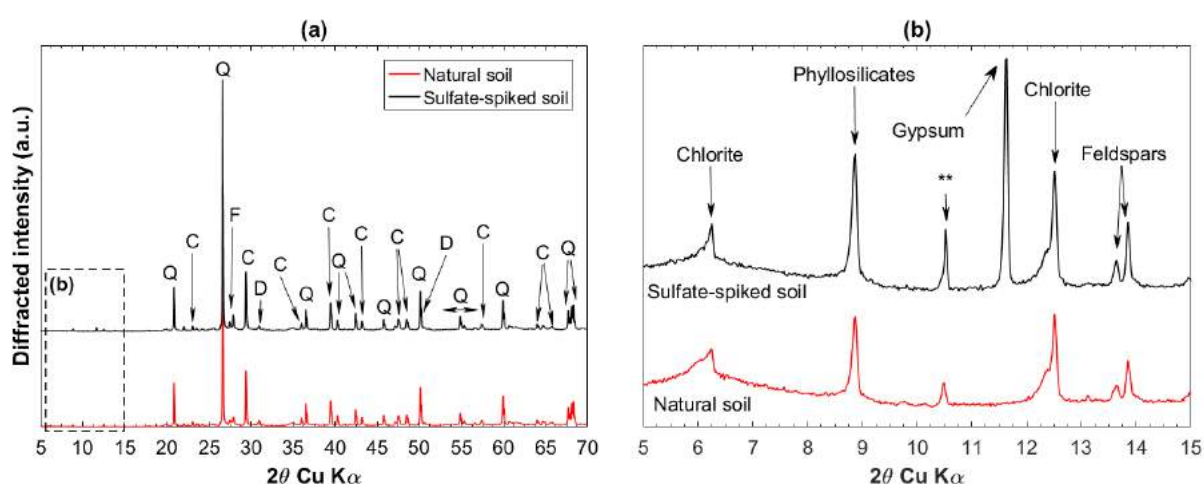
Figure 2.13 - XRD pattern obtained from the natural soil and sulfate-spiked soil **(a)** range from 2θ 5° to 70°, **(b)** selected range from 2θ 5° to 15º showing the appearance of gypsum peaks in the sulfate-spiked soil. **Q:** quartz, **C:** calcite, **F:** feldspars, **D:** dolomite, ****:** unidentified mineral present in the original soil.

2.1.2.2 Binders

Four binders, with the ability to chemically consume sulfates during their hydration process, were tested to stabilize sulfates contained in the soil. The chemical and mineralogical compositions of each of the anhydrous binders are listed in Table 2.4. The binders used in this part of the study were:

- **CEM I:** One ordinary Portland cement (OPC) (cf. CEM I presented in section 2.1.1.1).

- **Clinker Y:** One commercial sulfoaluminate clinker mainly composed of ye'elimite ($C_4A_3\overline{S}$ in cement notation) and belite (C_2S in cement notation). In this binder, the SO_3 content is of about 8%, which is about half of the SO_3 content found in classic calcium sulfoaluminate binders [51]. The main hydration phases of this type of binder are AFt, Ms, AH_3 and the phase straetlingite (C_4ASH_8) may also precipitate because of the presence of C_2S [55].

- **CEM III/C:** One blast furnace slag CEM III/C cement (cf. CEM III/C presented in section 2.1.1.1).

- **90%GGBS+10%OPC:** One experimental binder composed of 90% GGBS and 10% OPC (the OPC designation refers to CEM I 52.5 N R CE CP2 NF). The GGBS used in this binder corresponds to the GGBS used for the alkali-activated slag presented in section 2.1.1.1. The addition of Portland cement to the slag is required to provide the necessary alkalinity to start the reaction of GGBS [60]. In this binder, the main hydration products are C-(A)-S-H, hydrotalcite (M_5AH_{13}), and in contact with sulfates AFt and Ms phases may also precipitate.

Table 2.4 - Chemical and mineralogical compositions of the soil and each of the anhydrous binders (% by weight). The GGBS and OPC binders presented in this table were used to fabricate the experimental binder "90%GGBS+10%OPC".

		Soil[b]	CEM I[a]	Clinker Y[a]	CEM III/C[a]	Experimental binder	
						GGBS[b]	OPC[b]
Oxide composition (% mass)	CaO	13.2	64.5	45.1	46.1	43.8	64.0
	SiO_2	57.7	20.2	10.5	31.3	37.4	21.9
	Al_2O_3	7.2	5.2	23.5	10.5	10.2	3.96
	Fe_2O_3	2.9	3.3	9.7	0.91	0.60	3.1
	MgO	1.1	0.8	1.0	5.8	6.4	1.3
	Mn_2O_3	0.1	ND	0.01	ND	0.20	0.03
	Na_2O	0.7	0.28	0.17	0.53	0.21	0.15
	K_2O	16	0.76	0.27	0.65	0.28	0.74
	TiO_2	0.64	0.00	1.3	ND	0.70	0.17
	P_2O_5	0.21	ND	0.11	ND	0.10	0.10
	SO_3	0.05*	3.0	8.1	2.5	0.10	3.4
	Cl-	-	0.07	0.01	0.30	ND	ND
Clinker composition (% mass)	C_3A	-	8.6	-	8.4	-	8.0
	C_3S	-	60.3	-	63.0	-	53.9
	C_2S	-	12.6	20.3	ND	-	22.2
	C_4AF	-	10.1	-	10.5	-	9.4
	$C_4A_3\bar{S}$	-	-	54.3	-	-	-
	C_3MS_2	-	-	4.50	-	-	-
	C_3FT	-	-	9.30	-	-	-
	$C\bar{S}$	-	5.1	0.40	-	-	5.7
	LOI (loss on ignition)	14.6	1.8	0.23	1.40	NG	1.26

* SO_3 concentration in the natural soil. This soil was spiked with 1.8% gypsum to obtain 1% of sulfates (SO_4^{2-}).

ND: Not determined, NG: Negligible

[a]: compositions were obtained from the technical data sheet of the binders

[b]: compositions were determined from ICP-AES analyses

2.1.2.3 Specimen preparation and curing

All of the samples were fabricated in accordance with the French Standard NF P 94-100. The aim of this standard is to evaluate the mechanical performance of a soil treated with either lime or hydraulic binders. Before sample fabrication, the soil was dried at 40 °C and reduced to a particle size below 5 mm. Then, it was mixed dry with 1.8% by mass of gypsum. Before compaction of the samples, the water content of all the formulations was determined in accordance with the European Standard NF EN 13286-2. This standard specifies a method for determining the relationship between the water content and the dry density of untreated or treated soils with hydraulic binders using Proctor compaction.

The sulfate-spiked soil without treatment was used as the reference or control formulation (F1). For the other mixtures (F2, F3, F4 and F5), the sulfate-spiked soil was mixed dry with the

binders using a dosage of 10% by weight of dry soil. This binder dosage level was selected in order to ensure sufficient mechanical properties for all of the treatments (justification is presented in Chapter 4 section 4.1.2).

Table 2.5 – Designations and compositions of all the formulations studied (% by weight of dry soil).

Formulation	Composition	Water[a] to solid ratio (w/s)
F1 (untreated soil)	Soil + 1% SO_4^{2-}	0.17
F2	Soil + 1% SO_4^{2-} + 10% CEM I	0.15
F3	Soil + 1% SO_4^{2-} + 10% Clinker Y	0.15
F4	Soil + 1% SO_4^{2-} + 10% CEM III/C	0.17
F5	Soil + 1% SO_4^{2-} + 10% (90% GGBS+10% OPC)	0.17

[a] Water content determined in accordance with the European Standard NF EN 13286-2
1% sulfates = 1.8 wt% gypsum

The formulations tested are described in Table 2.5 and schematically represented in Figure 2.14. This representation shows the hydration products normalized to 100%; therefore, the remaining anhydrous phases are not represented in this figure.

Compaction was carried out by using cylindrical test molds (50 mm in height and 50 mm in diameter) at 96% of the maximum dry density. All of the samples were protected in hermetically sealed bags to preserve the water content and stored in a room at 20 °C until tests were conducted. The preparation of samples and the materials used in this part of the study are presented in Figure 2.15 and in Figure 2.16.
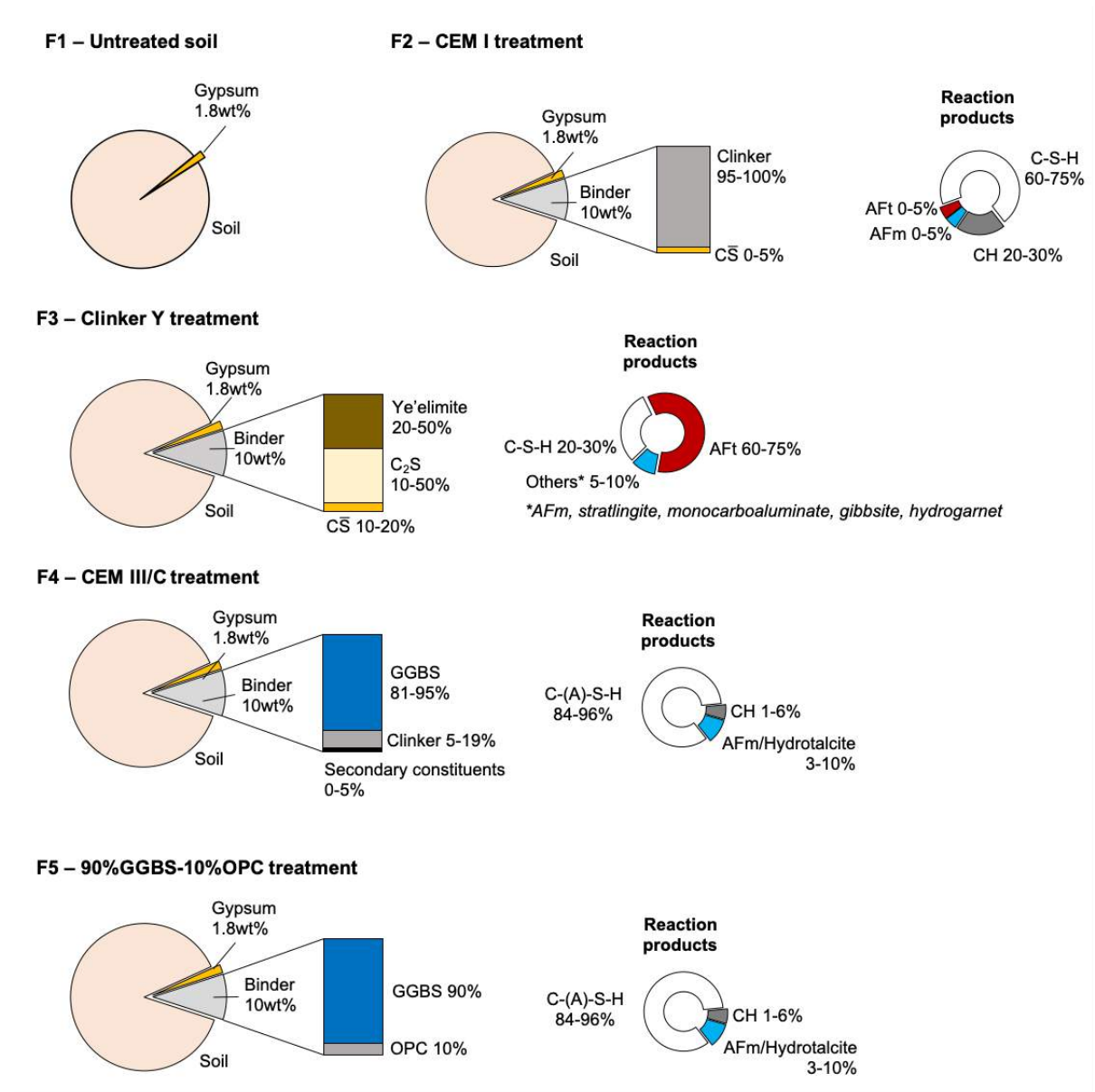
Figure 2.14 – Schema of treatments tested in the study of stabilization of sulfates. Percentages are expressed in weight of dry soil. Hydration products were normalized at 100%. This schema is a representation of the distribution of the anhydrous and reaction products of each binder used for the treatments. This distribution may vary as long as the composition of the binder change.

Figure 2.15 – Preparation of soil samples. **From left to right: (i)** dry soil with particle size below 5 mm, **(ii)** addition of 1.8 wt% gypsum, **(iii)** addition of 10 wt% binder, **(iv)** dry mixture for homogenization, and **(v)** addition of water for mixture and future compaction.

Figure 2.16 – **From left to right: (i)** compaction device with soil uncompacted, **(ii)** and **(iii)** compaction press and compacted soil sample, **(iv)** several compacted soil samples with and without cylindrical molds.

2.1.3 Stabilization of molybdenum

2.1.3.1 Molybdenum source

Sodium molybdate (Na_2MoO_4) commercially purchased from Alfa Aesar (sodium molybdate anhydre - Mo 46.2%) was chosen to artificially contaminate three different binders with molybdenum (Mo). The XRD pattern of this mineral is presented in Figure 2.17.

As presented in Chapter 1 - Table 1.8, sodium molybdate is one of the main anthropogenic sources of Mo in soil commonly used in the agriculture industry as a fertilizer of soil presenting Mo deficiency. In addition, it has the highest solubility in water among all the Mo sources (65 g/100 ml at 20ºC), which is an advantage when binders are spiked with Mo via the mixing water. Moreover, in Na_2MoO_4 the Mo oxidation state is +6, which is one of the most common and stable Mo oxidation state [144] (cf. Chapter 1 - Figure 1.18).
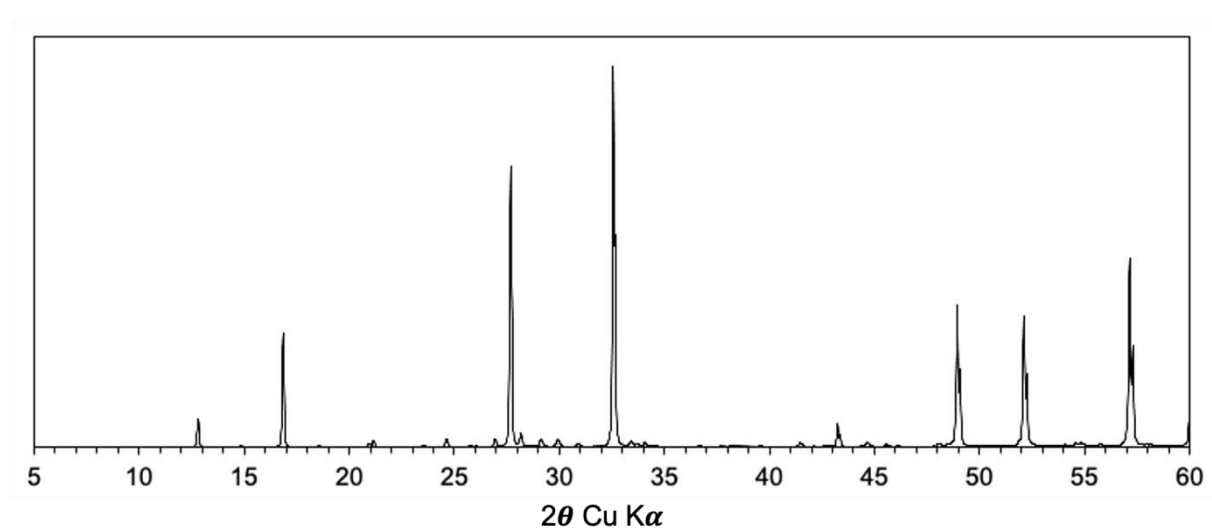
Figure 2.17 – XRD pattern of sodium molybdate (Na$_2$MoO$_4$).

2.1.3.2 Binders

Three binders were tested to evaluate their capacity to immobilize Mo. The binders tested in this part of the study were:

- **OPC:** One ordinary Portland cement. (cf. CEM I presented in section 2.1.1.1).

- **SSC:** Supersulfated GGBS cement (SSC) (cf. SSC presented in section 2.1.1.1).

- **90%GGBS+10%OPC:** referred to as "90-10". This experimental binder is composed of 90% of ground granulated blast furnace slag (GGBS) and 10% of an Ordinary Portland cement (OPC), (cf. 90%GGBS+10%OPC presented in section 2.1.2.2).

2.1.3.3 Specimen preparation and curing

Samples were obtained by spiking the binders at six different Na$_2$MoO$_4$ concentrations via the mixing water. Mo concentrations were chosen to observe their influence on Mo stabilization mechanisms and to guarantee Mo detection. First, Na$_2$MoO$_4$ was dissolved in the mixing water. Then, the binder was added to the Mo-solution keeping a liquid to binder (L/B) ratio of 0.4. The fresh mixture was vibrated for 30 s in a vibration table in order to expel air bubbles. Samples were cured for 28 days in a room at 20 °C and kept into plastic molds and protected in hermetical recipients in order to keep a constant water content. Description and curing of all

formulations are presented in Table 2.6 and Figure 2.18 presents an example of Mo-spiked samples.

Table 2.6 – Designation (ID) of binders and initial Mo concentration used to artificially contaminate the binders.

Binder/ID	Initial Mo concentration		
	Mo (wt%)	Mo (mg/kg of dry binder) [a]	
B1(CEM I) B2(90-10) B3(SSC)	0	0	Found in natural soil/contaminated materials
	0.005	50	
	0.05	500	
	0.1	1000	
	1	10000	To guarantee Mo detection
	5	50000	
	10	100000	

wt%: % by weight of binder
[a] 120 g of binder were used to fabricate each formulation with a water to binder (w/b) ratio of 0.4
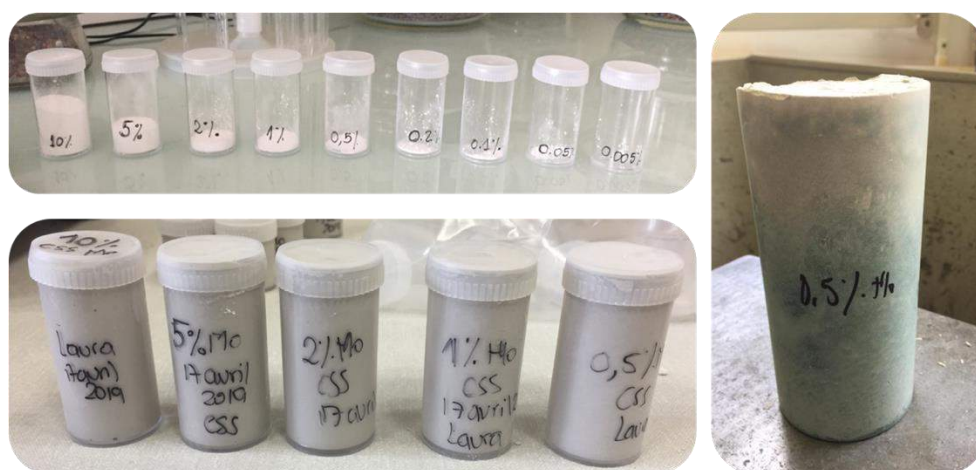
Figure 2.18 – **At top left**, Na_2MoO_4 at different concentrations for fabrication of samples. **At bottom left**, example of Mo-spiked binders. **At right**, example of Mo-spiked sample after 28 days curing destined for leaching tests.

2.1.3.4 Synthesis of calcium silicate hydrate (C-S-H) with Mo

The synthesis of pure C-S-H phases was carried out in order to evaluate their capacity to immobilize Mo. Synthetic C-S-H phases were prepared in accordance with the protocol presented by Roosz et al. [163]. Synthetic C-S-H phases were made by using three different chemical reactants: lime (CaO), amorphous silica (SiO_2) and sodium molybdate (Na_2MoO_4).

First, CaO was calcined in a furnace for 8 h at 1000 °C in order to unsure the absence of portlandite ($Ca(OH)_2$) and calcite. Second, Na_2MoO_4 was dissolved in purified water (18 MΩ.cm) in order to obtain five different Mo concentrations: 0, 0.25, 1, 2.5 and 5 wt% (% by weight of solid, solid= total mass of $CaO+SiO_2$). These concentrations were chosen to observe the capacity of C-S-H to immobilize Mo at different levels in addition to guarantee Mo detection. Then, CaO and SiO_2 were added to the Mo-solution keeping a liquid to solid (L/S) ratio of 50 and the target stoichiometric Ca/Si ratio was set at 1.6 (the justification of this ratio is presented in Chapter 5). The description of all the syntheses is presented in Table 2.7.

Table 2.7 – Description of all the syntheses of C-S-H with Mo (% by weight of solid[c]).

	Solid							
ID	**CaO (g)**	**SiO2 (g)**	**Initial Mo concentration (wt%) [a]**	**Mo (g)**	**Total reactants (g)**	**Total water (g)[b]**	**Initial Mo concentration (mg/L)**	**Initial Mo concentration (mg/kg of dry solid) [c]**
CSH			0	0	20	1000	0	0
CSH_0.25			0.25	0.05	20.11	1005.4	50	2500
CSH_1	11.98	8.02	1.0	0.2	20.43	1021.5	100	10000
CSH_2.5			2.5	0.5	21.07	1053.6	500	25000
CSH_5			5.0	1	22.15	1107.3	1000	50000

[a] % by weight of solid (total mass of $CaO+SiO_2$)
[b] Keeping a liquid to solid reactants (L/S) ratio of 50.
[c] Solid = 20 g of $CaO+SiO_2$

All the synthetic C-S-H phases were prepared using a glovebox under nitrogen flush in order to minimize carbonation. Finally, all the solutions were stored in 250 ml polypropylene bottles and shaken in an end-over-end tumbler at 7 rpm for 30 days. The solid residue was separated by centrifugation and filtration using a vacuum device and 0.22 µm membrane filters and stored in a desiccator until analyses were performed. After filtration, pH was measured in the resulting solutions and then they were stabilized to 2 v% nitric acid (HNO_3) solution and stored at 4 °C until analyses. Materials and devices used for the synthesis of C-S-H with Mo are presented in Figure 2.19.

Figure 2.19 – **At left**, glovebox under nitrogen employed for the synthesis of C-S-H with Mo. **At top right**, end-over-end tumbler used to shake solutions. **At bottom right**, synthetic C-S-H samples obtained after filtration.

2.2 Methods

2.2.1 Mineralogical characterization

2.2.1.1   Hydration stoppage

Hydration of concretes and pastes were stopped before characterization. Hydration stoppage is necessary to suppress the further progress of hydration and to minimize carbonation. In the present study, hydration stoppage was carried out in accordance with RILEM TC-238 SCM recommendations by using isopropanol ($(CH_3)_2CHOH$) as an organic solvent, which replaces the water and then is evaporated. To this end, samples were submerged for several minutes into isopropanol, filtered and dried a few minutes at 40ºC.

2.2.1.2   X-ray diffraction

X-ray diffraction (XRD) was used to characterize crystalline phases. XRD gives patterns of peak positions and relative intensities that characterize different crystal structures present in the samples. XRD was performed using a Bruker D8 diffractometer with the Bragg-Brentano configuration and copper radiation (*Cu Kα*, *λ*=1.54Å). The anode voltage was 40 kV and the electric current intensity was 40 mA. XRD analyses were carried out on powder with particle size below 80 µm previously grounded manually in an agate mortar, then placed on a rotary sample holder. The acquisitions were made between 4° and 70° 2θ, with a step size of 0.02° and an acquisition time of 0.25 seconds per step. Qualitative analyses were performed for 30 minutes and data were treated using EVA software provided with the Powder Diffraction

data File (PDF) of The International Centre for Diffraction Data (ICDD). For the purpose of comparison of the peaks of different XRD patterns, samples were spiked with 5 wt% of rutile (TiO_2).

2.2.1.3 Thermogravimetric analysis

Thermogravimetric analysis (TGA) was used to identify hydration phases (both crystalline and amorphous). This technique measures the weight loss of a sample by increasing the temperature. TGA was performed using two different devices: a Netzsch STA449-F3 and a TG2 Mettler Toledo. All analyses were carried out on powder previously crushed to a particle size below 80 μm. The heating rate was 10 ºC/min over the temperature range 40-1000 ºC.

2.2.1.4 Microscopic characterization

Chemical and microstructural analyses were carried out using Scanning Electron Microscopy with Energy Dispersive Spectroscopy (SEM/EDS). For observations of samples in powder form, the powder was dispersed on an adhesive carbon tab and coated with carbon. SEM observations of fracture surfaces were carried out on unpolished sections coated with carbon and using secondary electron (SE) imaging; while observations of polished sections, previously mounted in resin and coated with carbon, were made by using back-scattered electrons (BSE). Polishing was conducted on samples by using isopropanol as lubricant and silicon carbide grinding (SiC) paper at three different grades, 800, 1200 and 4000, for 5 minutes per paper. Figure 2.20 presents some examples of samples used for microstructural observations.

In this study, two different scanning electron microscopes were used, a JEOL JSM-6380LV and a JEOL JSM 7800, equipped with Rontec XFLASH 3001 and SDD X-Max 80mm2 EDS detectors, respectively. Images were obtained with magnifications between 50x and 10000x. SEM observations coupled with EDS mapping and EDS punctual analyses were also carried out in order to identify correlations between various chemical elements. The SEM images presented in this study provide a representative picture of the analyzed samples.

Figure 2.20 – Examples of samples used for microstructural observations. From left to right**: (i)** concrete fracture sections**, (ii)** soil treated samples mounted in resin, and **(iii)** Mo-spiked binders mounted in resin.

2.2.1.5   Fourier transform infrared spectroscopy (FT-IR)

Fourier transform infrared spectroscopy (FT-IR) is a "*technique based on the vibrations of atoms in a molecule or in a mineral*" [164]. This technique was used to identify functional groups in molecules to detect structural modifications. Molecular vibrations can be related to the symmetry of molecules. FT-IR analyses were carried out on powder using a Perkin Elmer UATR1 device with a diamond crystal. Data was collected over the wavenumber range 4000-600 cm^{-1}. Petit and Madejova [164] explained that the stretching and bending vibrations of OH groups absorb in the 3700-3500 and 950-650 cm^{-1} regions, respectively. The Si-O stretching modes occur in the 1050-980 cm^{-1}, while the most intense bending bands appear in the far-infrared region (FIR) (550-400 cm^{-1}). However, this last region cannot be observed in the current FT-IR used in this project.

2.2.2 Chemical analyses

2.2.2.1   Leaching tests

In this study, the element immobilization efficacy (sulfates and heavy metals) was evaluated by carrying out leaching tests in accordance with the European Standard NF EN 12457-2 as

required by the French Ministerial Decree of 12 December 2014 [88]. The Standard NF EN 12457-2 allows the characterization and evaluation of leachable constituents of waste materials in a single step batch procedure at natural pH condition by using distilled water as a leachate. In order to perform the test, samples were crushed to a particle size below 4 mm (the grain size distribution below 4 mm is not controlled) and placed in 1 L polypropylene bottles containing distilled water with a liquid to solid ratio (L/S) of 10 L/kg. All bottles were shaken for 24 h in an end-over-end tumbler at 7 rpm. The solid residue was separated by filtration using a vacuum device and 0.45 µm membrane filters. Materials used for leaching tests are presented in Figure 2.21. After filtration, the conductivity and pH were measured in each of the eluates (cf. Figure 2.22), which were then stabilized to 2 v% nitric acid (HNO_3) solution. All solutions were stored at 4 ºC until the chemical analyses were performed. A minimum of two specimens were used per formulation. Arithmetic average results are presented with a confidence interval of 95%.

Concerning the treated soil samples, leaching tests were carried out at 28 days and 6 months of curing. The first age was established to evaluate the sulfate immobilization in the short-term and the second curing was used to evaluate the sulfate immobilization in the long-term. These curing times are not normalized but they are currently used in the industrial applications. Concerning the Mo-spiked samples, leaching tests were conducted on samples cured for 28 days.

Figure 2.21 – **At left**, end-over-end tumbler for leaching tests. **At right**, vacuum device used for filtration.

Figure 2.22 – At left, device for conductivity measures. At right, device for pH measures.

2.2.2.2 Ion chromatography

Leachable sulfate, chloride and fluoride concentrations were measured using ion chromatography (Dionex Ion Chromatography System (ICS-3000)). Before analyses, all solutions were diluted by factors of 10, 25 or 100 using ultrapure water (18 MΩ.cm). In this study, the ICS-3000 generates a potassium hydroxide (KOH) eluent for anion exchange separations with a concentration range from 1 mM to 60 mM, and a flow rate of 1.5 ml/min.

2.2.2.3 Inductively coupled plasma atomic emission spectrometry

Major, minor and heavy metal concentrations in solutions were determined using Inductively Coupled Plasma Atomic Emission Spectrometry (ICP-AES) (Optima 7000 DV machine). In this case, all solutions were diluted by factors of 10, 25 or 100 using ultrapure water (18 MΩ.cm) with 2 v% HNO_3.

2.2.3 Concrete tests

2.2.3.1 Compressive strength tests

Compressive strength tests were used to characterize the concretes in hardened state at 28 days of curing in accordance with the European Standard EN 12390-3. A total of 3 samples were used per formulation, and arithmetic average results are presented with a confidence interval of 95%. The testing machine used for compressive strength tests and an example of a cube sample is presented in Figure 2.23.
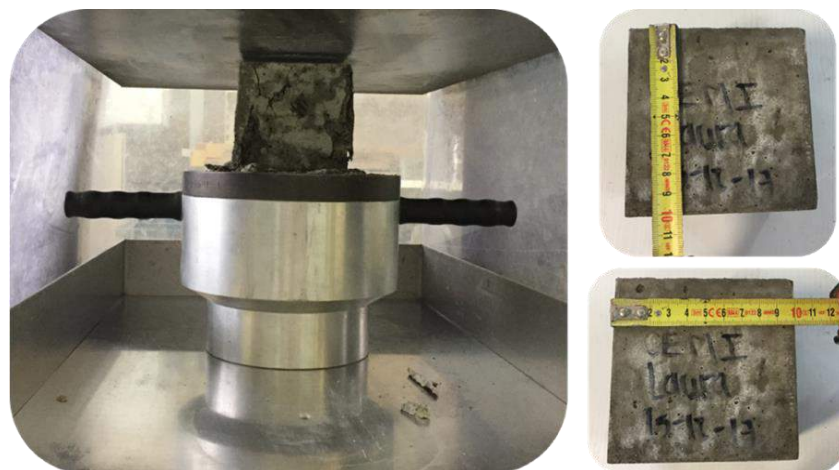
Figure 2.23 – At left, testing machine "3R RP4000QC/LC" used for compressive strength tests with one cube sample. **At right,** example of a cube concrete sample of 100x100x100 mm^3 used for compressive strength tests.

2.2.3.2 External sulfate attack tests

Two standardized tests were considered to study the resistance of concretes to external sulfate attack (ESA) and they are presented in Table 2.8. Between these two tests, the protocol presented by Swiss Standard SIA 262/1:2013 Appendix D was chosen to study the capacity of concretes under ESA because of the acceleration period and the test of duration.

Table 2.8 – Comparison of two standardized tests to study the resistance of concretes to external sulfate attack (ESA).

	Parameter	ASTM C1012	SIA 262
Sample	Dimension	2.5x 2.5 x 28.5 cm	d = 2.8± 0.2 cm L =15±2 cm
	Material	Mortar	Concrete
	Pre-conditioning	Submersion in water for 1 h	Submersion in water for 1 h
Solution of immersion	Sulfate source	Na_2SO_4	Na_2SO_4
	Concentration	50 g/L	50 g/L
	Volume ratio (Vol. solution/Vol. sample)	4 to 5	4 to 5
	Solution renewal	No	No
	pH control	No	No
	Temperature control	No	No
Damage period	Drying/submersion cycles	No	Yes
Test duration	Test duration	6 – 12 months	3 months

The principle of the SIA 262 test consists of accelerating the sulfate attack on concrete by exposure of samples to 4 cycles of drying/submersion followed by a consecutive submersion in a sulfate solution. Each drying cycle was carried out for 5 days using an oven at 50°C while

each submersion cycle was carried out for 2 days in a sulfate solution prepared with distilled water and 50 g/L of sodium sulfate (Na_2SO_4). The Na_2SO_4 solution was stored in individual plastic and closed buckets -one bucket per composition- and the solution to concrete volume ratio was kept equal to 4.5. All the buckets were stored in a room at 20ºC. The disposition of samples is schematically represented in Figure 2.24 and Figure 2.25. After the drying/submersion cycles, concretes were submerged in the Na_2SO_4 solution for 56 consecutive days, without renewing the solution. The test duration was 84 days and measurements of length variations were done at the end of each drying/submersion cycle and during the subsequent submersion phase at 7, 14, 28, 42 and 56 days. A total of 8 samples were used per formulation. Longitudinal expansion is presented as the arithmetic average value of all results with a confidence interval of 95%.

Additional concretes were tested following the same protocol (drying/submersion cycles and constant submersion) but using only water as the immersion solution. The aim of these additional tests was to verify if the expansion of concretes was either produced by the uptake of water or by the reaction with sulfates. A total of 3 samples were used per formulation and longitudinal expansion is presented as the arithmetic average value of all results with a confidence interval of 95%.
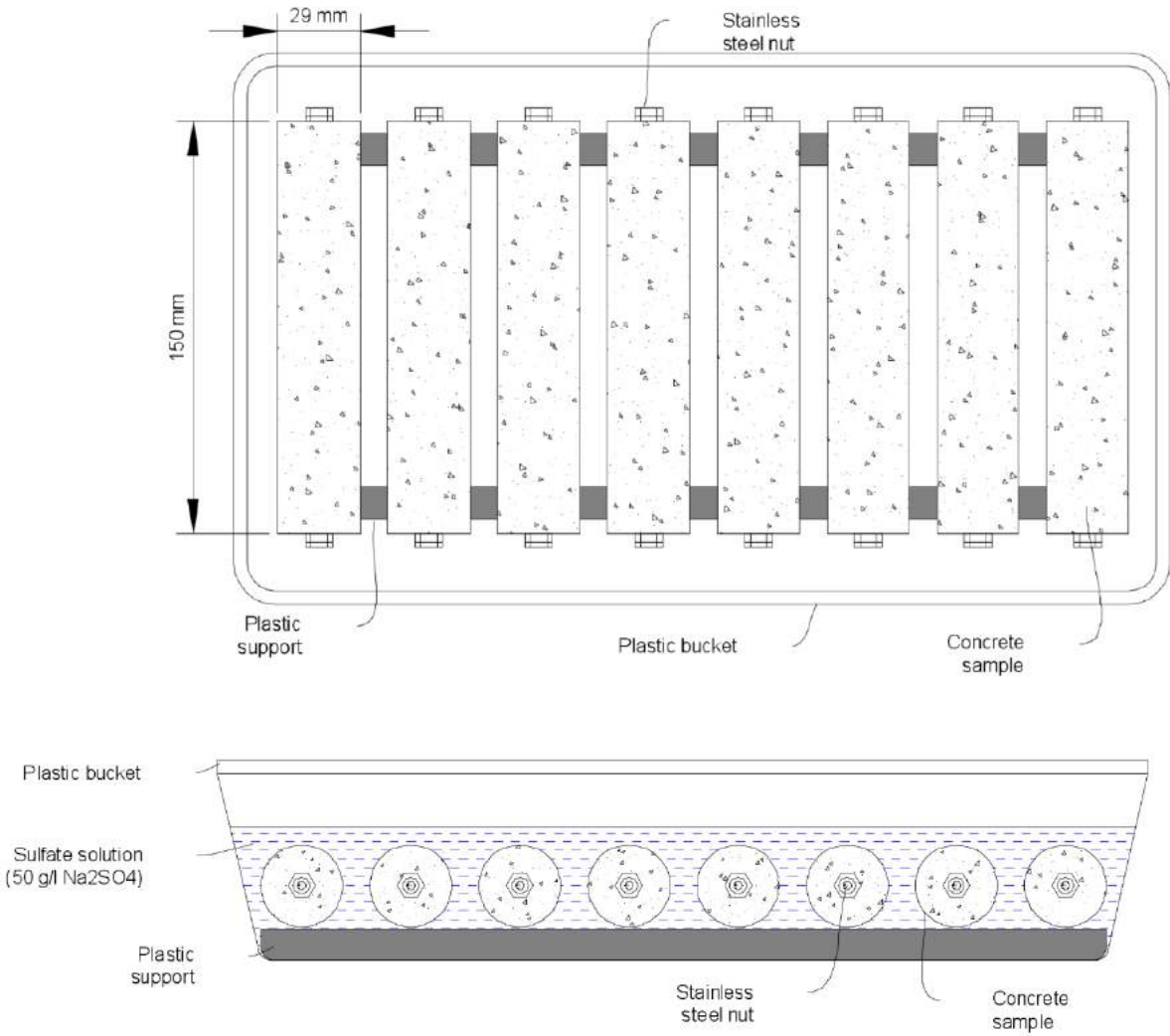
Figure 2.24 – Schematic drawing of the bucket and concrete samples used for the external sulfate attack tests.

Figure 2.25 – At left, example of a series of samples submerged in the sulfate solution. At right, extensometer device used to measure length variations.

2.2.3.3 Pore solution extractions

For the purpose of better understanding the behavior of the materials under ESA, pore solutions extractions of concretes were performed before and after sulfate attack by carrying out squeezing tests using a high-pressure device [165]. The squeezing process resulted in the extraction of some milliliters of pore solution for all the concretes except for C-SSC and C-CSA (a higher pressure is required to extract their pore solutions). The materials used for this test are presented in Figure 2.26.

After extractions, solid residue was separated by filtration using 0.45 µm membrane filters, pH measurements were made and then, solutions were stabilized to 2 v% nitric acid (HNO$_3$) and stored at 4ºC until analyses were performed.

Figure 2.26 – High-pressure device for squeezing tests. At right, example of solution extracted from C-I concrete after external sulfate attack.

2.2.4 Geotechnical properties of treated soils

2.2.4.1 Swelling potential in the short-term

After treatment of sulfate-rich soil, several properties have to be evaluated in order to ensure the mechanical stability of the soil application. In the short-term, swelling potential was evaluated in all of the soil treatments by carrying out volume expansion tests in accordance with the French Standard NF P 94-100. This standard proposes the submersion of all treated soil samples in water at 40 ºC for 7 days using a heated bath (presented in Figure 2.27). The objective of this immersion is to accelerate the hydration of binders and to verify whether the treatment leads to expansion of the material [74]. Before the submersion period, this standard recommends a specific curing time for treated soils. When soil is treated with lime, the curing period is 3 days ± 4 h. For treatments with other binders, the minimum curing time recommended is 4 h ± 15 min and the maximum curing time is 7 days. Therefore, in this study,

the minimum and maximum curing times were tested (results are presented in Chapter 4). Preliminary testing showed that a 4-h curing time appeared to be insufficient to meet the requirements for splitting tests. For this reason, a curing time of 7 days was chosen for both volume expansion and splitting tests.

Initial geometrical measurements of samples were taken after 7 days of curing using a digital sliding caliper and final volumes were measured at the end of the submersion period by applying Archimedes' principle (cf. Figure 2.27). Three samples were used per formulation and arithmetic average results are presented with a confidence interval of 95%.

Figure 2.27 – From left to right: (i) heated bath employed for keeping water at 40ºC for volume expansion tests, **(ii)** device of Archimedes' principle, and **(iii)** example of a series of samples used for volume expansion tests according to the French Standard NF P 94-100.

2.2.4.2 Indirect tensile strength in the short-term

Samples used to measure indirect tensile strength followed a similar preparation to that for volume expansion tests (cf. 2.2.4.1). At the end of the immersion period, the indirect tensile strength was assessed by carrying out splitting tests in accordance with European Standard NF EN 13286-42, which proposes diametral compression tests on compacted soil samples (cf. Figure 2.28). Three samples were used per formulation and arithmetic average results are presented with a confidence interval of 95%.

Figure 2.28 – Device used for splitting tests according to European Standard NF EN 13286-42. **At bottom right:** example of the fracture of a soil sample after splitting test.

2.2.4.3 Criteria to assess the performance of treated soils

The French Standard NF P 94-10 takes two criteria into account to assess the performance of a soil treated with hydraulic binders: (i) volume expansion, and (ii) indirect tensile strength. These criteria and their guideline values are presented in Table 2.9.

Table 2.9 – Criteria and guideline values to evaluate the performance of a soil treated with hydraulic binders according to the French Standard NF P 94-100.

Performance of the treated soil	Parameter (after immersion for 7 days)	
	Volume expansion (Gv) in %	Indirect tensile strength (Rtb) in MPa
Suitable	≤ 5	≥ 0.2
Doubtful	$5 < Gv \leq 10$	$0.1 \leq Rtb < 0.2$
Unsuitable	> 10	< 0.1

2.2.4.4 Workability delay

In the treatment of soil, the evaluation of workability is very important in order to fix the longest possible duration of the construction operations. Therefore, low workability of a mixture leads to difficulties for construction applications. Before evaluating the workability of the mixture, the optimum water content of the mixture has to be determined by carrying out the Modified Proctor Compaction test presented by the French Standard NF P 94-093. This test is used to

determine the relationship between water content and dry unit weight (dry density) of soil. The procedure of compaction is repeated for a sufficient number of water contents to establish a relationship between the dry density and the water content for the mixture. Then, the workability delay is evaluated by carrying out delayed compaction tests according to the French Standard NF P 98-231-6 and using the optimum water content determined by the Modified Proctor Compaction test. The delay proposed by this standard is presented in Table 2.10.

Table 2.10 – Delay proposed by the French Standard NF P 98-231-6 for the workability test.

Sample	1	2	3	4	5
Estimated compaction delay (h)	0	1	3	5	7

The workability delay consists of the time where the dry density reaches 98% of the initial dry density (a decrease in 2% of the dry density). According to the French Technical Guide GTR (*Guide technique pour la réalisation des remblais et des couches de forme*) [65], for the majority of constructions, a workability delay value of about 4 and 6 hours seems suitable.
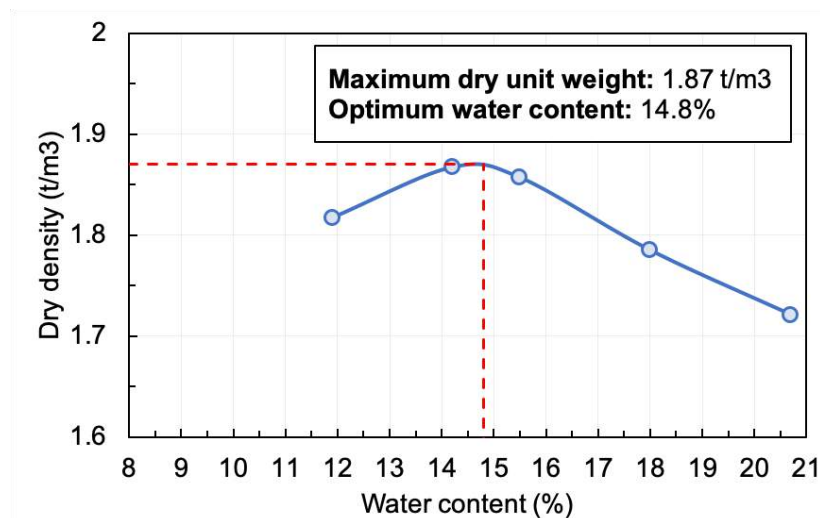
Figure 2.29 – Compaction curve of formulation F5 and obtained in accordance with the French Standard NF P 94-093.

In the present study, the workability test was conducted on the formulation F5 (cf. section 2.1.2.3 – Table 2.5). The compaction curve obtained from the Modified Proctor Compaction test is presented in Figure 2.29 (workability results are presented in Chapter 4 - section 4.3.3.2).

2.2.4.5 Compressive strength in the medium and long-term

In the medium-term, compressive strength tests were carried out in formulation F5 samples F5 (cf. section 2.1.2.3 – Table 2.5) that were previously compacted following the protocol presented by the French Standard NF P 94-100. All the samples measured 100 mm in height and 50 mm in diameter.

All tests were conducted by using four different curing conditions:

- 60 days air
- 28 days air + 32 days in water at 20ºC
- 180 days air
- 90 days air + 90 days in water at 20ºC

Curing in water were carried out to evaluate the sensibility of the mixture to water. Three samples were used per curing condition and arithmetic average results are presented with a confidence interval of 95%.

Compressive strength tests conducted on samples following an air cure and a humid cure gives compressive strength values referred to as "Rci" and "Rc", respectively. According to French Technical Guide GTR (*Guide technique pour la réalisation des remblais et des couches de forme*) [65], the Rci/Rc ratio determined at 60 days of curing indicate the mechanical performances of treated soils in the medium-term as a function of the methylene blue value (V_{BS}), which indicates the clay content of the material. For research purposes, the mechanical performance was also evaluated at 180 days of curing (in the long-term).

Table 2.11 – Criterion to evaluate mechanical performance in treated soils according to the technical guide SETRA for V_{BS}>0.5.

Criterion from SETRA	
Ratio	V_{BS}
$\dfrac{Rci}{Rc60} \geq 0.6$	>0.5

2.2.4.6 Mechanical performance class in the long-term

When treated soil is destined for geotechnical applications such as sub-grades (i.e. underlying ground in a pavement), it is necessary to determine the mechanical performance class in the long-term. In this classification, there are five different zones and thus the treated soil is classified into five different mechanical classes. This classification allows to estimate the

thickness of the sub-grade. In this study, the mechanical performance class was obtained according to the French Standard NF P 94-102-1. To this end, the indirect tensile strength (Rit) and the Young modulus (E) have to be determined. Rit and E were obtained by carrying out splitting tests according to NF EN 13286-42 as a function of six different curing conditions:

- 60 days air
- 28 days air + 32 days in water at 20ºC
- 28 days air + 32 days in water at 40ºC
- 180 days air
- 90 days air + 90 days in water at 20ºC
- 90 days air + 90 days in water at 40ºC

According to the French Technical Guide GTR (*Guide technique pour la réalisation des remblais et des couches de forme*) [65], the Rit/E ratio obtained from a treated soil at 90 days of curing should lead to a minimum mechanical class of 5. Figure 2.30 presents the different zones of classification of a treated soil in accordance with their mechanical properties (R_{it} and E) [65]. Furthermore, the different zones and mechanical class are presented in Table 2.12.

Table 2.12 – Determination of the mechanical performance class of a treated soil at 90 days curing according to the French Technical Guide GTR [65] and the French Standard NF P 94-102-1.

In-situ treatment		Zone 1	Zone 2	Zone 3	Zone 4
Mechanical class	1	2	3	4	5
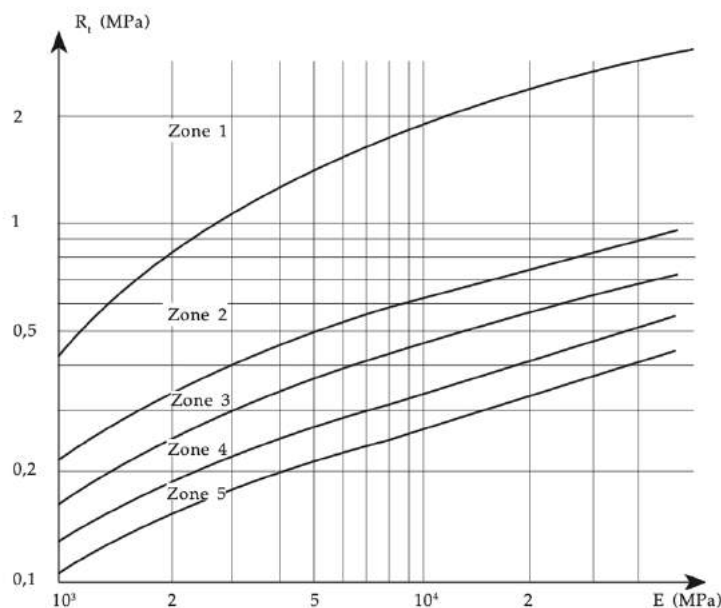
Figure 2.30 – Classification of treated soil in accordance with the mechanical properties (Rit and E) determined at 90 days of curing. Taken from [65].

2.2.4.7 Swelling potential in the long-term

Swelling potential was evaluated in formulation F5 in long-term following the protocol presented by the French Standard NF P 94-100 (cf. Chapter 2 - section 2.2.4.1). However, in this case, different curing conditions were chosen (industrial requirement):

- 28 days air + 32 days in water at 20ºC
- 28 days air + 32 days in water at 40ºC
- 90 days air + 90 days in water at 20ºC
- 90 days air + 90 days in water at 40ºC

2.2.5 Modeling

The modeling made in this study was carried out in order to increase the understanding of the phenomena involved in each part of this study and to predict the behavior of pollutants at low concentrations. Modeling was carried out using the computer code PHREEQC version 3.0 [151], a speciation and reaction path program produced by the US Geological Survey. As explained in the literature review (cf. Chapter 1 - section 1.4), this code allows to develop models that are built on the fundamental laws of thermodynamics. The type of model used in this study is a "speciation-solubility geochemical model". The explanation of how this model works is presented in Chapter 1 - section 1.4.

2.2.5.1 Thermodynamic calculations of saturation index for concrete under external sulfate attack

Saturation Indices (SI) of ettringite (AFt), calcium monosulfoaluminate (Ms) and gypsum were calculated using PHREEQC and the ion concentrations obtained from pore solution extractions (cf. Chapter 2 - section 2.2.3.3). The thermodynamic properties used in this work came from the Thermoddem database version 1.10 [166]. Any pH adjustments necessary to match experimental and numerical data were made by using the "pH charge" function [47].

In this geochemical model, the initial solutions were defined using a temperature of $T=25°C$ and the pH was adjusted by PHREEQC in order to achieve a charge balance and decrease the uncertainty of results. All the SI were calculated before and after sulfate attack for each concrete except for C-SSC and C-CSA because no data was obtained from their pore solutions (justification was presented in Chapter 2 - section 2.2.3.3). The input data used in this part of the study is presented in Annex 1 (presented at the end of this chapter).

2.2.5.2 Modeling for the study of the stabilization of sulfates

The thermodynamic properties used in this part of the work came from the Thermoddem database version 1.10 [166]. Hydrogarnet phase ($C_3(A,F)S_{0.84}H_{4.32}$), which is a typical cementitious phase in the studied system, was added to this database using the Gibbs free energy of formation presented by Lothenbach et al. [167].

In this geochemical model, the initial solution was defined using a liquid to solid ratio of L/S=10 L/kg, a temperature of T=25°C and a pH of 7.0. The soil was defined as a combination of four main constituents represented in the form of quartz (SiO_2), calcite ($CaCO_3$), illite ($K_{0.85}Al_{2.85}Si_{3.15}O_{10}(OH)_2$) and magnetite ($Fe_2O_3$) in molar proportions (mol%) of 72.8%, 21.2%, 4.4%% and 1.6%, respectively. Sulfate was introduced into the model using 10.4 mmol of gypsum (a constant sulfate concentration of 1% was used for all of the simulations). Finally, the binder was defined by its elemental chemical composition expressed in moles (cf. Chapter 2 - section 2.1.2.2). The input data used in this part of the study is presented in Annex 1.

2.2.5.3 Modeling for the study of stabilization of molybdenum

Two different geochemical models were performed: (i) a geochemical model simulating the interaction between the C-S-H constituents with different concentrations of sodium molybdate (Na_2MoO_4), and (ii) a geochemical model representing the interactions between Na_2MoO_4 and the three binders tested (cf. Chapter 2 - section 2.1.3.2). The thermodynamic properties used in this work came from Minteqv4 database, enriched by typical cementitious phases from Thermoddem database version 1.10 [166]. The Mo reactions added to the model are presented in Table 2.13.

Table 2.13 – Molybdenum reactions added to the model.

Aqueous speciation reactions	Equilibrium constants (log K)	Reference
$Ca^{2+} + MoO_4^{-2} = CaMoO_4$	2.57	[168]
$Na^+ + MoO_4^{-2} = NaMoO_4$	1.66	[168]
Solid mineral		
$Ca^{2+} + MoO_4^{-2} = CaMoO_4(s)$	8.05	[168]

Modeling of Mo-spiked binders

In order to better understand the Mo stabilization in the binders at low Mo concentrations, numerical modeling was performed for all the formulations -B1(CEM I), B2(9010) and B3(SSC) (cf. Chapter 2 - section 2.1.3.3). Thus, Mo immobilization in the Mo-spiked binders was evaluated by varying the dosage of sodium molybdate (Na_2MoO_4) in solution in order to obtain Mo concentrations ranging from 0% to 10% (percentage by mass). Assuming congruent dissolution in the model, all the binders were defined by its elemental chemical composition expressed in moles (cf. Chapter 2 - Table 2.2).

Since few thermodynamic data exist for reaction of Mo with cementitious binders, calculations were made by assuming powellite precipitation as the only mechanism of Mo stabilization. On the other hand, since the hydration of GGBS and OPC mixes is more complex than the one of Portland cement, in the current investigation the hydration degree of the GGBS was considered and assumed to be 30% at 28 days of curing (inspired by the literature review, [169], [170]).

The kinetics of chemical reactions were not taken into account in this model, which represents only the state of equilibrium reached by the system. The results of batch-reaction calculations were compared to leachable Mo and leachable major element concentrations obtained experimentally.

Modeling of synthetic C-S-H with Mo

In this geochemical model, the initial solution was defined using two main constituents represented in the form of amorphous silica and lime. Sodium molybdate (Na_2MoO_4) was introduced into the model using different concentrations at different steps ranging from 0% to 5%. In this model, the phenomenon of adsorption was not taken into consideration but only the phenomenon of the co-precipitation of powellite.

Annex 1 – Input modeling – PHREEQC

-   Estimation of saturation indices for external sulfate attack

```
TITLE C-I Before attack
SOLUTION 1
    temp    25
    pH      11.54 charge
    pe      4
    redox   pe
    units   mol/l
    density 1
    Ca      0.01346
    Al      3e-05
    Fe      2e-05
    Mg      2e-05
    Si      8e-05
    Na      0.0159
    K       0.00444
    S(6)    0.00227
    -water  1 # kg
END

TITLE C-I after attack
SOLUTION 2
    temp    25
    pH      12.74 charge
    pe      4
    redox   pe
    units   mol/l
    density  1
    Ca      0.00427
    Al      0.00008
    Fe      0.00001
    Mg      0.00001
    Si      0.00032
    Na      1.15013
    K       0.01545
    S(6)    0.43466
    -water  1 # kg
END

TITLE C-0 Before attack
SOLUTION 3
    temp    25
    pH      11.74 charge
    pe      4
    redox   pe
    units   mol/l
    density 1
    Ca      0.015924
    Al      0.000029
    Fe      0.000021
    Mg      0.000012
    Si      0.000111
    Na      0.0159
    K       0.00444
    S(6)    0.00227
    -water  1 # kg
END
```

```
TITLE C-0 after attack
SOLUTION 4
    temp    25
    pH      12.90 charge
    pe      4
    redox   pe
    units   mol/l
    density 1
    Ca      0.013134
    Al      0.000098
    Fe      0.000050
    Mg      0.000036
    Si      0.000675
    Na      0.590078
    K       0.006882
    S(6)    0.100579
    -water  1 # kg
END

TITLE C-III before attack
SOLUTION 5
    temp    25
    pH      12.70 charge
    pe      4
    redox   pe
    units   mol/l
    density 1
    Ca      0.003578
    Al      0.000134
    Fe      0.000013
    Mg      0.000005
    Si      0.000270
    Na      0.030196
    K       0.006966
    S(6)    0.001738
    -water  1 # kg
END

TITLE C-III after attack
SOLUTION 6
    temp    25
    pH      12.55 charge
    pe      4
    redox   pe
    units   mol/l
    density 1
    Ca      0.003922
    Al      0.000254
    Fe      0.000057
    Mg      0.000049
    Si      0.001175
    Na      0.582681
    K       0.010102
    S(6)    0.206
    -water  1 # kg
END

TITLE AAS before attack
SOLUTION 7
    temp    25
    pH      12.72 charge
    pe      4
    redox   pe
    units   mol/l
    density 1
    Ca      0.000275
```

```
    Al      0.000371
    Fe      0.000018
    Mg      0.000012
    Si      0.002496
    Na      0.079547
    K       0.000865
    S(6)    0.012357
    -water  1 # kg
END

TITLE C-AAS after attack
SOLUTION 8
    temp    25
    pH      12.16 charge
    pe      4
    redox   pe
    units   mol/l
    density 1
    Ca      0.003426
    Al      0.000216
    Fe      0.000022
    Mg      0.000036
    Si      0.001589
    Na      0.988251
    K       0.004387
    S(6)    0.413962
    -water  1 # kg
END

TITLE C-GP before attack
SOLUTION 9
    temp    25
    pH      9.13 charge
    pe      4
    redox   pe
    units   mol/l
    density 1
    Ca      0.000194
    Al      0.000139
    Fe      0.000012
    Mg      0.000013
    Si      0.000412
    Na      0.076588
    K       0.000112
    S(6)    0.002449
    -water  1 # kg
END

TITLE C-GP After attack
SOLUTION 10
    temp    25
    pH      9.84 charge
    pe      4
    redox   pe
    units   mol/l
    density 1
    Ca      0.000864
    Al      0.000094
    Fe      0.000028
    Mg      0.000136
    Si      0.000177
    Na      1.051784
    K       0.001759
    S(6)    0.472821
    -water  1 # kg
END
```

- Study of the stabilization of sulfates – formulation F5

PHASES
C3AFS0.84H4.32
Ca3AlFeSi0.84O7.68:4.32H2O + 12H+ = Fe+3 + 3Ca+2 + Al+3 + 8.64H2O + 0.84H4SiO4
  log_K   67.45

SOLUTION 1 # Water - 1L
   temp   25
   pH   7
   pe   4
   redox   pe
   units   mg/l
   density 1
   #C   245
   -water 1 # kg

EQUILIBRIUM_PHASES 1 # Soil 100 g

#Quartz(alpha)	0 0.860194848	
Calcite	0 0.250377259	
Illite(Al)	0 0.051573588	
#Maghemite(disordered)	0 0.018699651	
Gypsum	0 0.010406381	

C1SH   0 0
MSH06   0 0
MSH12   0 0
Monosulfoaluminate 0 0
Ettringite   0 0
C3AH6   0 0
C4AH13   0 0
Gibbsite   0 0
Portlandite   0 0
C3AFS0.84H4.32   0 0

REACTION 1 # 10% GGBS hydration level
Ca11.502Si3.329Al0.981Fe0.401Mg0.198Na0.0797K0.168S0.387O21.716 0.1 #OPC
Ca7.811Si6.226Al2.001Fe0.075Mg1.588Ti0.088Na0.068K0.059S0.0125O25.241 0.09# (10% GGBS)
H2O 553.26 #Water for L/S=10
0 0.001003321 0.002006642 0.003009963 0.004013284 0.005016605 0.006019926 0.007023247 0.008026569 0.00902989 0.010033211 0.011036532 0.012039853 0.013043174 0.014046495 0.015049816 0.016053137 0.017056458 0.018059779 0.0190631 0.020066421
moles
END
USE equilibrium_phases 1
USE solution 1

REACTION 2 # 20% GGBS hydration level
Ca11.502Si3.329Al0.981Fe0.401Mg0.198Na0.0797K0.168S0.387O21.716 0.1 #OPC
Ca7.811Si6.226Al2.001Fe0.075Mg1.588Ti0.088Na0.068K0.059S0.0125O25.241 0.18# (20% GGBS)
H2O 553.26
0 0.001003321 0.002006642 0.003009963 0.004013284 0.005016605 0.006019926 0.007023247 0.008026569 0.00902989 0.010033211 0.011036532 0.012039853 0.013043174 0.014046495 0.015049816 0.016053137 0.017056458 0.018059779 0.0190631 0.020066421
moles
END
USE equilibrium_phases 1
USE solution 1

REACTION 3 # 30% GGBS hydration level
Ca11.502Si3.329Al0.981Fe0.401Mg0.198Na0.0797K0.168S0.387O21.716 0.1 #OPC
Ca7.811Si6.226Al2.001Fe0.075Mg1.588Ti0.088Na0.068K0.059S0.0125O25.241 0.27# (30% GGBS)
H2O 553.26
0 0.001003321 0.002006642 0.003009963 0.004013284 0.005016605 0.006019926 0.007023247 0.008026569 0.00902989 0.010033211 0.011036532 0.012039853 0.013043174 0.014046495 0.015049816 0.016053137 0.017056458 0.018059779 0.0190631 0.020066421
moles

```
END
USE equilibrium_phases 1
USE solution 1

REACTION 4 # 40% GGBS hydration level
Ca11.502Si3.329Al0.981Fe0.401Mg0.198Na0.0797K0.168S0.387O21.716 0.1 #OPC
Ca7.811Si6.226Al2.001Fe0.075Mg1.588Ti0.088Na0.068K0.059S0.0125O25.241 0.36# (40% GGBS)
H2O 553.26
0 0.001003321 0.002006642 0.003009963 0.004013284 0.005016605 0.006019926 0.007023247 0.008026569 0.00902989 0.010033211
0.011036532 0.012039853 0.013043174 0.014046495 0.015049816 0.016053137 0.017056458 0.018059779 0.0190631 0.020066421
moles
END
```

- <u>Study of the stabilization of molybdenum</u>

<u>Binder B1(CEM I)</u>

```
PHASES
Powellite   #Essigton 1990
CaMoO4 = Ca+2 + MoO4-2
    log_k        -8.05


TITLE B1_Initial
SOLUTION 1 # Eau - 1L
   temp    25
   pH       7 charge
   pe      4
   redox    pe
   units    mol/l
   density   1
   #C       245
   -water   1 # kg

EQUILIBRIUM_PHASES 1
Amorphous_silica 0 0
Lime   0 0
#Calcite 0 0
Powellite 0 0
C0.7SH 0 0
C0.8SH 0 0
C0.9SH 0 0
C1SH 0 0
C1.1SH 0 0
C1.2SH 0 0
C1.3SH 0 0
C1.4SH 0 0
C1.5SH 0 0
C1.6SH 0 0
Hydrotalcite 0 0
Monosulfoaluminate 0 0
Ettringite 0 0
C3AH6    0 0
C4AH13    0 0
Gibbsite  0 0
Portlandite 0 0
Goethite 0 0
Lepidocrocite 0 0
Fe(OH)2 0 0
Thenardite 0 0
Mirabilite 0 0

REACTION 1 # Composition B1
    Ca1.15Si0.34Al0.102Fe0.0413Mg0.02Na0.01K0.02S0.04O2.18 1 # 100g CEM I
```

116

```
   H2O 1.2121 # 40g H2O
    1 moles in 1 steps

SAVE equilibrium_phases 1
SAVE solution 1
TITLE B1_Ajouts Na2MoO4

USE equilibrium_phases 1
USE solution 1

REACTION 1
   H2O      2.5
   Na2MoO4    1
   0  5.20833e-05  0.000520833  0.001041667  0.010416667  0.052083333  0.104166667 moles
END
```

Binder B2(90-10)

```
REACTION 1 # Composition B2
   Ca1.143Si0.364Al0.078Fe0.039Mg0.032Mn0Na0.005K0.016S0.042Cl0O2.217 0.1 #10%OPC for 100g
   Ca0.781Si0.622Al0.2Fe0.008Mg0.159Mn0.003Na0.007K0.006S0.001Cl0O2.51 0.3 # 30%hyd for 90%GGBS for 100g
   H2O 2.22 # 40g H2O
    1 moles in 1 steps

SAVE equilibrium_phases 1
SAVE solution 1
```

Binder B3(SSC)

```
REACTION 1 # Composition B3
   Ca11.502Si3.329Al0.981Fe0.401Mg0.198Na0.0797K0.168S0.387O21.716 0.05 #OPC # 5% OPC
   Ca7.811Si6.226Al2.001Fe0.075Mg1.588Ti0.088Na0.068K0.059S0.0125O25.241 0.27# (30% GGBS hydrationt)
   gypsum 0.20#gypsum
   H2O 1.2121 # 40g H2O
    1 moles in 1 steps

SAVE equilibrium_phases 1
SAVE solution 1
```

C-S-H + Mo

```
PHASES

Powellite  #Essigton 1990
CaMoO4 = Ca+2 + MoO4-2
    log_k       -7.2 #-8.05


TITLE Reaction avec masses initiales
SOLUTION 1 # Eau - 1L pour 20g de solide ajouté
    temp    25
    pH      7 charge
    pe      4
    redox   pe
    units   mol/l
    density 1
   #C       245
    -water  1 # kg (5*200mL)

EQUILIBRIUM_PHASES 1
Amorphous_silica 0 0.13346
```

```
Lime   0 0.21353
Calcite 0 0
Powellite 0 0
C0.7SH 0 0
C0.8SH 0 0
C0.9SH 0 0
C1SH 0 0
C1.1SH 0 0
C1.2SH 0 0
C1.3SH 0 0
C1.4SH 0 0
C1.5SH 0.075 0

REACTION 1
   Na2MoO4   1
   H2O       312.121
   0  0.0000000208  0.0000000417  0.0000000625  0.000000083333  0.0000001042  0.0000002083
   0.000002083  0.000004166667  0.0000104167  0.0000208333  0.0000416667  0.00021  0.00052  0.00104
   0.00208  0.00313  0.00417  0.00521  0.00625  0.010416667 moles
END
```

<u>C-S-H + Mo low concentrations</u>

```
PHASES
Powellite   #Essigton 1990
CaMoO4 = Ca+2 + MoO4-2
    log_k       -7.2 #-8.05

TITLE Reaction avec masses initiales

SOLUTION 1 # Eau - 1L pour 20g de solide ajouté
   temp     25
   pH       7 charge
   pe       4
   redox    pe
   units    mol/l
   density  1
  #C        245
   -water    1 # kg (5*200mL)

EQUILIBRIUM_PHASES 1
Amorphous_silica 0 0.13346
Lime   0 0.21353
Calcite 0 0
Powellite 0 0
C0.7SH 0 0
C0.8SH 0 0
C0.9SH 0 0
C1SH 0 0
C1.1SH 0 0
C1.2SH 0 0
C1.3SH 0 0
C1.4SH 0 0
C1.5SH 0.075 0

REACTION 1
   Na2MoO4   1
   H2O       312.121
   0  0.0000000208  0.0000000417  0.0000000625  0.000000083333  0.0000001042  0.0000002083
   0.000002083  0.000004166667  0.0000104167  0.0000125  0.0000145833  0.0000166667  0.00001875  0.0000208333
   0.0000416667  0.00021  0.00052  0.00104  0.00208  0.00313 moles
END
```

CHAPTER 3 – CONCRETE UNDER EXTERNAL SULFATE ATTACK

Table of Contents

3. Chapter 3 – Concrete under external sulfate attack

Résumé

Ce troisième chapitre présente les résultats obtenus sur l'étude de l'attaque sulfatique externe dans des bétons à base de liants alternatifs.

Cette partie de la recherche visait à : (i) réaliser un benchmark de plusieurs liants en testant leur capacité à résister l'attaque sulfatique externe dans des conditions expérimentales similaires, et (ii) contribuer à la compréhension des mécanismes associés à l'expansion ou non-expansion des liants en utilisant des analyses microstructurales et minéralogiques et des calculs thermodynamiques.

Ce chapitre est organisé de la manière suivante :

(i) La première partie se concentre sur la présentation des matériaux et la caractérisation mécanique des bétons à l'état durci avant attaque sulfatique externe.

(ii) Ensuite, il présente les résultats d'expansion longitudinale et de variation de masse obtenus lors de l'essai de l'attaque sulfatique externe afin d'évaluer et comparer la résistance des bétons vis-à-vis de ce phénomène.

(iii) La troisième partie présente les analyses chimiques, minéralogiques et microstructurales réalisées sur l'ensemble des bétons avant et après attaque. Les résultats sont regroupés par catégorie de béton étudié.

Une comparaison de tous les résultats est présentée en Table 3.3.

Sept différents liants ont été utilisés pour fabriquer sept bétons afin de comparer leur résistance vis-à-vis de l'attaque sulfatique externe. Trois ciments Portland et quatre liants alternatifs ont été utilisés pour fabriquer ces bétons. Les liants alternatifs ont été regroupés en deux catégories : (i) liants alcali-activés avec ou sans oxydes de calcium et (ii) liants ettringitiques (ciment sursulfaté et ciment sulfoaluminaux).

Les bétons étudiés sont :

1. C-I : béton à base de ciment Portland classique (CEM I)
2. C-0 : béton à base de ciment Portland résistant aux sulfates (CEM-SR)
3. C-III : béton à base de laitier de haut fourneau de type CEM III/C
4. C-SSC : béton à base de ciment sursulfaté (SSC)
5. C-CSA : béton à base de ciment sulfoalumineux (CSA)
6. C-GP : géopolymère à base de métakaolin
7. C-AAS : béton à base de laitier alcali-activé par des carbonates

La capacité à résister à l'attaque sulfatique externe a été évaluée en utilisant les mêmes conditions expérimentales suivant la norme Suisse SIA 262 :2013 (0,1% est la valeur maximale d'expansion recommandée par cette norme).

Les bétons fabriqués avec des ciments Portland à haute et faible teneur en C_3A ont présenté des expansions de 0,4% et 0,07%, respectivement (la valeur limite maximale étant 0,1%). Les expansions des liants alternatifs se sont avérées être, quant à elles, beaucoup plus faibles (entre 0,01 à 0,03%). Les variations longitudinales sont reportées en Figure 3.3.

L'expansion du béton à base du ciment Portland classique a été expliquée en raison de la formation d'ettringite en excès après hydratation du béton causée par la réaction entre les aluminates anhydres (C_3A) et les sulfates provenant de la solution. Le ciment Portland sans C_3A a présenté des expansions plus faibles (6 fois plus faible

que celle du ciment Portland classique), mais l'apparition des fissurations à des âges ultérieurs a été attribuée à la formation du gypse. Celle-ci s'est produite car le gypse est devenu la phase la plus stable à précipiter du fait de la limitation de la source d'aluminates. On rappelle que ce béton, en effet, ne présente pas de phase C_3A mais il contient de C_4AF. Même si la phase C_4AF est une source d'aluminates, la littérature montre que la cinétique de dissolution est plus lente que celle de C_3A, permettant la précipitation de l'ettringite mais en quantités relativement faibles comparées à celles produites dans un ciment Portland classique.

Par ailleurs, les bétons à base de laitier de haut fourneau de type CEM III/C testés à 28 et 90 jours de cure avant attaque sulfatique externe ont présentés des expansions 3 et 7 fois plus faibles que celle du béton à base du ciment Portland classique. Ces bétons contenaient autour de 15% de clinker permettant la diminution des aluminates (C_3A) disponibles pour réagir avec les sulfates. De plus, les résultats d'expansion ont aussi mis en évidence que la résistance vis-à-vis de l'attaque sulfatique externe dépendait de l'âge de cure avant l'immersion dans la solution riche en sulfates. En effet, les échantillons suivant une cure de 28 jours avant attaque ont présenté une expansion 40% supérieure à celle obtenue pour les bétons suivant une cure de 90 jours. Cela pourrait s'expliquer par la diminution de la structure poreuse avec le temps réduisant ainsi la pénétration des ions sulfate dans les matrices.

D'un autre côté, les faibles expansions trouvées dans les liants alternatifs ont été expliquées par l'absence de C_3A et de portlandite en plus de la formation d'ettringite lors de l'hydratation (cas des liants ettringitiques) et de l'absence de calcium (cas du géopolymère à base de métakaolin teneur en CaO dans la matrice (<2 wt%, % par poids de liant anhydre)).

Introduction

This chapter presents the results obtained in the study of concrete under external sulfate attack. This part of the research aimed to: (i) realize a benchmark of several binders by testing their capacity to resist external sulfate attack (ESA) under similar experimental conditions, and (ii) contribute to the understanding of the mechanisms associated with the expansion or non-expansion of the binders by using microstructural and mineralogical analyses, and thermodynamic calculations. The study of concrete under external sulfate attack was carried out following the approach presented in Figure 3.1.
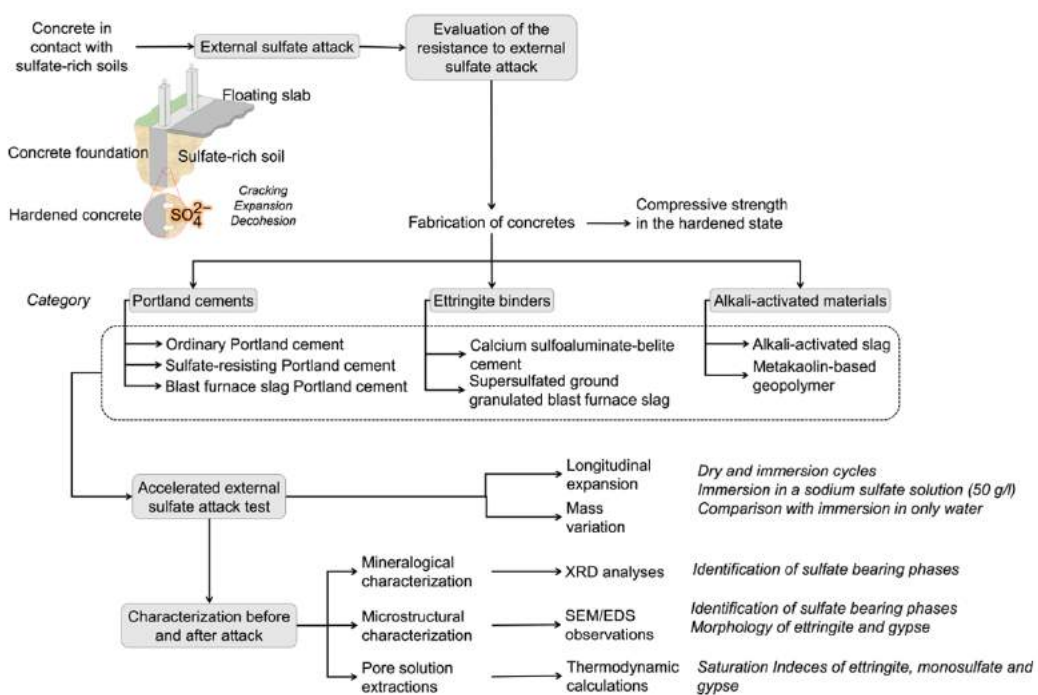
Figure 3.1 – Concept mapping of the approach adopted in the study of concrete under external sulfate attack.

The first part of this chapter describes the materials used in the study of ESA and the compressive strength results obtained in the hardened state. The second part presents the results obtained from the analyses carried out in the concretes before and after attack. The results of longitudinal expansion and mass variation are shown, followed by the microstructural observations, chemical and mineralogical analyses are presented. The third part of this chapter focuses on the discussion of all the results, which is presented by type of concrete and refers to previous research works in this field. Table 3.3 presents a benchmark of all the results obtained in this part of the study. Additionally, a few suggestions for further investigation are addressed.

3.1 Concretes

3.1.1 Binders

As a reminder, seven binders grouped into three categories were tested under external sulfate attack (ESA). The description of the binders and their chemical and mineralogical compositions are presented in Chapter 2 – section 2.1.1. Table 3.1 presents the summary of all the concretes tested in this part of the study.

Table 3.1 – Summary of concretes tested in the study of concrete under external sulfate attack.

Category	Portland cements	Ettringite binders	Alkali-activated binders
Binder ID	CEM I CEM-SR CEM III/C	SSC CSA	AAS GP

3.1.2 Compressive strength of the hardened concretes at 28 days

For the purpose of comparing the concretes in the hardened state, compressive strength tests were carried out in all the concretes at 28 days of curing according to the protocol presented in Chapter 2 – section 2.2.3.1. Figure 3.2 shows the compressive strength (f_c on concrete cubes) results expressed in MPa and obtained for each concrete at 28 days of curing.
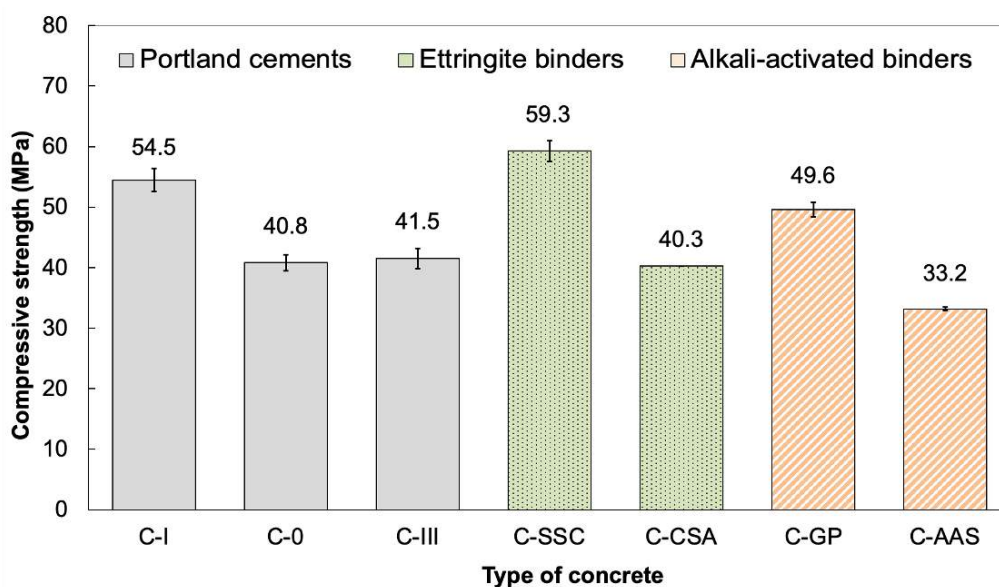
Figure 3.2 – Compressive strength (fc) on concrete cubes at 28 days of curing. All values are expressed in MPa.

The Standard NF EN 206/CN (French national addition to EN 206) sets C35/45[2] as the minimum strength class when using the recommended limiting values for the XA2 exposure class. As shown in Figure 1, C-0, C-III, C-CSA and C-AAS concretes were not conform to this strength class because of their low compressive strengths. However, the strength class of these concretes was closer to the C30/37 class set by the XA2 exposure class in the general European Standard EN 206:2013.

Among all the Portland cement-based concretes, C-I reached the highest value of f_c and it presented a difference in the compressive strength of about 10 MPa with C-0 and C-III concretes. In the ettringite binders´ category, C-SSC and C-CSA concretes presented a difference in the compressive strength of about 20 MPa. CSA-based binders are generally designed to develop fast compressive strength at early ages (first 7 days of curing), but not always very high strength in the long-term [171]–[173]. On the contrary, strength increases with time in slag blended cements or cements containing GGBS leading to quite high long-term strength [174]. In the present work, binders containing GGBS ((C-III, C-SSC and C-AAS) were tested only at 28 days for comparison. But a few studies have shown that in these materials the strength increased with time. For example, Baux et al. [174] showed that SSC mortars with water to binder (w/b) ratios of 0.4 and 0.5 increased significantly in strength after 28 days of curing. The increase in strength over the time was more evident in mortars batched with the w/b ratio of 0.4.

On the other hand, in the alkali-activated concrete category, C-GP presented the highest compressive strength. In contrast, C-AAS presented the lowest compressive strength value among all the concretes. Kovtun et al. [175] showed that sodium carbonate AAS presented slow strength development. However, with increasing OPC replacement the short-term strength increases but it could be harmful for later age performances.

3.2 External sulfate attack test results

The resistance to ESA was studied by measuring the longitudinal expansion and mass changes of concretes following the protocol presented in Chapter 2 – section 2.2.3.2.

---

[2] Characteristic strength, i.e. value of strength below which 5% of the population of all possible strength determinations of the volume of concrete under consideration are expected to fall [EN 206]; the first value is for cylinders, the second for cubes.

Table 3.3 presents, at the end of this chapter, a benchmark of all the results obtained in the study of concretes under external sulfate attack.

3.2.1 Longitudinal expansion results

Figure 3.3 shows the longitudinal expansions measured for each concrete during the ESA and expressed in percentage as a function of time in days. As a reminder, concretes containing GGBS (C-III, C-SSC and C-AAS) were cured for 90 days to ensure their hydration, which is known to be slower than OPCs. In Figure 3.3 the red dotted line represents the maximal guideline value of 0.1% set by the Swiss Standard.

Expansion measured for concretes submerged in the Na_2SO_4 solution and cured for 28 days and 90 days before attack are presented in Figure 3.3(a) and Figure 3.3(b), respectively. In addition, expansion of concretes submerged in only water are presented in Figure 3.3(c) and Figure 3.3(d). In this last case, as the concretes did not present noticeable expansions (<0.03%), it can be assumed that expansions measured in sulfate solutions (cf. Figure 3.3(a) and (b)) were due to a possible effect of the sulfates, and not only to water intake.

As shown in Figure 3.3(a), C-I had the highest expansion (0.4%±0.1%) at the end of the test and seemed to be in a high kinetics of swelling. In contrast, C-0 had an expansion of 0.07%±0.02%, which was close to the upper limit of 0.1% established by the Swiss Standard. However, this value was about 6 times lower than the one of C-I. On the other hand, C-III cured for 28 days before test showed an expansion of 0.13%±0.01%, which was higher than the upper limit value of 0.1%. Nevertheless, when C-III was tested after 90 days of curing (cf. Figure 3.3(b)), the final expansion was significantly reduced to 0.05%±0.02%, which was 2 times lower than the limit set by the Swiss Standard and about 8 times lower than the one of C-I.

As shown in Figure 3.3(a) and Figure 3.3(b), alternative binder based-concretes (C-SSC, C-CSA, C-GP and C-AAS) had expansions much lower than Portland cement–based concretes (range 0.01-0.03%), with values about 10 times lower than the limit of 0.1%.
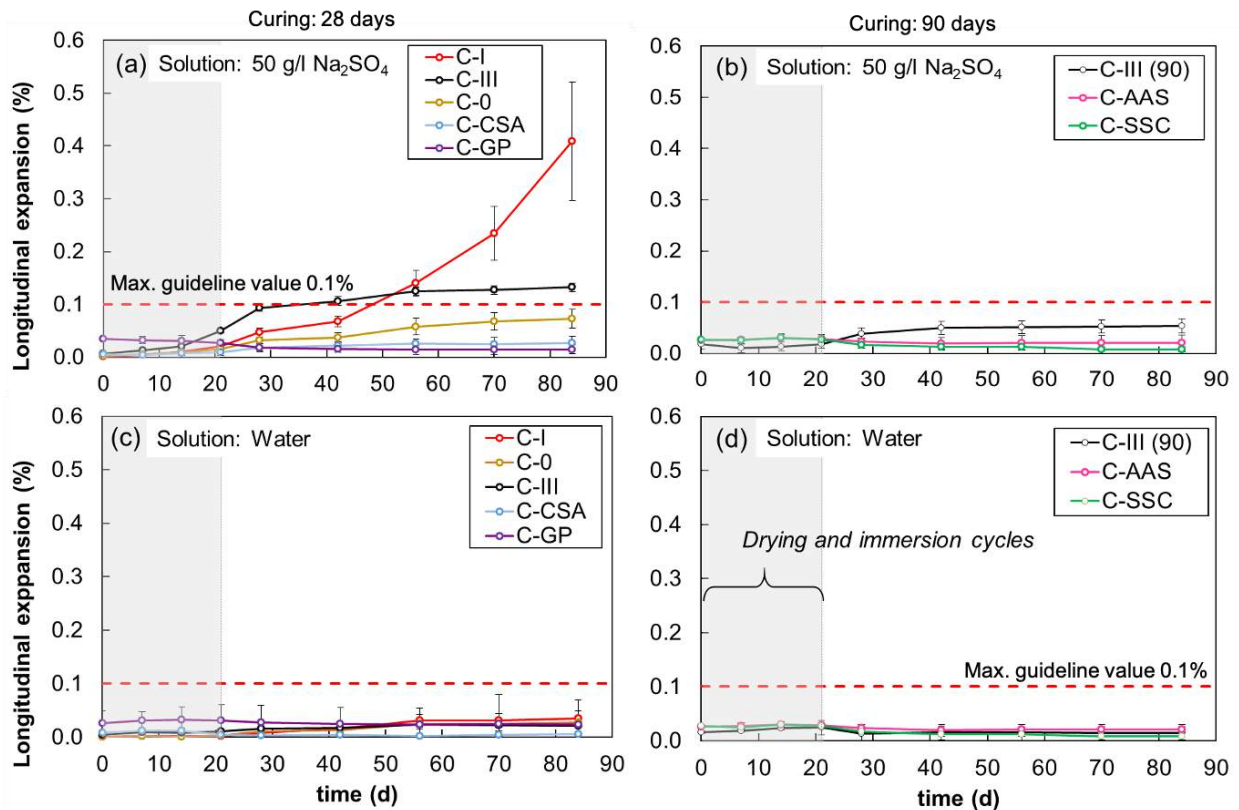
Figure 3.3 - Longitudinal expansion in percentage (%) as a function of time in days of concretes submerged in: **(a)** 50 g/L Na₂SO₄ and cured for 28 days before test, **(b)** 50 g/L Na₂SO₄ and cured for 90 days before test, **(c)** water and cured for 28 days before test, **(d)** water and cured for 90 days before test. The red dotted line represents the maximal guideline value of 0.1% set by the Swiss Standard.

3.2.2 Mass variation results

Figure 3.4 shows the mass change values measured for each concrete during the ESA and expressed in percentage as a function of time in days. It should be noted that the zone before 20 days corresponds to the period of drying and immersion cycles.

Figure 3.4(a) and Figure 3.4(b) present the mass change values measured for concretes submerged in the Na₂SO₄ solution and cured for 28 and 90 days before attack, respectively. In addition, the mass change graphics of concretes submerged in only water are presented in Figure 3.4(c) and Figure 3.4(d), in which the mass change values were of about 50% lower than the ones measures in the sulfate solution.
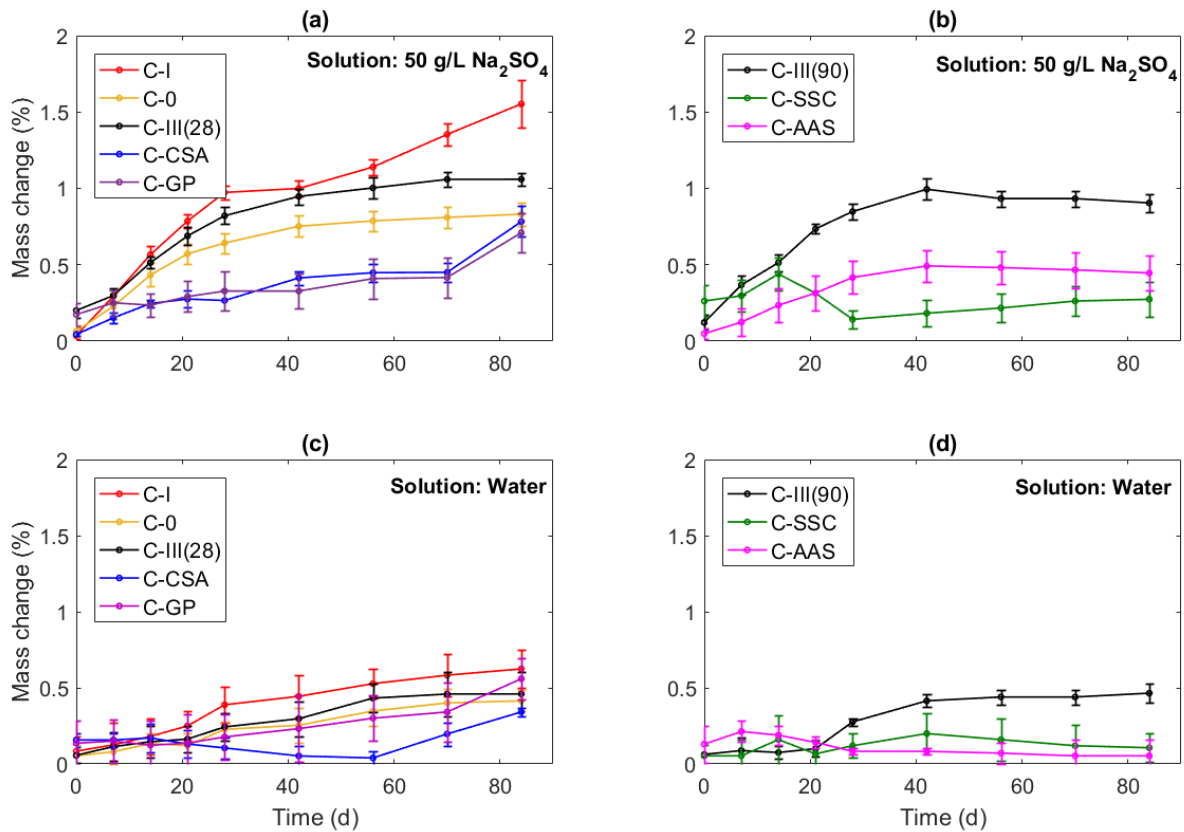
Figure 3.4 – Mass change in percentage (%) as a function of time in days of concretes submerged in: **(a)** 50 g/L Na$_2$SO$_4$ and cured for 28 days before test, **(b)** 50 g/L Na$_2$SO$_4$ and cured for 90 days before test, **(c)** water and cured for 28 days before test, **(d)** water and cured for 90 days before test.

Figure 3.4(a) shows that C-I concrete had the highest mass change (1.6%±0.1%) at the end of the test and seemed to be in a high kinetics of swelling. This behavior is in agreement with the longitudinal expansion presented in C-I (cf. Figure 3.3(a)). C-0 had a mass change of 0.8%±0.1%, which was of about 2 times lower than C-I. On the other hand, C-III cured for 28 days before test showed a mass change of 1.06%±0.04%, and the trend of the curve was similar to the one presented for longitudinal expansion. Concerning the mass change of the C-III concretes (cured at 28 and 90 days before test), they were almost the same for both concretes.

Regarding the ettringite binder-based concretes (C-SSC and C-CSA), they presented different trends in the curves of mass change. In the case of C-CSA, the mass changes increased gradually in time and the last measure was 0.8%±0.1% (about 2 times lower than C-I). In contrast, C-SSC presented lower mass changes than those presented in C-CSA; however, the mass also seemed to increase gradually in time. At the end of the test, this concrete presented a mass change of 0.3%±0.1%, which was about 3 and 6 times lower than those on C-CSA and C-I, respectively. During the period of drying/immersion cycles, the mass change of C-SSC

increased gradually, and before 20 days, it decreased suddenly. From that point, the mass change increased gradually in time. We can also observe that the trend of the curves obtained for C-SSC in water and in sulfates were similar.

Finally, alkali-activated binder based-concretes (C-GP and C-AAS) presented different trends of mass variation. For C-GP, the last measure was 0.7%±0.1% (about 2 times lower than C-I) and the trend of the curve was very similar to the one obtained for C-CSA. It means that the mass change increased gradually in time. For C-AAS, the mass increased during the first 30 days of test (during the drying/immersion cycles) and after that, the mass change stopped increasing and seemed to stabilize at 0.4%±0.1% (about 3 times lower than C-I).

Longitudinal expansion vs. mass change

In order to correlate the longitudinal expansion and the mass variation measured in concretes, Figure 3.5 presents a plot where the x-axis and y-axis correspond to the mass change and the longitudinal expansion, respectively.
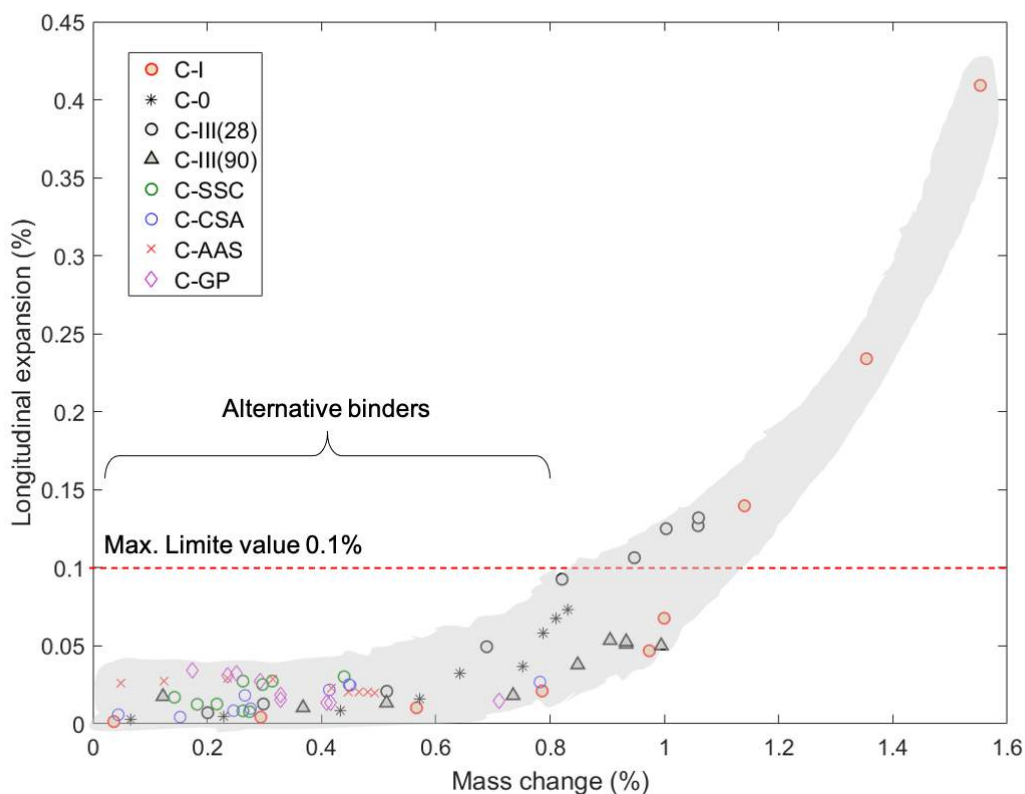
Figure 3.5 – Mass change as a function of longitudinal expansion in percentages (%) for all concretes submerged in the solution at 50 g/L Na2SO4.

Figure 3.5 shows that when the values of mass changes exceeded 0.8%, the longitudinal expansions of concretes increased gradually and were near the limit value of 0.1%. This was the case for all the Portland cement-based concretes (C-I, C-0, C-III(28) and C-III(90)). Moreover, this figure suggests that concretes, having mass changes inferior to 0.8%, presented dimensional variations due to the water intake. Mass changes greater than 0.8% may be due to the formation of expansive phases.

3.3 Microstructural and mineralogical characterization and thermodynamic calculations

Microstructural and mineralogical analyses and thermodynamic calculations were carried out before and after ESA in order to improve the understanding of the mechanisms associated with the existence/absence of expansion in the binders tested. Figure 3.6 summarizes the analyses performed in all the concretes. The analyses are presented by separating the concretes in three categories:

- Portland cement concretes (C-I, C-0, C-III)
- Ettringite binder concretes (C-SSC, C-CSA)
- Alkali-activated binder concretes (C-GP, C-AAS)

Objective	Method
Identify sulfate bearing phases (ettringite, monosulfoaluminate and gypsum) before and after attack	Punctual analyses by using SEM/EDS on polished sections
Observe the morphology of phases and corroborate the presence of ettringite before and after attack	SEM/EDS observations on fracture sections
Verify the presence of crystalline sulfate bearing phases before and after attack	XRD analyses on crushed concrete
Estimate the Saturation Indices of ettringite, monosulfoaluminate and gypsum (precipitation or dissolution conditions)	Poral solution extractions Chemical analyses in solution Thermodynamic calculations with PHREEQC

Figure 3.6 – Analyses performed in all the concretes before and after external sulfate attack.

As a reminder, we present a benchmark of all the results obtained in the study of concretes under external sulfate attack at the end of this chapter (cf. Table 3.3).

- EDS punctual analyses and SEM observations:

EDS punctual analyses gave a semi-quantitative composition of the reaction products before and after ESA. The results are represented in charts where x-axis and y-axis plot the Al/Ca and S/Ca atomic ratios, respectively. Stoichiometric composition of ettringite (AFt) and calcium monosulfoaluminate (Ms) are located on the plots, as well as the zone of gypsum. The two slopes allow the identification of either AFt or Ms formation when the products are mixed with other anhydrous/hydration products without Al and S. Figure 3.7 presents a schema explaining how to read this type of plot.

It should be noted that the number and position of EDS points were selected arbitrary avoiding the anhydrous grains. All the EDS plots are presented in Figure 3.8, Figure 3.11, Figure 3.14 and Figure 3.18.
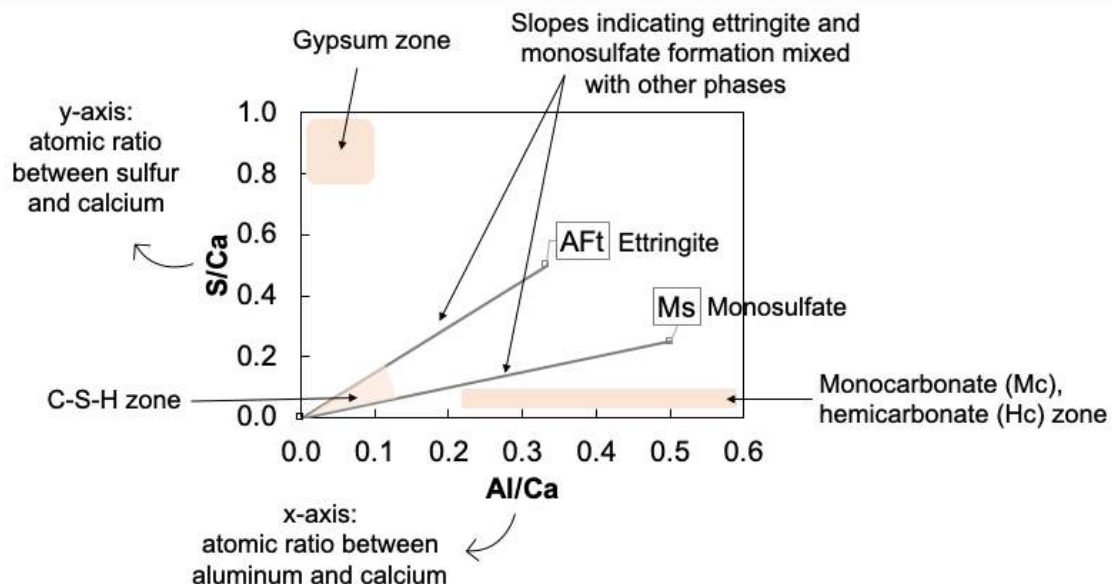
Figure 3.7 – How to read the S/Ca vs. Al/Ca charts. Monosulfate = monosulfoaluminate

SEM observations and qualitative EDS analyses were carried out in order to corroborate the presence of expansive phases after ESA and observe their morphology. SEM observations are presented in Figure 3.9, Figure 3.10, Figure 3.12, Figure 3.15, Figure 3.16 and Figure 3.19. The SEM images provide a representative picture of the analyzed samples.

- XRD analyses:

XRD qualitative analyses allowed to confirm the presence/absence of sulfate bearing phases, mainly for AFt and gypsum. All the XRD patterns are presented in Figure 3.23. As all the

analyses were made on concrete, several peaks were attributed to the minerals present in the aggregates: micas 2θ 8.5°-9°, chlorite in the ranges 2θ 12°-13° and 2θ 18⁰-19⁰, and feldspars 2θ 13°-14°.

- Pore solution extraction for estimation of Saturation Indices (SI):

Pore solutions of concretes were obtained by extraction of concretes in accordance with the protocol presented in Chapter 2 – section 2.2.3.3. The elemental concentrations measured in solution are presented in Figure 3.13 and Figure 3.22. These concentrations allowed to estimate the Saturation Indices (SI) of ettringite (AFt), monosulfoaluminate (Ms) and gypsum before and after sulfate attack. SI were calculated with the code PHREEQC. As a reminder, SI>0 means that the mineral is in condition to precipitate, while it should be in dissolution condition when SI<0 [176]–[178]. SI values are presented in Table 3.2.

3.3.1 Portland cement-based concretes (C-I, C-0 and C-III)

Figure 3.8 presents the EDS punctual analyses of C-I and C-0 before (left) and after (right) ESA. Figure 3.8(a) and Figure 3.8(c) show the EDS analyses performed before attack. In these plots, it was possible to detect a few points of AFt and Ms in C-I, while only Ms was detected in C-0. In this last case, the low sulfate content in the cement (1.52 wt%), combined with the low kinetics of dissolution of C_4AF (no C_3A in that cement), led to the production of Ms only.

Figure 3.8(b) and Figure 3.8(d) show the EDS analyses performed after attack. These analyses showed a large population of points in the AFt area (along the line between 0 and AFt). It means that ettringite precipitated after ESA. Moreover, XRD analyses (cf. Figure 3.23) confirmed presence of AFt in both concretes after attack (peaks in the ranges 2θ 9°-9.5° and 2θ 15°-16). Concerning C-0, results suggests that the sulfate-resisting cement released aluminum (probably from C_4AF as it was the only source of aluminum in that cement) to form AFt at later ages. The precipitation of AFt was also verified by the calculation of the SI (cf. Table 3.2), which were superior to zero in both concretes.
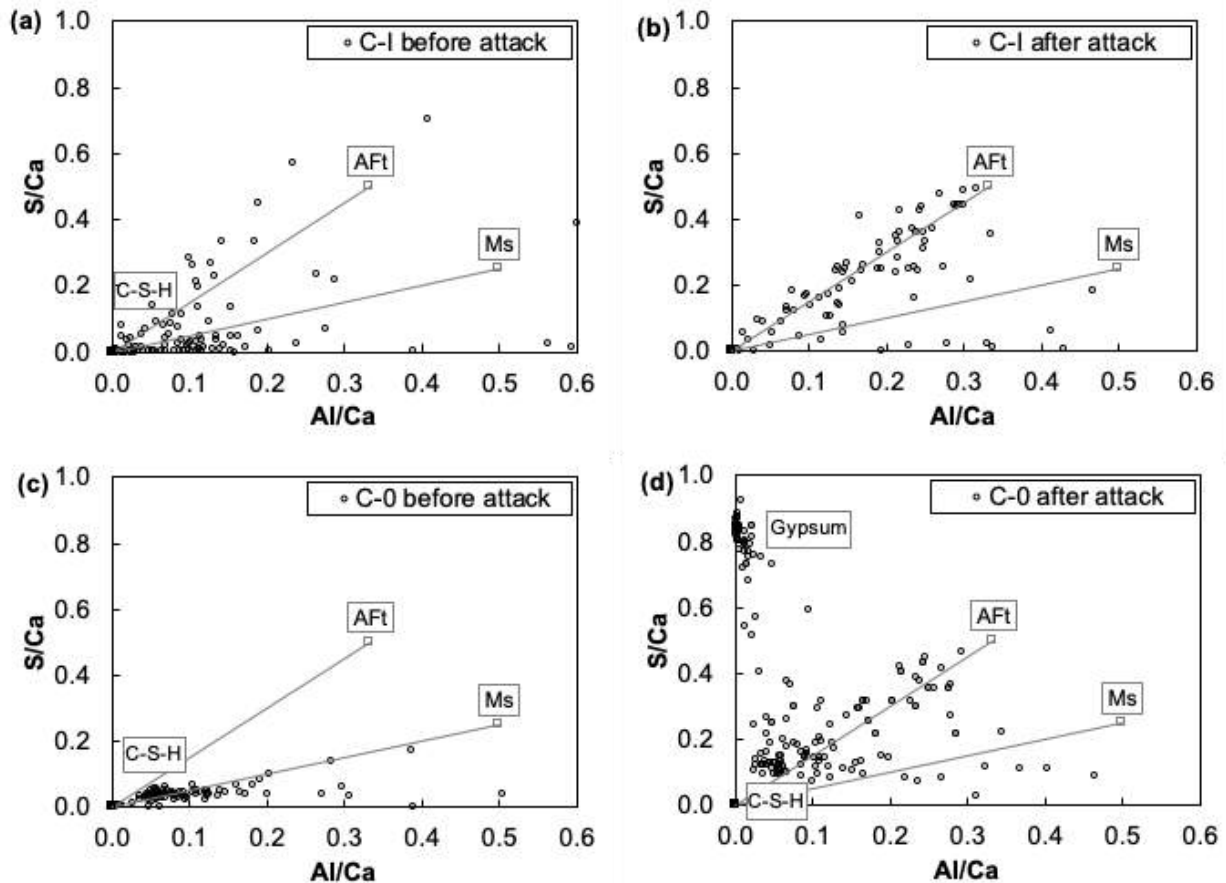
Figure 3.8 – EDS plots of Al/Ca versus S/Ca atomic ratios (AFt – ettringite, Ms – calcium monosufoaluminate) on C-I and C-0 concretes cured for 28 days before attack **(a)** C-I before and **(b)** after attack, **(c)** C-0 before and **(d)** after attack.

SEM observations allowed for identification of ettringite in both concretes C-I and C-0 after sulfate attack. Figure 3.9 shows large cracks filled with ettringite in addition to the presence of ettringite in all the studied surface of C-I concrete, in which ettringite crystals seemed thick and measured 6-10 µm in length. In contrast, for C-0, Figure 3.10 shows that ettringite was not present in all the studied surface but it was mostly grouped in the cracks and it had thinner and smaller crystals than those observed in C-I.

Moreover, EDS (cf. Figure 3.8(d)) and XRD analyses (cf. Figure 3.23) and SEM observations (cf. Figure 3.10) showed the presence of gypsum in C-0 concrete after ESA. In this case, gypsum precipitated because of the unavailability or very low concentration of aluminum due to the low kinetics of C_4AF dissolution [21]–[23], leading to the saturation of sulfate and thus its precipitation with calcium. The absence of gypsum in C-I was probably related to the presence of aluminum in high amount, coming from the dissolution of C_3A, which was abundant in this binder and mainly led to the formation of ettringite.
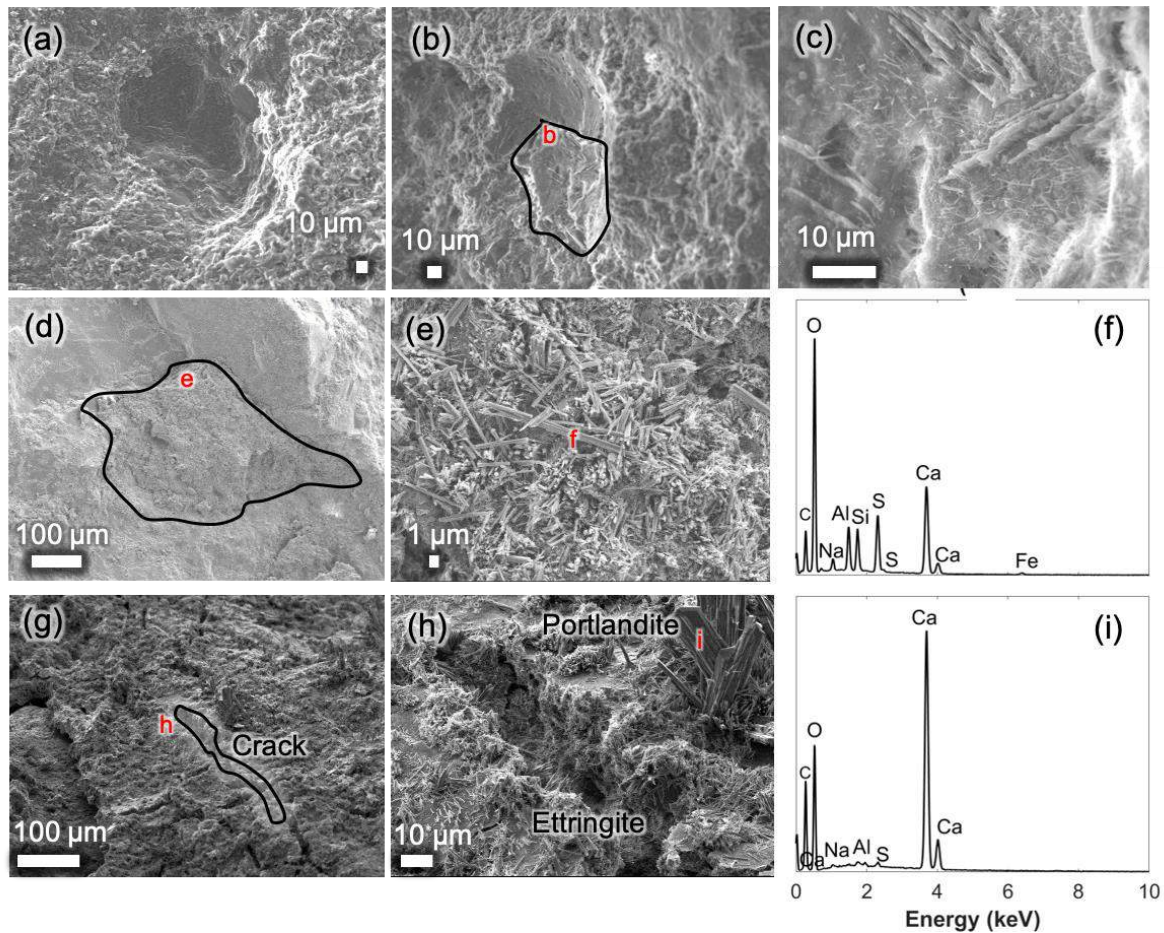
Figure 3.9 – SEM/EDS analyses of C-I. **Before ESA: (a)** air void in the matrix, **(b)** cement-aggregate interface, **(c)** magnification image *b* showing the presence of small crystals. **After ESA: (d)** Cement matrix, **(e)** magnification of image *d* (zone e) showing ettringite crystals, **(f)** EDS spectrum obtained from point f showed in image *e*, **(g)** crack observed in the matrix, **(h)** magnification of zone h from image *g* showing ettringite crystals filling cracks and portlandite, **(i)** EDS spectrum obtained from portlandite observed in image *h* (point i).

In reference to the SI of gypsum in C-0, it remained near saturation but negative. A few studies indicated that gypsum often forms on the surface of samples under ESA, and progressively grows producing cracking, which allows for rapid influx of sulfate ions towards the interior [13], [179]. Feng et al. [179] explained that the formation of gypsum on the surfaces of Portland cement-based samples is due to the leaching of portlandite(CH) near the surface providing calcium to react with free sulfates in solution. Despite this, Feng et al. [179] indicated that modeling predicts the formation of gypsum only after the ettringite has stopped forming due to the consumption of all aluminate sources. They pointed out that modeling does not consider the free solution near the solid surface where conditions for the formation of gypsum may be more favorable than the formation of ettringite. Feng et al. [179] also explained that ettringite is more favored thermodynamically than gypsum in the solid matrix when both aluminates and

sulfates are still available in the pore solution. This could explain why the SI of gypsum resulted inferior to zero although this mineral was detected in C-0 samples by using different analyses.
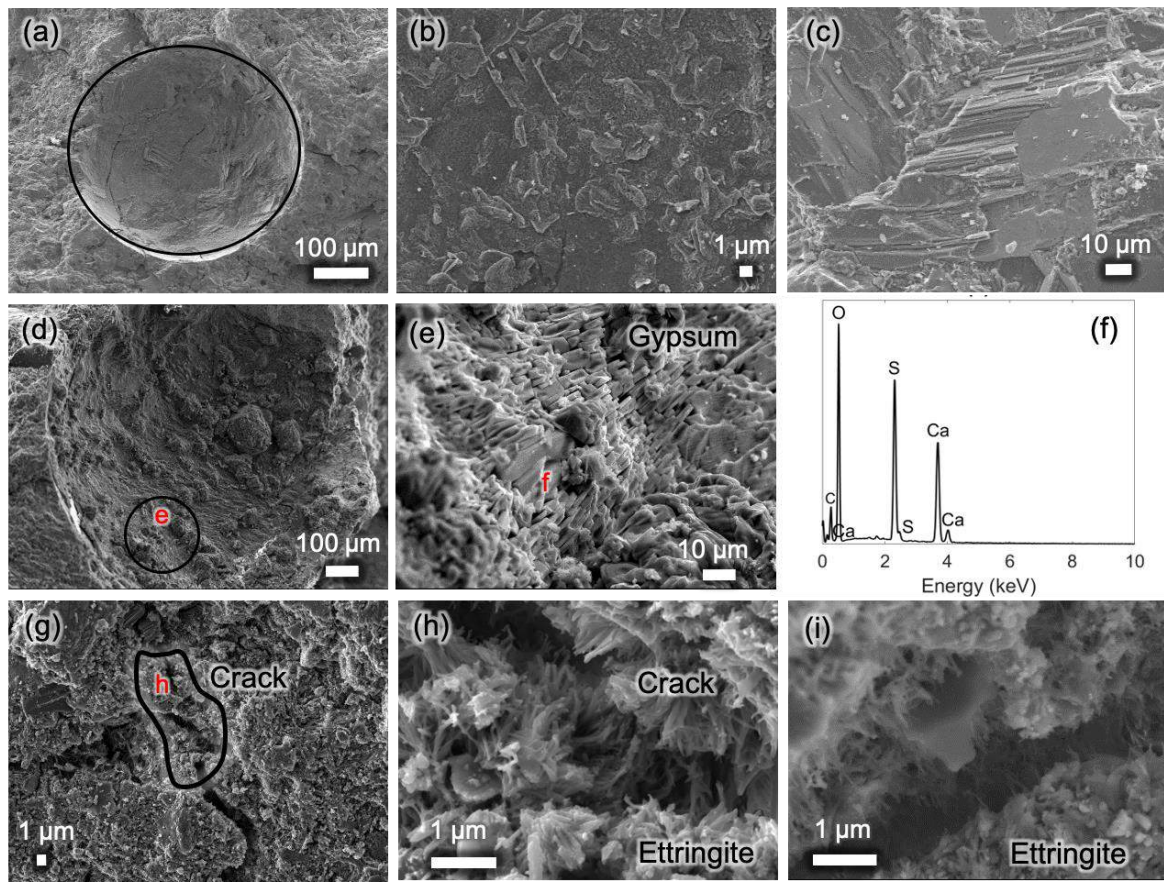
Figure 3.10 – SEM/EDS analyses of C-0. **Before ESA** no gypsum nor ettringite observed: **(a)** air void, **(b)** magnification of image *a*, **(c)** cement matrix. **After ESA: (d)** cement paste-aggregate interface, **(be)** magnification of image *d* (zone e) showing abundant deposition of gypsum, **(f)** EDS spectrum obtained from gypsum observed in image *e* (point f), **(g)** crack in the cement matrix, **(h)** and **(i)** magnification of image *g* (zone h) showing the presence of small ettringite crystals.

Figure 3.11 presents the EDS analyses of C-III concretes exposed to ESA at 28 and 90 days of curing, referred to as C-III(28d) and C-III(90d), respectively. Before attack, it was possible to detect a few points of Ms (cf. Figure 3.11(a)), meanwhile, analyses after attack showed that C-III(28d) presented a large population of points around AFt and between the AFt/Ms slopes (cf. Figure 3.11(b)). For C-III(90d), EDS analyses showed that the population of points was predominantly located around the Ms slope.
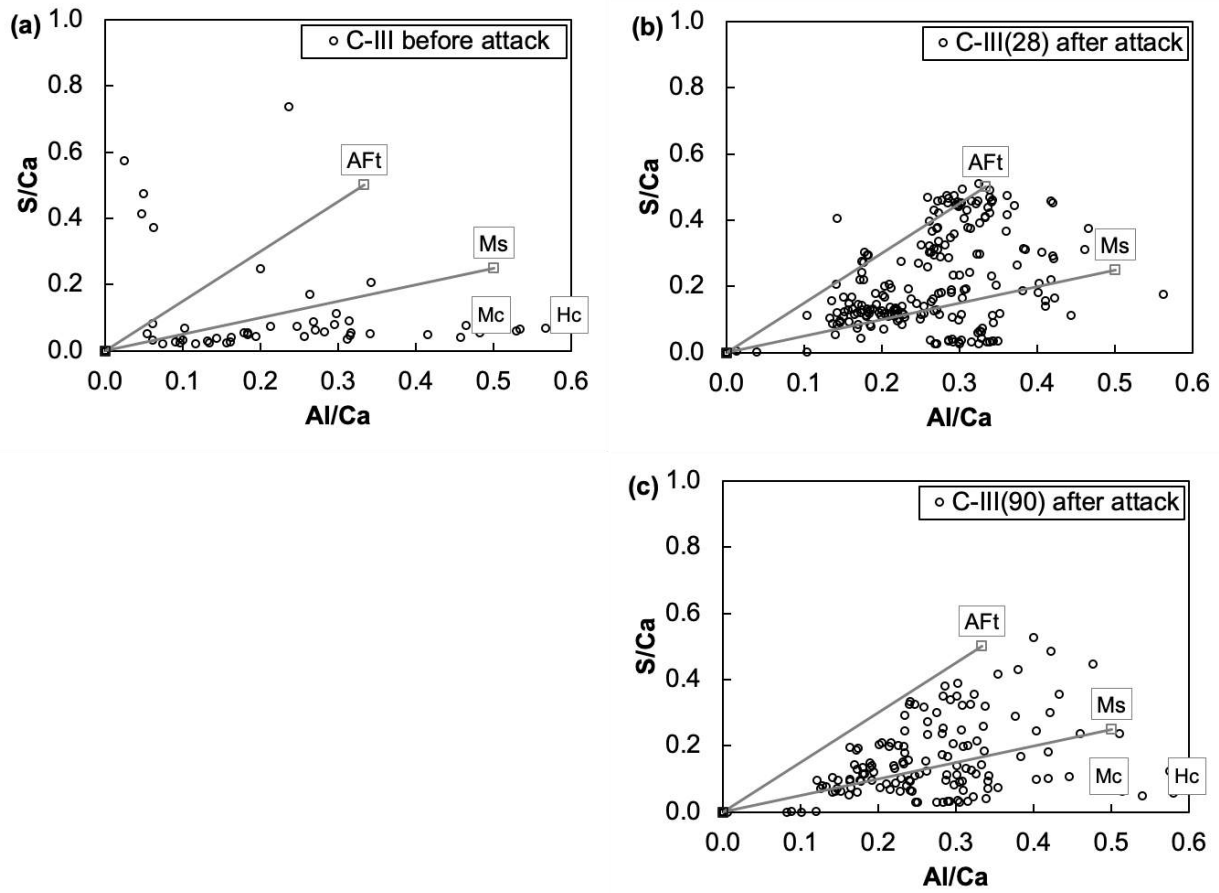
Figure 3.11 – EDS plots of Al/Ca versus S/Ca atomic ratios (AFt – ettringite, Ms – calcium monosufoaluminate, Mc – monocarbonate, Hc – hemicarbonate) on C-III concretes **(a)** before and **(b)** after attack cured for 28 days before test, **(c)** after attack cured for 90 days before test.

The presence of ettringite was verified by SEM/EDS in both concretes but to a lesser extent than for C-I. Figure 3.12 presents the SEM/EDS observations of C-III concretes, in which higher magnifications were used to observe the ettringite compared to those used for C-I (cf. Figure 3.9).

As shown in Figure 3.12(c) and Figure 3.12(d), ettringite crystals in C-III(28d) were observed in cracks and they seemed thinner than those observed in C-I. The crystals in this concrete measured 8-10 μm in length. On the contrary, in C-III(90d) ettringite seemed to mostly develop in air voids and they were grouped in small balls having a diameter of about 10 μm (cf. Figure 3.12(e) and Figure 3.12(f)). In this last case, ettringite crystals were very small and measured around 2 μm in length, which was about 5 times smaller than ettringite crystals observed in C-III(28d). XRD analyses also showed the presence of ettringite in C-III because of the peaks in the ranges 2θ 9°-9.5° and 2θ 15°-16 (cf. Figure 3.23). Finally, thermodynamic calculations showed that the Saturation Indices of AFt and Ms were superior to zero (cf. Table 3.2) meaning

that both minerals were in right conditions for precipitation. It should be noted that even though ettringite was detected in these matrices, the expansions measured were much lower than that in C-0, this point will be developed in more detail in the discussion section.
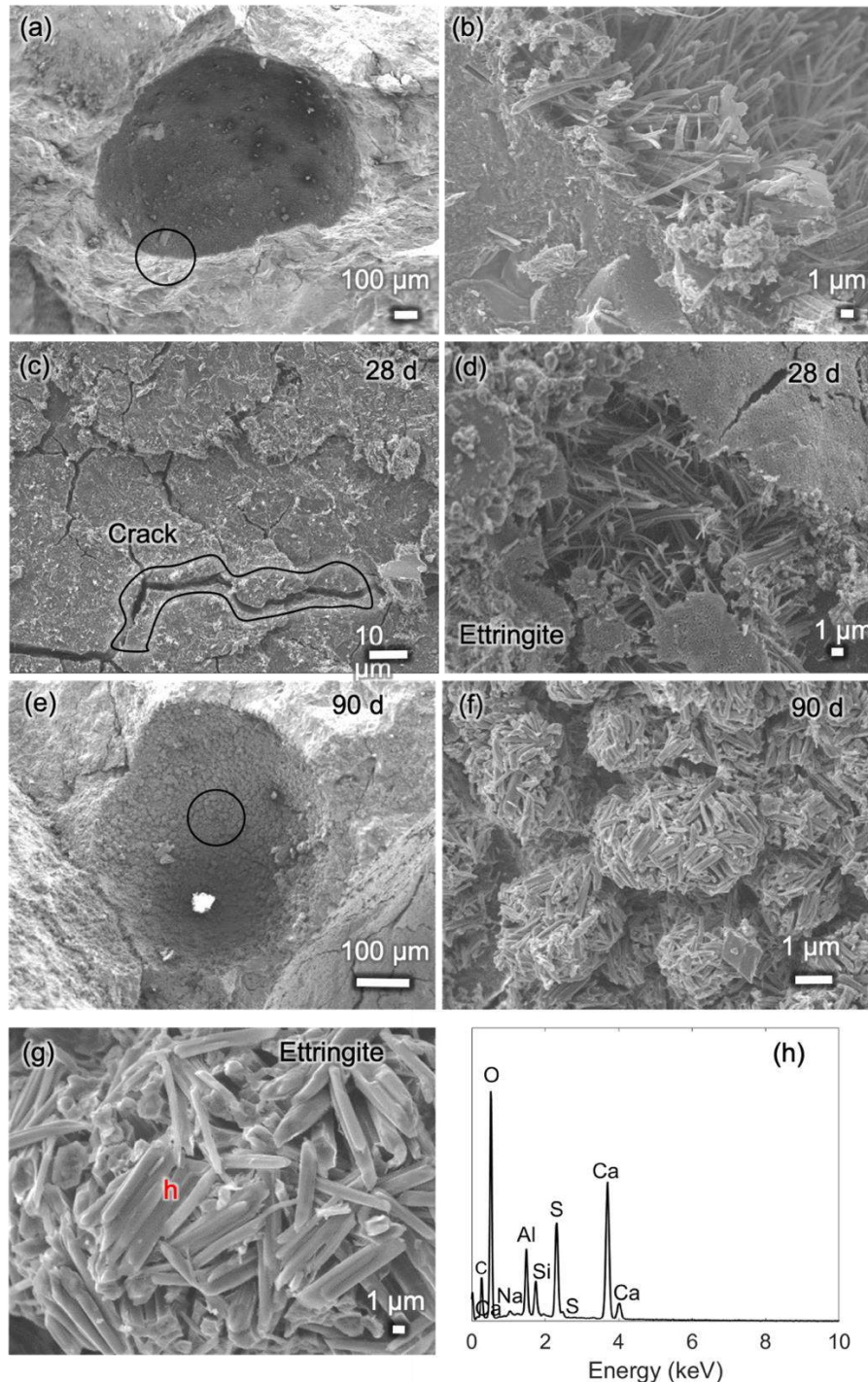
Figure 3.12 – SEM/EDS analyses of C-III. **Before ESA**: **(a)** Air void in the cement matrix, **(b)** magnification of image *a* (black circle) showing the presence of ettringite in an air void. **After ESA: (c)**, **(d)** C-III(28d) showing the presence of cracks filled with fine ettringite crystals. **(e)** pore of C-III(90d), **(f)** magnification of image *e* (black circle) showing the presence of ettringite grouped in small balls, **(g)** magnification of image *f* showing ettringite crystals morphology, **(h)** EDS spectrum obtained from image *g* (point h).

Figure 3.13 presents the element concentrations (sulfate, Na, Ca, Al, Si and Mg) measured in the pore solution of Portland cement-based concretes (C-I, C-0 and C-III) before and after ESA. Concentrations are given in mg/L and the horizontal pointed lines in Figure 3.13(a) and (b) indicate the initial concentrations of sulfates and Na in the immersion solution, respectively. As shown in Figure 3.13(a), solutions presented low concentrations of sulfates (<250 mg/L) before attack. After immersion in the sulfate solution, all the pore solutions presented higher sulfate concentrations. Regarding the C-I concrete, the sulfate concentration after ESA was higher than the initial concentration of sulfates in the immersion solution. This may suggest that (i) sulfates entered into the material and reacted to form ettringite and gypsum, and (ii) C-I released sulfates into the solution due to the degradation of the material. Regarding the C-0 and C-III concretes, sulfate concentrations after ESA were lower than the initial sulfate concentrations in the immersion solution (16000 mg/L). This may suggest that (i) sulfate concentrations in the matrices were not in equilibrium with the immersion solution and/or (ii) sulfates were still reacting in the matrices at the end of the tests to form phases such as gypsum and ettringite. The behavior of sulfate concentrations in solution agreed with the concentrations of sodium in the pore solutions (cf. Figure 3.13(b)) before and after ESA.

Moreover, Figure 3.13(c) shows that Ca concentrations in the pore solution of C-I and C-0 concretes decreased by 50% and 15%, respectively after attack. This was probably due to the consumption of free Ca in solution to react with the high concentration of sulfates to form gypsum and ettringite. In contrast, Ca concentration seemed constant before and after ESA in C-III concrete. Furthermore, Figure 3.13(d) shows that Al concentrations were a little higher after attack than before ESA probably due to the dissolution of aluminate phases such as C_3A (in the case of C-I) and C_4AF (for C-0) to react with sulfates to form ettringite. On the other hand, Figure 3.13(e) shows that silicon concentrations also increased in the pore solution after sulfate attack. This behavior may be explained by the dissolution of anhydrous phases such as C_3S and C_2S or the destabilization of the calcium silicate hydrate (C-S-H) [12] (which may explain the decohesion of C-I concrete). Finally, Mg concentrations in pore solution increased after attack, this was probably due to the destabilization of minerals present in the aggregates containing Mg (e.g. micas).
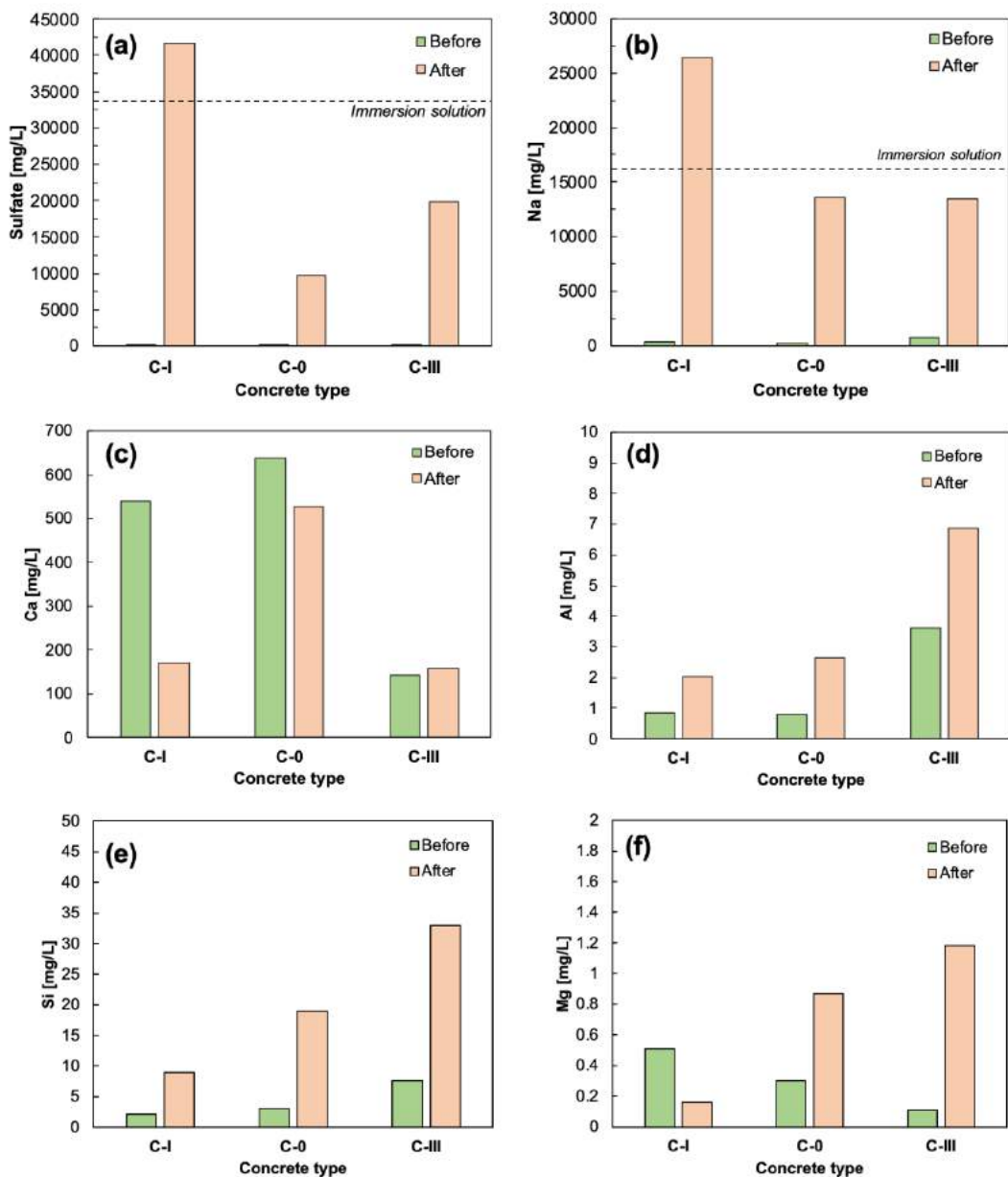
Figure 3.13 – Element concentrations (Sulfate, Na, Ca, Al, Si and Mg) of pore solutions of Portland cement-based concretes (C-I, C-0, C-III(90d)). Concentrations are expressed in mg/L and the horizontal dotted lines in **(a)** and **(b)** indicate the initial concentrations of sulfate and Na in the immersion solution (34000 mg/L and 16000 mg/L, respectively).

3.3.2 Ettringite binders-based concretes (C-SSC and C-CSA)

Figure 3.14 presents the chart of EDS analyses obtained from C-SSC and C-CSA concretes before and after ESA. For both concretes, EDS analyses showed a concentration of points between the two slopes (AFt and Ms) meaning that AFt and Ms were present in these two

139

concretes before and after ESA. These results were expected since these materials are ettringite-based binders and produce ettringite as the main mineral during hydration.
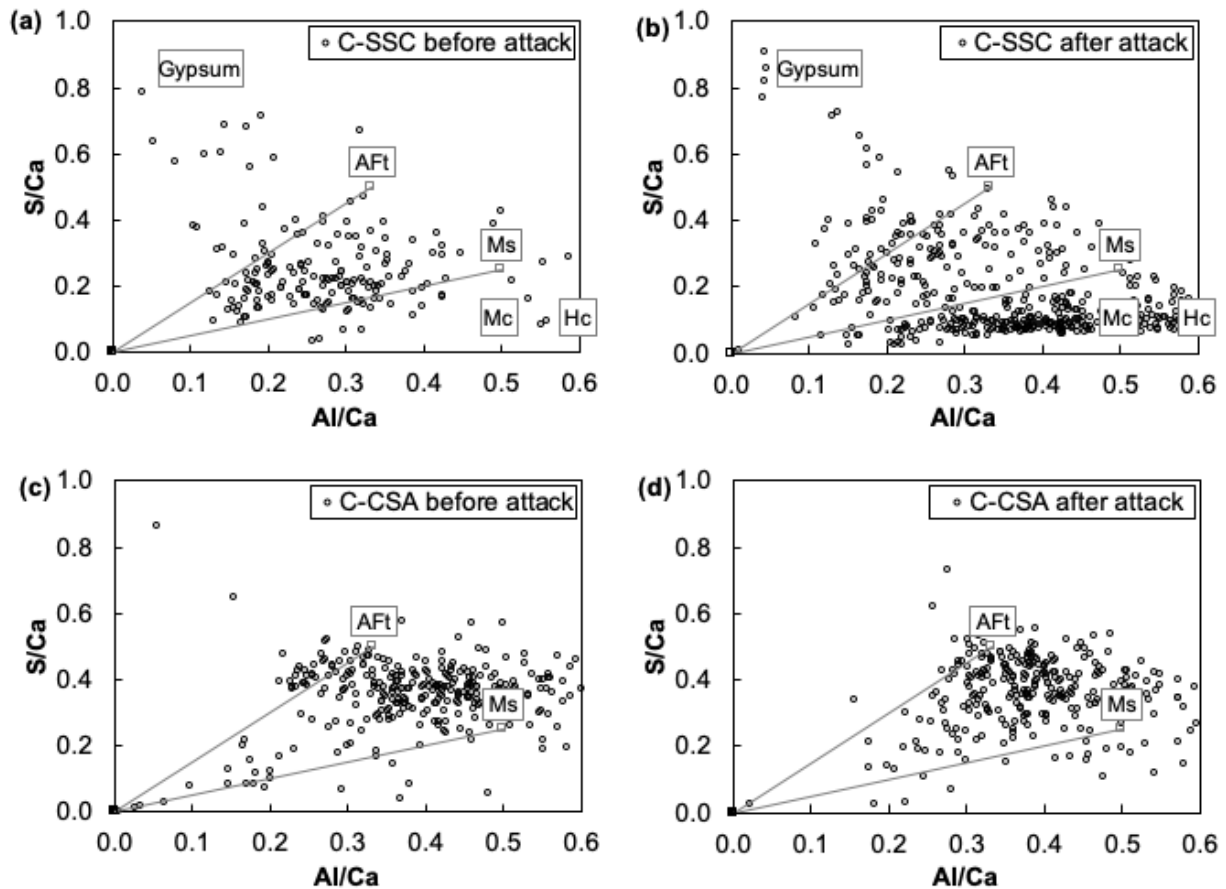
Figure 3.14 – EDS plots of Al/Ca versus S/Ca atomic ratios (AFt – ettringite, Ms – calcium monosufoaluminate, Mc – monocarbonate, Hc – hemicarbonate) on **(a)** C-SSC before and **(b)** after attack cured for 90 days before test, **(c)** C-CSA before and **(d)** after attack cured for 28 days before test.

Gypsum was also detected by EDS analyses in C-SSC after ESA as shown in Figure 3.14(b). Gypsum was formed by the reaction between calcium and the sulfate ions in excess. The presence of gypsum in C-SSC was verified by XRD patterns, which showed the appearance of a peak between 2θ 11° and 12° (cf. Figure 3.23). Even though, ettringite and gypsum were present before and after attack in these materials, we remind that non-expansion was detected during and after sulfate attack. A more detailed analysis about the absence of expansion in these binders will be presented in the discussion part.

The presence of ettringite in these concretes (C-SSC and C-CSA) was corroborated by XRD analyses (cf. Figure 3.23) and SEM/EDS observations (cf. Figure 3.15 and Figure 3.16). Figure 3.15 presents the SEM observations in C-SSC. From this figure, it can be observed that the

morphology of ettringite did not show significant changes before and after attack. Furthermore, ettringite was observed in air voids having thin crystals that measured 10-12 µm in length. For C-CSA concrete, Figure 3.16 also revealed that the morphology of ettringite did not change before and after attack. It can also be observed that this concrete presented two types of morphology: (i) constrained or massive ettringite crystals present in all the analyzed surface (cf. Figure 3.16(d)), and (ii) thick crystals of ettringite grouped in balls of about 20 µm in diameter (cf. Figure 3.16(f)).
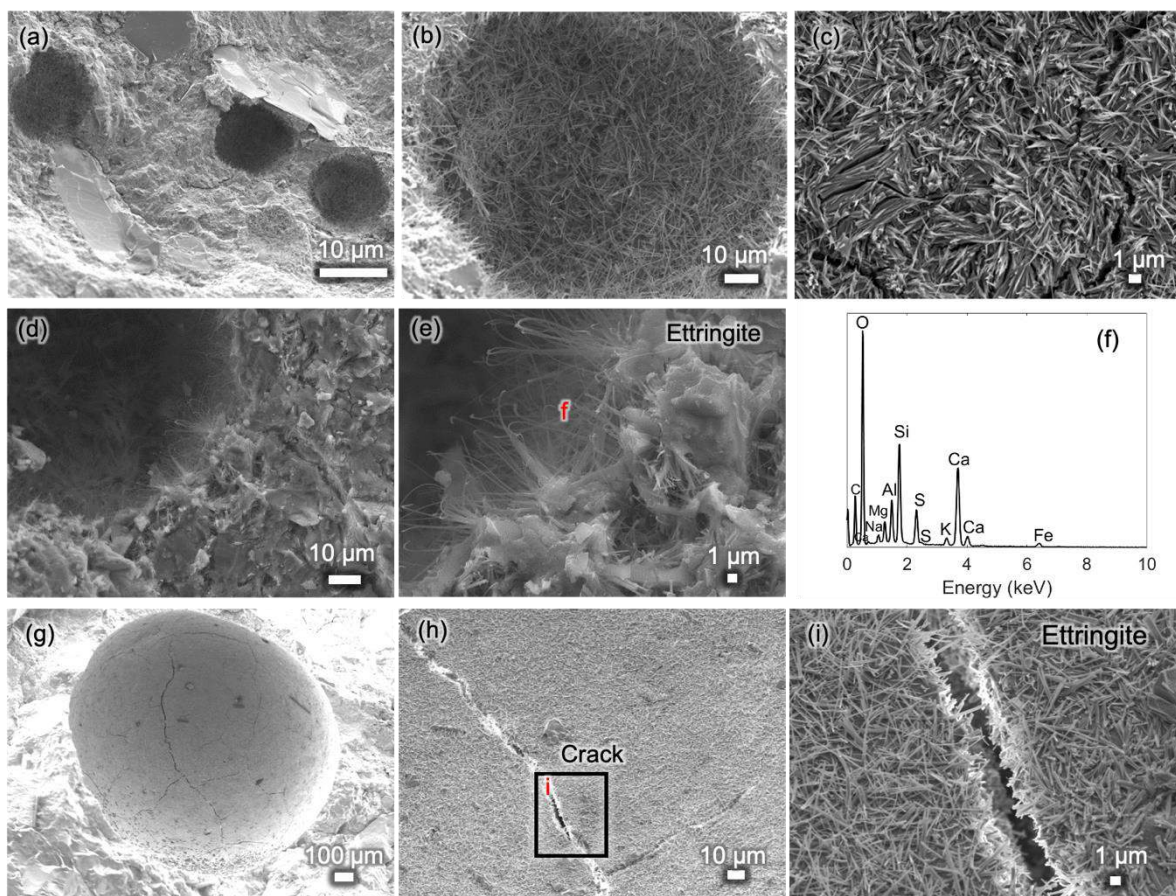
Figure 3.15 – SEM/EDS analyses of C-SSC cured for 90 days before test. **Before ESA: (a)** Air voids, **(b), (c)** magnification of image *a* showing the presence of ettringite in air voids. **After ESA: (d)** Air voids, **(e)** magnification of image *d* showing the presence of fine ettringite crystals, **(f)** EDS spectrum obtained from image *e* (point f), **(g)** binder paste-aggregate interface, **(h)**, **(i)** magnification of image *g* showing the presence of a small crack and abundant ettringite crystals.
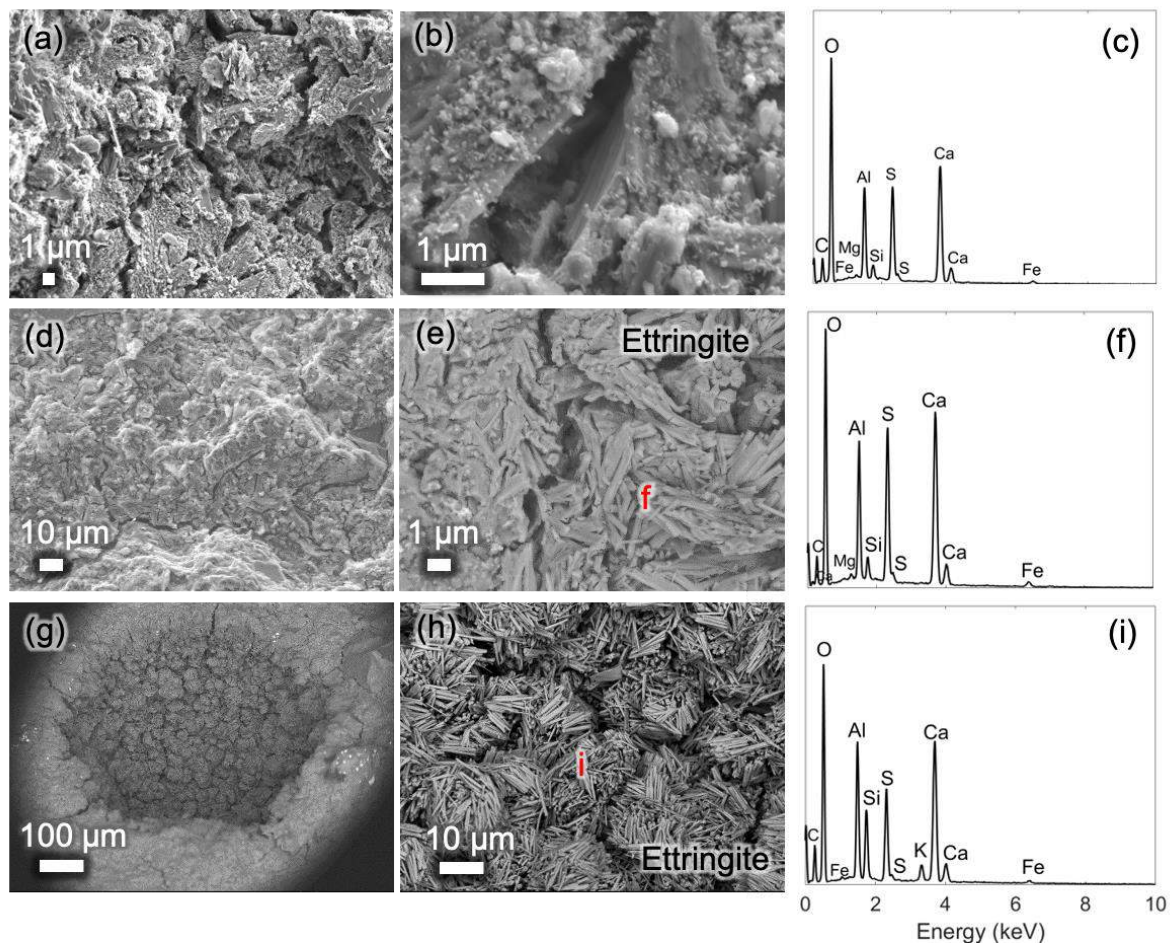
Figure 3.16 – SEM/EDS analyses of C-CSA cured for 28 days before test. **Before ESA: (a)** cement matrix, **(b)** magnification of image *a* showing the presence of abundant and interconnected ettringite crystals, **(c)** EDS spectrum obtained from image *b*. **After ESA: (d)** cement matrix showing the presence of abundant ettringite, **(e)** magnification of image *d* showing interconnected ettringite crystals, **(f)** EDS spectrum obtained from image *e*, **(g)** air void showing the presence of ettringite grouped in balls, **(h)** magnification of image *g*, **(i)** EDS spectrum obtained from image *h*.

It should be noted that Figure 3.14(b) also shows a few points below the Ms slope in C-SSC after attack. These points formed a constant tendency along the y-axis, and they can be explained by the transformation of monosulfoaluminate to mono/hemicarbonate (Mc/Hc) due to carbonation, as indicated by Komljenović et al. [40]. Mc and Hc are both located on the y-axis (Al/Ca-axis) having an Al/Ca atomic ratio of 0.5 and 0.68, respectively [40]. Furthermore, these points may also represent the presence of hydrotalcite as shown in Figure 3.17, where x-axis and y-axis plot the Mg/Si and Al/Si atomic ratios, respectively. The slopes presented in Figure 3.17 represent the Mg/Al atomic ratio of the hydrotalcite phases [40], [42]. In both materials, a decrease in the Mg/Al atomic rations were observed after ESA. A more detailed analysis will be presented in the discussion part.
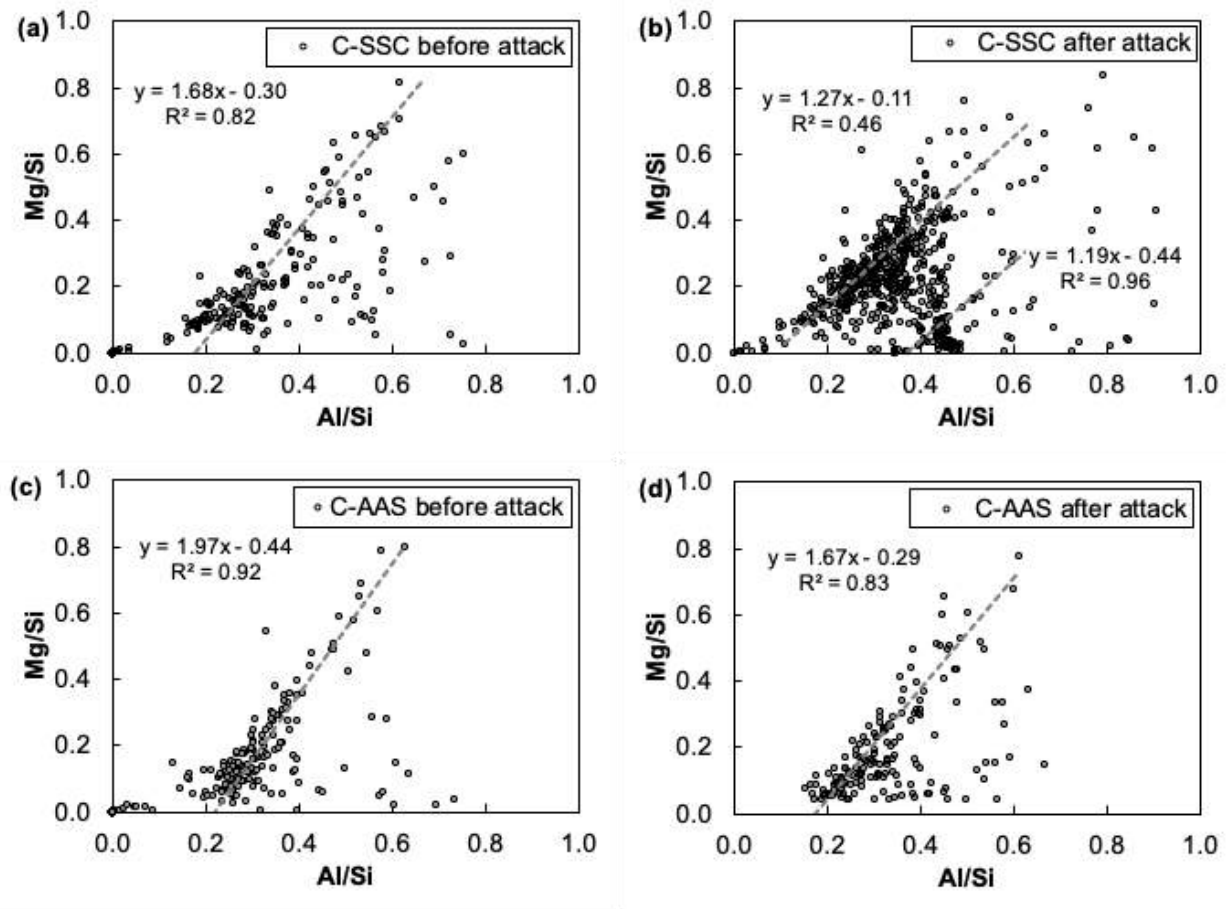
Figure 3.17 – EDS plots of Mg/Si versus Al/Si atomic ratios on **(a)** C-SSC before and **(b)** after attack cured for 90 days before test, **(c)** C-AAS before and **(d)** after attack cured for 90 days before test.

3.3.3 Alkali-activated concretes (C-AAS and C-GP)

Figure 3.18 and Figure 3.20 present the chart of EDS punctual analyses obtained from alkali-activated concretes (C-AAS and C-GP, respectively) before and after ESA.

In C-AAS concrete, it was possible to detect a few points in the Ms area before attack as shown in Figure 3.18(a). In addition, a significant population of points was below the Ms slope and all along the y-axis (as observed for C-SSC). As mentioned previously, these points were attributed whether to the presence of AFm phases (monocarbonate (Mc) and hemicarbonate (Hc)) or the presence of hydrotalcite. After sulfate attack in C-AAS, it was possible to identify a few more points in the Ms and AFt areas as shown in Figure 3.18(b) and the points attributed to Mc and Hc placed all along the y-axis remained present. Further details will be given in the discussion.
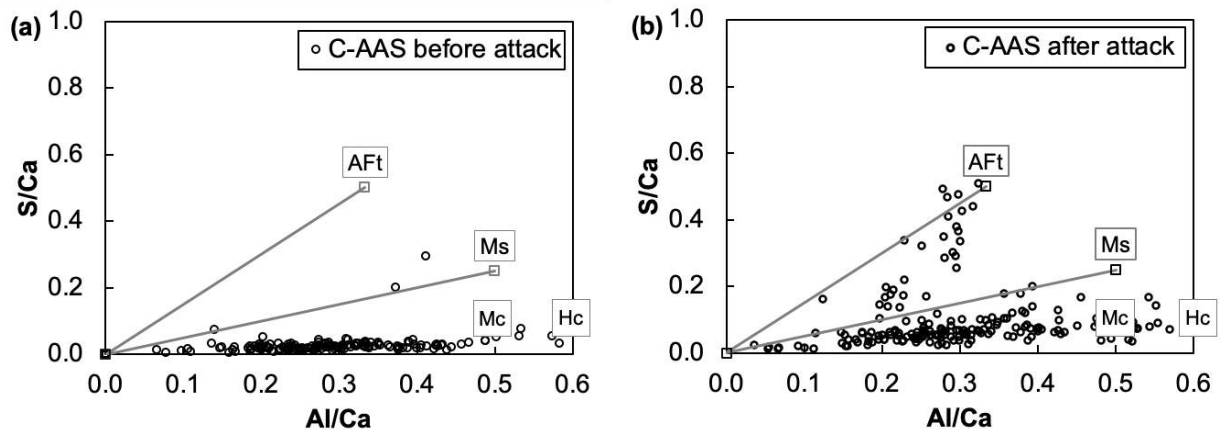
Figure 3.18 – EDS plots of Al/Ca versus S/Ca atomic ratios (AFt – ettringite, Ms – calcium monosufoaluminate, Mc – monocarbonate, Hc – hemicarbonate) on **(a)** C-AAS before and **(b)** after attack cured for 90 days before test.

On the other hand, XRD patterns (cf. Figure 3.23) and SEM/EDS analyses (cf. Figure 3.19) did not show the presence of ettringite in this concrete, probably because it formed at low quantities. According to the literature, the presence of carbonate may limit the formation of ettringite, probably because of the competition of carbonate and sulfate ions [42], [180]. In this concrete, the SI values (cf. Table 3.2) of Ms and gypsum were inferior to zero, meaning that these minerals did not precipitate. In contrast, the SI of ettringite was superior to zero indicating that this mineral might precipitate after ESA.
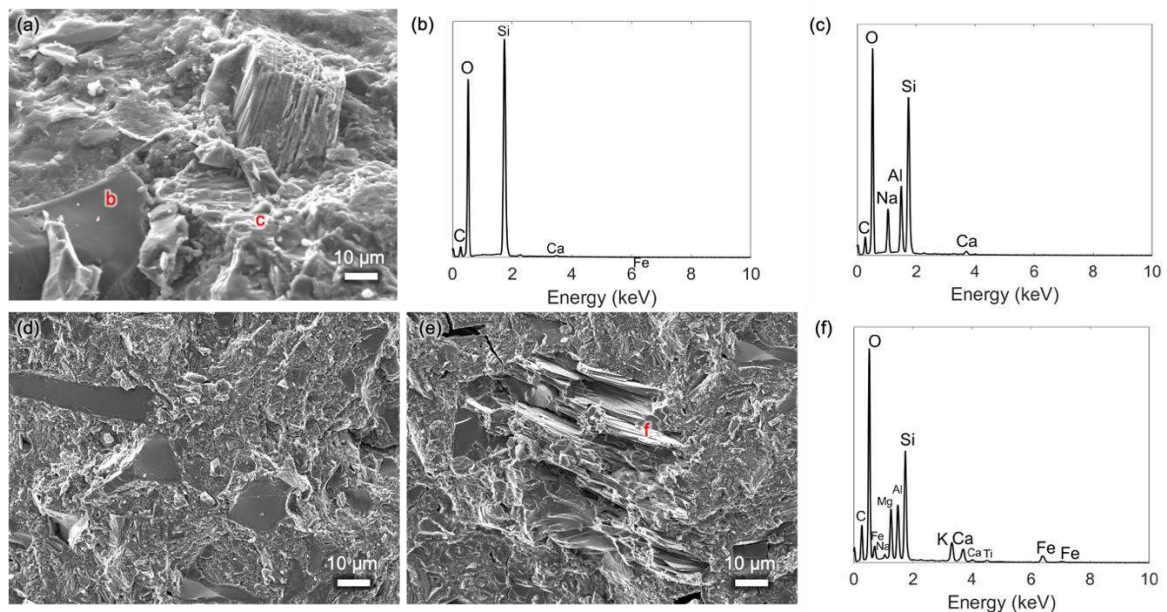
Figure 3.19 – SEM/EDS analyses of C-AAS. **Before ESA: (a)** concrete matrix, **(b)**, **(c)** EDS spectrum obtained from image *a* (points b and c). **After ESA: (d), (e)** Concrete matrix **(f)** EDS spectrum obtained from image *e* (point f).

In C-GP, EDS analyses did not show the presence of neither AFt nor Ms before and after ESA as shown in Figure 3.20. EDS plots in this material are shown at different scales in order to observe all the points taken in the analyses. This was a product of the very low content in calcium oxides (<2 wt%), leading to very high off-chart Al/Ca values. Furthermore, SEM/EDS analyses (cf. Figure 3.21) and XRD patterns (cf. Figure 3.23) did not show the presence of neither ettringite nor gypsum before and after ESA. Finally, the SI of AFt, Ms and gypsum (cf. Table 3.2) were inferior to zero, meaning that these minerals did not precipitate in C-GP.
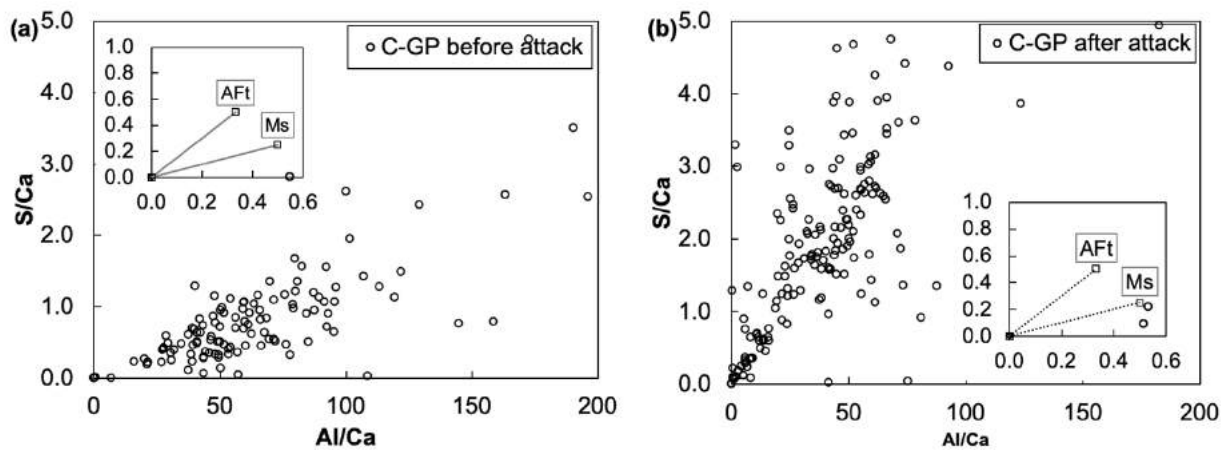
Figure 3.20 – EDS plots of Al/Ca versus S/Ca atomic ratios (AFt – ettringite, Ms – calcium monosufoaluminate) on **(a)** C-GP before and **(b)** after attack cured for 28 days before test.
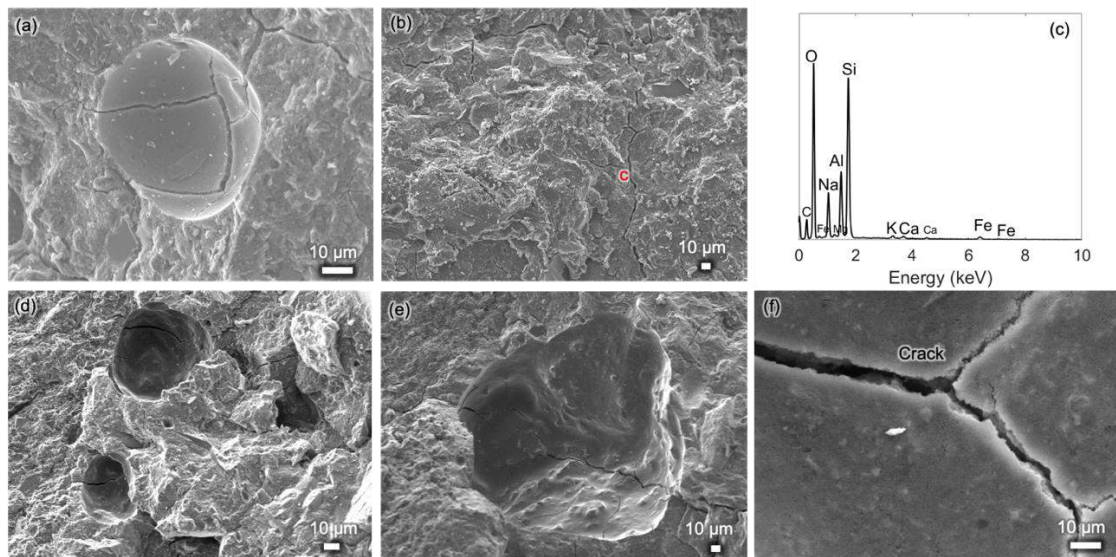
Figure 3.21 – SEM/EDS analyses of C-GP cured for 28 days before test. **Before ESA: (a)** air void, **(b)** concrete matrix**, (f)** EDS spectrum obtained from image *b* (point c). **After ESA: (d), (e)** air voids, **(f)** magnification of image *e*.

Figure 3.22 presents the element concentrations (sulfate, Na, Ca, Al, Si and Mg) measured in the pore solution of alkali-activated binders-based concretes (C-AAS and C-GP). Concentrations are given in mg/L and horizontal pointed lines in Figure 3.22(a) and (b) indicate the initial concentrations of sulfates and Na, respectively in the immersion solution.
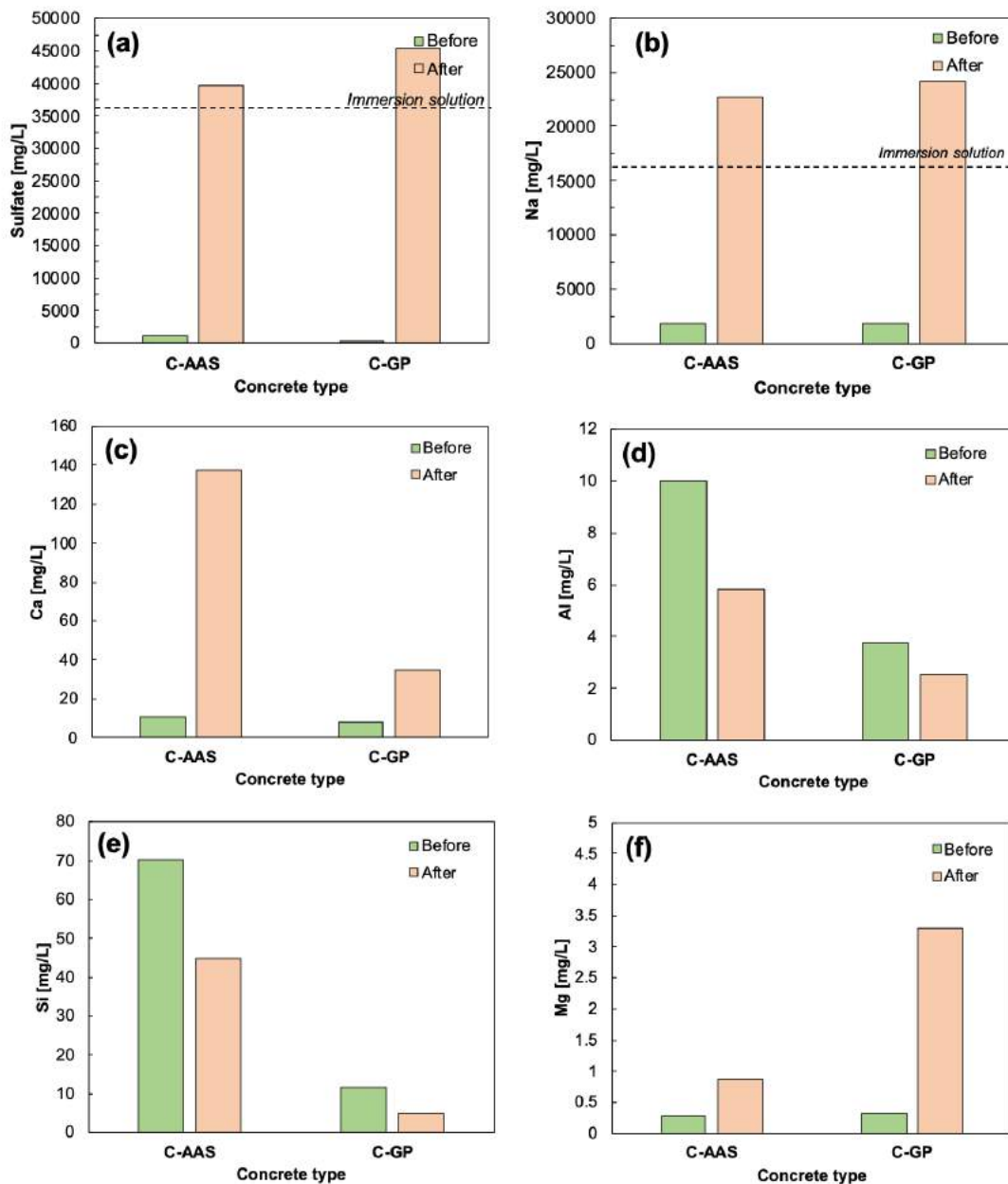
Figure 3.22 – Element concentrations (Sulfate, Na, Ca, Al, Si and Mg) expressed in mg/L of pore solutions of alkali-activated-based concretes (C-AAS and C-GP). Horizontal lines in **(a)** and **(b)** indicate the initial concentrations of sulfate and Na in the immersion solution (34000 mg/L and 16000 mg/L, respectively).

Figure 3.22(a) shows the sulfate concentrations before and after attack. As shown, sulfate concentrations increased after attack and presented higher values than the initial sulfate concentration in the immersion solution. On the other hand, Na concentrations before attack were higher than the ones measured for Portland concretes. This can be explained by the composition of these two binders. As a reminder, C-AAS was activated by sodium carbonate (Na_2CO_3) and C-GP was activated by using a solution containing Si and Na. After attack, Na concentrations increased in the pore solution and were superior to the initial concentration of the immersion solution.

Furthermore, Ca concentrations increased after ESA for both concretes. In the case of C-AAS, Ca concentration may come from the dissolution of GGBS or the destabilization of C-S-H. However, the release of Ca in C-GP may be explained by the 2 wt% CaO in the matrix and the dissolution of some minerals in the aggregates containing calcium such as the plagioclase feldspars (e.g. anorthite). Moreover, Si and Al concentrations were lower after sulfate attack. Two hypotheses could explain these variations: (i) in C-AAS less free Al was available because this concrete possibly continued hydrating over the period of the test, and (ii) in C-GP probably the geopolymerization of the material continued and Si and Al were consumed to build the network of Si-O-Al-O. As explained for Portland cement concretes, Mg concentrations in pore solution increased after attack probably due to the destabilization of minerals present in the aggregates containing Mg (e.g. micas).
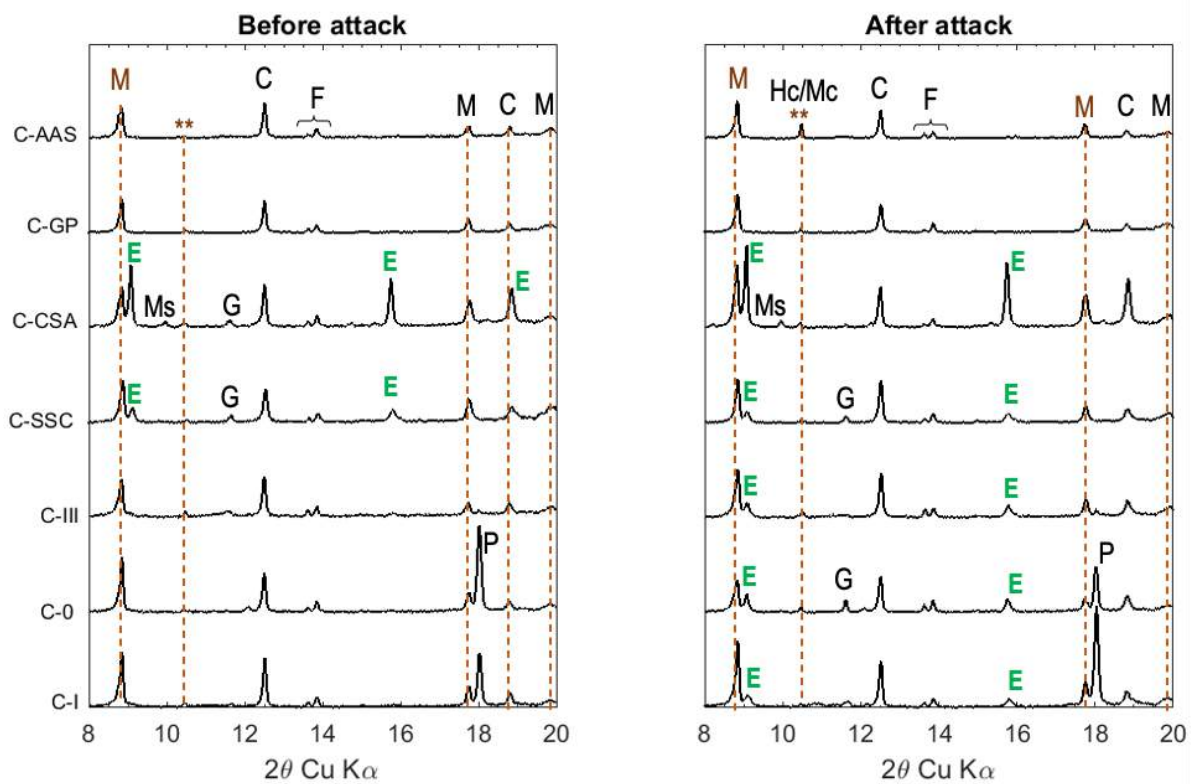
Figure 3.23 – XRD patterns before and after external sulfate attack. Selected range varying from 8° to 20°. <u>Minerals coming from the aggregates:</u> **M:** Mica, **C:** Chlorite, **F:** Feldspars, ****:** unidentified mineral. <u>Minerals coming from the binders:</u> **E:** Ettringite, **Ms:** monosulfoaluminate, **Hc/Mc:** Hemi/mono-carbonates, **P:** Portlandite, **G:** Gypsum.

Table 3.2 – Saturation indices of ettringite (AFt), calcium monosulfoaluminate (Ms) and gypsum before and after ESA. Values were calculated with PHREEQC V3.

	C-I		C-0		C-III		C-AAS		C-GP	
Mineral	Before	After	Before	After	Before	After	Before	After	Before	After
AFt	6.0	7.1	6.4	10.0	3.9	7.6	-0.2	6.8	-3.2	-1.9
Ms	1.0	1.4	1.3	4.0	0.0	1.9	-3.1	1.1	-4.5	-2.7
Gypsum	-0.9	-0.5	-0.9	-0.4	-1.5	-0.5	-2.0	-0.5	-2.8	-1.0

3.4 Benchmark of results

Table 3.3 presents a benchmark of all the results obtained in the study of concretes under external sulfate attack. It should be noted that the amount of the reaction products is qualitative and serves for the merely purpose of comparison.

Table 3.3 – Benchmark of concretes before and after external sulfate attack.

Category			Portland cements				Ettringite binders		Alkali-activated binders	
Concrete			C-I	C-0	C-III	C-III	C-SSC	C-CSA	C-AAS	C-GP
f_c [a] (MPa)			54.5	40.8	41.5	-	59.3	40.3	33.2	49.6
Age [b] (days)			28	28	28	90	90	28	90	28
Tests SIA 262:2013	Longitudinal expansion (%)	Sulfates	0.4	0.07	0.13	0.05	0.008	0.03	0.021	0.015
		Water	0.04	0.03	0.02	0.01	0.007	0.005	0.010	0.020
	Mass change (%)	Sulfates	1.6	0.8	1.1	0.9	0.3	0.8	0.45	0.7
		Water	0.6	0.4	0.5	0.5	0.1	0.3	0.05	0.6
Mineral phases detected by XRD/SEM/EDS — Qualitative estimation	Ettringite	before [c]	Low	Not found	Not found	Not found	Moderate	High	Not found	Not found
		after [d]	High **+**	High-Moderate **+**	Moderate **+**	Moderate	Moderate	High	Low	Not found
	Gypsum	before	Low	Not found	Low	Not found	Moderate	Low	Not found	Not found
		after	Moderate	High **+**	Low	Not found	Moderate	Low	Not found	Not found
	Monosulfo-aluminate	before	Not found	Low	Low	Low	Moderate	High	Low	Not found
		after	Not found	Low	Moderate	Moderate	Moderate	High	Low	Not found
	Hemi/mono-carbonate	before	Not found	Not found	Low	Low	Moderate	Not found	High	Not found
		after	Not found	Not found	Moderate	Moderate	High	Not found	High	Not found
	Portlandite	before	High	Moderate	Low	Low	Not found	Not found	Not found	Not found
		after	High	Moderate	Low	Low	Not found	Not found	Not found	Not found
Cracking			High	Low	Not found	Not found	Not found	Not found	Not found	Not found
Capacity to resist ESA based on longitudinal expansions (max. guideline value: 0.1%)			Bad	Regular	Regular	Good	Good	Good	Good	Good

[a] f_c: Compressive strength at 28 days of curing
[b] Age of curing in days before external sulfate attack (ESA)
[c] Before ESA
[d] After ESA

Content (qualitative)	High	High-Moderate	Moderate	Low	Not found	Expansive product
Legend	●	◑	◐	◔	○	Red cross **+**

3.5 Discussion

3.5.1 Portland cement-based concretes

Ordinary Portland cement and sulfate-resisting Portland cement:

Ordinary Portland cement-based concrete (C-I) was selected as the control material and it was expected that it would present the largest longitudinal expansion among all the concretes. C-I expansion was produced by the chemical reaction between the aluminate phases (especially C_3A) and the high concentration of sulfates present in the immersion solution. As observed in Figure 3.3, C-I expansion increased slowly during the first 25 days of attack, and then it increased suddenly. Similar behavior has also been reported in the literature on studies carried out on OPC-based concretes under ESA [8], [12]–[14].

Degradation kinetics on C-I were faster than on the sulfate-resisting Portland cement-based concrete (C-0) in which the expansion increased slowly and at uniform rate. About the end of the test (around 70 days of immersion), noticeable cracks were observed in C-I, which explains the high dispersion obtained in the last two expansion values. At the end of the test, supplementary submersion was carried out for visual inspections. After one year of supplementary submersion, C-I samples developed decohesion. Pictures of C-I are presented in Figure 22.

Figure 3.24 – Pictures of some samples of the C-I concrete **(a)** at 70 days of tests showing the presence of cracks, and **(b)** after one year of supplementary submersion showing the decohesion of the samples.

On the other hand, C-0 was expected to present lower expansion than C-I due to the slow reaction of C_4AF and the absence of C_3A. The final expansion in C-0 was indeed 6 times lower

than the one in C-I. Unlike C-I, C-0 did not present any noticeable cracks during and at the end of the test (duration test of 84 days). This result supports the fact that low or absence of C_3A content improves the durability of materials under ESA [19], [20]. This means that the damage is delayed in time when the source of aluminum content has a lower kinetics of dissolution, as it is the case for C_4AF. At the end of the test, supplementary submersion was carried out for visual inspections. This showed that C-0 developed cracks after 550 supplementary days. In C-0, calcium and aluminum ions are available from C_4AF; however, this aluminate phase reacts with a lower kinetics compared to the one of C_3A [21]–[23]. As a result, ettringite forms at a very slow rate and in minor quantities than in presence of C_3A [24]. Therefore, cracking in C-0 was mostly attributed to the formation of gypsum as shown in Figure 3.8. This finding reinforces previous results reporting that gypsum is often formed besides ettringite in materials with low C_3A content when exposed to high sulfate concentrations [12]–[14], [21]–[24].

Blast furnace slag Portland cement:

Regarding the blast furnace slag cement-based concretes (C-III) cured for 28 days (C-III(28d)) and 90 days (C-III(90d)) before attack, they showed similar reaction kinetics under ESA (cf. Figure 3.3) but different magnitude of expansion at the end of the test. C-III(28d) presented an expansion 40% higher than C-III(90d), meaning that curing can be a relevant parameter influencing the resistance of concretes to ESA. The different behavior between these two concretes can be explained probably by the difference in their porosity. Hydration degree in slag blended cements is not very high at early ages compared to OPC and the rate of hardening is slower than that in OPC during the first 28 days [60], [169]. Therefore, early sulfate exposure of slag blended cements can affect their sulfate resistance because at early ages these materials present low reactivity and thus their pore network is not completely developed, which increases the ingress of sulfates ions and allows their reaction in the matrix [181]. This may indicate that slag blended cements should present lower expansions when exposure occurs at late ages of curing.

Yu et al. [30] explained that slag blended cements present a smaller pore size structure that favor their resistance to sulfate attack. They pointed out that these materials may not show expansion within the period of the tests even though they present degradation. Moreover, they explained that failure of slag blended cements under sodium ESA is dominated by the loss of surface rather than expansion. The authors showed that in these types of cement, the incoming sulfate ions are fixed close to surface by aluminate phases such as Ms and anhydrous slag due to the pore structure. Only when all phases have been reacted, the sulfate ion concentration can increase in pore solution and when the supersaturation level is reached, fine crystals of ettringite can be formed from Ms to produce expansion.

Aside from this, C-III(28d) and C-III(90d) concretes presented lower final expansions than C-I (3 times and 7 times lower, respectively). According to the literature, the behavior of slag blended with clinker cements under ESA depends on the level of replacement and composition of slag [182]. Whittaker et al. [182] explained that high slag levels (>70%) improves the resistance of cements under ESA. Low expansion in C-III can be explained by the important proportion of slag (82%) and the low content of clinker (15%), which reduces the C_3A content and thus the availability of aluminum to react with sulfates. In addition to this, clinker is consumed by the GGBS to be activated, it means that GGBS reaction became the dominant reaction and the amount of clinker can be considered insufficient to enable the precipitation of large amounts of expansive phases [81], [83], [183]. Moreover, the absence or low content of portlandite reduces the expansive nature of ettringite. Furthermore, the unavailability of aluminum for reaction with sulfates can also be explained by the formation of C-A-S-H and hydrotalcite phases [40] during hydration. Allahverdi et al. [41] pointed out that slag cements produce C-S-H with lower Ca/Si ratios than those in OPC, thereby increasing their capacity to bind more aluminum in their structure and reducing the free aluminum to react with sulfates.

3.5.2 Alternative binders-based concretes

Results presented in this paper confirmed that the use of the alternative binders studied (C-SSC, C-CSA, C-AAS and C-GP) is useful to improve the durability of concretes under ESA because: (i) longitudinal expansions were inferior to the ones obtained for OPC, (ii) expansion were lower than the limit value of 0.1% set by the Swiss Standard, and (iii) no visual signs of damage was observed during and after ESA.

3.5.2.1 Ettringite binders

The calcium sulfoaluminate-belite cement-based concrete (C-CSA) did not show any significant expansion (0.03%±0.01%) after ESA and it did not develop cracks or visual deterioration during and after attack. These results are in agreement with Bescher et al. [52], who indicated that after an immersion period of two years in sulfate solutions, CSA-belite mortars cubes did not present visual signs of deterioration. They suggested that different factors may contribute to the sulfate resistance of CSA against ESA: (i) the lack of C_3A, (ii) the formation of low amounts of C-S-H, which may favor the good resistance to sulfate attack because there is not decalcification of this phase, and (iii) the formation of ettringite during hydration, which is not deleterious for the material. Chen et al. [46] explained that if ettringite is formed after hydration without producing expansion, this probably means that ettringite had

space to grow without exerting pressure on the CSA rigid matrix. On the contrary, Hargis et al. [47] showed that CSA pastes presented expansion at different levels as a function of the gypsum content. They suggested that CSA expanded not only for the crystallization pressure exerted by ettringite but also by other hydrates such as monosulfoaluminate, straetlingite, CAH_{10}, and AH_{13}.

With respect to the supersulfated GGBS cement-based concrete (C-SSC), no significant expansion (<0.01%) was presented after ESA and no cracks were detected during and after attack. This finding supports previous studies indicating the good resistance of SSC cements under ESA. Grounds et al. [53] showed that SSC mortars did not present expansion or visible signs of attack after calcium or sodium sulfate exposure. Cerulli et al. [63] showed that SSC-based mortars did not expand very much under ESA and the authors attributed such resistance to the low calcium hydroxide (CH) content. They explained that hydrated lime seemed to favor the formation of colloidal ettringite, which could be able to absorb water responsible for a deleterious swelling. Similarly, Niu et al. [54] indicated that SSC mortars presented expansion of about 4 times lower than that in OPCs. The authors also attributed such sulfate resistance to the low CH content, which was consumed by the pozzolanic reaction to form ettringite and C-S-H; therefore, free CaO was insufficient to react with the sulfate ions coming from the sulfate solution. In summary, the sulfate resistance of SSC cements has been attributed in the literature to: (i) the low content or absence of CH, and (ii) the consumption of most of the free alumina, coming from the slag, to form ettringite during hydration [53], [54], [60], [63].

Ettringite morphology:

Moreover, SEM observations and EDS analyses (cf. Figure 3.14, Figure 3.15 and Figure 3.16) showed that ettringite-based concretes (C-SSC and C-CSA) presented ettringite with different morphology. In C-SSC, fine ettringite of about 10-12 μm in length was observed in air voids. In contrast, two types of ettringite morphology were observed in C-CSA: (i) thick crystals of ettringite grouped in balls of about 20 μm in diameter, and (ii) constrained or massive ettringite in all the analyzed surface. Kharchenco et al. [184] suggested that crystallization pressure of ettringite and its morphology depends on the pH value of the reaction solution. Yu et al. [185] suggested that ettringite crystals formed during hydration, which are interlocked with each other, lead to a more compact structure and higher compressive strength in CSA materials. It should be noted that some previous studies have linked this interlocked, massive or constrained ettringite to expansion in OPCs [3], [181], [186]. However, this relation has been mostly made in heat-cured concretes when delayed ettringite formation takes place. Tosun et al. [186] pointed out that non-expansive ettringite would take the form of ball type and would form in spherical spaces such as entrapped air voids. Meanwhile, ettringite formed in narrow

spaces (named as massive or constrained ettringite) would exert pressure causing expansion. According to the literature, one can conclude that: (i) ettringite morphology depends on the composition of each binder and the space where it is formed, and (ii) there is no clear relationship between the amount and morphology of ettringite and the absence or presence of expansion. The presence of hydrotalcite in C-SSC was verified by EDS analyses plotted in Figure 3.17(a) and Figure 3.17(b). The Mg/Al atomic ratio of hydrotalcite before ESA was about 1.68 and decreased to 1.27 after attack.

Effect of high sodium concentrations in the solution of attack:

According to the literature, high sodium concentrations can lead to the instability of ettringite. Several studies have shown that the presence of high content of alkalis (sodium or potassium) inhibits the formation of ettringite [187], [188]. Sodium increases the alkali conditions in the pore solution and modifies the stability of ettringite. High alkali conditions enhance the solubility of ettringite constituents, mainly sulfate, as a result, the amount of ettringite decreases in the hydrated binder [188]. High amounts of sodium (> 25 mass % of Na_2SO_4) can also lead to the formation of the U-phase $((CaO)_4(Al_2O_3)_{0.9}(SO_3)_{1.1}(Na_2O)_{0.5}:16H_2O)$, which causes deterioration in the hardened materials. Elakneswaran et al. [189] investigated the formation of the U-phase when one Portland cement and one slag-bended cement samples were exposed to a sodium sulfate water solution with a concentration of 1300 mmol/L of Na_2SO_4. After several months of exposure, they detected the U-phase. However, in the present study, we did not detect this phase by microstructural or mineralogical characterization of samples after ESA. The sulfate solution used to study the external sulfate attack contained of about 300 mmol/L of Na_2SO_4 (5% Na_2SO_4), which is about 4 times lower than the concentration used by Elakneswaran et al.

3.5.2.2 Alkali-activated concretes (C-AAS and C-GP)

Alkali-activated slag:

Alkali-activated slag based-concrete (C-AAS) presented an expansion of 0.021%±0.015%, which is about 19 times lower than that in C-I. Moreover, C-AAS concrete did not display any signs of deterioration or the presence of cracks at the end of the test or during the visual inspection. This result is in agreement with Bakharev et al. [26] and Dzunuzović et al. [31] who did not find signs of deterioration during visual examination of AAS concretes exposed to a Na_2SO_4 solution. In contrast, Allahverdi et al. [41] reported surface scaling during visual inspection of AAS mortars under ESA due to the crystallization of sodium sulfate; however,

they did not detect signs of expansion or cracking. Additionally, they showed that AAS mortars reached negligible length changes (0.03%) compared to OPC mortars (0.36%).

In the present study, XRD analyses in C-AAS did not show the presence of ettringite (AFt) or gypsum even though EDS analyses revealed a small population of points in the AFt area (cf. Figure 3.18(a) and (b)). SEM and XRD analyses carried out in this study are consistent with results reported by Dzunuzović et al. [31] who did not detect new phases in an alkali-activated fly ash/slag after sulfate attack. Similarly, Ye et al. [42] reported the absence of ettringite in a sodium carbonate AAS exposed to a Na_2SO_4 solution. The presence of carbonate may prevent or limit the formation of ettringite, probably because of the competition of carbonate and sulfate ions [42], [180]. In accordance with the literature, AAS materials resist better to ESA than OPC because of the absence of portlandite and the unavailability of aluminum for reaction with sulfates due to the formation of C-A-S-H and hydrotalcite phases during hydration [40]. As mentioned previously, materials containing slag form C-S-H with lower Ca/Si ratios than those in OPC, increasing the C-S-H capacity to bind more aluminum in their structure and reducing the free aluminum to react with sulfates [41].

The presence of hydrotalcite in C-AAS was corroborated by EDS analyses plotted in Figure 3.17(c) and Figure 3.17(d). The Mg/Al atomic ratio of hydrotalcite before ESA was about 1.97 and decreased to 1.67 after attack. Ben Haha et al. [190] showed that alkali-activated slags presented hydrotalcite with Mg/Al atomic ratios between 2.06 and 1.29. The authors showed that high amounts of aluminum reduced the Mg/Al atomic ratios of hydrotalcite. In this study, the decrease of Mg/Al ratio after ESA suggests that C-AAS continued hydrating despite the ESA.

Metakaolin-based geopolymer:

Finally, the metakaolin-based geopolymer (C-GP) presented a very low expansion of 0.015%%±0.009% (about 27 times lower than that in C-I). All analyses performed in C-GP showed the absence of sulfate phases such as ettringite or gypsum. This finding was expected due to the very low content of calcium oxides (CaO) (<2 wt%, % by weight of metakaolin) in the metakaolin (MK). Alcamand et al. [45] explained that low or absence of CaO content in alkali-activated materials increases their durability with respect to sulfate attack due to the non-formation of calcium hydroxide (CH), which is highly affected by sulfate attack. Duan et al. [32] studied the influence of partial replacement of calcareous fly ash by MK in a fly ash geopolymer under ESA. They verified that with increasing the addition of MK in the geopolymer, its durability to sulfate attack increased due to the decrease in the calcium content and thus the formation of expansive products.

3.6 Conclusions

The aim of this paper was twofold: (i) to realize a benchmark of several binders by testing their capacity to resist external sulfate attack (ESA) under similar experimental conditions, and (ii) to contribute to the understanding of mechanisms associated with the expansion or non-expansion of the binders by using microstructural and mineralogical analyses, and thermodynamic calculations. Table 3.4 presents the conclusions of this chapter.

Table 3.4 – Conclusions of Chapter 3 – Concrete under external sulfate attack.

Category	Portland cements	Ettringite binders	Alkali-activated binders
What was done?	Three different concretes: - one Ordinary Portland cement (C-I), - one sulfate-resisting Portland cement (C-0), - one blast furnace slag cement (C-III).	Two different concretes: - one supersulfated GGBS cement (C-SSC) - one calcium sulfoaluminate (C-CSA).	Two different concretes: - one calcium carbonate alkali-activated slag (C-AAS) - one metakaolin-based geopolymer (C-GP).
	All concretes were exposed to an accelerated external sulfate attack in accordance with the Swiss Standard SIA 262-2013.		
Results	**C-I:** maximal expansion (0.4%) and noticeable cracking. **C-0:** low expansion (0.07%) and no cracking. Visual inspections identified cracking after 550 days of immersion. **C-III:** no visual damage. The magnitude of the final expansion depended on the curing time before sulfate exposure. Concretes cured for 90 days had 40% less expansion than those cured for 28 days.	**C-SSC** and **C-CSA:** low expansions (range 0.01-0.03%) and no visual damage was observed.	**C-AAS** and **C-GP:** Very low expansions (<0.03%) and no cracking or damage was observed during and after attack.
Why?	**C-I:** dense amounts of ettringite in all the analyzed surface due to the reaction between C_3A and sulfates in solution. **C-0:** presence of gypsum in all the analyzed surface due to the release of aluminates from C_4AF. **C-III:** ettringite was found in minor extent and in air voids.	**C-SSC** and **C-CSA:** - Ettringite and calcium monosulfoaluminate formed during hydration. - Ettringite morphology differs from one concrete to another. - No portlandite	Low expansions explained by the uptake of water. **C-GP:** low content of calcium prevented the precipitation of typical expansive phases. **C-AAS:** low portlandite content and the unavailability of aluminum to precipitate with sulfates to form significant amounts of ettringite.

Suggestions for further research

- Pore solution extractions for ettringite binders

For the purpose of better understanding the behavior of the concretes under ESA, pore solutions extractions were performed before and after sulfate attack by carrying out squeezing tests. Element concentrations can be measured in the solutions as presented in this chapter in Figure 3.13. This information was used to calculate the Saturation Indices of different phases in order to verify their dissolution or precipitation conditions. The squeezing process resulted in the extraction of some milliliters of pore solution for all the concretes except for C-SSC and C-CSA because higher pressures are required to extract their pore solutions. Therefore, it would be interesting to complete the study.

- Modeling

In this study, we calculated the saturation indices of ettringite, monosulfoaluminate and gypsum by using PHREEQC and the element concentrations of poral solutions. It was assumed that these saturation indices were the result of the state of equilibrium of the poral solution. It would be also interesting to estimate the equilibrium states of the reaction products of the hardened binders at the different steps by varying the concentration of sulfates. These results could be compared with experimental data if the quantification of phases was carried out.

- Evaluate other parameter of concrete under external sulfate attack

In this thesis, we studied the capacity of binders to resist external sulfate attack by measuring longitudinal expansions. However, other parameters can be also evaluated in order to ensure their capacity to resist external sulfate attack. For example, it would be interesting to measure their mechanical properties (e.g. compressive strength) during the period of sulfate exposure.

CHAPTER 4 – STABILIZATION OF SULFATES

Table of Contents

4. Chapter 4 – Stabilization of sulfates

Résumé

Ce quatrième chapitre présente les résultats obtenus sur l'étude de la stabilisation des sulfates dans des sols traités par des liants alternatifs.

Cette partie de la recherche visait à (i) comparer la capacité de plusieurs liants alternatifs à immobiliser les sulfates dans un sol enrichi en sulfates dans des conditions de pH naturel, (ii) comprendre les mécanismes d'immobilisation des sulfates, et (iii) évaluer le potentiel de gonflement et les propriétés mécaniques des traitements du sol sulfaté.

Ce chapitre est organisé de la manière suivante :

(i)   La première partie se concentre sur la justification des formulations utilisées pour les traitements du sol sulfaté.

(ii)   Ensuite, il présente les résultats obtenus lors des essais de lixiviation pour évaluer l'immobilisation des sulfates ainsi que les résultats des essais d'aptitude des traitements (gonflement et résistance mécanique).

(iii)   La troisième partie présente l'étude approfondie faite sur un traitement particulier du sol sulfaté. L'immobilisation des sulfates ainsi que les propriétés géotechniques du traitement ont été évaluées à court, moyen et long termes.

De plus, tous les résultats expérimentaux obtenus lors des essais de lixiviation ont été comparés avec des calculs numériques obtenus à partir d'un modèle géochimique développé avec le code PHREEQC. Ce travail de modélisation a été effectué afin de mieux comprendre les mécanismes de stabilisation des sulfates pour ce traitement en particulier.

Vu l'indisponibilité d'un sol naturellement sulfaté, il a été choisi de doper artificiellement en sulfates un sol limon provenant de Saclay, France. Les détails de ce dopage ont été présentés dans le Chapitre 2- section 2.1.2.3.

Récapitulatif des formulations :

Le sol sulfaté a été traité par quatre liants différents et cinq formulations ont été obtenues au total :

- Formulation 1 (F1) : sol sulfaté sans traitement ;
- Formulation 2 (F2) : sol sulfaté traité avec 10% de ciment Portland CEM I ;
- Formulation 3 (F3) : sol sulfaté traité avec 10% d'un clinker sulfoalumineux nommé dans cette étude « Clinker Y » ;
- Formulation 4 (F4) : sol sulfaté traité avec 10% de ciment CEM III/C ;
- Formulation 5 (F5) : sol sulfaté traité avec 10% d'un liant expérimental composé de 90% de laitier et de 10% de ciment Portland nommé dans cette étude « liant 90-10 ».

Concernant le dosage de liant utilisé pour ces traitements, il a été choisi d'employer 10% de liant. Cette teneur en liant a été déterminée suite à des essais d'aptitude réalisés en accord avec la norme française NF P 94-100 sur la formulation F5, sous l'hypothèse d'un durcissement plus lent comparé aux autres formulations (voir Figure 4.2).

Concernant le temps de cure pour les essais d'aptitude, il a été choisi la cure maximale permise par la norme française NF P 94-100 pour des liants hydrauliques différents de la chaux. C'est-à-dire, qu'une cure normale (à

l'air) de 7 jours a été utilisée. Cette cure a permis d'obtenir des résistances à la traction indirecte supérieures à 0.2 MPa pour la formulation F5 (voir Figure 4.2).

La synthèse de l'ensemble des résultats est présenté en Table 4.5.

Stabilisation des sulfates :

Cette partie de l'étude s'est concentrée sur (i) l'évaluation de l'immobilisation des sulfates en accord avec la norme européenne NF EN 12457-2, et (ii) l'étude des propriétés géotechniques (gonflement et résistance mécanique) en effectuant des essais d'aptitude selon la norme française NF P 94-100.

- Résultats des essais de lixiviation

Lors des essais de lixiviation, il a été observé une réduction importante de la teneur en sulfates en solution pour toutes les formulations sauf pour F1 (sol sulfaté sans traitement). Dans ce cas, la formulation F1 a relargué en solution plus de 90% de la concentration initiale en sulfates. En revanche, une immobilisation de sulfates dans le solide de 98%, 92%, 90% et 92% a été mesurée pour les formulations F2, F3, F4 et F5, respectivement. Cela indique que tous ces traitements ont permis d'immobiliser des sulfates en solide, les teneurs en sulfates relargués étant inférieures à 1000 mg/kg de matière sèche (limite imposée par l'arrêté 12 décembre 2014 pour la catégorie de déchets inertes non-dangereux). D'autre part, les formulations F2 et F3 ont relargué des métaux lourds en solution, notamment du chrome (Cr), dépassant la limite du 0.5 mg/kg de matière sèche. Par contre, pour les formulations F4 et F5 (où le laitier de haut fourneau a été utilisé) la teneur en métaux lourds détectée en solution est restée inférieure à la limite imposée.

- Résultats des essais d'aptitude

Pour la formulation F1 (sol sulfaté sans traitement), un gonflement volumique égal à 7.1% $\pm$ 1.1% a été mesuré, valeur supérieure à celle de 5% recommandée par la norme française NF P 94-100. Par ailleurs, l'essai de traction indirecte n'a pas pu être réalisé sur cette formulation, la décohésion des échantillons rendant impossible sa réalisation. Pour la formulation F2, la traction indirecte obtenue est égale à 0.26 MPa $\pm$ 0.01 MPa, valeur dépassant la limite inférieure de 0.2 MPa. Cependant, la valeur limite de 5% sur le gonflement n'a pas été respectée et par conséquent ce traitement a été classifié comme « douteux » (voir Chapitre 2 - Table 2.11). Concernant la formulation F3, un gonflement de 4.2% $\pm$ 0.6% et une résistance à traction indirecte de 0.19 MPa $\pm$ 0.002 MPa ont été obtenus. Par conséquent, ce traitement est également considéré comme « douteux ». Enfin, les formulations F4 et F5 ont été classifiées comme « acceptables » car elles ont présenté des gonflements inferieurs à 2% et des résistances mécaniques supérieures à 0.2 MPa. Parmi ces deux formulations, la formulation F5 a été retenue pour approfondir la compréhension des mécanismes de stabilisation des sulfates à moyen et long termes. Le choix de cette formulation s'est basé sur une meilleure connaissance de la composition des matériaux utilisés, puisque le liant a été reproduit en laboratoire à partir de CEM I et de laitier, sans autre additif qui peut être trouvé dans les liants composés commerciaux.

Étude à long terme sur la formulation F5 :

Cette partie de l'étude s'est concentrée sur une évaluation approfondie de la formulation F5 afin de de vérifier la stabilisation de sulfates. Pour cela, des études minéralogiques, microstructurales et numériques ont été réalisées.

Vu que cette solution pourrait être employé en projet de génie civil (ex : construction routière), cette formulation a été aussi étudiée à travers l'évaluation des propriétés géotechniques de la formulation F5 à moyen et long termes en utilisant des essais de maniabilité, résistance à la compression, traction indirecte et de gonflement pour différentes conditions de cure.

- Immobilisation des sulfates à court et long termes

Des analyses en diffractométrie de rayons X (DRX) ont montré qu'une partie de sulfates ont précipité dans la matrice pour former de l'ettringite. La présence d'ettringite a été confirmée à 28 jours de cure par des observations au microscope électronique à balayage (MEB) couplé à de la spectroscopie de rayons X à dispersion d'énergie (EDS). Cependant, les observations n'ont pas révélé une morphologie de l'ettringite typique (voir Figure 4.6 et Figure 4.11). Il faut préciser que l'ettringite ici formée n'est pas de nature gonflante, les gonflements étant inferieurs à 2%. De plus, les résultats expérimentaux et numériques obtenus sont cohérents avec l'hypothèse d'un dégrée d'hydratation du laitier de 30%. Ce modèle géochimique a révélé que l'ettringite semblait être la phase contrôlant la solubilité des sulfates se trouvant dans la matrice (voir Figure 4.14).

Par ailleurs, il est important de s'assurer de l'immobilisation des sulfates à long terme. Pour cela, des essais de lixiviation à 6 mois ont été réalisés. Les résultats ont montré :

- Une diminution de la teneur en sulfates à faibles concentrations de liant (2% et 5%) par rapport aux résultats obtenus à 28 jours de cure.
- Après l'ajout de 7% de liant 90-10, la teneur en sulfates en solution est restée inférieure à 1000 mg/kg de matière sèche et constante tout au long de l'addition du liant (voir Figure 4.17).

- Propriétés géotechniques à moyen et long termes

Plusieurs propriétés géotechniques ont été évaluées sur la formulation F5, d'abord, le délai de maniabilité qui est lié au démarrage de la prise. D'après le guide technique GTR (Guide technique pour la réalisation des remblais et des couches de forme) [65], il peut varier entre 2 h et 24 h, voire 48 h après traitement. Ce délai est très important dans les traitements de sol car il fixe la durée possible des opérations de mise en œuvre. Pour la majorité des chantiers, une valeur entre 4 à 6 h est satisfaisante. Ainsi, le délai de maniabilité a été déterminé en utilisant le protocole décrit dans le Chapitre 2 – section 2.2.4.4. Un temps de maniabilité de 6 h a été obtenu, ce qui correspond à un délai satisfaisant.

Concernant les essais de gonflement volumique, pour toutes les conditions de cure considérées, il est resté inférieur à 1% (5% est la limite maximale recommandée par la norme française NF P 94-100).

En ce qui concerne les performances mécaniques à long terme, la classification mécanique du matériau a été déterminée en fonction de la résistance à la traction indirecte (Rit) et le module de Young (E) obtenus à 90 jours de cure. D'après le guide technique GTR, ce couple de valeurs doit conduire au minimum à une classe mécanique 5. Cette classification permet d'estimer l'épaisseur des couches de forme (plus la zone augmente, plus l'épaisseur de la couche de forme augmente). La formulation F5 a été traitée sur site et classifiée entre la zone 2 et 3 (classe mécanique entre 3 et 4) en accord avec la norme NF P 94-102-1 et le guide technique GTR (voir Figure 4.20). La classification obtenue du sol traité lors de cette étude est donc très convenable pour des applications géotechniques comme les couches de forme.

Introduction

This chapter presents the results obtained in the study of stabilization of sulfates by using hydraulic binders. This part of the research aimed to (i) compare the capacity of several alternative binders to immobilize sulfates in a sulfate-spiked soil in natural pH conditions, (ii) understand the sulfate immobilization mechanisms, and (iii) evaluate the swelling potential and the mechanical properties of sulfate-spiked soil treatments. The study of stabilization of sulfates was carried out following the approach presented in Figure 4.1.
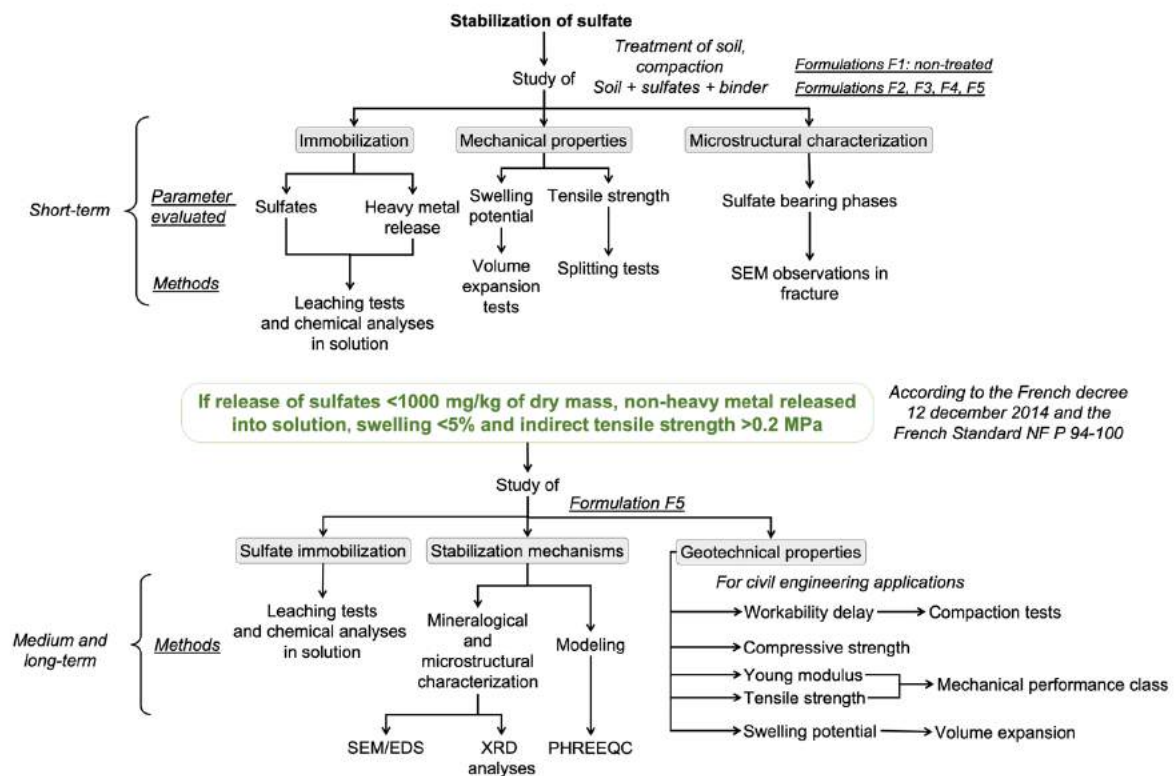
Figure 4.1 – Concept mapping of the approach followed in the study of stabilization of sulfates.

The first part of this chapter describes the formulations used in the treatment of the sulfate-spiked soil. Then, the results obtained from leaching tests and the evaluation of swelling and mechanical properties of all the treatments are presented. The third part of this chapter focuses on one specific treatment, which seemed to give the best results in terms of sulfate immobilization and swelling. A summary of results is presented in Table 4.5. Then, the discussion of all the results is presented and refers to previous research in this field. A few suggestions for further investigation are also addressed.

4.1 Sulfate-spiked soil treatments

4.1.1 Formulations

As a reminder, since a natural sulfate-rich soil was not available, it was chosen to artificially contaminate a soil from the Paris region with sulfates at 10000 mg/kg of dry mass (1 wt%, % by weight of dry soil) using 1.8 wt% gypsum. The chemical composition of this natural soil before sulfate contamination is presented in Chapter 2 - Table 2.4.

Five different formulations were studied to evaluate the immobilization of sulfates in soil as described in Chapter 2 – section 2.1.2. The chemical and mineralogical compositions of the binders used were presented in Chapter 2 – Table 2.4 and the description of the formulations were presented in Chapter 2 - Table 2.5.

The justification for the selection of these formulations and binders is presented as follow:

- **Formulation F1:** sulfate-spiked soil without binder was used as the reference or control formulation (F1).

- **Formulation F2:** sulfate-spiked soil treated with Portland cement (referred to as CEM I). CEM I was chosen to verify a large immobilization of sulfates due to the expected reaction between the aluminate phases (C_3A) and the gypsum contained in the soil to form ettringite, which was expected to produce expansion in the treated soil.

- **Formulation F3:** treatment with a sulfoaluminate clinker (referred to as Clinker Y). It was expected that this binder would also consume a large amount of sulfates because its main hydration product is ettringite, which is formed until sulfates are consumed and, then, monosulfoaluminate is precipitated [55], [191].

- **Formulation F4:** treatment with a blast furnace slag cement (referred to as CEM III/C). This binder was chosen to verify the effect of the proportion of slag and Portland clinker on the immobilization of sulfates and the reduction of swelling potential.

- **Formulation F5:** the mixture 90% ground granulated blast furnace slag (GGBS) and 10% Ordinary Portland cement (OPC) was used. Similar to F4, this binder was chosen to verify the effect of the proportion of slag on the immobilization of sulfates and the decrease in swelling potential.

4.1.2 Binder dosage and curing of the treatments

The sulfate-spiked soil treated with the mixture of 90% GGBS and 10% OPC (formulation F5) was selected as the reference material for selection of dosage binder and curing time of all the formulation because of its large amount of GGBS, leading to a delayed hydration process compared with the other binders. This formulation was evaluated at two different binder dosages: 5 wt% and 10 wt%, and at two different curing times: 4 h and 7 days for minimum and maximum curing times, in accordance with the French Standard NF P 94-100. In order to assess the treatments with both dosages (5 and 10 wt%; % by weight of dry soil), splitting tests were carried out in compacted soil as described in Chapter 2 – section 2.2.4 and results are presented in Figure 4.2.

Figure 4.2(a) shows the indirect tensile strength values in MPa as a function of the binder dosage level at 4 h and 7 days of curing. The red dotted line represents the minimum limit of 0.2 MPa set by the French Standard NF P 94-100. As observed in Figure 4.2(a), 4-h curing appeared to be insufficient to meet the requirements for splitting tests because of mechanical strength was not sufficient to perform the tests whatever the percentage of binder used in the treatment. In contrast, it was possible to measure indirect tensile strength values for both dosages at 7 days of curing but only the soil mixed with 10 wt% of binder reached the upper limit of 0.2 MPa (the value was 0.1 MPa for the soil treated at 5 wt% of binder).

Furthermore, Figure 4.2(b) shows the volume expansion given in percentage as a function of binder dosage and curing time. The red dotted line represents the upper limit of 5% set by the French Standard NF P 94-100. Volume expansion results indicated that treatment at 5% of binder level and cured for 4 h expanded more than 5%. In contrast, curing of samples for 7 days showed that swelling remained inferior to the upper limit of 5% (2.9% and 1.4% for 5 and 10 wt% of binder, respectively). The same was true for sample with 10 wt% of binder cured for 4 h (volume expansion of 3.2%).

According to these results, the binder dosage level of 10 wt% was selected to ensure sufficient mechanical properties for all of the treatments. On the other hand, a curing of 7 days was chosen for both volume expansion and splitting tests. It should be noted that leaching tests were carried out after a minimum of 28 days curing.
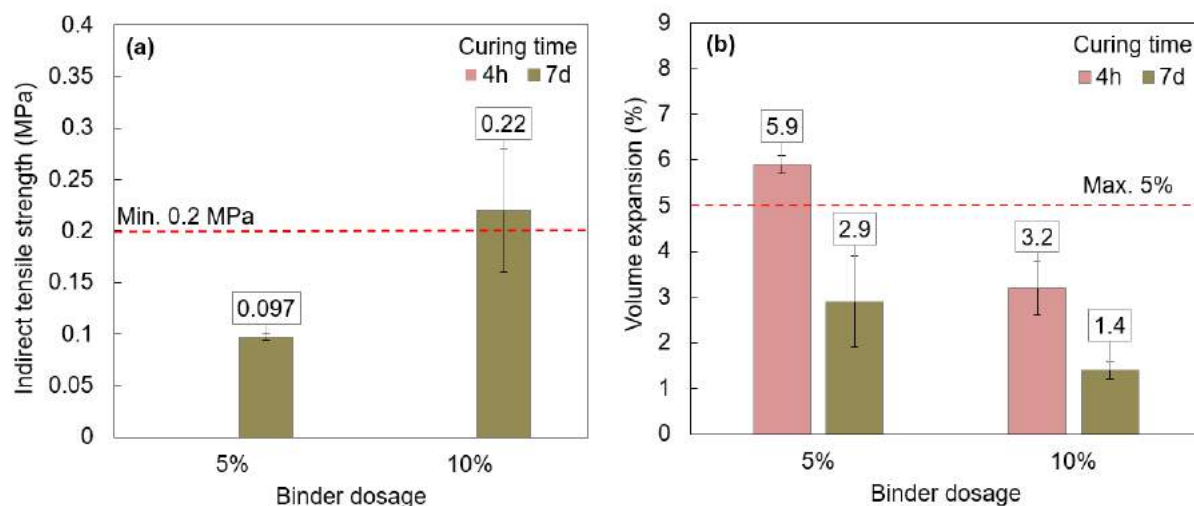
Figure 4.2 – Swelling and splitting tests for selection of binder dosage (soil treated with 5 or 10 wt% binder) and curing time (4 h or 7 days) for the treatment of sulfate-spiked soil. The red dotted lines represent the guideline established by French Standard NF P 94-100. Treatment was made with formulation F5. **(a)** Indirect tensile strength is expressed in MPa, and **(b)** volume expansion is given in percentage.

4.2 Stabilization of sulfates results

4.2.1 Leaching tests

Leachable sulfate and heavy metal concentrations, conductivity, and pH of eluates extracted from leaching tests for each of the formulations are presented in Table 4.1. Concentrations exceeding the thresholds are in red bold. Leachate concentrations are expressed in mg/kg of dry mass of solid (solid= mass of soil+binder). Results were compared to the "inert and non-hazardous waste" thresholds established by the French Ministerial Decree of 12 December 2014 [88] in order to verify that no significant heavy metal concentrations were released into solution after binder treatment.

Leachate concentrations of all formulations are schematically represented in radials and Figure 4.3 shows how to read this type of diagrams. Figure 4.4 presents all the leachate concentrations, in which the axes represent the concentrations measured for each element normalized by their thresholds, which are established by the French Decree and represented by the red dotted line. Outside this line, thresholds are not respected.

Table 4.1 - pH, conductivity values and leachable sulfate, chloride, fluoride and heavy metal concentrations of all formulations. Leachate concentrations are expressed in mg/kg of dry mass of soil. Red bold values indicate that the concentrations exceeded the thresholds established by French Decree [88].

Chemical species	Units	Inert and non-hazardous waste Threshold	F1	F2	F3	F4	F5
pH	-	-	7.5	12.4	11.7	11.3	11.4
Conductivity	μS/cm	-	1662	3425	747	653	1050
Sulfates (SO$_4^{2-}$)	mg/kg	1000	**9174**	138	759	986	785
Arsenic (As)	mg/kg	0.5	<0.2	<0.2	<0.2	<0.2	<0.2
Barium (Ba)	mg/kg	20	0.5	0.6	0.2	0.2	0.3
Cadmium (Cd)	mg/kg	0.04	<0.002	<0.002	<0.002	<0.002	<0.002
Chromium (Cr)	mg/kg	0.5	<0.1	**0.8**	**2.3**	<0.1	<0.1
Copper (Cu)	mg/kg	2	<0.2	0.4	<0.2	<0.2	<0.2
Mercury (Hg)	mg/kg	0.01	<0.001	<0.001	<0.001	<0.001	<0.001
Molybdenum (Mo)	mg/kg	0.5	0.1	0.1	0.3	<0.01	0.2
Nickel (Ni)	mg/kg	0.4	<0.1	0.3	<0.1	<0.1	0.1
Lead (Pb)	mg/kg	0.5	<0.1	<0.1	<0.1	<0.1	<0.1
Antimony (Sb)	mg/kg	0.06	<0.002	<0.002	<0.002	<0.002	<0.002
Selenium (Se)	mg/kg	0.1	<0.01	<0.01	<0.01	<0.01	<0.01
Zinc (Zn)	mg/kg	4	<0.2	<0.2	<0.2	<0.2	<0.2
Chlorides (Cl-)	mg/kg	800	18.6	3.7	50.4	156.7	27.1
Fluorides (F-)	mg/kg	10	3.3	6.9	2.0	2.2	2.1
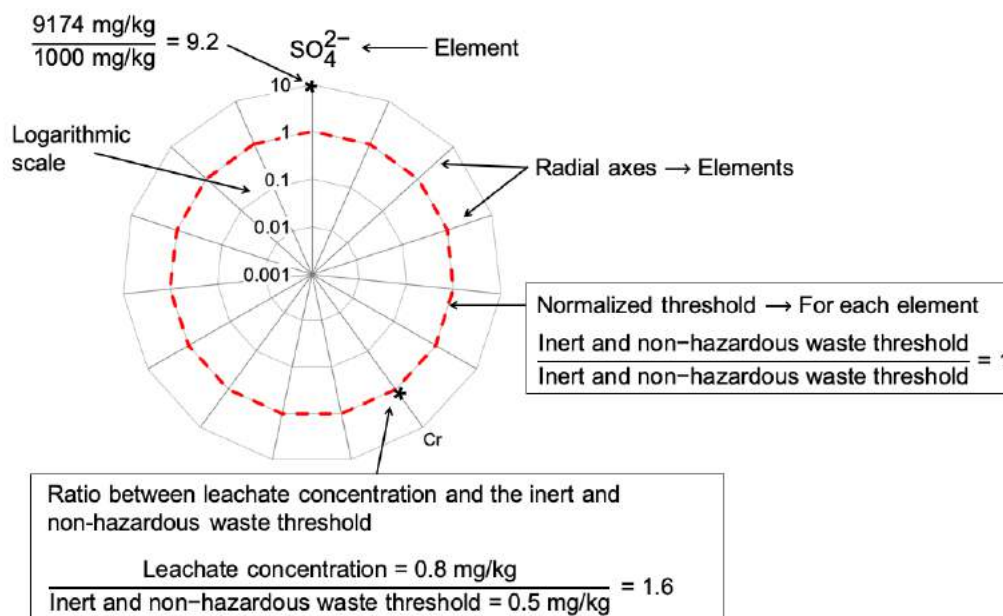
Figure 4.3 – Diagram showing how to read the radials presented in this study. Leachate concentration given in mg/kg of dry mass of soil.
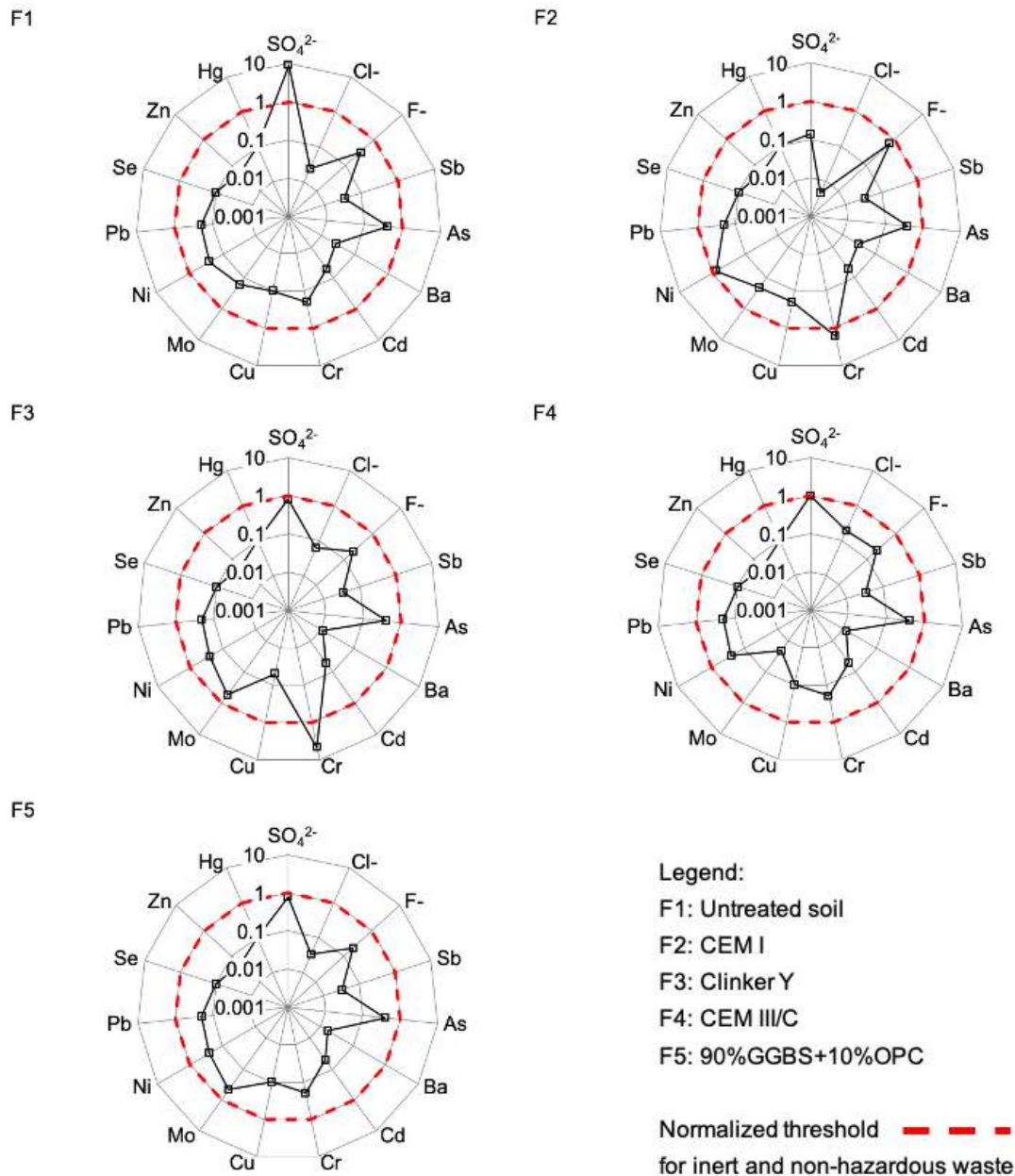
Figure 4.4 - Ratio between leachate concentrations of each formulation and the "inert and non-hazardous waste" limit for each element normalized by their thresholds (red dotted line). A logarithmic scale is used.

As a reminder, soil was artificially contaminated with sulfates at 10000 mg/kg of dry mass of soil (1 wt%). When leaching tests were carried out in the untreated sulfate-spiked soil (formulation F1), it was found that the leachable sulfate concentration was approximately 10 times higher than the guideline value for "inert and non-hazardous waste" (1000 mg/kg of dry mass of soil) established by the French Decree [88]. As shown in Table 4.1 and Figure 4.4, for the untreated soil (F1), the leachable sulfate concentration was about 9174 mg/kg of dry

mass of soil ± 16% and the content of heavy metals was much lower than the guideline values. In contrast, treatment of the sulfate-spiked soil with CEM I binder (formulation F2) showed a noteworthy decrease in leachable sulfate concentration. In this case, the sulfate concentration released into solution was about 138 mg/kg of dry mass of soil ± 9%, which was below the guideline value. Similarly, treatment of sulfate-spiked soil with the sulfoaluminate binder "Clinker Y" (formulation F3) significantly decreased the leachable sulfate concentration. In this treatment, a sulfate concentration of 759 mg/kg of dry mass of soil ± 12% was detected in solution. However, in both formulations F2 and F3, chromium (Cr) was also detected in solution at higher concentrations than the limit for "inert and non-hazardous waste" (0.5 mg/kg of dry mass of soil). Therefore, the use of these two binders in the treatment of the sulfate-spiked soil represents a disadvantage due to the high concentration of Cr released in solution. More details will be addressed in the discussion section.

On the other hand, sulfate-spiked soil treated with GGBS-binders (formulations F4 and F5), showed the decrease in leachable sulfate concentration and leachable heavy metal concentrations were well within the established limits. For the formulation F4 (CEM III/C), the sulfate concentration released into solution was 986 mg/kg of dry mass of soil ± 21% and for formulation F5 (90%GGBS+10%OPC), the leachable sulfate concentration was 785 mg/kg of dry mass of soil ± 8%.

For all formulations, leachable chlorides (Cl$^-$) and fluorides (F$^-$) concentrations were below the "inert and non-hazardous waste" thresholds established by the French Decree, with less than 800 mg/kg of dry mass of soil for Cl$^-$ and less than 10 mg/kg of dry mass of soil for F$^-$.

4.2.2 Swelling and mechanical properties

Figure 4.5 shows the mechanical and swelling results for all the formulations and obtained from compacted soil. The indirect tensile strength values and the volume expansion results for each formulation are presented in Figure 4.5(a) and Figure 4.5(b), respectively. The red dotted lines represent the minimum limit of 0.2 MPa for indirect tensile strength obtained by splitting tests and the upper limit of 5% for volume expansion set by the French Standard NF P 94-100. For formulation F1 (untreated soil), splitting tests were not performed because of insufficient mechanical strength. Therefore, an indirect tensile strength of 0 MPa is indicated in Figure 4.5(a).
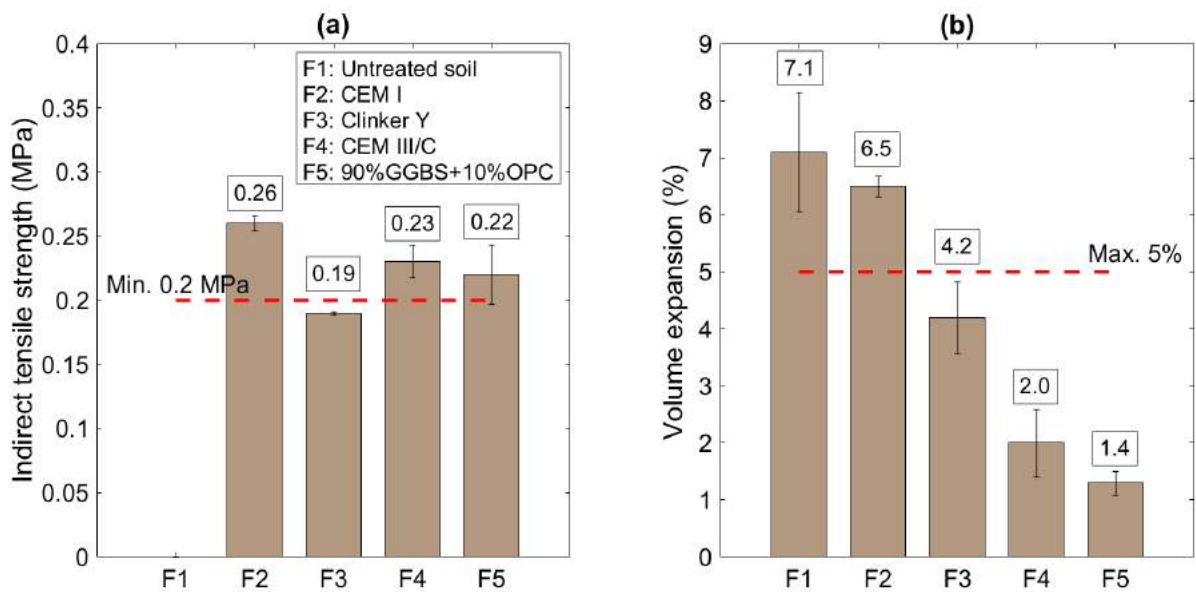
Figure 4.5 – Evaluation of mechanical properties and swelling for all formulations. The red dotted lines represent the guideline established by the French Standard NF P 94-100. **(a)** Indirect tensile strength is expressed in MPa, **(b)** volume expansion values are expressed in percentage.

From Figure 4.5, it can be observed that formulation F1 (untreated soil) had a volume expansion of 7.1% ± 1.1%, which is greater than the maximum guideline value of 5%. The soil expansion was probably due to the presence of swelling clays. On the other hand, soil treatment with CEM I (formulation F2) presented an indirect tensile strength of 0.26 MPa ± 0.01 MPa, which is higher than the minimum guideline value of 0.20 MPa. However, the volume expansion value was higher than 5% (6.5% ± 0.2%), classifying this treatment as "doubtful" (cf. Chapter 2 – Table 2.9). Treatment of the sulfate-spiked soil with the "Clinker Y" binder (formulation F3) was also classified as "doubtful" because the indirect tensile strength reached approximately 0.19 MPa ± 0.002 MPa, which was lower than the accepted guideline value (0.2 MPa). In addition, the volume expansion was close to the limit of 5% (4.2% ± 0.6%).

Treatment of the sulfate-spiked soil with binders containing high levels of GGBS, such as CEM III/C and "90%GGBS+10%OPC" (formulations F4 and F5, respectively) resulted in a significant decrease in the swelling and maintained an indirect tensile strength above 0.20 MPa. For formulations F4 and F5, the volume expansion reached 2.0% ± 0.6% and 1.4% ± 0.2%, respectively; and the indirect tensile strengths were about 0.23 MPa ± 0.03 MPa and 0.22 MPa ± 0.06 MPa, respectively. As such, both treatments F4 and F5 were classified as "suitable".

4.2.3 Mineralogical and microstructural characterization

SEM observations were carried out on fracture sections of all the formulations and the images obtained are presented in Figure 4.6.
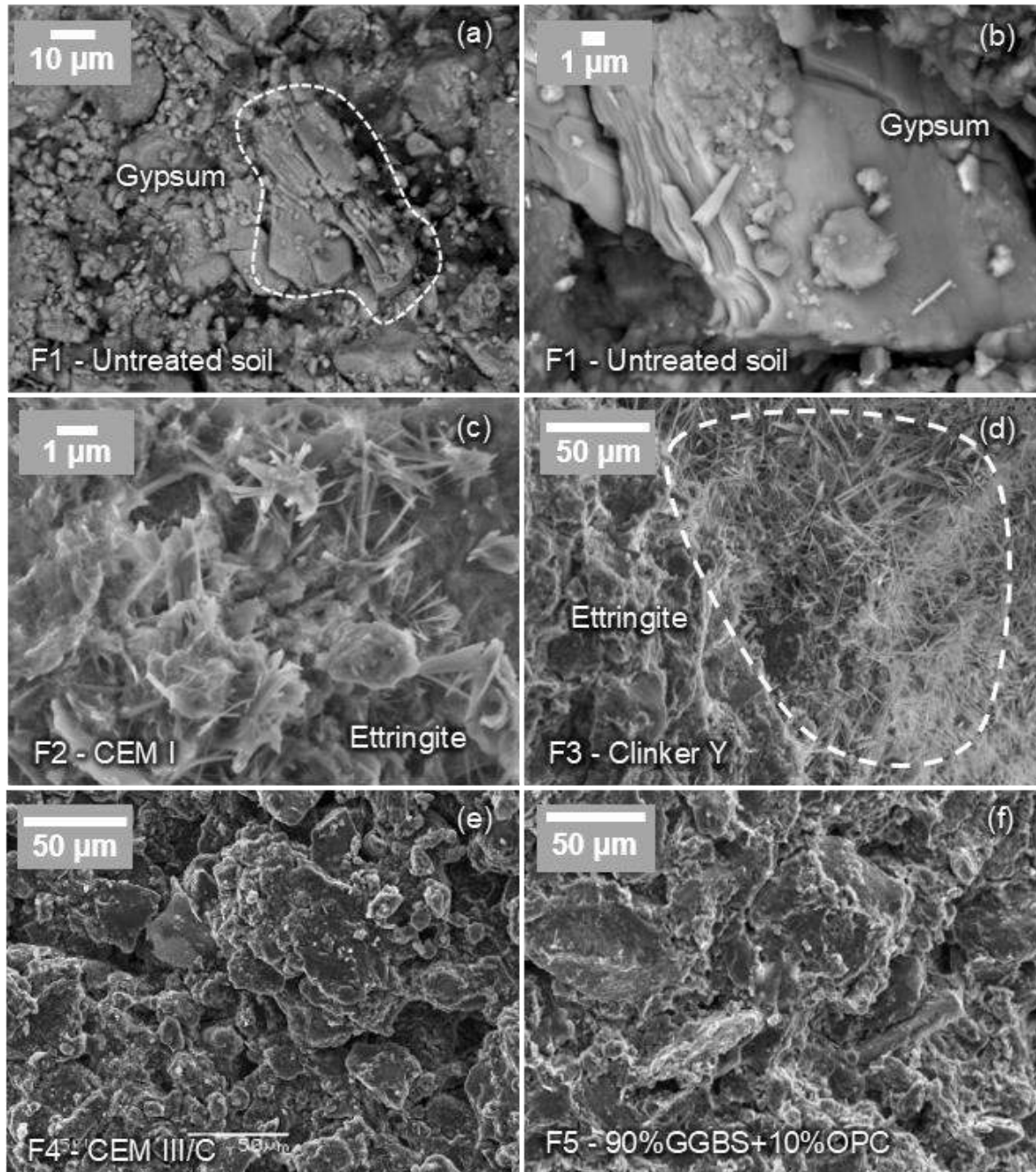
Figure 4.6 – SEM images obtained from untreated and treated soils. **(a), (b)** Formulation F1 (untreated soil) showing sulfate in the form of gypsum, **(c)** Formulation F2 (CEM I) showing ettringite crystals, **(d)** Formulation F3 (Clinker Y) showing ettringite precipitates, **(e)** Formulation F4 (CEM III/C) showing agglomeration of phases and, **(f)** Formulation F5 (90%GGBS+10%OPC) showing agglomeration of phases without typical morphology of sulfate-bearing crystal. Dotted lines highlight the areas of interest.

SEM images of formulation F1 (untreated soil) are presented in Figure 4.6(a) and Figure 4.6(b). As shown, gypsum was the sulfate specie observed and its chemical composition (CaO to SO_3 molar ratio of 1) was verified by EDS punctual analyses.

SEM images of fracture surfaces of formulations F2 and F3 are shown in Figure 4.6(c) and Figure 4.6(d), respectively. In both formulations, ettringite crystals were easily identified. For soil treated with CEM I binder (F2), ettringite was observed at higher magnifications than for soil treated with "Clinker Y" binder (F3). Conversely, for formulations containing high GGBS levels (F4 and F5), no expansive phases were observed on the fracture surfaces. As presented in Figure 4.6(e) and Figure 4.6(f), the SEM images of F4 and F5 formulations showed a microstructure consisting of an agglomeration of phases, without the typical morphology of sulfate-bearing minerals such as ettringite or gypsum.

Additional analyses:

As follow, we present some additional SEM/EDS analyses carried out in formulations F1 (untreated soil), F2 (treatment with CEM I) and F3 (treatment with Clinker Y).

Regarding the formulations F4 (treatment with CEM III) and F5 (treatment with 90%GGBS+10%OPC), both formulations have similar composition (>80% of GGBS and <15% of OPC). However, we chose to further investigate formulation F5 because it gave better results than F4 in terms of sulfate stabilization and because their chemical composition was better known. These additional analyses consisted of mineralogical and microstructural analyses and modeling. Moreover, sulfate stabilization in formulation F5 was also studied in the long term in order to verify the capacity of this formulation to stabilize sulfates after 6 months of curing.

On the other hand, as the treatment of soil for reuse is an important issue. It was also chosen to verify the geotechnical properties of formulation F5. Therefore, several mechanical tests were carried out in the medium and long-term.

All the results obtained from formulation F5 (90% GGBS+10% OPC) are presented in section 4.3).

Additional SEM/EDS analyses performed in F1, F2 and F3

Formulation F1 – untreated soil

Figure 4.7 presents SEM/EDS analyses obtained from untreated soil (formulation F1).
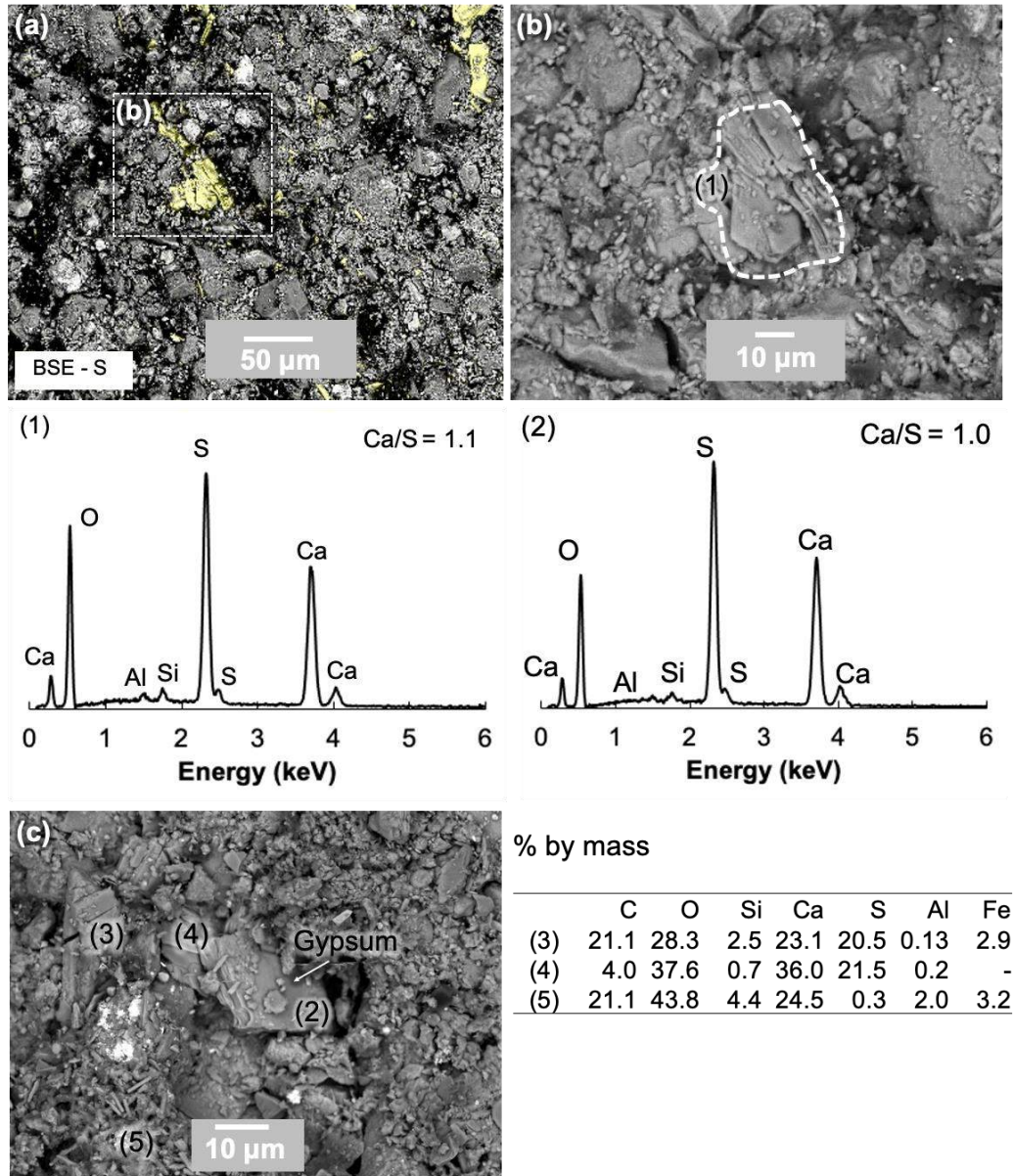
Figure 4.7 – SEM images obtained from formulation F1 (untreated soil). **(a)** BSE image and EDS mapping showing the presence of S (in yellow), **(b)** BSE image showing the presence of gypsum and its EDS spectrum (spectrum (1)), **(c)** BSE image showing the presence of gypsum and its EDS spectrum (spectrum (2)), and the composition of other phases present in the soil (points (3), (4) and (5)).

Figure 4.7(a) shows one EDS mapping analysis, which provided information about the distribution of sulfates in this sample, and Figure 4.7(b) shows a magnification from image (a).

173

In this case, spectrum (1) confirmed the presence of gypsum, which showed to have flattened and slim crystals. Moreover, Figure 4.7(c) presents another BSE image from formulation F1, where gypsum was also detected and identified in the spectrum (2). Points (3), (4) and (5) show the composition of other phases present in the soil.

Formulation F2 – CEM I-treated soil

Figure 4.9 presents the SEM images obtained from formulation F2. Figure 4.9(a) and Figure 4.9(b) present the distribution of sulfates in the sample, and Figure 4.9(c) shows the EDS punctual analyses plotted in a chart where x-axis and y-axis plot the Al/Ca and S/Ca atomic ratios, respectively. Stoichiometric composition of ettringite (AFt) and calcium monosulfoaluminate (Ms) are located on the plot. The two slopes allow the identification of either AFt or Ms formation when the products are mixed with other phases without Al and S. Figure 4.8 presents a schema explaining how to read this type of plot.
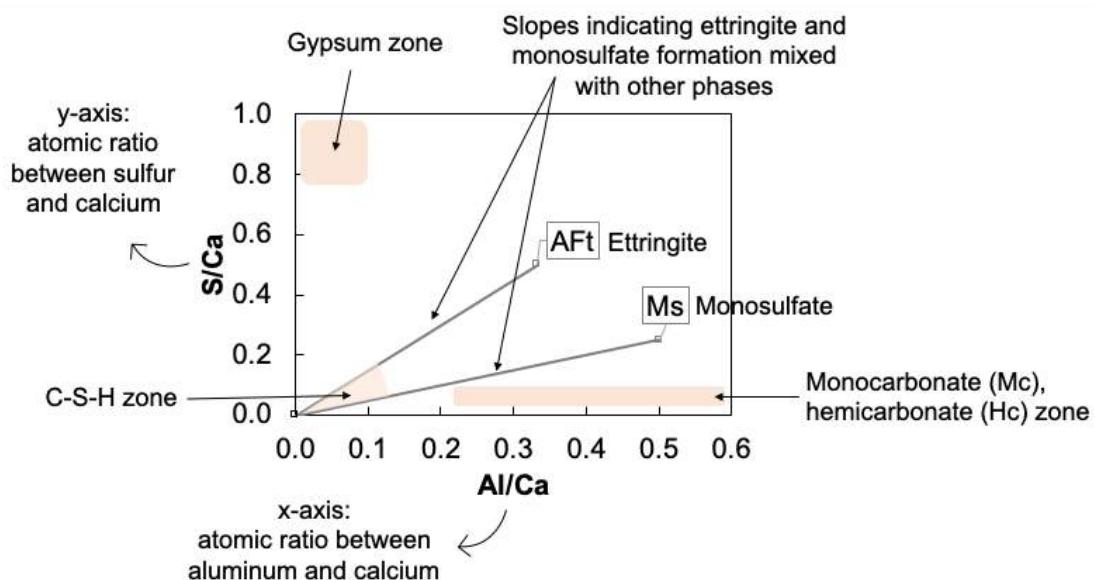
Figure 4.8 – How to read the Al/Ca vs. S/Ca EDS chart. Monosulfate = monosulfoaluminate.

In Figure 4.9(c), punctual analyses showed a few points on the AFt and Ms slopes. Furthermore, Figure 4.9(d) and Figure 4.9(e) shows the presence of ettringite (AFt) and showed that AFt crystals were of about 2-3 µm long. The composition of ettringite is presented in the spectrum in Figure 4.9(f).
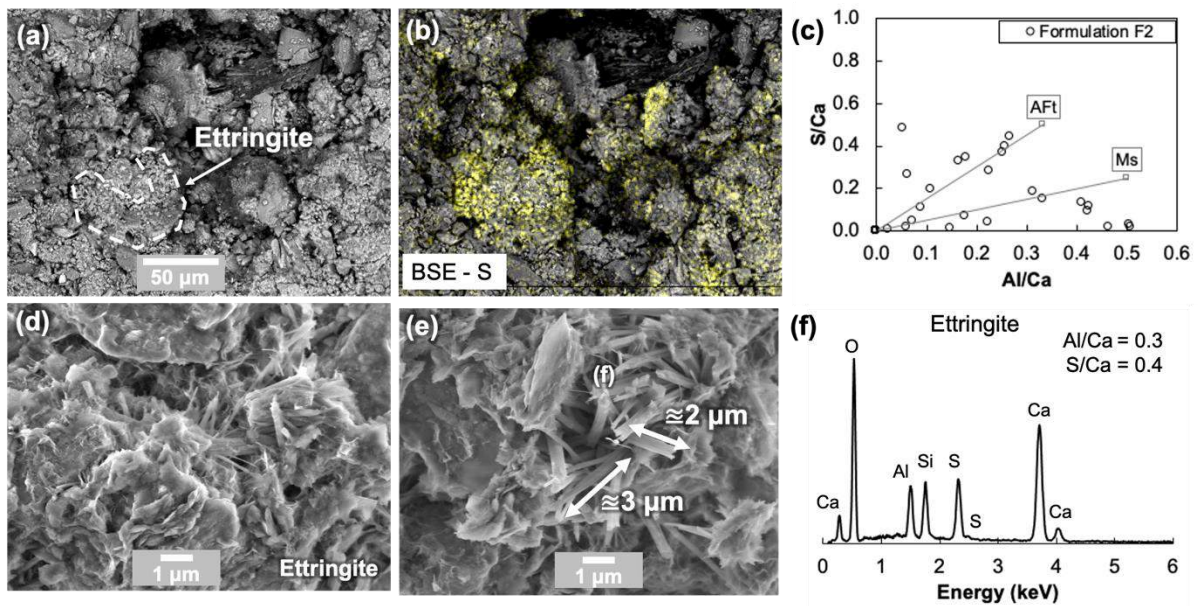
Figure 4.9 – SEM/EDS analyses obtained from formulation F2 (sulfate-spiked soil treated with CEM I). **(a)** BSE image showing the presence of ettringite, **(b)** BSE image and EDS mapping showing the presence of S (in yellow), **(c)** EDS plots of Al/Ca versus S/Ca atomic ratios (AFt: ettringite, Ms: calcium monosufoaluminate), **(d)** and **(e)** SE images showing the size and morphology of ettringite and **(f)** EDS spectrum showing average composition of point f from the image *e*.

Formulation F3 – Clinker Y-treated soil

On the other hand, Figure 4.10 presents SEM images from formulation F3. Figure 4.10(a) presents one BSE image where small cracks were observed. EDS punctual analyses were carried out and are presented in Figure 4.10(b) where the presence of ettringite was confirmed because of the population of points on the AFt slope. Figure 4.10(c) to Figure 4.10(e) show the presence of ettringite in all the analyzed sample. Observations showed that AFt crystals were of about 10-100 µm long and its composition is presented in spectrum (1).
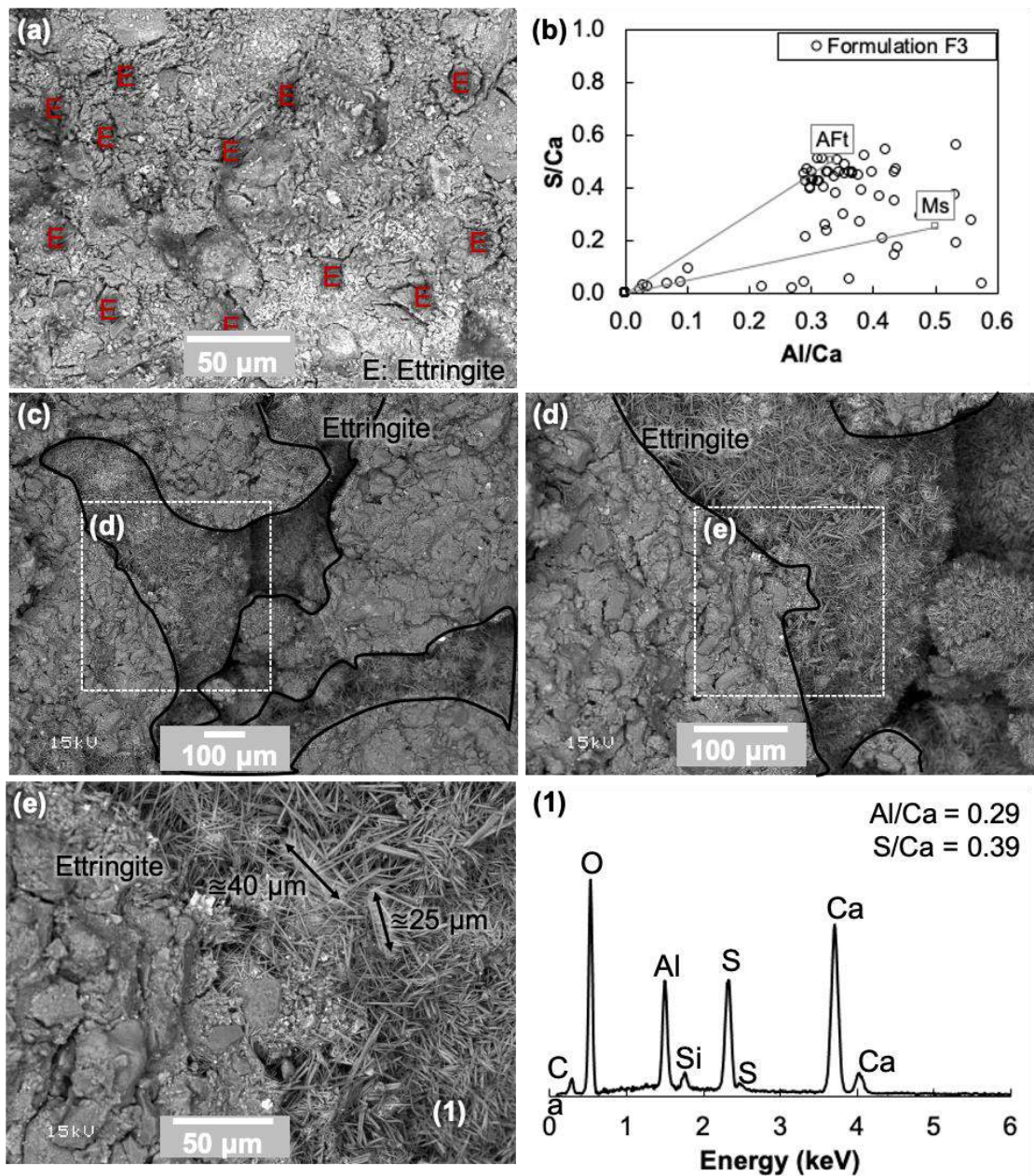
Figure 4.10 – SEM/EDS analyses obtained from formulation F3 (sulfate-spiked soil treated with Clinker Y). **(a)** BSE images showing the presence of small cracks that indicate ettringite formation, **(b)** EDS plot of Al/Ca versus S/Ca atomic ratios (AFt: ettringite, Ms: calcium monosufoaluminate) from image a, **(c)** BSE images showing a large presence of ettringite, **(d)** magnification of image c, **(e)** magnification of image d showing the size and morphology of ettringite and EDS spectrum showing the average composition of the observed ettringite.

176

4.3 Focus on Formulation F5 (treatment with 90%GGBS+10%OPC)

Particular attention was paid to the experimental binder composed of 90% GGBS and 10% OPC (formulation F5) due to its capacity to immobilize sulfates (sulfate retention 92%) without releasing heavy metals into solution. Additionally, this treatment did not show significant volume expansions, as was seen in Figure 4.5. In order to better understand the sulfate stabilization mechanisms in this formulation, it was decided to extend the microstructural analyses and to compare experimental data with numerical calculations.

4.3.1 Microstructural characterization

As explained previously, the identification of mineral phases containing sulfates was difficult and no typical morphology of sulfate-bearing crystals such as ettringite and gypsum was observed on the fracture surfaces of formulation F5 (cf. Figure 4.6(f)). Therefore, SEM observations coupled with EDS mapping and EDS punctual analyses were carried out on polished sections of this formulation. Results are shown in Figure 4.11 and Figure 4.12.

Figure 4.11(a) shows one BSE image obtained from formulation F5, where the anhydrous slag is highlighted by black lines. Furthermore, red dotted lines contoured the area where ettringite was detected and the EDS punctual analyses performed in these zones are presented in Figure 4.11(b). EDS mapping analyses, presented in Figure 4.11(c), provided information about the distribution of sulfates in this sample. They revealed that sulfates were always associated with calcium. The distribution of sulfates in this sample allowed the identification of ettringite. Figure 4.12(a) shows another BSE image obtained from formulation F5, the anhydrous slag grains being also highlighted by black lines. Figure 4.12(b) is a magnification of image (a) and the red dotted lines contoured the area where EDS punctual analyses, presented in Figure 4.12(c), were taken. These points correspond to the zones having high concentrations of sulfates presented in Figure 4.12(d).
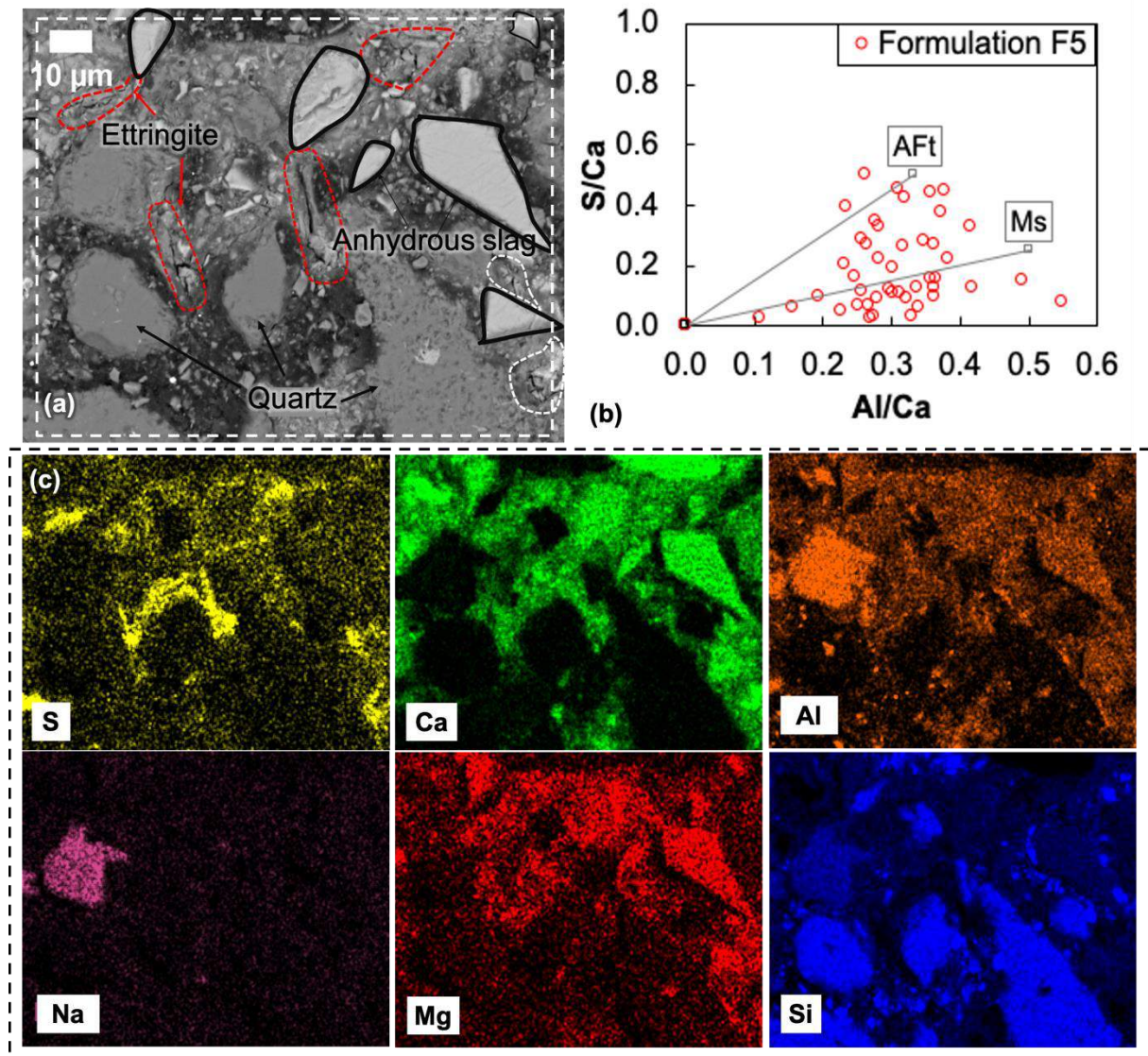
Figure 4.11 – BSE images of polished section of formulation F5 at 28 days of curing. **(a)** indicates the zones where ettringite phase was found (dotted red lines) and highlighted the anhydrous slag contoured by black lines. **(b)** EDS plot of Al/Ca versus S/Ca atomic ratios (AFt: ettringite, Ms: calcium monosufoaluminate) from image (a). **(c)** EDS mapping showing the zonation of sulfur (S), calcium (Ca), aluminum (Al), sodium (Na), magnesium (Mg) and silicon (Si) elements of image (a).
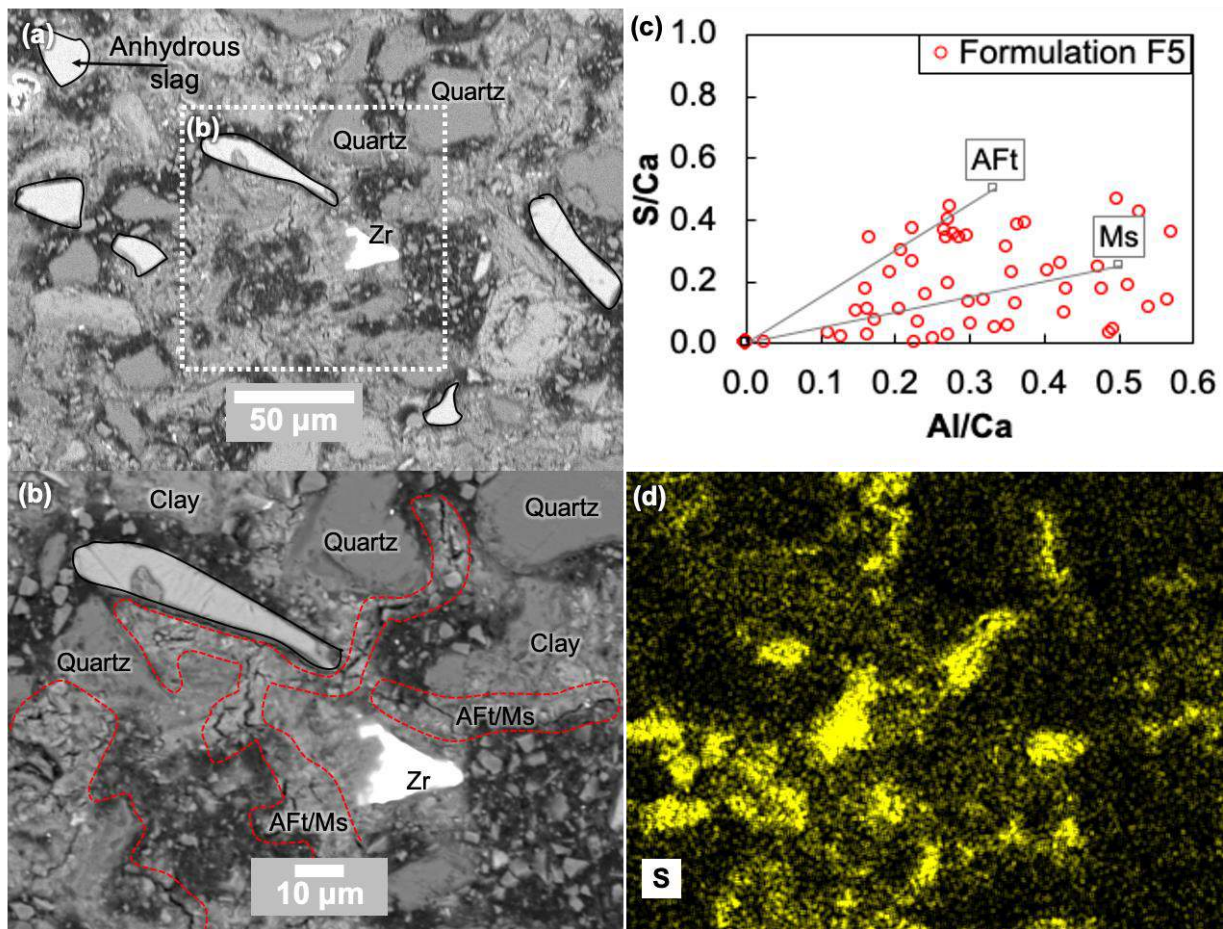
Figure 4.12 – **(a)** BSE image of polished section of formulation F5 at 28 days of curing. **(b)** magnification of image (a) indicating with a dotted red line the zones where ettringite phase was found. **(c)** EDS plot of Al/Ca versus S/Ca atomic ratios (AFt: ettringite, Ms: calcium monosufoaluminate). **(d)** EDS mapping showing the zonation of sulfur (S).

SEM/EDS analyses were completed by carrying out XRD analyses in the soil before (F1) and after treatment (F5). XRD patterns are presented in Figure 4.13 in the range from 2θ 5° and 70°. The red pattern represents the untreated soil (F1) and revealed a large peak between 2θ 11° and 12°, which is characteristic of the presence of gypsum. The black pattern represents the formulation F5 and showed a decrease in the intensity of gypsum peaks and revealed the appearance of new peaks between 2θ 9° and 10° and 15° and 16°, which are characteristic of ettringite. Therefore, ettringite seemed to be the phase controlling the solubility of sulfates.

However, residual gypsum in formulation F5 revealed that gypsum was not completely dissolved by the (probably insufficient amount of) water provided to the system during the fabrication of the samples. The water to solid (w/s) ratios were presented in Chapter 2 – Table 2.6.
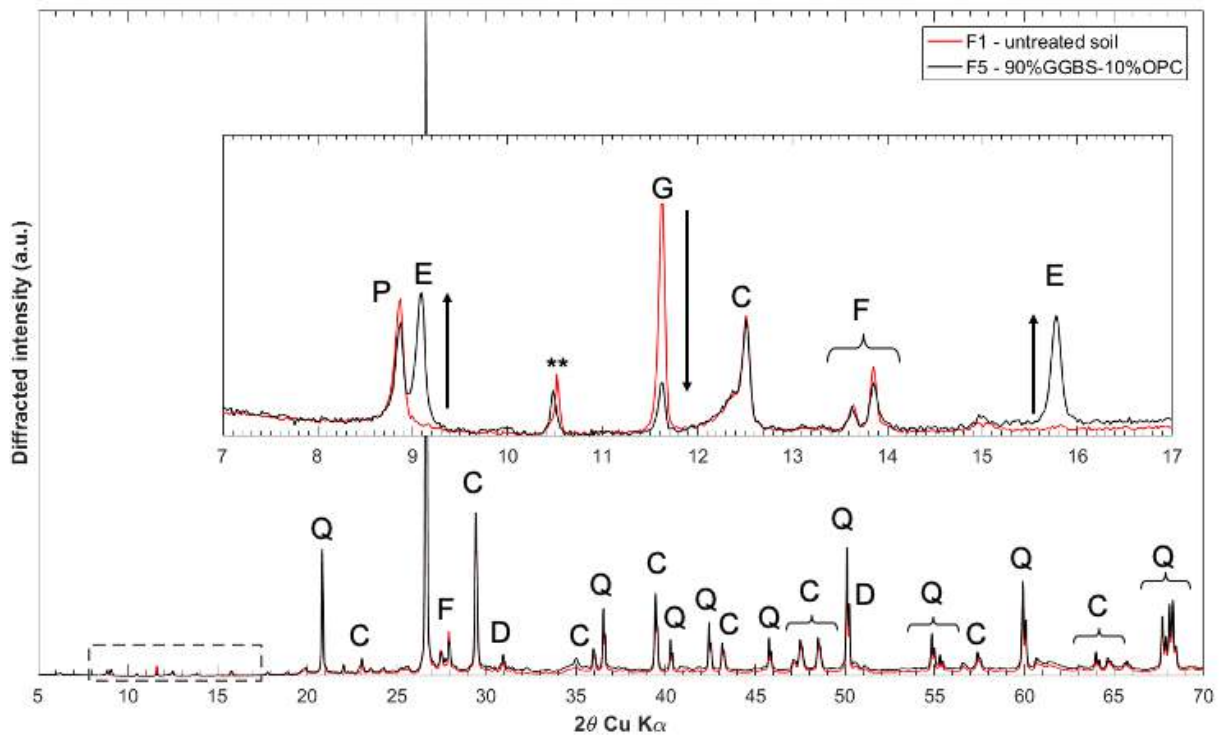
Figure 4.13 – XRD patterns of untreated - formulation F1 (red line) and treated soil - formulation F5 (black line) from 2θ 5° and 70°. Magnification in the selected range from 2θ 7° and 17° showing the decrease in intensity of the gypsum peak (G) and the appearance of ettringite peaks (E) in formulation F5. **C:** Chlorite; **P:** Phyllosilicates; **F:** Feldspars; ****:** mineral coming from the original soil.

4.3.2 Modeling

Numerical modeling was performed for formulation F5 in order to better understand sulfate stabilization mechanisms. The influence of the proportion of GGBS+OPC binder on sulfate immobilization in the sulfate-spiked soil was evaluated by varying the dosage of the binder from 0% to 20% (in percentage by dry mass of soil) as presented in Table 4.2. Assuming congruent dissolution in the model, this experimental binder was defined by its elemental chemical composition expressed in moles (cf. Chapter 2 – Table 2.4). The results of batch-reaction calculations were compared to leachable sulfate and leachable major element concentrations obtained experimentally and determined after leaching tests at 28 days of curing.

The kinetics of chemical reactions were not taken into consideration in this model, which represents only the state of equilibrium reached by the system. For some minerals defining the soil constituents in the model, such as quartz and iron(III) oxide (magnetite), the dissolution

was not permitted due to their very slow kinetics of dissolution at 20 °C in alkaline conditions [192]–[194].

Table 4.2 – Proportion of binder added to the soil to verify the sulfate stabilization mechanisms in formulation F5 (90% GGBS+10%OPC). For all the formulations, 1 wt% sulfates were added to the soil. Percentages are expressed by dry mass of soil.

Binder (wt%)	20	15	12	10	8	7	5	2

GGBS hydration degree:

Since few thermodynamic data exist for GGBS binder, several calculations were made by assuming its hydration at four different degrees: 10, 20, 30 and 40%. As reported in the literature, the hydration of GGBS and OPC mixes is more complex than that of Portland cement. GGBS reacts more slowly with water and not all the GGBS binders react in the same way [60]. It is largely recognized that the rate of hardening of GGBS binders is slower than that of Portland cement during the first 28 days of curing [60]. Lothenbach et al. (2012) [169] showed that, over one month, approximately 70% of the slag had reacted in a system containing about 60% slag and a water to binder (w/b) ratio of 1.1. Taylor et al. [170] reported that, over two years, approximately 68% of the slag had reacted in a Portland-slag system containing about 50% slag and an w/b ratio of 0.4. It seems that higher hydration degrees are estimated in systems containing large amounts of available water. They showed that the degree of slag hydration in a slag-blended system also depended on the proportion of slag provided. This means that, over the same time period, a system containing high proportions of slag presents lower rates of slag reaction compared with systems containing lower slag amounts. Taylor et al. [170] estimated that, over two years of reaction, only 36% of slag had reacted in a formulation containing 90% GGBS and 10% OPC.

Therefore, in the current investigation, it is important to consider the hydration degree of the GGBS as a significant factor influencing the immobilization of sulfates in formulation F5.

Experimental vs numerical data:

Experimental and numerical data of pH values, sulfate, calcium, aluminum, silicon and magnesium concentrations in solution are plotted in Figure 4.14, where element concentrations are given in mg/L and plotted as a function of the binder dosage (ranging from 0 to 20 wt%, % by dry mass of soil). Experimental data are represented by black circles while model calculations are given by red lines. Numerical data are given for 10, 20, 30 and 40% GGBS hydration levels. Solution concentrations are also completed by the quantities of solid phases involved in the modeled reactions assuming a GGBS hydration level of 30% and are

presented in Figure 4.15. These quantities are divided into two groups here for ease of reading: silicon dominant phases (M-S-H, C-S-H and illite) are shown in Figure 4.15(a) and aluminous dominant phases (ettringite, hydrogarnet and gibbsite) in Figure 4.15(b).
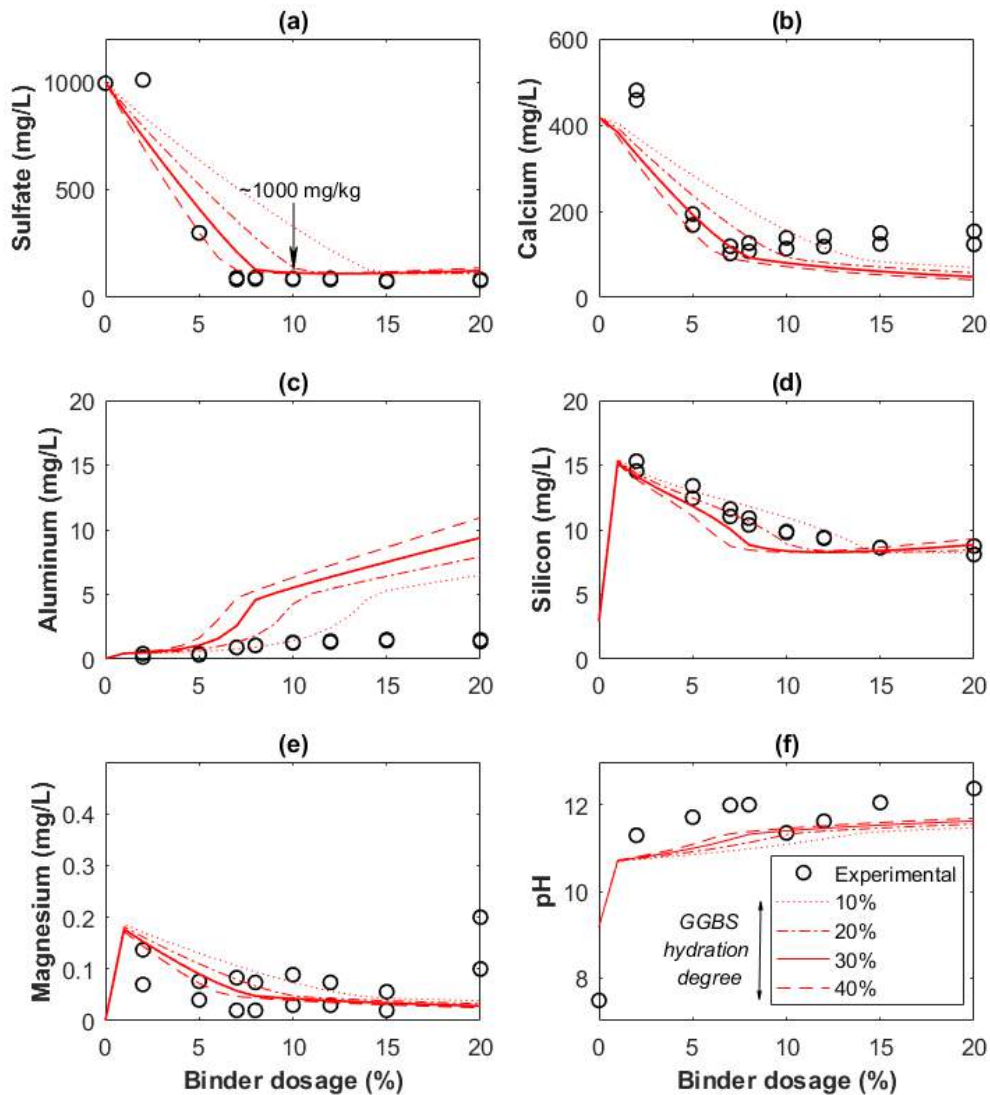
Figure 4.14 – Comparison between numerical and experimental data obtained from formulation F5 (90%GGBS+10%OPC). Element concentrations in solution are given in mg/L and plotted as a function of the binder dosage. Black circles: experimental data. Red lines: numerical data. **Hydration GGBS levels:** Line with larger dots: 40%. Solid line: 30%. Line with smaller dots: 20% and 10%. **(a)** Sulfate, **(b)** calcium, **(c)** aluminum, **(d)** silicon, **(e)** magnesium, **(f)** pH values.
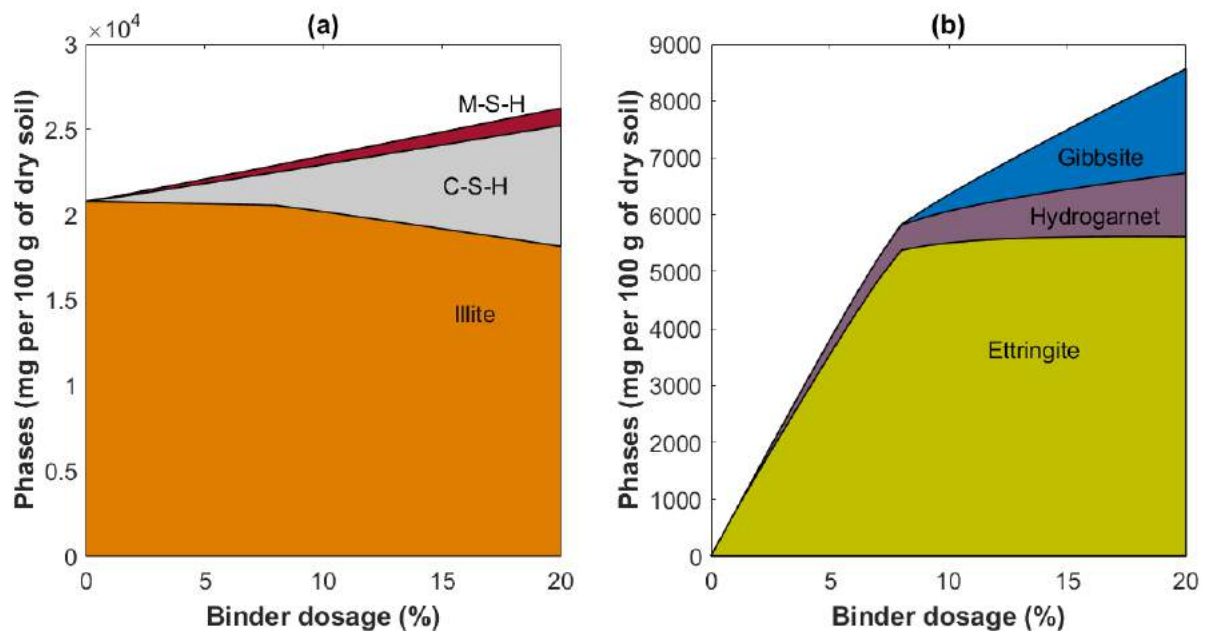
Figure 4.15 – Quantities of major phases calculated from the modeling of formulation F5 (90%GGBS+10%OPC) assuming a GGBS hydration level of 30%. All the data are plotted as a function of the binder dosage given in % by dry mass of soil. **(a)** Illite, C-S-H and M-S-H, **(b)** Ettringite, gibbsite and hydrogarnet.

<u>Sulfate concentration in solution:</u>

As shown in Figure 4.14(a), experimental and numerical data were in good agreement for the sulfate concentrations in solution. Experimental data and modeling showed that sulfate concentration in solution decreased with increasing the content of the binder added to the soil. Experimentally, the sulfate concentration in solution remained relatively stable for formulations containing more than 7% of binder. This behavior can be explained by the ettringite stability as shown in Figure 4.15(b). For ease of comparing, Figure 4.16(a) and Figure 4.16(b) show the concentrations of sulfates in solution and the amount of ettringite that precipitated in the system, respectively. All data were plotted as a function of the binder dosage added to the soil. This figure shows that the solubility of sulfates was indeed controlled by the precipitation of ettringite.

In addition, modeling showed that the GGBS hydration level seemed to have an impact on the slope of the curve representing the sulfate concentration in solution. Depending on the GGBS hydration level considered, a modification on the sulfate concentration in solution was observed. However, the GGBS hydration level no longer affected the sulfate concentrations calculated beyond 15% of binder dosage. The best agreement between experimental and numerical data was obtained when a GGBS hydration level of 30% was assumed.
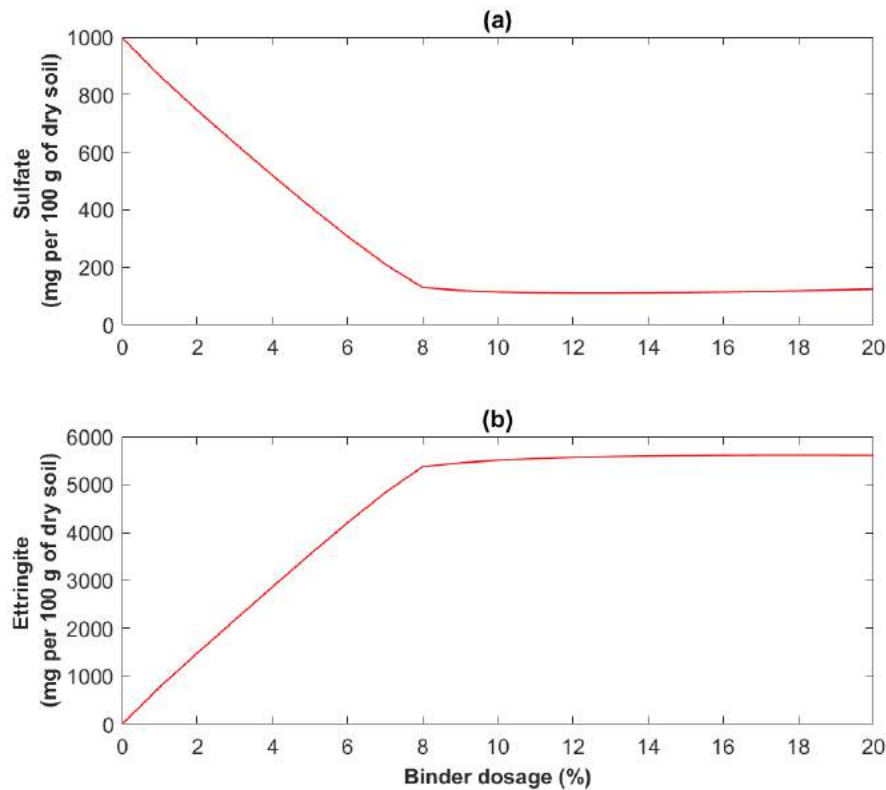
Figure 4.16 – Stabilization of sulfates by the precipitation of ettringite obtained from modeling using 30% as the GGBS hydration level. **(a)** sulfate concentration in solution **(b)** ettringite precipitated in the system. Concentrations are expressed in mg per 100 g of dry soil.

Major element concentrations in solution:

The results obtained for other leached elements are shown from Figure 4.14(b) to Figure 4.14(e). As for sulfates, the most important changes were observed for formulations containing less than 10% of binder. Calcium, silicon and magnesium concentrations calculated in solution were mostly controlled by C-S-H and M-S-H as shown in Figure 4.14(b), Figure 4.14(d), Figure 4.14(e) and Figure 4.15(a). On the other hand, aluminum concentrations in solution presented a more complex behavior due to the competition between aluminous phases (cf. Figure 4.14(c)). For formulations ranging from 0% to 10% of binder, aluminum presented a first evolution mainly dominated by ettringite formation as shown in Figure 4.15(b). Experimental data for formulations with high binder dosage (>10%) showed that a maximum aluminum concentration was reached between 10% and 15% of binder dosage and then remained relatively stable. However, this behavior was not well modeled. The differences found between numerical and experimental results in aluminum behavior can be partially explained by the aluminum mineral phases used in the model. In fact, it was verified that the type of aluminum phase chosen to represent the soil could modify the amount of aluminum present in solution.

For example, it was found that decreasing the aluminum content present in the illite by 1% led to over a 50% reduction in the aluminum concentration in solution. It would also be interesting to calculate the precipitation of C-A-S-H phases, which can play an important role in the behavior of the concentration of aluminum in solution. Despite the differences in experimental and modeled aluminum concentrations, the trend of the curve shown in Figure 4.14(c) remained the same.

On the other hand, pH values measured and calculated in solutions are shown in Figure 4.14(f). The first value measured in the system without binder (untreated soil F1) was close to 7.4. After the addition of the binder to the soil, pH increased significantly in the solution (pH 11-12). It seems that the proportion of binder in the treatment had a little effect on the variation of pH in the solution since it stayed relatively constant between pH values 11 and 12. The pH evolution was well reproduced by the model and was mainly controlled by the C-S-H composition. However, the calculated values tended to be slightly lower than the experimental ones probably due to the database used in the model.

In the previous section, it was shown that treatment of sulfate-spiked soil by adding the experimental binder "90% GGBS and 10% OPC" (formulation F5) led to:
- high sulfate immobilization (sulfate retention of 92%),
- decrease of the swelling (volume expansion <2%),
- indirect tensile strength superior to 0.2 MPa.

All the experimental analyses were carried out at short term (≤ 28 days of curing). For the purpose of evaluating this formulation in the medium and long-term (to ensure sulfate stabilization and the mechanical properties), additional tests were carried out:
- Leaching tests
- Geotechnical experiments:
   o Workability delay
   o Compressive strength
   o Mechanical performance class
   o Swelling potential

All the results are present in the following sections.

4.3.3 Immobilization of sulfates and geotechnical properties in the medium and long-term

Since leaching tests were carried out in treated soil in the short-term (28 days of curing). It may be possible that this curing time can underestimate the capacity of binders containing GGBS to immobilize sulfates due to their low rate of hydration. Therefore, leaching tests were performed in formulation F5 in the long-term (at 180 days of curing).

Furthermore, longer hydration of the binder can lead to expansive reactions; therefore, the geotechnical properties of formulation F5 were studied in detail evaluating the mechanical properties and the swelling potential at different curing conditions.

4.3.3.1 Leaching tests

Figure 4.17 groups the results of leachable sulfate concentration obtained from formulation F5. Concentrations are given in mg/kg of dry mass of soil and all the data were plotted as a function of the binder dosage (ranging from 0% to 20%). The red dotted line represents the "inert and non-hazardous waste threshold" set by the French Decree.

Figure 4.17(a) and Figure 4.17(b) present the leachable sulfate concentrations obtained from leaching tests carried out at 28 days and 180 days of curing, respectively. Figure 4.17(c) shows the numerical calculations of this formulation assuming 10, 20, 30 and 40% of GGBS hydration degree, and Figure 4.17(d) shows the comparison of all the experimental and numerical data only for 30% of GGBS hydration degree. In this figure, experimental data are represented by markers while model calculations are given by lines.

It can be noted that the leachable sulfate concentration at 180 days of curing, using 2 and 5 wt% binder dosage, were 1.3 and 2.4 times than sulfate concentrations in solution obtained at 28 days of curing. This means that at low binder levels, sulfate was more immobilized at later ages. Meanwhile, for higher binder dosages (>5 w%, % by dry mass of soil), leachable sulfate concentrations remained relatively constant and close to the threshold of "inert and non-hazardous waste" of 1000 mg/kg by dry mass of soil set by the French Decree. Additionally, for higher binder dosages (>5 w%) leachable sulfate concentrations at 180 days were similar to those obtained at 28 days of curing.
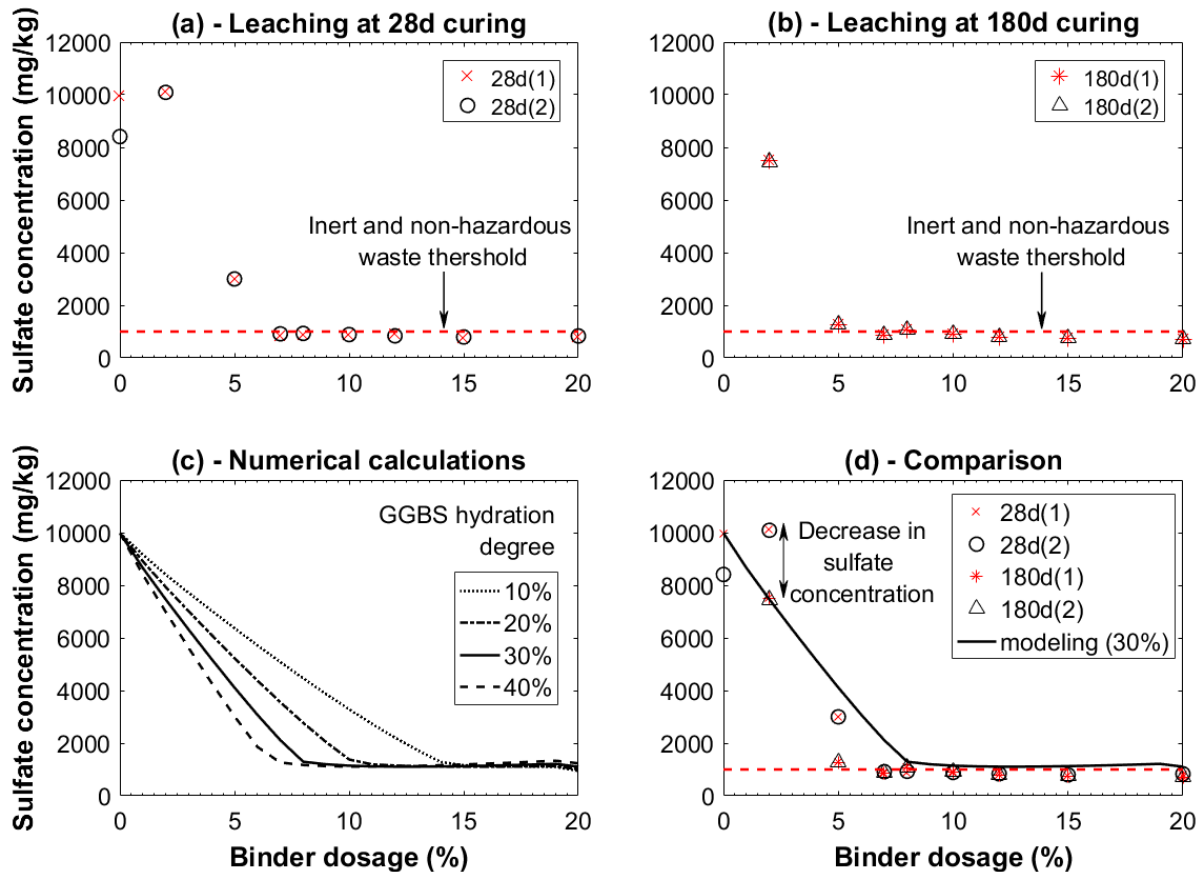
Figure 4.17 – Leaching results obtained from formulation F5 (90%GGBS+10%OPC) given in mg/kg of dry mass of soil. All the data are plotted as a function of the binder dosage. Markers: experimental data. Lines: numerical data. **GGBS hydration level:** line with larger dots: 40%. Solid line: 30%. Line with smaller dots: 20% and 10% GBBS hydration. The red dotted line represents the "inert and non-hazardous waste" limit set by the French Decree. **(a)** Leachable sulfate concentration at 28 days of curing, and **(b)** 180 days of curing. **(c)** Numerical calculations as a function of the GGBS hydration degree, and **(d)** Comparison between numerical and experimental data.

4.3.3.2 Workability delay

As a reminder, in the treatment of soil, the evaluation of workability is very important in order to determine the longest possible duration of the construction operations. Low workability of a mixture leads to difficulties for construction applications. The workability delay of formulation F5 was evaluated by carrying out delayed compaction tests according to the French Standard NF P 98-231 section 6 (protocol was presented in Chapter 2 – section 4.3.3.4).

Table 4.3 presents the experimental data obtained from delayed compaction tests and Figure 4.18 presents the dry density given in t/m³ as a function of the compaction or workability delay given in hours (h). Figure 4.18 shows that the workability delay was 6.5 hours at 98% of the initial dry density resulting in a dry density of 1.837 t/m³. According to the French Technical Guide GTR (*Guide technique pour la réalisation des remblais et des couches de forme*) [65],

for the majority of constructions, a workability delay value of about 4 and 6 hours seems suitable. Thus, the workability delay obtained for formulation F5 was conformed to the industrial needs.

Table 4.3 – Experimental data obtained from the workability tests of the formulation F5 (90% GGBS+10%OPC) according to the French Standard NF P 98-231-6.

Sample	1	2	3	4	5
Water content (%)	14.5	14.1	14.0	13.6	13.1
Dry density (t/m³)	1.875	1.874	1.866	1.854	1.826
Compaction delay (h)	0	1	3	5	7
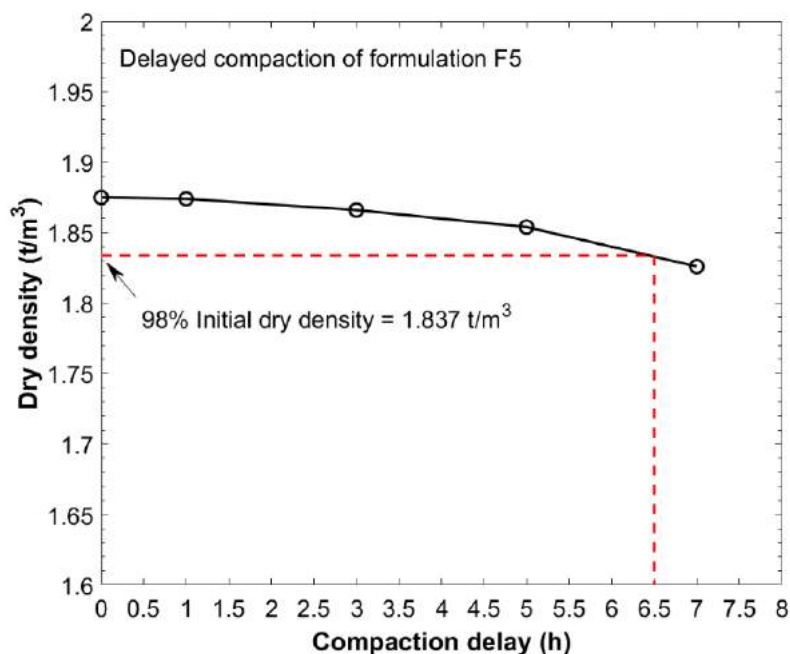
Figure 4.18 – Delayed compaction of formulation F5 to evaluate the workability of the treatment. Dry density expressed in t/m³ is plotted as a function of the compaction delay (workability) in hours. The red dotted lines indicate the 98% initial dry density and the final compaction delay.

4.3.3.3 Compressive strength in the medium and long-term

Compressive strength tests were carried out in formulation F5 samples according to the protocol presented in Chapter 2 – section 2.2.4.5. Figure 4.19 presents the compressive strength results given in MPa as a function of curing conditions (60 and 180 values indicate

the total curing time in days). Rci indicates normal curing (air cure) and Rc indicates partial curing in air and in water at 20ºC.
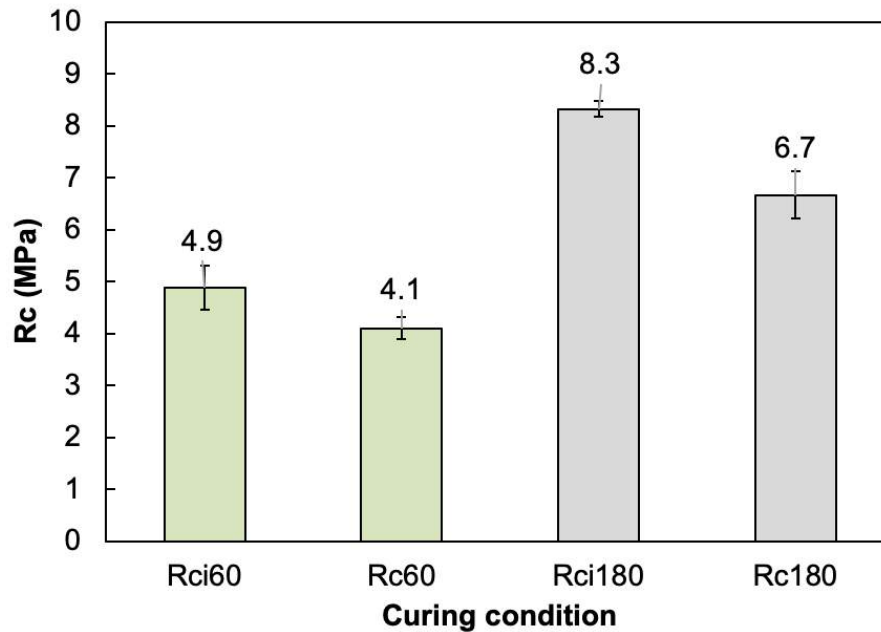
Figure 4.19 – Compressive strength values in MPa for formulation F5 samples as a function of curing time and water sensibility at 20ºC. Long-term curing conditions: Rci60 = 60 days air; Rc60 = 28 days air + 32 days in water; Rci180 = 180 days air; Rc180 = 90 days air + 90 days in water.

As observed in Figure 4.19, compressive strength values are about 2 times higher at 180 days of curing than those obtained at 60 days of curing. Furthermore, it can be noted that compressive strength decreased when samples were submerged in water at 20ºC. As a reminder, the Rci/Rc ratios allow to evaluate the mechanical performances of treated soil in the medium-term as a function of the methylene blue value (V_{BS}) (cf. Chapter 2 – section 4.3.3.5). The soil used in this study presented a V_{BS} equal to 2.15.

The Rci/Rc ratios obtained from compressive strength tests are presented in Table 2.11 and compared with the criterion presented by the French Technical Guide GTR [65] for 60 days of curing. It can be seen that mechanical performance criterion is accomplished for the formulation F5 as Rci/Rc60 was superior to 0.6 (0.84 and 0.80 for 60 days and 180 days, respectively).

Table 4.4 – Rci/Rc ratios obtained from compressive strength tests of formulation F5 and compared to the criterion to evaluate mechanical performance according to French Technical Guide GTR [65].

Criterion from SETRA		Experimental ratio
Ratio	V_{BS}	
$\dfrac{Rci}{Rc60} \geq 0.6$	>0.5	$\dfrac{Rci}{Rc60}=0.84$ $\dfrac{Rci}{Rc180}=0.80$

4.3.3.4 Mechanical performance class

As a reminder, when treated soil is destined for geotechnical applications such as sub-grades (i.e. underlying ground in a pavement), it is necessary to determine the mechanical performance class in the long-term. In this classification, there are five different zones and thus, the treated soil is classified into five different mechanical classes (cf. Chapter 2 - Table 2.12). This classification allows to estimate the thickness of the sub-grade.

In this study, the mechanical performance class was obtained according to the French Standard NF P 94-102-1 and the protocol was presented in Chapter 2 – section 2.2.4.6. Results are presented in Figure 4.20 where tensile strength values are given in MPa and plotted as a function of Young modulus in MPa. As observed in Figure 4.20, all values behaved similarly except for the longest curing condition in water at 40ºC (90 days air + 90 days in water at 40ºC) and one result obtained for the same curing time but at 20ºC. As all the values presented a Rit/E ratio close to zones 2 and 3, the formulation F5 was classified into zone 3 meaning that its mechanical performance class was 4. According to the French Technical Guide GTR [65], the Rit/E ratio obtained from a treated soil at 90 days of curing should lead to a minimum mechanical class of 5.
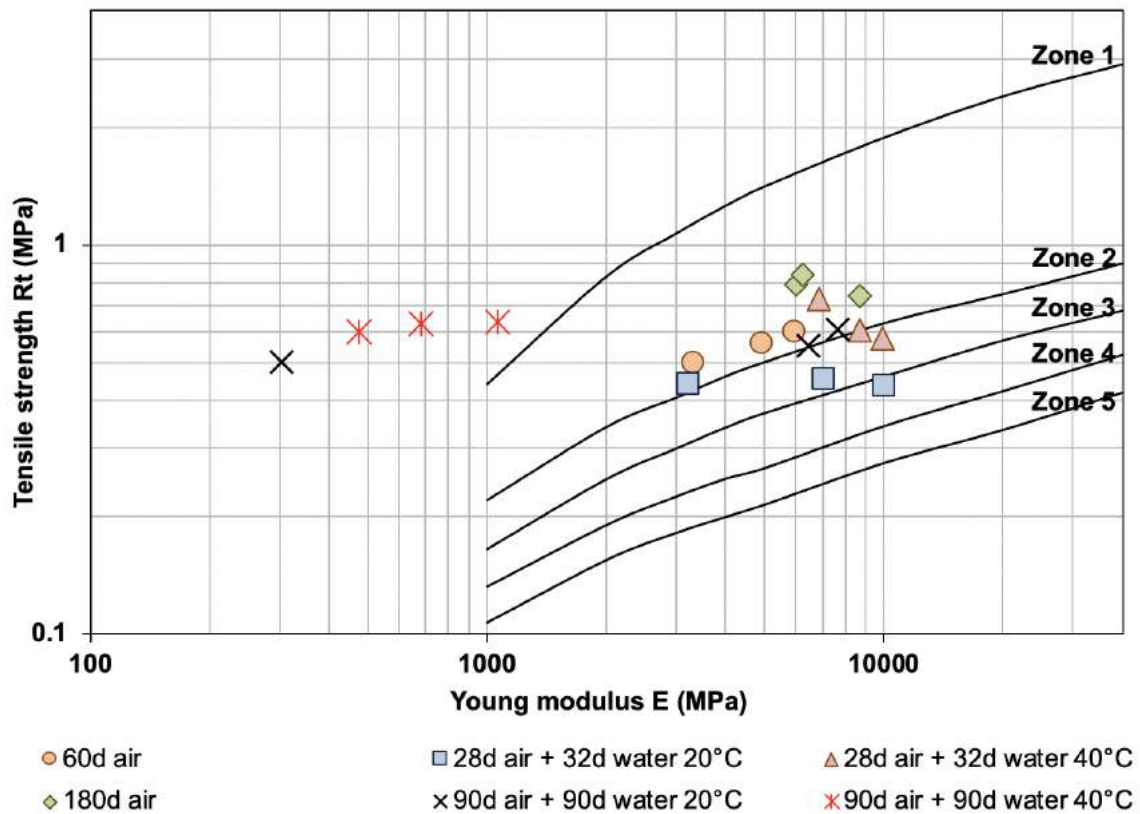
Figure 4.20 – Tensile strength (Rit) versus Young modulus (E) for mechanical classification of formulation F5 as a function of different curing conditions. Values are given in MPa and a logarithmic scale is used. The lines indicate the different five zones according to the European Standard NF P 94-102-1.

4.3.3.5 Swelling potential in the long-term

Swelling potential was evaluated in formulation F5 following the protocol presented in Chapter 2 -section 2.2.4.7 in order to verify if the hydration of the binder at long term conducted to expansion in the soil. Results are presented in Figure 4.21 where all values are given in percentage as a function of the different curing conditions. For the purpose of comparison, the value of volume expansion obtained in short-term is also presented in this figure.

As observed, volume expansion remained much lower than the upper limit of 5% established by the French Standard NF P 94-100. Moreover, the highest volume expansion among all the curing conditions tested was obtained at short-term using 7 days air + 7 days in water at 40ºC. Meanwhile, for the results in long-term, all the volume expansions remained below 1%.
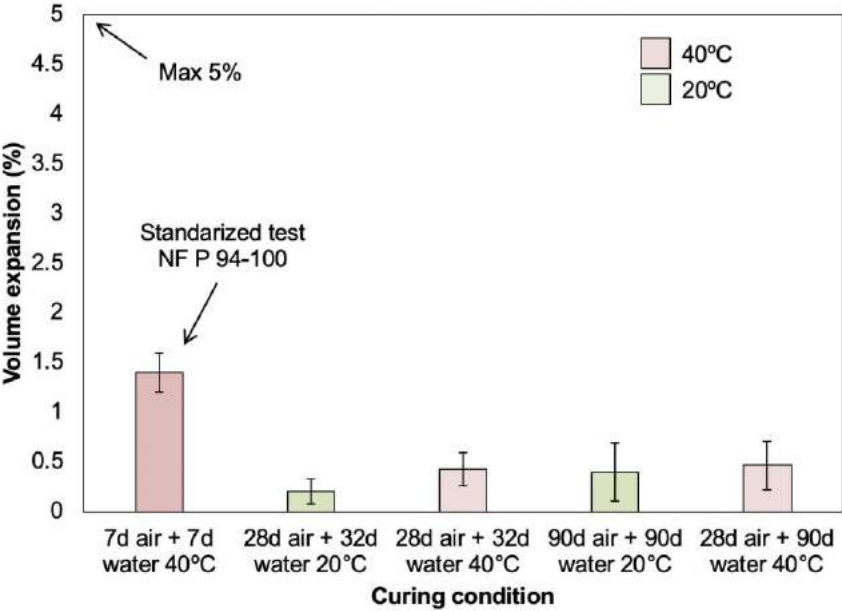
Figure 4.21 – Swelling test results of formulation F5 using different curing conditions. Volume expansion values are given in percentage.

4.4 Summary of the results

Table 4.5 presents a benchmark of all the results obtained in the study of stabilization of sulfates. It should be noted that the amount of ettringite is qualitative and serves for the merely purpose of comparison.

Table 4.5 – Summary of results of chapter 4 – stabilization of sulfates. Concentrations are expressed in mg/kg of dry soil.

	Formulation	F1	F2	F3	F4	F5
	Binder	Untreated	CEM I	Clinker Y	CEM III/C	90-10 [a]
Short term	Sulfate in solution (mg/kg) [b]	9174	138	759	986	785
	Heavy metals in solution (mg/kg)	-	Cr: 0.8	Cr: 2.3	-	-
	Volume expansion (%) [c]	7.1	6.5	4.2	2.0	1.4
	Tensile strength (MPa) [d]	-	0.26	0.19	0.23	0.22
	Ettringite amount [e]	○ (Not found)	● + (High, Expansive)	● + (High, Expansive)	◑ (High-Moderate)	◑ (High-Moderate)
Medium and long term	Sulfate in solution (mg/kg)					907
	Workability (h)					6.5
	Compressive strength Rci/Rc60					0.84
	Mechanical class g					4
	Swelling (%)					<1
	Modeling					✓[1]

[a] Experimental binder composed of 90%ground granulated blast furnace slag and 10% ordinary Portland cement
[b] Average of two values
[c] Max. guideline value 5%
[d] Min. guideline value 0.20 MPa
[e] Qualitative estimation by using SEM/EDS and XRD
[f] VBS = 2.14, criterion Rci/Rc60 ≥ 0,60
[g] As function of Rit and E

Content (qualitative)	High	High-Moderate	Moderate	Low	Not found	Expansive product	Done
Legend	●	◑	◧	◔	○	Red cross +	✓

[1] Modeling was carried out in F5 and showed good agreement with experimental results. Modeling was able to predict the stabilization of sulfates as a function of the binder dosage added to the soil. Moreover, modeling showed that sulfate solubility was controlled by the precipitation of ettringite.

4.5 Discussion

4.5.1 Sulfate stabilization with CEM I and Clinker Y binders

Results presented in this chapter confirm that treatment of sulfate-contaminated soil with cementitious binders is useful to decrease sulfate leaching. As presented previously, untreated sulfate-spiked soil (formulation F1) released into solution about 90% of sulfates. It was verified that the treatment with ordinary Portland cement (formulation F2) and Clinker Y (formulation F3) showed a large decrease in sulfate concentration in solution after leaching tests. For formulation F2, it was calculated that a mass fraction of about 99% of sulfates were fixed in the solid fraction. For formulation F3, the percentage of sulfates fixed in the solid fraction was 92%. As explained in the literature, these binders provided aluminum to the system and also increased the pH [68], which led to the instability of gypsum contained in the soil and to the precipitation of ettringite as shown in Figure 4.6 and Table 4.1. Ettringite is reported to be the most stable phase under these conditions permitting the decrease in leachable sulfate concentration [187], [195]–[197].

<u>Release of heavy metals into solution:</u>

Untreated sulfate-spiked soil (formulation F1) did not release heavy metals into solution while the use of binders CEM I and Clinker Y (formulation F2 and F3) might be limited to treat the sulfate-spiked soil because of the release of chromium (Cr) into solution in addition to the significant swelling measured ($\geq$5%). In fact, chemical analyses of eluates after leaching tests showed that both formulations F2 and F3 released Cr into solution at concentrations that were higher than the established "inert and non-hazardous waste" threshold (0.5 mg/kg of dry soil) (cf. Table 4.1 and Figure 4.4). Previous studies have investigated the presence of Cr in cements [198]–[200]. Sinyoung et al. [198] conducted leaching tests in cement clinker and found that Cr exceeded the allowable leachable concentration established by the United States Environmental Protection Agency (US EPA). Eštoková et al. [200] indicated that the concentration of soluble Cr in binders was proportional to the OPC clinker content. That explains why some types of cements, such as CEM III or CEM V, have a low Cr content; in these cases, Cr content decreases with decreasing the OPC content. In addition, it has been shown that slag can reduce Cr(VI) to Cr(III) due to the reducing properties of this material. As reported in the literature, Cr(III) is less soluble than Cr(VI), therefore, slag binders decrease the leachable Cr concentration [123], [201].

Swelling and tensile strength:

In terms of swelling, both formulations F2 (CEM I-treatment) and F3 (clinker Y-treatment) had larger volume expansions than the expansions measured in formulations F4 (CEM III-treatment) and F5 (90-10-treatment). Volume expansion on formulation F2 was greater than that measured for formulation F3 (6.5% and 4.2%, respectively) (cf. Figure 4.5) in which the C_3A phase is not present. Greater expansion in F2 than F3 may be explained by the difference in the type of ettringite formed. Ettringite was observed at higher magnifications in F2 than for F3 (cf. Figure 4.6). Mehta in 1983 [202] reported that differences in the crystal habit and size of ettringite can affect the expansion behavior of the material. The author proposed two types of ettringite crystals. Ettringite of type 1 has large lath-like crystals ranging from 10 µm to 100 µm and several micrometers thick and it is usually formed during the hydration of supersulfated cements such as the sulfoaluminate clinker used in the present formulation F3. This type of ettringite is not expansive. Conversely, ettringite of type 2, presenting small rod-like crystals (1 µm to 2 µm long), is considered as expansive notably because of large amounts of these crystals have been found in deteriorated concretes under sulfate attacks. Additionally, some observations have shown that microcrystalline ettringite is capable of adsorbing large amounts of water on the surface, causing volume changes [17]. Type 2 ettringite is assumed to be the ettringite observed in formulation F2. Moreover, the marked expansion in formulation F2 was expected due to the large aluminate content in the form of C_3A (8.6%), which reacted with gypsum to form ettringite. These results support previous findings in the literature where noteworthy swelling was reported on sulfate-contaminated soil treated with OPC or lime [73]–[76].

In contrast, significant volume expansion was not expected on samples treated with the "Clinker Y" binder (formulation F3) because the main hydration product of sulfoaluminate clinker is ettringite, which usually precipitates during the consumption of the calcium sulfate after 1 to 2 days of hydration [55]. However, we think that the volume expansion observed for this formulation can be explained by a delay in hydration due to the unavailability of water at the beginning of the hydration process. It should be noted that the water to solid ratio (W/S) of formulation F3 was about 0.15, meaning that not enough water was available to hydrate the binder during the first few days of curing. As explained previously, volume expansion tests were conducted at 7 days of curing and samples were immersed in water at 40°C for 7 days. Under these conditions, the additional water provided to the system could lead to the precipitation of secondary ettringite and consequently the expansion of the samples.

4.5.2 Sulfate stabilization with GGBS binders

Immobilization of sulfates:

As presented in Table 4.1 and Figure 4.4, treatments of sulfate-spiked soil with GGBS binders (formulations F4 and F5) showed a large decrease in sulfate concentration in solution after leaching tests. It was calculated that more than 89% of sulfates were immobilized in the solid fraction. Reduced species of sulfur present in GGBS as sulfides and native sulfur [123], [203] could play an important role to decrease the leachable sulfate concentration in formulation F4 (CEM III-treatment) and F5 (90-10 treatment). However, it should be noted that the amount of sulfur provided to the treatment by the addition of GGBS binder is about 0.009 wt% (% by dry mass of soil), which seems very low to significantly decrease the leachable sulfate concentration.

Binders containing slag can also release metals into solution; however, leachable heavy metal concentrations obtained in this study were well within the established limits for formulations F4 and F5. Several hypotheses can be taken into consideration to explain this:

- pH values: the pH values measured in the eluates of formulations F4 and F5 were lower than those measured in formulations F2 and F3. This condition could have decreased the release of anionic heavy metals such as chromate, which is strongly pH dependent [94], [134], [204].
- Redox reactions: as mentioned previously, GGBS has reducing properties due to reduced sulfur species. It has been shown that Cr(VI) can be reduced to Cr(III) when GGBS is added to OPC mixtures. Thus, leachable Cr concentration decreases after leaching tests [123], [201].
- Some studies have reported that Cr may be present as Cr(III) in slag products and indicated that Cr solubility is controlled by the formation of a phase similar to chromite (Fe-Cr_2O_4) which is a stable form [205].

Swelling and indirect tensile strength:

GGBS-treated soil had volume expansions lower than 5%, which demonstrated the ability of GGBS binders to stabilize sulfates without producing significant swelling. This finding reinforces previous studies reporting the usefulness of binders other than lime or OPC in the treatment of sulfate-rich soil [70], [73], [79], [81], [82], [121]. Celik and Nalbantoglu [70] found that soil containing sulfates at a concentration of about 10000 mg/kg of dry soil that was treated with only lime showed swelling of about 8% with respect to the initial volume of the sample. However, when GGBS was added, the swelling was reduced to 1%. Similarly, Wild and Tasong

[81] showed a significant reduction in expansion when clays containing sulfates where stabilized by using 83% GGBS and 17% lime. They measured little expansion (< 2%) in the samples during the first 7 days of moist curing. Wild et al. [83] explained that, in a GGBS-lime soil system, the proportion of GGBS influenced the magnitude of expansion. Higher GGBS content led to lower expansions (< 5%) in sulfate-rich soils.

The decrease in expansion in this type of system can be explained by the consumption of lime, which usually precipitate in the form of portlandite in clinker-rich binders, by the GGBS to be activated [83]. In this case, GGBS reaction became the dominant reaction and the amount of lime is considered insufficient to enable the precipitation of large amounts of expansive phases [83]. As mentioned previously, Wild et al. [83] explained that, in a sulfate-rich soil treated with mixtures with low lime and high slag content, gypsum is consumed and no crystalline ettringite can be formed. We think that the low hydration rate of the GGBS binder used in formulations F4 and F5 led to small volume changes over the 7 days of immersion test.

Sulfate stabilization mechanism:

Further research was carried out in formulation F5 (90-10 treatment) due to the high sulfate retention and low volume expansions. In this formulation, SEM/EDS and XRD analyses showed that sulfates were partially consumed by the formation of ettringite when the sulfate-spiked soil was treated with 10 wt% of binder (cf. Figure 4.11). These experimental observations were confirmed by modeling, in which ettringite was the most stable phase at the equilibrium of the system. In this study, the precipitation of ettringite was defined as the main mechanism controlling the immobilization of sulfates in the treated soil. Unlike formulations F2 and F3, the formation of ettringite in formulation F5 was not a source of large volume expansions.

- GGBS hydration degree:

As explained in section 4.3.2, the rate of hardening of GGBS binders is slower than that of Portland cement during the first 28 days of curing [60]. Lothenbach et al. [169] showed that, over one month of curing, approximately 70% of the slag had reacted in a system containing about 60% slag and a water to binder (w/b) ratio of 1.1. Taylor et al. [170] showed that over two years of curing approximately 68% of the slag had reacted in a Portland-slag system composed of 50% slag and with an w/b ratio of 0.4. They indicated that higher degrees of GGBS were reached for large amounts of available water and for high proportion of slag. Taylor et al. estimated that, over two years of reaction, only 36% of slag had reacted in a formulation containing 90% GGBS and 10% OPC. Therefore, four different GGBS hydration degrees (10, 20, 30 and 40%) were tested in the modeling of the stabilization of sulfates by adding the

experimental binder 90-10 at different proportions. It was shown that a hydration level of 30% for the GGBS binder enabled good agreement between numerical and experimental results.

The low hydration level of GGBS binder at 28 days can explain the difficulty in experimentally identifying by SEM/EDS the phases containing sulfates in formulation F5 as well as the presence of other possible mechanisms of sulfate stabilization such as adsorption in amorphous minerals or inclusion. Wild et al. [206] studied the stabilization of sulfates in sulfate-rich clay treated with GGBS-lime binders. They proposed that the amorphous phase C-A-S-$\bar{S}$-H was initially formed, which seems to be a precursor of ettringite formation. Similarly, Wild et al. [83] suggested that, in lime-slag systems, gypsum is consumed but part of the products formed during the reaction are not crystalline.

Medium and long-term study in formulation F5:

- Leaching tests:

Leaching tests carried out in the long-term (6 months) showed that sulfates remained immobilized in the solid over the whole range of binder dosage levels (cf. Figure 4.17). This may indicate that no further reactions took place in the samples and that GGBS hydration degree did not increase in time, except for treatments at low binder dosages where the retention of sulfate was greater at 6 months of curing than that calculated at 28 days of curing.

- Geotechnical experiments:

The reuse of soil for civil engineering applications demands the evaluation of the geotechnical properties of treated soil. Therefore, several geotechnical experiments were carried out on formulation F5.

Workability results indicated that the compaction delay of formulation F5 was 6.5 h, which is suitable for the industrial requirements (cf. Figure 4.18) for construction applications. This result can be explained because the binder 90%GGBS-10%OPC used in formulation F5 that takes time to setting due to the high amount of GGBS. This means that the hardening process is longer enough to manipulate the mixture. In this formulation, when the compaction delay of 6.5 h was reached, the workability of the mixture decreases, and then, compaction becomes difficult. In this study, workability tests were carried out in summer season, which is important to know as heat speeds the chemical reactions of the constituents. This suggests that compaction delay may be higher in other seasons. On the other hand, compressive strength and swelling potential results are presented in Figure 4.19 and Figure 4.21, respectively. These properties in formulation F5 were investigated in the long-term as a function of different curing conditions. The curing conditions were inspired by the French Standard NF P 94-102-1. It was

verified that compressive strength of formulation F5 at 60 and 180 days of curing were superior to the criterion presented by the French Technical Guide GTR [65]. Additionally, volume expansions remained inferior to 2% for all the curing conditions tested. This indicated that no further chemical reactions took place in the samples. Moreover, the contact of samples with water at 20ºC and 40ºC did not speed the chemical reactions. Finally, formulation F5 was classified into the mechanical performance class 4. This classification indicated that formulation F5 can be used for sub-grade applications (cf. Figure 4.20).

4.6 Conclusions

This part of the research aimed to (i) compare the capacity of several alternative binders to immobilize sulfates in a sulfate-spiked soil in natural pH conditions, (ii) understand the sulfate immobilization mechanisms, and (iii) evaluate the swelling potential and the mechanical properties of sulfate-spiked soil treatments.

Formulations	Soil spiked with 1 wt% sulfates ~10000 mg$_{sulfates}$/kg of dry soil. Five different formulations were studied: - F1: untreated sulfate-spiked soil, - F2: ordinary Portland cement (OPC), - F3: alternative clinker, - F4: blast furnace slag Portland cement (82% slag), - F5: experimental binder composed of 90% ground granulated blast furnace slag and 10% OPC. The binder dosage used for all formulations were 10 wt%.		
	What was done?	**Results**	**Why?**
Sulfate stabilization	- Leaching tests at 28 days curing according to the European Standard NF EN 12457-2. - Chemical analyses in solution. - Mineralogical and microstructural analyses	**F1:** more than 90% of sulfates released into solution, no heavy metal was detected in solution. **F2, F3, F4** and **F5:** high immobilization of sulfates (>80%). **F2** and **F3**: chromium (Cr) released into solution in excess.	Sulfate solubility controlled by the precipitation of ettringite in all the binders. **F2** and **F3:** Cr in solution due to the high content of clinker. **F4** and **F5:** very low content of heavy metal in solution attributed to: - Low content of clinker/Portland cement - Reducing properties of GGBS (known to reduce the solubility of anionic species).
Swelling and mechanical properties assessed in accordance with the French Standard NF P 94-100	- **Volume expansions** tests (5%: maximum limit for expansion) - **Spitting tests** (0.2 MPa: minimum value for tensile strength).	Tensile strength values were superior to 0.2 MPa for all formulations except for F1 and F3 **F2:** volume expansions superior to 5%. **F3:** 4.2% of expansion. **F4** and **F5:** expansions inferior to 2%. .	**F1** did not present mechanical properties due to the absence of treatment and **F3** presented 0.19 MPa **F2** and **F3:** large volume expansions explained by: - the precipitation of expansive ettringite - delayed hydration due to the unavailability of water during the first 7 days of curing. **F4** and **F5:** low expansion attributed to: - Low kinetics of precipitation of ettringite - Low content of portlandite (often related to the formation of expansive ettringite).
Study at medium and long-term in Formulation F5	Leaching tests, Geotechnical experiments: - workability, - compressive strength, - swelling, - mechanical class performance. Modeling by using PHREEQC.	- Stabilization of sulfates remained stable in time, - **Geotechnical properties** of the treated were acceptable for being used in civil engineering projects (e.g. road construction). - **Modeling:** predicted correctly the sulfate concentrations in solution as a function of the binder dosage used in the treatment.	Sulfate concentrations in solution remained stable probably due to: - the low kinetics of reaction of GGBS. - ettringite was no longer formed due to the unavailability of aluminum in solution.

Suggestions for further research

The results and analyses presented in this chapter showed that the treatment of sulfate-rich soil with GGBS binders is to be useful for the stabilization of sulfates. Below are some suggestions, which could be taken into consideration for future research works to improve the understanding of the sulfate stabilization mechanisms.

- Use of a real sulfate-rich soil

The current work was restricted to a soil artificially contaminated with sulfates. Nevertheless, this system may be expected to behave in a similar manner to a natural sulfate-rich soil where the main source of sulfates is gypsum. In order to ensure the stabilization of sulfates, the same formulations should be tested in a natural sulfate-rich soil. In this case, several factors may be taken into account to evaluate the stabilization of sulfates:

- ion competition,

- harmful effect of organic in the hydration of the binder,

- source of sulfates and concentration.

- Hydration degree of GGBS

In this study, the GGBS hydration degree was estimated by modeling and based on literature. However, it would be interesting to experimentally estimate the GGBS hydration degree in a complex system such as the mixture soil and binder.

In the literature, several methods have been used to estimate the hydration degree of GGBS-based systems (i.e. binder paste or mortars) such as images processing [207]. In this case, SEM images are analyzed, and magnesium is usually used as the component indicating the anhydrous slag grains and thus the unreacted volume of binder can be estimated. However, not much information has been addressed about the hydration degree in complex systems as mixtures of soil and binder. In this case, several factors should be taken into consideration: first, the soil should be characterized, and the clay content determined. Some clays present in the soil may contain magnesium (Mg) and can lead to mistakes in the identification of Mg coming from anhydrous binders. Second, image processing should be made on polished sections, but the small particles present in the soil could hinder the polishing process and the quality of the BSE images may have an effect in the reliability of information obtained from the image processing. Finally, the dilution effect should be taken into consideration as the amounts of binder generally used to treat soil are very low (in this study varied from 2 to 20 wt%), this may lead to a representativeness issue because of the heterogeneity of the sample.

- Characterization of the particle size for leaching tests

In this study, leaching tests were carried out in accordance with the European Standard NF EN 12457-2 as required by the French Decree [88]. This leaching method is presented in the literature as a dynamic test that simulates the worst case of leaching behaviors, mainly because of the L/S (10 L/kg) and the particle size used (below 4 mm) [208]. It should be noted that NF EN 12457-2 procedure does not require the characterization of the particle size below 4 mm. As reported in the literature, this condition led to discrepancies between several results from an identical waste source [208]–[210]. Zandi et al. [210] explained that concentrations in eluates are underestimated when the dust fraction (<0.5 mm) is discarded from the leaching tests. Conversely, results are overestimated if only the finer fraction is considered because larger proportion of fine grain fraction leads to larger concentrations of elements in leachates. Therefore, further experimental investigations are needed to estimate the disparity between results coming from similar wastes by performing this leaching test. Characterization of particle size below 4 mm would increase the reliability of this leaching test.

CHAPTER 5 – STABILIZATION OF MOLYBDENUM

Table of Contents

5. Chapter 5 – Stabilization of molybdenum

Résumé

La stabilisation des matériaux contaminés au Mo (ex : sous-produits, sol excavé) peut être effectuée à l'aide de liants cimentaires. Dans ce chapitre, nous avons étudié la capacité de plusieurs liants cimentaires à stabiliser le Mo. Pour ce faire, nous avons contaminé artificiellement plusieurs liants avec du Mo et avons étudié l'interaction entre les liants et le Mo. Cette approche est justifiée par :

- De très faibles concentrations de Mo dans le sol disponible qui est contaminé naturellement au Mo (<3 mg/kg de masse sèche). Par conséquent, l'étude des mécanismes de stabilisation du Mo à des concentrations aussi faibles est difficile en utilisant les techniques disponibles en laboratoire qui ont des limites de détection élevées.

- Les matériaux contaminés (sol, sous-produits) sont des systèmes complexes à analyser lorsqu'ils sont mélangés avec des liants et plusieurs facteurs doivent être pris en considération (ex : compétition ionique, effet néfaste de la matière organique sur l'hydratation des liants, effet de dilution).

Ainsi, l'étude du système « liant + Mo » semble être une première approche correcte pour étudier les mécanismes de stabilisation du Mo en utilisant des liants.

Par conséquent, dans cette thèse, les échantillons étudiés ont été obtenus en dopant trois liants à différentes concentrations de Mo. La description des matériaux et la fabrication des échantillons ont été présentées au chapitre 2 - section 2.1.3. Pour rappel, le molybdate de sodium (Na_2MoO_4) a été utilisé comme source de Mo pour contaminer artificiellement les liants. Nous avons décidé d'utiliser ce minéral pour les raisons suivantes :

- Le molybdate de sodium contient le composé molybdate (MoO_4^{2-}), qui est l'oxyanion de Mo le plus courant dans la nature à un pH> 4.

- Le molybdate est un anion contenant du Mo dans son état d'oxydation le plus élevé de +6 (l'état d'oxydation le plus courant du Mo).

- Le molybdate de sodium est très soluble dans l'eau, contrairement à la molybdénite (MoS_2) qui est la forme solide insoluble la plus courante de Mo trouvée dans les sols.

Nous rappelons les trois liants sélectionnés :

- B1 : ciment Portland ordinaire (OPC), pris ici comme référence.
- B2 : liant expérimental composé de 90% de laitier de haut fourneau granulé broyé (GGBS) et 10% d'OPC.
- B3 : ciment sursulfaté (SSC).

Ce chapitre présente donc les résultats obtenus sur l'interaction du molybdène avec plusieurs liants contaminés au Mo. Ce travail vise à : (i) comparer la capacité de plusieurs liants à immobiliser le Mo, et (ii) contribuer à la compréhension des mécanismes associés à la stabilisation du Mo.

L'étude de la stabilisation du Mo par des liants cimentaires a été réalisée en suivant l'approche présentée en Figure 5.1. Ce chapitre est organisé de la manière suivante :

(i) La première partie se concentre sur la présentation des résultats des tests de lixiviation des liants dopés en Mo et la compréhension des mécanismes de stabilisation à partir de la caractérisation minéralogique et d'un modèle géochimique développé avec le code PHREEQC.

(ii)   Ensuite, les résultats obtenus sur l'étude de la synthèse de C-S-H avec Mo sont présentés. Cela comprend le pourcentage de Mo retenu dans la fraction solide après filtration du C-S-H ainsi que la caractérisation microstructurale et minéralogique de toutes les phases C-S-H synthétisées. De plus, un modèle géochimique a été développé afin de mieux comprendre les mécanismes de stabilisation du Mo à de faibles concentrations.

Liants dopés en Mo

Pour étudier l'interaction du Mo avec les liants et évaluer leur capacité à immobiliser du Mo, les concentrations des éléments en solution ont été mesurées dans tous les éluats. La Table 5.2 et le Figure 5.4 présentent les concentrations de molybdène, sulfate, calcium, aluminium, sodium et silicium ainsi que les valeurs de pH des éluats obtenus pour tous les liants dopés en Mo.

De manière générale, les concentrations de Mo sont restées bien inférieures aux concentrations initiales de Mo. Des pourcentages élevés de rétention de Mo ont ainsi été obtenus pour tous les liants en fonction des concentrations de Mo. De plus, une augmentation des concentrations de sulfates, d'aluminium, de sodium et de silicium avec la teneur initiale en Mo a été observée. En revanche, le calcium est resté relativement stable pour les formulations ayant des teneurs initiales en Mo inférieures à 5% en masse alors que pour des teneurs initiales en Mo plus élevées, la concentration du calcium a diminué en solution. Cela suggère que le Mo a été probablement immobilisé par la précipitation d'un minéral contenant du calcium : la powellite $CaMoO_4$.

Plusieurs analyses ont ensuite été réalisées sur les liants dopés en Mo afin d'identifier les mécanismes de stabilisation du Mo. La Figure 5.2 résume la démarche expérimentale suivie pour étudier les mécanismes de stabilisation du Mo par l'utilisation des liants.

Des analyses DRX ont permis de vérifier :

-     la présence de la powellite ($CaMoO_4$) lorsque les liants ont été dopés en Mo à des teneurs >5% en masse et,

-     la modification des phases existantes comme celle de l'ettringite.

Pour la formulation à base de ciment Portland (B1), le pic caractéristique de l'ettringite a disparu lorsque le liant a été dopé à des teneurs en Mo supérieures à 5% en masse. Pour la formulation à base de ciment sursulfaté (B3), les spectres ont montré que le pic d'ettringite s'est décalé vers des degrés inférieurs et a perdu en intensité avec l'augmentation de la teneur en Mo.

D'autre part, des observations au MEB/EDS ont permis de cibler d'autres mécanismes d'immobilisation comme l'adsorption du Mo par des C-S-H et par des phases contenant des sulfates.

Ainsi, certaines hypothèses ont été prises en considération pour expliquer les mécanismes d'immobilisation du Mo en utilisant les liants B1, B2 et B3 :

-     Le Mo a été partiellement immobilisé par la précipitation de powellite,

-     Le Mo a été probablement adsorbé sur la surface des C-S-H,

-     Le Mo a été immobilisé avec des phases contenant des sulfates (AFt et Ms),

-     La molybdénite (MoS_2) n'a pas été identifiée dans les liants à base de laitier B2 et B3 probablement parce qu'ils ne présentaient pas d'environnements internes suffisamment réducteurs ou à cause des limites de détection élevées des techniques utilisées.

Par conséquent, nous avons décidé d'utiliser la modélisation pour étudier l'immobilisation du Mo par les trois liants et mieux comprendre les mécanismes, notamment pour de faibles concentrations de Mo. Cette modélisation avait également pour but de mieux comprendre la précipitation de la powellite. De plus, nous avons également décidé d'étudier l'immobilisation du Mo par la synthèse de C-S-H.

Ainsi, des calculs numériques ont montré que la précipitation de powellite contrôle partiellement la solubilité du Mo. Les modèles ont aussi permis de mettre en évidence l'existence d'autres mécanismes de stabilisation du Mo car les teneurs de Mo déterminées expérimentalement en solution se sont révélées être plus faibles que celles calculées par le modèle.

L'étude de la stabilisation du Mo s'est poursuivie avec la synthèse de C-S-H. Les raisons principales de ce choix sont :

- Cette phase est présente comme l'un des principaux produits d'hydratation dans les trois liants étudiés et les analyses EDS ont montré que les C-S-H étaient mélangés avec le Mo.

- Selon la littérature, les phases C-S-H présentent des caractéristiques pour immobiliser les métaux lourds anioniques par co-précipitation ou adsorption sur leur surface.

- Dans la littérature, les phases ettringite et monosulfoaluminate ont déjà fait l'objet de recherches pour expliquer l'immobilisation du Mo alors que la capacité des C-S-H à immobiliser le Mo est peu discutée.

Synthèse des phases C-S-H avec du Mo :

Le Mo a été largement immobilisé (> 95%) dans les phases de C-S-H. Par conséquent, quatre hypothèses ont été proposées pour expliquer l'immobilisation de Mo dans ces phases : (i) co-précipitation du Mo avec des ions calcium pour former de la powellite ($CaMoO_4$), (ii) incorporation du Mo entre les feuillets de C-S-H, (iii) substitution du Si^{4+} par Mo^{6+}, et (iv) adsorption du Mo sur la surface des C-S-H.

Les analyses en solution ont montré une diminution progressive de la concentration de calcium après filtration des C-S-H, ce qui peut s'expliquer par la précipitation du Mo avec des ions calcium. En effet, les analyses DRX ont montré la présence de powellite (cf. Figure 5.18). Les pics caractéristiques de la powellite sont devenus plus importants pour les concentrations de Mo les plus élevées (2,5 et 5% en masse). De plus, des analyses FT-IR (cf. Figure 5.21) ont montré une légère modification de l'intensité des bandes Si-O placées entre 850 et 750 cm^{-1}. Cette intensité a d'ailleurs augmenté avec la concentration en Mo, ce qui peut être dû à la présence de powellite. En effet, la bande Mo-O chevauche la bande Si-O. Les observations au MEB/EDS ont montré la présence de taches blanches attribuées au Mo. De plus, les analyses EDS ont montré que le Mo était mélangé avec les C-S-H et que de la powellite s'était formée. Cela veut dire que la powellite a peut-être précipité à la surface des C-S-H ou que le Mo a été adsorbé sur la surface de ces phases.

Finalement, les observations expérimentales et la modélisation ont montré que la powellite était le mécanisme contrôlant la solubilité du Mo pour les concentrations étudiées. La modélisation a aussi montré que la powellite ne précipitait pas pour des teneurs en Mo inférieures à 90 ppm ($1,9 \times 10^{-5}$ mol/L), c'est-à-dire que pour les concentrations plus faibles de Mo (<90 ppm), le Mo est plutôt immobilisé par l'adsorption sur les surfaces de C-S-H. Ce mécanisme a notamment été observé expérimentalement. La mise en évidence de l'existence d'autres mécanismes d'immobilisation (substitution, inclusion) nécessiterait l'utilisation de techniques plus précises avec des limites de détection plus faibles.

Introduction

The release of molybdenum (Mo) into solution from contaminated materials and by-products (including excavated soil) is a serious concern as it can lead to significant risks for both human health and the environment.

The source of Mo in soil can be either from natural origin (e.g. granite rocks, volcanic rocks and limestone) or from anthropogenic activities (e.g. mining, oil and agriculture industries). Mo concentrations in soil are relative low (in the range of 0.2-74 mg/kg of dry mass[3]) [94], [100], but they can reach about 570 mg/kg of dry mass in soil containing organic matter (e.g. black shale) [94]. Larger concentrations are expected from anthropogenic sources.

Mo is considered as an essential nutriment for plants and animals; however, large amounts of this metal can be toxic and produce an illness known as "molybdenosis" [94], [99], [103], [104]. As a reminder, in France, the French Ministerial decree on waste classification for disposal (*Arrêté du 12 décembre 2014*) classifies the waste materials in three categories depending on the leachable Mo concentration: 0.5, 10 and 30 mg/kg of dry soil for inert and non-hazardous, non-inert and non-hazardous and hazardous waste, respectively (cf. Chapter 1 -Table 1.7). Therefore, the immobilization of Mo is required, and understanding the underlying stabilization mechanisms is necessary.

Stabilization of Mo-contaminated materials, by-products and excavated soil can be done by using cementitious binders. Therefore, this chapter aims to: (i) compare the capacity of several binders to immobilize Mo in a single-step batch procedure, and (ii) contribute to the understanding of the mechanisms associated with Mo stabilization. To this end, we decided to study the stabilization of Mo from a few ppm (50 ppm) to several thousand ppm (100000 ppm), as:

- Mo can be present in a large range of concentrations in natural soil/materials or anthropic by-products.

- The mechanisms of stabilization can differ depending on the concentration tested.

It should be noted that, as the available natural Mo-contaminated soil contained small amounts of Mo (< 3 mg/kg), which is lower than the detection limits of the laboratory techniques (e.g. X-ray diffraction and Scanning Electron Microscopy), we decided to study higher Mo concentrations and their interaction with cementitious binders. In this way, we ensured the detection of Mo to identify its mechanisms of stabilization. However, these mechanisms may

---

[3] mg/kg of dry mass = ppm

not be the same at low Mo concentrations (<50 ppm). Therefore, modeling would help to verify Mo stabilization for those low Mo concentrations.

The study of stabilization of Mo was carried out following the approach presented in Figure 5.1.
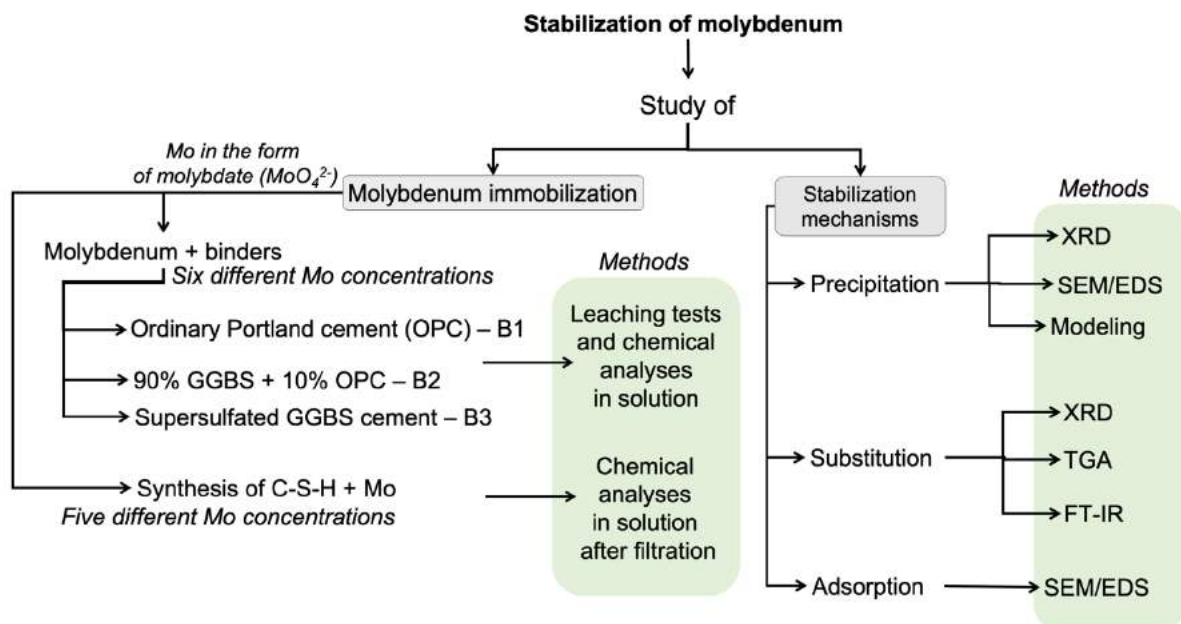
Figure 5.1 – Concept mapping of the approach adopted in the study of stabilization of molybdenum by using alternative binders.

In the first part of this chapter, we present the results obtained from the study of Mo-spiked binders, and we provide information about the capacity of these binders to immobilize Mo. We study the Mo stabilization mechanisms by using mineralogical and microstructural characterization and modeling. We also decided to study the capacity of synthetic C-S-H to immobilize Mo. Therefore, in the second part of this chapter, we give the results obtained from the study of synthetic C-S-H phases with Mo. This includes the Mo concentration in solution after filtration of C-S-H, as well as the microstructure and mineralogical characterization of all the synthetic phases followed by the numerical calculations obtained in the modeling. Then, the discussion of all the results is addressed.

All the results are presented by technique and a summary of results is shown in Table 5.10 and Figure 5.27.

5.1 Molybdenum-spiked binders

As mentioned previously, we studied the capacity of several cementitious binders to stabilize Mo. To this end, we artificially contaminated several binders with Mo and only investigated the interaction between the binders and Mo. This approach is justified by:

- Very low Mo concentrations (<3 mg/kg of dry mass) in the available natural Mo-contaminated soil. Hence, it is not possible to study the mechanisms of Mo stabilization at such low Mo concentrations by using the available technics with high detection limits (e.g. X-ray diffraction and Scanning Electron Microscopy).

- Contaminated materials (soil, by-products) are complex systems to analyze when they are mixed with binders and several factors should be taken into consideration (e.g. ion competition, harmful effect of organic in the hydration of the binders, dilution effect) to study the interaction of all the constituents.

Thus, the study of only "binder + Mo" seemed a correct first approach to investigate the mechanisms of Mo stabilization. Therefore, in this thesis, the samples investigated were obtained by spiking three binders at different Mo concentrations. Description of materials and fabrication of samples were presented in Chapter 2 - section 2.1.3. As a reminder, sodium molybdate (Na_2MoO_4) was the source of Mo used to artificially contaminate the binders. We decided to use this mineral because of:

- Sodium molybdate contains the compound molybdate (MoO_4^{2-}), which is the most common oxyanion of Mo found in nature at pH > 4.

- Molybdate is an anion containing Mo in its highest oxidation state of +6 (the most common oxidation state of Mo).

- Sodium molybdate is highly soluble in water. Unlike molybdenite (MoS_2), which is the most common insoluble solid form of Mo found in soil.

We recall the three binders selected to study the Mo stabilization:

- B1(CEM I): ordinary Portland cement (OPC), taken here as the reference.
- B2(90-10): experimental binder composed of 90% ground granulated blast furnace slag (GGBS) and 10% OPC.
- B3(SSC): supersulfated GGBS cement (SSC).

Table 5.1 summarizes the different binders and Mo concentrations studied. The Mo concentrations for spiking the binders were chosen in order to compare the immobilization of

Mo as a function of the Mo concentrations and to guarantee the detection of Mo. For ease of reading, in this chapter, we present almost all the results as a function of the initial Mo concentration in mg/kg of anhydrous binder and in percentage per weight of anhydrous binder (wt%).

Table 5.1 – Initial Mo concentration used to artificially contaminate the binders. % by weight of anhydrous binder.

Binder	Initial Mo concentration		
	wt%	mg_{Mo}/kg_{binder} [a]	
B1(CEM I) B2(90-10) B3(SSC)	0	0	**Found in natural soil/contaminated materials**
	0.005	50	
	0.05	500	
	0.1	1000	**To guarantee Mo detection**
	1	10000	
	5	50000	
	10	100000	

[a] 120 g of binder were used to fabricate each formulation with a water to binder (w/b) ratio of 0.4

Several techniques were used to study the immobilization of Mo in the binders and the mechanisms of stabilization. Figure 5.2 presents the approach followed in this part of the study.
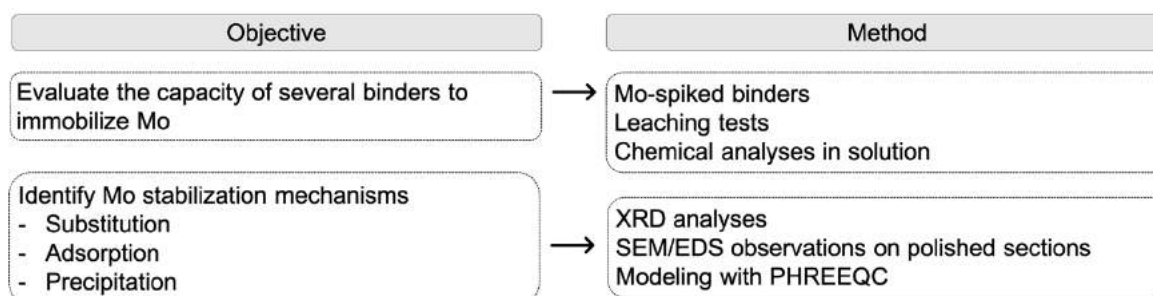
Figure 5.2 – Approach followed to study the stabilization of Mo by using binders.

The following subsections present all the results obtained in the study of the stabilization of Mo by using binders.

5.1.1 Leaching tests results

The immobilization of Mo was studied by carrying out paste leaching tests on the different Mo-spiked binders, in accordance with the protocol presented in Chapter 2 – section 2.2.2.1. As a

reminder, in this protocol, the pastes were crushed to a particle size below 4 mm (no characterization of the particle size below 4 mm) and 100 g of hydrated binder were put in contact with 1 L of distilled water in order to keep a liquid to solid (L/S) ratio of 10.

Figure 5.3 (at left) presents the concentrations in solution of molybdenum (Mo), calcium (Ca), sulfate (SO_4^{2-}) and sodium (Na), in the vertical axis as a function of the initial Mo concentration in the horizontal axis. Concentrations are given in mg/kg of binder. Figure 5.3 (at right) presents the same information by using a logarithmic scale, which allowed us to analyze the behavior of the elements at low initial Mo concentrations (<1 wt%~10000 mg_{Mo}/kg_{binder}).
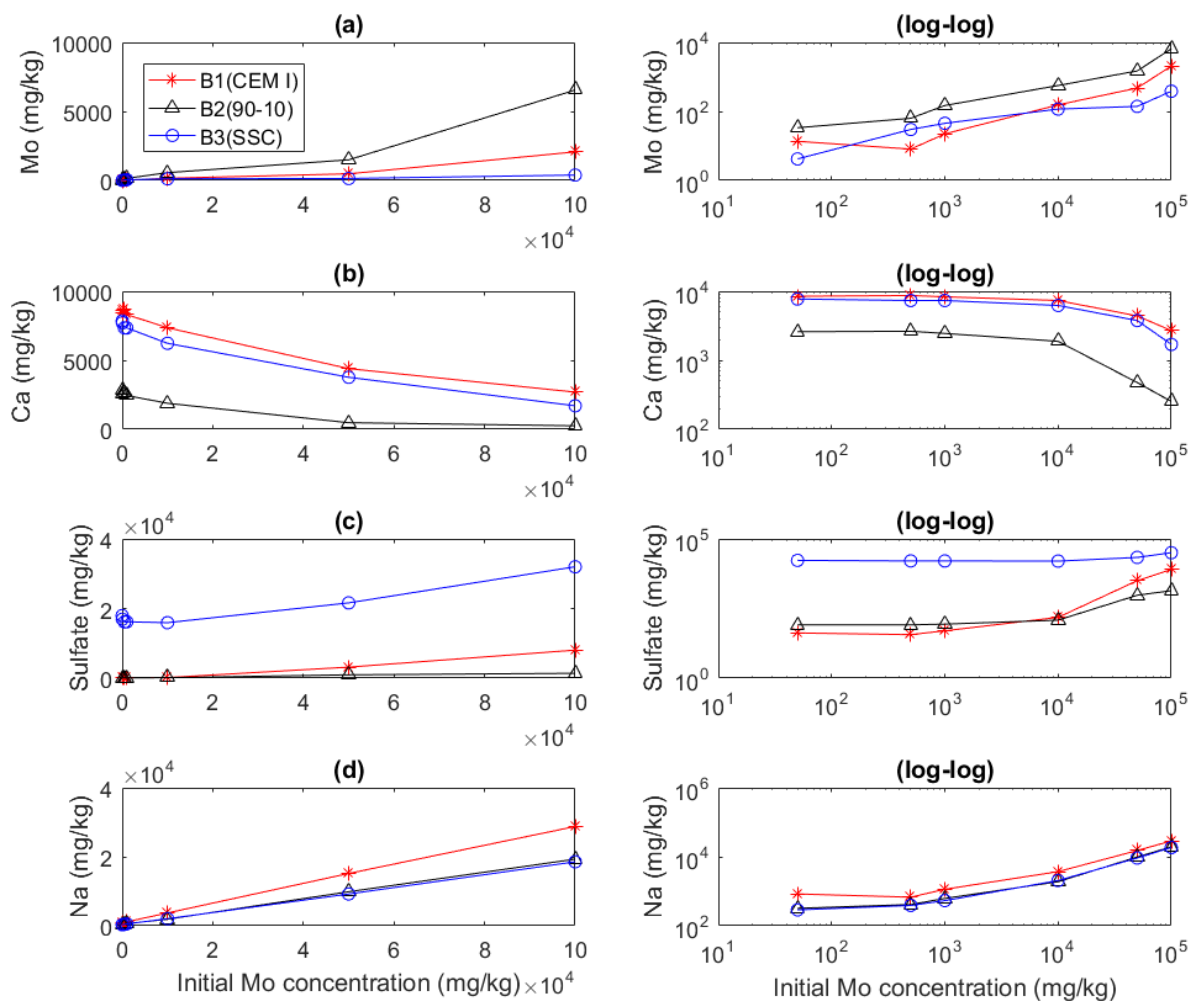
Figure 5.3 – Element concentrations in solution after paste leaching tests of all the formulations plotted as a function of the initial Mo concentrations. Concentrations are expressed in mg/kg$_{binder}$. **(left)** Linear scale**, (right)** logarithmic scale. (**a**) molybdenum, **(b)** calcium, **(c)** sulfate, and **(d)** sodium.

Furthermore, Table 5.2 gives all the information about the pH values and element concentrations measured in all the eluates and specifies the percentage of Mo retention calculated for each formulation.

Table 5.2 – Paste leaching results of Mo-spiked binders. Element concentrations in the eluates are given in mg/kg of anhydrous binder. Each point is the arithmetic average of two values.

	Initial Mo concentration		Concentration in eluates (mg/kg of binder) [b]							
	(wt%)[a]	(mg/kg of binder)	Mo	Na	Ca	Al	Sulfate	Si	pH	Retention of Mo (%)
B1 (CEM I)	0	0	0	634	8625	0.28	33	0.0	13.12	-
	0.005	50	14	835	8459	0.01	42	0.8	13.03	74.0
	0.05	500	8	673	8674	0.01	37	0.0	13.11	98.4
	0.1	1000	22	1142	8311	0.02	50	0.4	12.98	97.8
	1	10000	155	3707	7356	4.3	153	1.5	13.02	98.5
	5	50000	476	15160	4396	17	3162	5.2	13.10	99.0
	10	100000	2066	28770	2692	80	8045	28	13.20	97.9
B2 (90-10)	0	0	0	320	2870	32	74	17	12.60	-
	0.005	50	34	320	2595	34	82	19	12.52	32.0
	0.05	500	63	412	2635	37	82	20	12.61	87.4
	0.1	1000	148	619	2449	39	87	23	12.55	85.0
	1	10000	563	1895	1882	63	121	30	12.58	94.4
	5	50000	1492	9858	475	190	949	53	12.94	97.0
	10	100000	6549	19315	253	391	1386	130	13.02	93.5
B3 (SSC)	0	0	0	314	7852	1.0	17958	63	12.02	-
	0.005	50	4	289	7720	0.0	16928	51	11.78	92.0
	0.05	500	30	388	7344	0.0	16133	48	11.84	94.0
	0.1	1000	45	535	7344	0.3	16188	51	11.82	95.5
	1	10000	117	2044	6231	2.4	15929	47	11.95	98.8
	5	50000	140	9205	3767	3.6	21619	52	12.26	99.7
	10	100000	386	18545	1700	13.9	31995	93	12.40	99.6

[a] wt%: percentage by weight of anhydrous binder.
[b] by using a liquid to solid (L/S) ratio of 10

Molybdenum

Figure 5.3 shows that for all the formulations - B1(CEM I), B2(90-10) and B3(SSC), Mo concentrations in eluates increased with increasing the initial Mo concentration. However, the concentrations in eluates were much lower than the initial Mo concentrations used to spike the binders as presented in Table 5.2. For the purpose of better illustrating the retention of Mo by the binders, Figure 5.4 presents the curves of Mo retention as a function of the initial Mo concentrations using an x-axis semi-logarithmic scale.
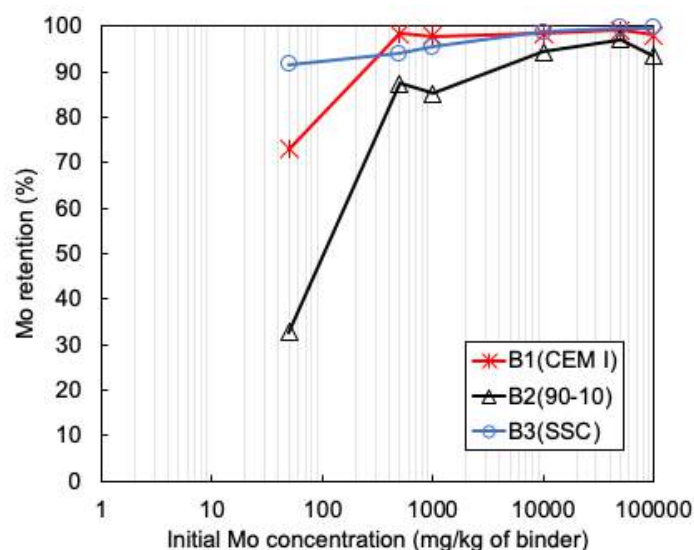
Figure 5.4 – Mo retention by the formulations B1(CEM I), B2(90-10) and B3(SSC). Retention values are given in percentage as a function of the initial Mo concentrations in mg/kg of binder by using an x-axis semi-logarithmic scale.

From Figure 5.4, it can be observed that Mo retention increased with increasing the initial Mo concentration. It can also be observed that at high Mo concentrations (>0.1 wt%~1000 mg/kg of binder) Mo was immobilized by all the binders in percentages superior to 85%. For example, when binders were spiked with the highest Mo concentration (10 wt% ~100000 mg/kg of binder), it was found that Mo concentrations in solution decreased to 2070, 6550 and 390 mg/kg of binder for the formulations B1(CEM I), B2(90-10) and B3(SSC), respectively. It means that Mo retentions were 97.9, 93.5 and 99.6% for these binders.

For the low Mo concentrations (<0.1 wt%), Mo was immobilized in the solid fractions at lower percentages of retention compared with those measured at high initial Mo concentrations. For example, for the lowest Mo concentration (0.005 wt% ~50 mg_{Mo}/kg_{binder}), it was seen that Mo concentrations in eluates decreased to 13, 34 and 4 mg_{Mo}/kg_{binder} for formulations B1(CEM I), B2(90-10) and B3(SSC), respectively. It means that Mo retentions were 74, 32 and 92% for these binders. This may indicate that the mechanisms of Mo stabilization differ from low to high Mo concentrations. Among the three binders, B3(SSC) was the one immobilizing the highest concentration of Mo over the whole range of initial Mo concentrations (from 92 to 99.6% of Mo retention). This suggests that this binder presents internal conditions allowing the stabilization of Mo at different Mo concentrations. Further details will be given in discussion.

214

Calcium, sodium and sulfate

It is clearly seen from Figure 5.3 that the leachate concentrations of the major elements did not remain constant while increasing the initial Mo concentration. Although the binder content was kept at the same level, the element concentrations varied, meaning that the presence of Mo in the systems had significant effects on the phase formation of the compounds.

It can be observed that the concentrations of calcium (Ca) in solution decreased with increasing the initial Mo concentration. This may suggest that Mo was immobilized by the precipitation of Ca with Mo (e.g. formation of powellite ($CaMoO_4$)). In contrast, sulfate (SO_4^{2-}) and sodium (Na) concentrations increased gradually with increasing the initial Mo concentration. The case of Na could be partially or totally explained by the fact that the Mo was added as a sodium salt. However, it should be noted that at high sodium molybdate concentrations, the instability of ettringite is expected due to the high concentration on Na. Several studies have shown that the presence of high content of alkalis (sodium or potassium) inhibits the formation of ettringite [187], [188]. The presence of sodium in solution increases the alkali conditions in the pore solution and modifies the stability of ettringite. High alkali conditions enhance the solubility of ettringite constituents, mainly sulfate, as a result, the amount of ettringite decreases in the hydrated binder [188]. Regarding sulfate concentration in solution (cf. Figure 5.3(c)), it can be observed that the binder B3(SSC) released the highest sulfate concentration in solution (which was expected due to the high sulfate content in SSC), followed by the binder B1(CEM I). This may suggest that Mo was partially immobilized by the substitution of sulfates in the sulfates-bearing phases or that part of these sulfate-bearing phases did not precipitate. Further details will be addressed in the discussion section.

From these analyses in solution, several hypotheses of Mo immobilization were taken into consideration. Mo solubility was probably (partially or totally) controlled by:

- the precipitation of powellite ($CaMoO_4$), which is formed by the reaction between calcium ions and molybdate (MoO_4^{2-}),

- the adsorption of Mo onto the surface of amorphous phases such as the calcium silicate hydrate (C-S-H),

- the substitution of sulfate by molybdate in sulfate-bearing phases such as ettringite and monosulfoaluminate,

- the reduction of molybdate due to redox reactions, which could be produced in binders with reducing internal environments such as the binder B2(90-10)

In order to identify the Mo stabilization mechanisms, mineralogical and microstructural analyses were carried out in Mo-spiked binders. Moreover, modeling was performed with PHREEQC to predict the immobilization of Mo at low Mo concentrations (cf. Figure 5.2).

5.1.2 XRD characterization

X-ray diffraction (XRD) analyses were carried out in all the Mo-spiked pastes at 28 days of curing and using rutile (TiO_2) as an internal standard. These analyses were carried out in order to:

- identify the formation of new Mo bearing phases,

- identify the modification of existent crystalline phases after spiking the binders with Mo.

Precipitation of powellite:

As the formation of powellite ($CaMoO_4$) was one of the hypotheses explaining the immobilization of Mo, we verified the appearance of the characteristic peaks of powellite in the XRD patterns. Therefore, Figure 5.5 shows the XRD patterns obtained from Mo-spiked binders and plotted in the selected ranges from 2θ 17º to 19º and from 2θ 27º to 30º. These ranges were selected in order to highlight the presence of powellite, which has its main peak in

between 2θ 28° and 29°. The peak of rutile in 2θ 27°-28° allowed us to confirm that the diagrams were correctly positioned. Moreover, ettringite (2θ 17.5°-18°), portlandite (2θ 28°-29°), gypsum (2θ 29°-29.5°) and calcite (2θ 29°-30°) were also detected.

In general, XRD patterns showed that powellite precipitated in all the binders containing 5 and 10 wt% Mo (50000 and 100000 mg/kg of binder, respectively). For binder B3(SSC), a modification of the pattern was observed at 1 wt% Mo, in which powellite seemed to appear. At Mo concentrations inferior to 1 wt% (10000 mg_{Mo}/kg_{binder}), powellite was not identified probably due to: (i) the relatively high detection limits of the XRD analyses, and/or (ii) the presence of other immobilization mechanisms such as adsorption, substitution and inclusion.

Figure 5.5 – XRD patterns obtained from Mo-spiked binders at 28 days of curing using rutile (TiO_2) as internal standard and plotted in the selected ranges from 2θ 17° to 19° **(left),** and from 2θ 27° to 30° **(right). (a)** and **(b)** B1(CEM I), **(c)** and **(d)** B2(90-10), **(e)** and **(f)** B3(SSC). **P:** Portlandite, **R:** Rutile, **C:** Calcite, **E:** Ettringite, **G:** Gypsum.

Modification of ettringite peaks:

The substitution of sulfate by molybdate in ettringite (or monosulfoaluminate) was one of the hypotheses explaining the immobilization of Mo. Therefore, we decided to verify the modification of the characteristic peaks of ettringite in the XRD patters. Thus, Figure 5.6 presents the patterns plotted in the selected ranges from 2θ 8.8º to 9.5º and from 2θ 15º to 17º (ranges selected in order to verify the modification of ettringite). Ettringite was identified in binders B1(CEM I) and B3(SSC) without Mo (0% Mo). Meanwhile, ettringite was not present as a reaction product in the formulation B2(90-10). As a reminder, formulation B1(CEM I) was fabricated with an OPC containing 3.4 wt% SO_3, and formulation B3(SSC) was fabricated with a supersulfated cement. Therefore, both binders present compositions able to form ettringite at different proportions during hydration. On the other hand, formulation B2(90-10) was fabricated with 10% OPC, which is a relatively low concentration to form high amounts of ettringite but enough to enable the reaction of the GGBS to mainly form C-S-H.

On the other hand, in formulation B1(CEM I), the peaks of ettringite (in 2θ 9º to 9.2º and 2θ 15.5º to 16º) disappeared when the binder was spiked with concentrations superior to 5 wt% Mo (% by weight of anhydrous binder). Meanwhile, in formulation B3(SSC), ettringite peaks shifted towards lower degrees and also decreased in their relative intensity for concentrations superior to 1 wt% Mo. Ettringite was probably modified due to: (i) the effect of sodium added to the system or/and (ii) the substitution of sulfate by molybdate. Further details will be given in the discussion section.

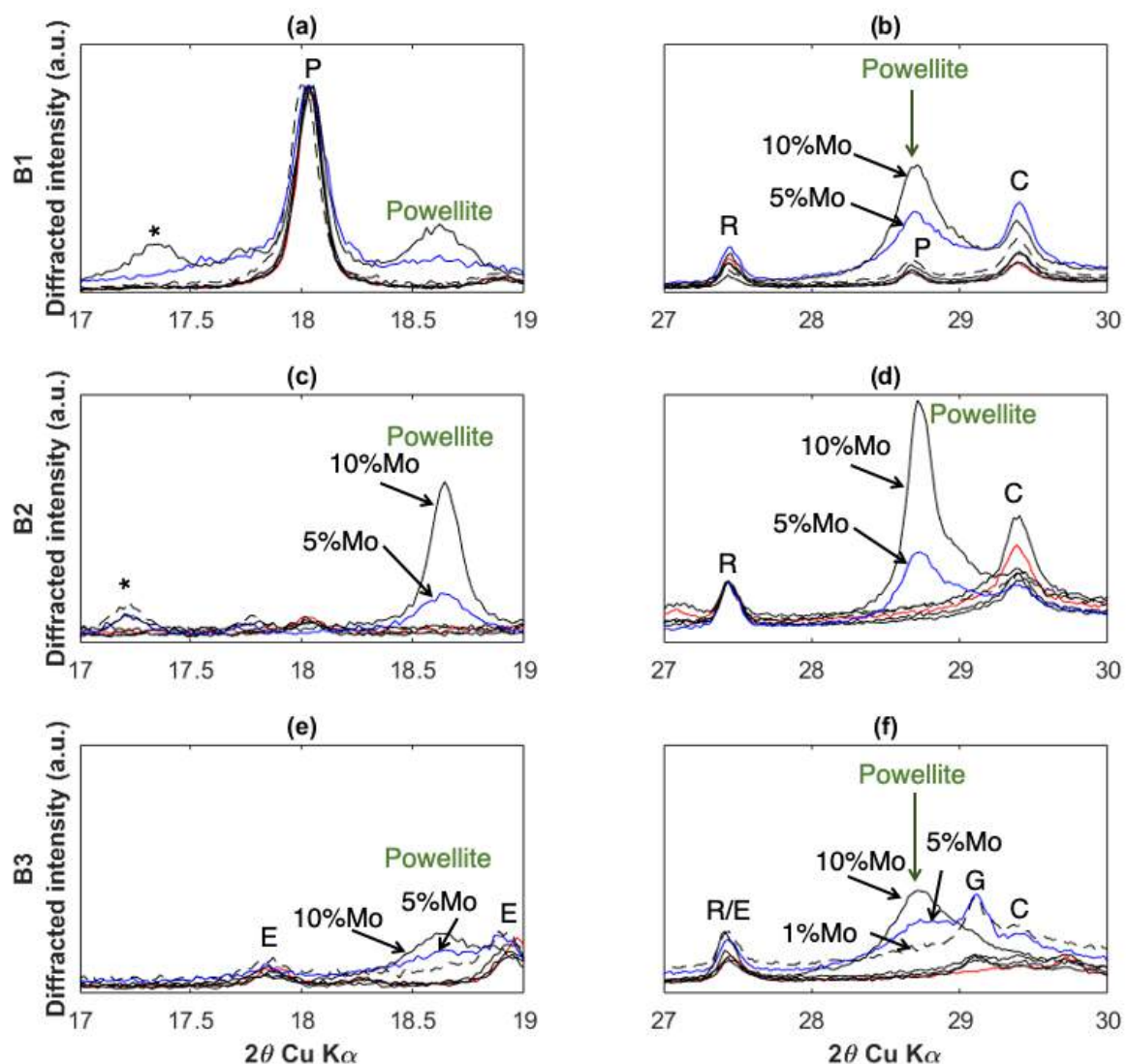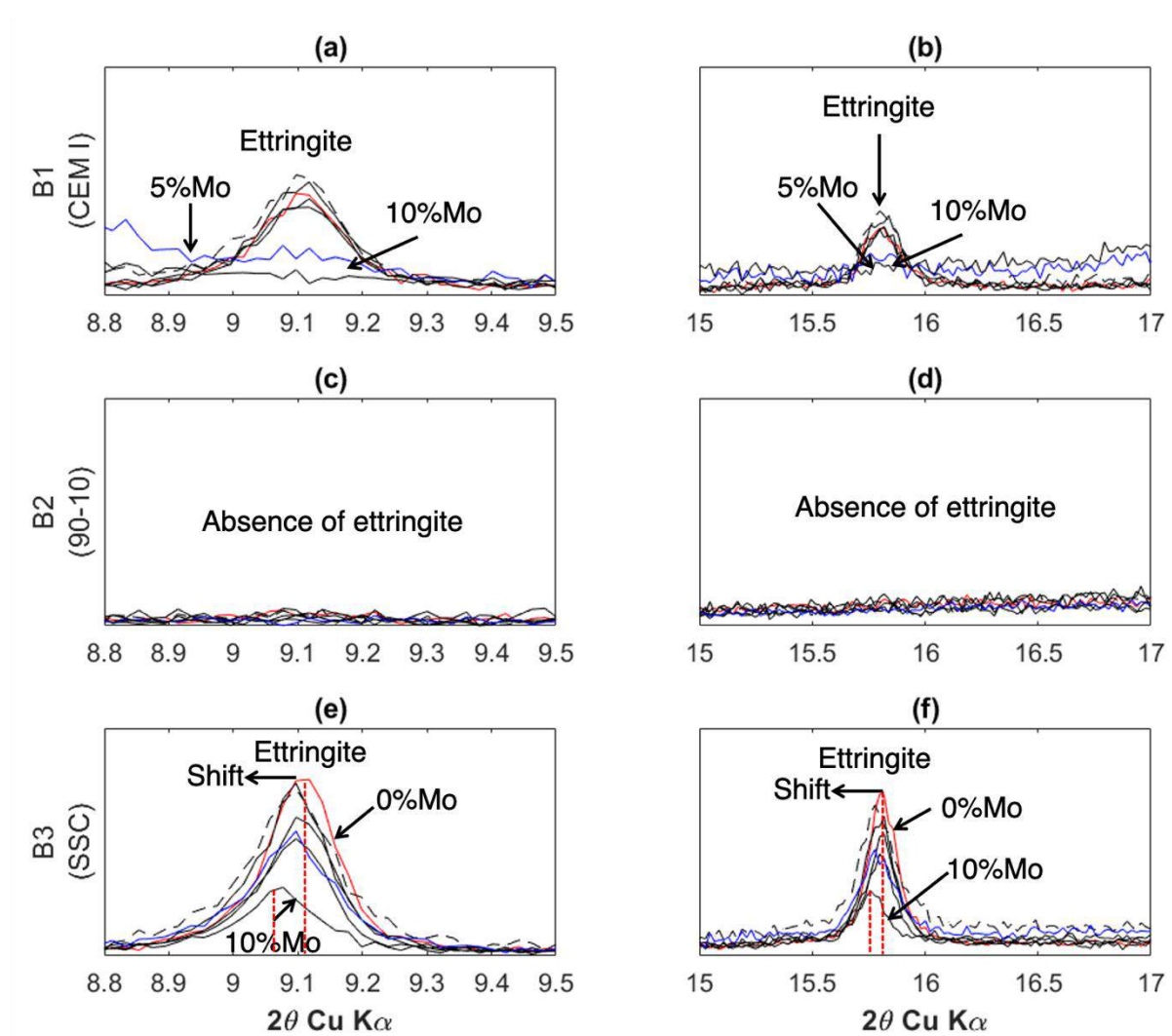**Figure 5.6** – Superposed XRD patterns obtained from Mo-spiked binders at 28 days of curing using rutile (TiO_2) as internal standard and plotted in the selected ranges from 2θ 8.8º to 9.5º **(left),** and from 2θ 15º to 17º **(right). (a)** and **(b)** B1(CEM I), **(c)** and **(d)** B2(90-10), **(e)** and **(f)** B3(SSC).

5.1.3 SEM/EDS observations of Mo-spiked binders containing GGBS

Oxidation-reduction (redox) and adsorption of Mo onto C-S-H surface:

As mentioned previously, Mo could also be immobilized by binders having reducing properties due to redox reactions. Binders containing GGBS, such as binders B2(90-10) and B3(SSC), were reported to be able to reduce anionic species (e.g. chromate) and thus, decrease their water solubility [85], [112], [116], [119], [120]. Mo is generally present in solution as the anion molybdate (with a Mo oxidation state of +6) and the reduction of this anion by binders containing GGBS may help to decrease Mo solubility. If the reducing internal conditions of the

binders are enough (low pH and negative electrochemical potential) (cf. Chapter 1 – Figure 1.19), it would be possible that molybdate transforms into molybdenite (MoS_2), which has a Mo oxidation state of +4 (cf. Chapter 1 – Figure 1.21) [115]. Hence, particular attention was paid to binders B2(90-10) and B3(SSC) because of their reducing internal environments (sulfur in GGBS).

Furthermore, B2(90-10) was particularly interesting because it did not form ettringite or monosulfoaluminate during hydration (cf. Figure 5.5) and even though it showed a high capacity for Mo immobilization. It means that this binder did not immobilize Mo by the substitution of sulfate by molybdate, but by the precipitation of powellite and probably another immobilization mechanism such as the reduction of molybdate or the adsorption of Mo onto the surface of C-S-H. In the case of B3 (SSC), aside from its reducing internal environment, it was also interesting to study other mechanisms of Mo stabilization, such as the presence of Mo in ettringite (AFt) or monosulfoaluminate (Ms) due to the substitution of sulfate by molybdate and the adsorption of Mo onto the surface of C-S-H. To this end, SEM/EDS analyses were carried out on polished sections of binders B2(90-10) and B3(SSC) spiked with the highest Mo concentration of 10 wt% Mo (concentration selected due to the high limits of detection of the SEM).

Figure 5.7 presents a SEM image obtained from the binder B2(90-10) with 10 wt% Mo. It can be observed that several white spots (corresponding to Mo) were found in all the surface of the analyzed sample. Moreover, it seemed that C-S-H phases were surrounded by white lines, which also corresponded to Mo. The Ca/Mo atomic ratios of these lines were calculated in order to verify if powellite was present (Ca/Mo atomic ratio of 1). However, the Ca/Mo was much greater than 1, meaning that it was not possible to confirm that powellite was formed around C-S-H. However, it is probable that: (i) powellite was near other compounds containing calcium, as the binders initially had a high Ca content, (ii) Mo was adsorbed onto the surface C-S-H, and (iii) grains of sodium molybdate were not completely dissolved or reprecipitated accumulating in those zones. The zone of analysis (a few μm wide) was not small enough to isolate the Mo reaction products.

O	Na	Mg	Al	Si	S	Ca	Mo	Ca/Mo	Ca/Si
56.2	3.8	2.5	3.7	11.6	0.4	18.7	2.8	6.8	1.6

O	Na	Mg	Al	Si	S	Ca	Mo	Ca/Mo
53.9	1.3	0.8	1.4	7.2	0.4	31.5	3.0	10.7
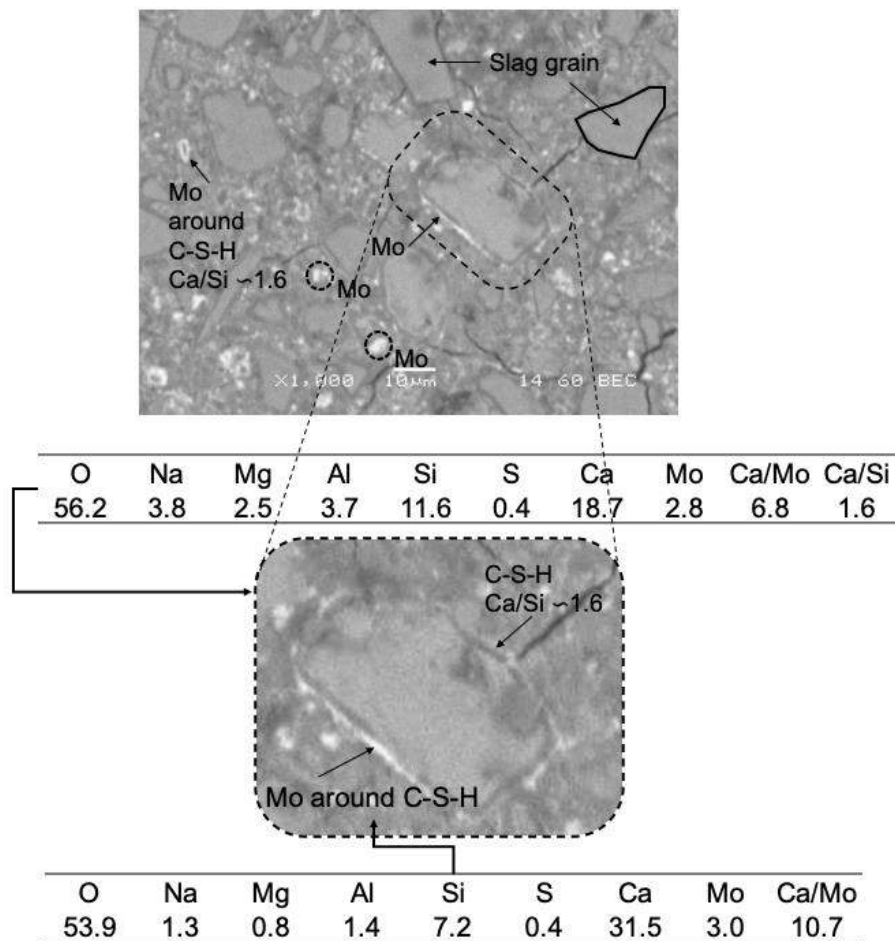
Figure 5.7 – SEM image from B2(90-10) 10 wt% Mo. Chemical compositions (EDS) are given in atomic concentrations (%).

Figure 5.8 presents a SEM image obtained from the binder B3(SSC) with 10 wt% Mo. It can be observed the presence of numerous white spots in all the surface of the analyzed sample. EDS analyses indicated the presence of Mo near Ca and S. This may suggest that Mo interacted with sulfate bearing phases such as gypsum or anhydrite. Like for B2(90-10), it seemed that C-S-H phases were surrounded by white lines, which corresponded to Mo. Moreover, Mo was also detected in the zones containing ettringite.

At. (%)										
O	Na	Mg	Al	Si	S	Ca	Mo	Ca/Mo	Ca/Si	Ca/S
57.4	3.4	0.1	0.2	1.6	7.4	20.0	9.9	2.0	12.5	2.7
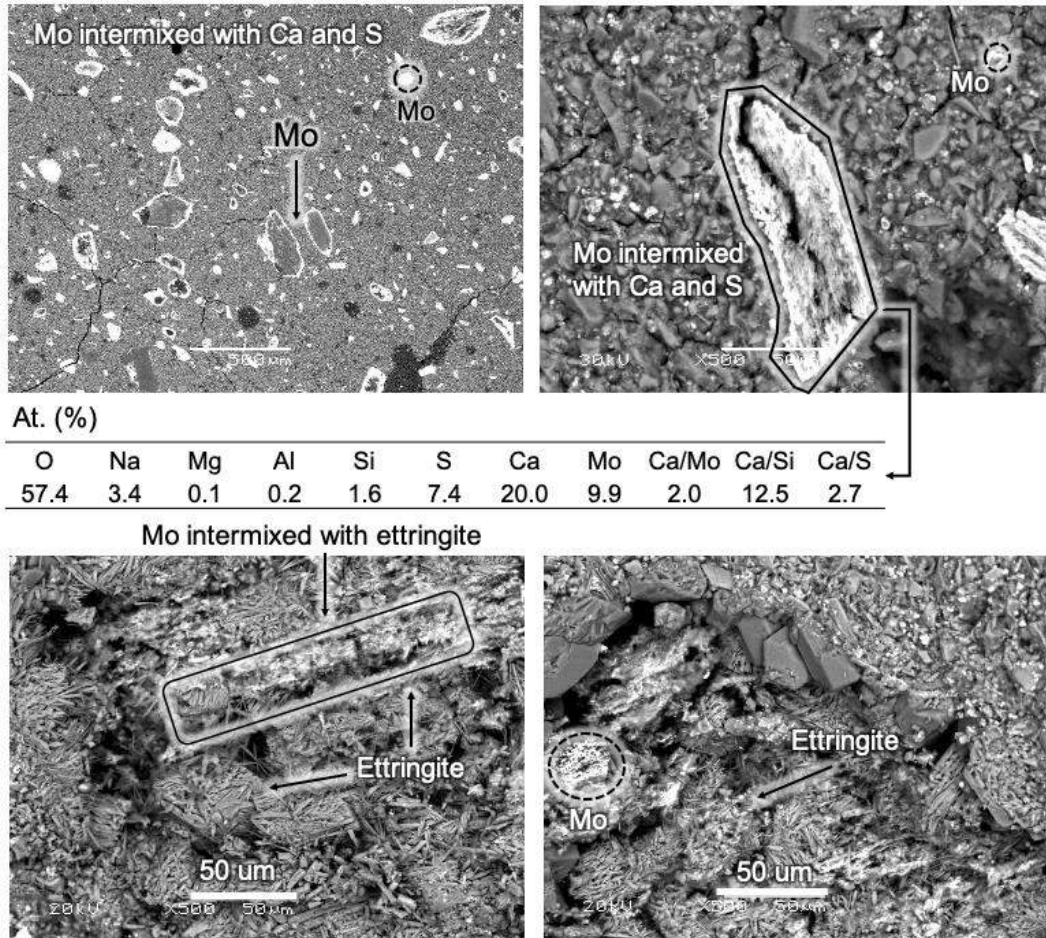
Figure 5.8 – SEM image from B3(SSC) 10 wt% Mo. Chemical composition (EDS) is given in atomic concentrations (%).

SEM/EDS observations were completed by EDS punctual analyses, plotted in three charts:

(i)   S/Ca vs. Mo/Ca EDS chart:

Figure 5.9 presents the S/Ca vs. Mo/Ca EDS charts obtained from binders B2(90-10) and B3(SSC) with 10 wt% Mo. Figure 5.9(a) presents a schematic explanation of how to read this type of chart. X-axis and y-axis represent the molybdenum to calcium (Mo/Ca) and sulfur to calcium (S/Ca) atomic ratios, respectively. This plot helps to identify different hydration products (C-S-H, gypsum, ettringite AFt and monosulfoaluminate Ms), as well as powellite, which has a Mo/Ca atomic ratio of 1.

From Figure 5.9(b), it can be confirmed that B2(90-10) with 10 wt% Mo did not form ettringite/monosulfoaluminate (AFt/Ms) during hydration, due to the relatively small amounts of sulfates. In this binder, the main population of points was in the zone of C-S-H containing more or less Mo. The Mo content reached around 20-30% in certain points. In contrast, Figure

222

5.9(b) shows that binder B3(SSC) with 10 wt% Mo presented a population of points in the gypsum and AFt/Ms zones and a population of points driving towards higher Mo concentrations. It means that Mo probably interacted with sulfate-bearing phases.
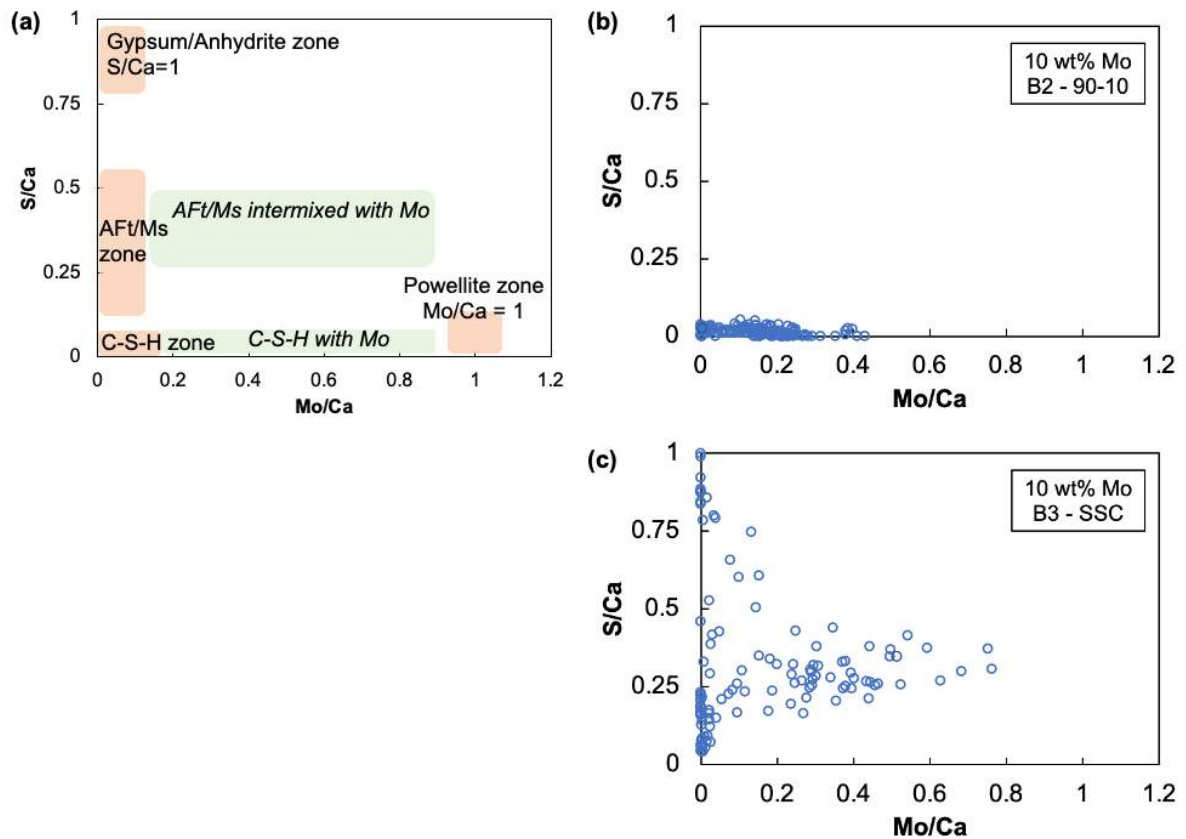
Figure 5.9 – **(a)** Interpretation of S/Ca vs. Mo/Ca EDS charts obtained from **(b)** B2(90-10) and **(c)** B3(SSC) with 10 wt% Mo.

(ii) S/Mo vs. Ca/Mo EDS chart:

Figure 5.10 presents the S/Mo vs. Ca/Mo EDS charts obtained from binders B2(90-10) and B3(SSC) with 10 wt% Mo. Figure 5.10(a) presents a schematic explanation of how to read this type of chart. X-axis and y-axis represent the calcium to molybdenum (Ca/Mo) and molybdenum to sulfur (S/Ca) atomic ratios, respectively. The zones marked in the plots correspond to powellite, which has an Ca/Mo atomic ratio of 1 and molybdenite having an S/Mo atomic ratio of 2. Furthermore, it is possible to identify if Mo interacted with sulfate-bearing phases.

It should be noted that no point was observed in the area of molybdenite (MoS_2), meaning that the mixtures did not had the necessary reducing internal environments to transform molybdate into molybdenite, although these binders contained a high proportion of GGBS with sulfur.

Nonetheless, the reduction of molybdate should be confirmed for the other Mo concentrations and thus, the study of the Mo speciation in the samples would be necessary. It can also be observed that for binder B3(SSC), Mo interacted with sulfate-bearing phases.
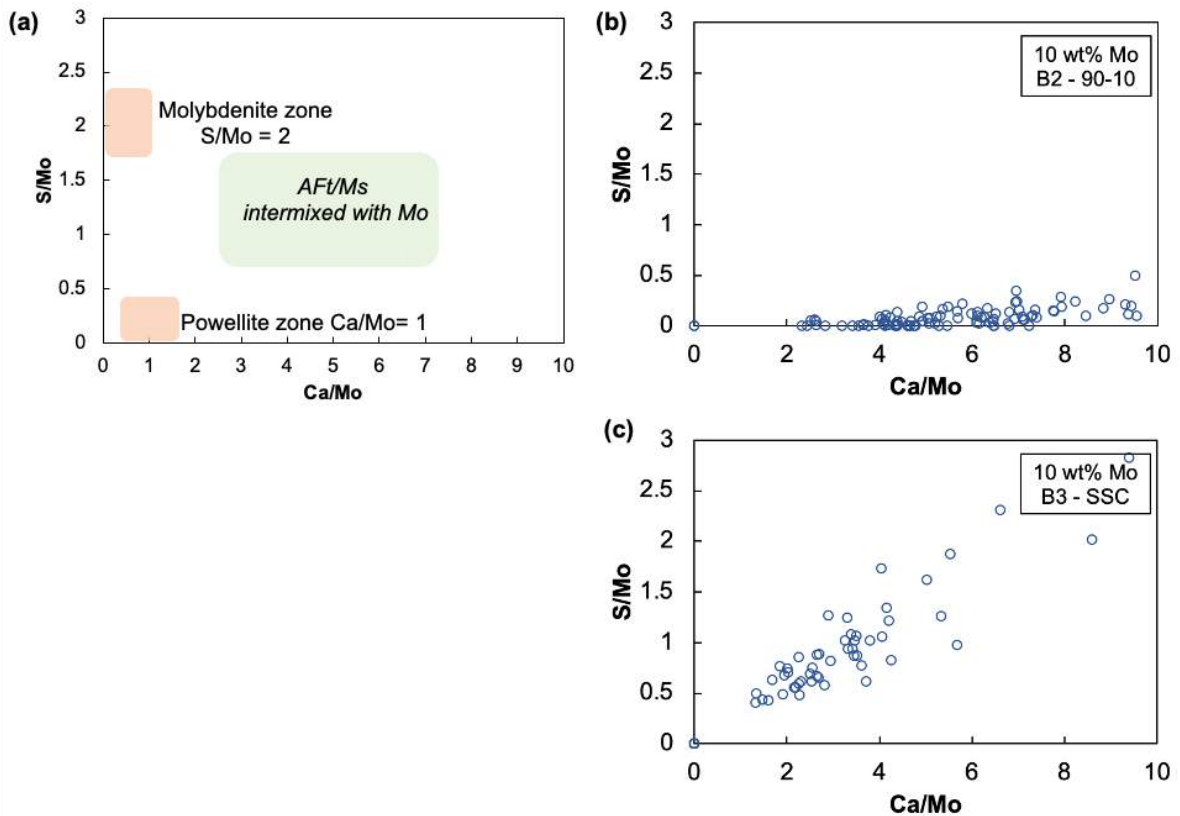
Figure 5.10 – **(a)** Interpretation of S/Mo vs. Ca/Mo EDS charts obtained from **(b)** B2(90-10) and **(c)** binder B3(SSC).

(iii)   Si/Ca vs. Mo/Ca EDS chart:

Figure 5.11 presents the Si/Ca vs. Mo/Ca EDS charts obtained from binders B2(90-10) and B3(SSC) with 10 wt% Mo. Figure 5.11(a) presents a schematic explanation of how to read this type of chart. X-axis and y-axis represent the molybdenum to calcium (Mo/Ca) and silicon to calcium (Si/Ca) atomic ratios, respectively. The zones marked in the plot correspond to the C-S-H phases having Ca/Si atomic ratios between 1.4 and 2.0 (Si/Ca of 0.7 and 0.48, respectively) and to the mineral powellite, which has an Mo/Ca atomic ratio of 1. The dotted line represents a slope allowing for identification of C-S-H mixed with powellite or for identification of Mo interaction with C-S-H (mainly at low Mo concentrations).

It can be observed that C-S-H precipitated in both materials but in minor extent in B3(SSC). In binder B2(90-10), Mo seemed to be adsorbed onto C-S-H (cf. Figure 5.11(b)); meanwhile, in binder B3(SSC), powellite seemed to be intermixed with C-S-H due to the big population of points placed towards the powellite area (cf. Figure 5.11(c)). Moreover, in binder B3(SSC), a big population of points was observed below the slope and they may indicate the presence of Mo in sulfate-bearing phases.
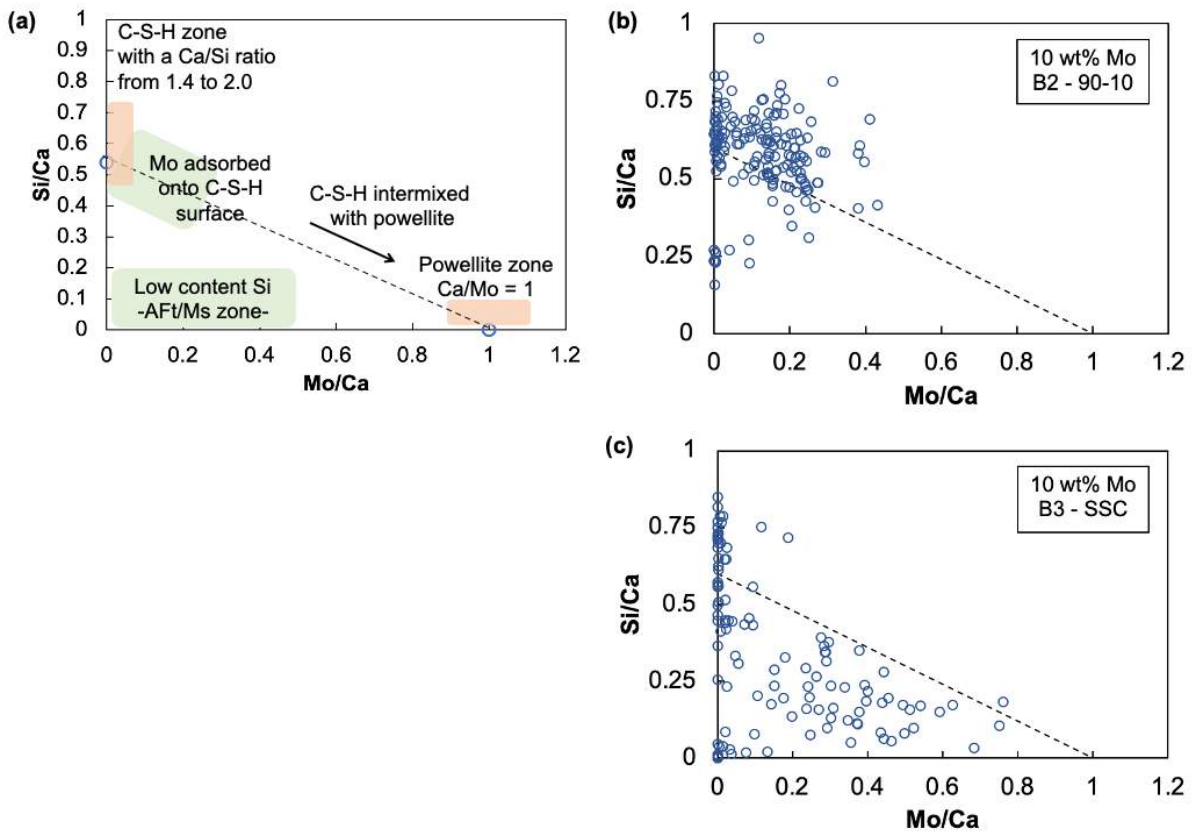
Figure 5.11 – **(a)** Interpretation of Si/Ca vs. Mo/Ca EDS charts obtained from **(b)** B2(90-10) and **(c)** binder B3(SSC).

As mentioned previously, some hypotheses were taken into consideration to explain the mechanisms of Mo immobilization by using the binders B1(CEM I), B2(90-10) and B3(SSC):

- the precipitation of powellite ($CaMoO_4$),
- the adsorption of Mo onto the surface of C-S-H,
- the substitution of sulfate by molybdate in ettringite (AFt) and monosulfoaluminate (Ms),
- redox reactions.

After the analyses of the results presented previously, we can partially conclude that:

- Mo was partially immobilized by the precipitation of powellite,
- Mo was probably adsorbed onto the surface of C-S-H, mainly at low Mo concentrations (<1 wt%),
- Mo was present in AFt and Ms,
- Molybdenite (MoS_2) was not identified in the binders probably because of binders containing GGBS, B2(90-10) and B3(SSC), did not present enough reducing internal environments (low pH and negative electrochemical potential) or because of the high detection limits of the techniques used.

This study was completed by modeling in order to better understand the precipitation of powellite. Moreover, we also decided to study the immobilization of Mo by the synthesis of C-S-H (more details about this choice are presented in the corresponding section 5.2).

In the following section, we present the modeling performed with PHREEQC for all the binders studied.

5.1.4 Modeling

Modeling was carried out in order to better understand the immobilization of Mo by the precipitation of powellite. The modeling was performed in accordance with the method

presented in Chapter 2 – section 2.2.5.3. As a reminder, the main hypotheses made in this modeling are:

- The initial solution was defined by using a liquid to solid ratio of *L/S*=10 L/kg, a temperature of *T*=25°C and a *pH* of 7.0. These parameters are similar to the ones used in the paste leaching tests.
- The binders were defined by their elemental chemical composition and the amount of water used to hydrate the binders was added to the system.
- Molybdenum was incorporated to the solution by using sodium molybdate, which was added at different steps and keeping the same Mo concentrations used experimentally.
- Congruent dissolution was assumed for all the constituents (binder and sodium molybdate).
- For the binders B2(90-10) and B3(SSC), the hydration of the GGBS was assumed to be 30% as presented in Chapter 4 – section 4.3.2.
- This modeling includes the thermodynamic data of powellite found in the literature [168].
- The adsorption of Mo onto C-S-H and the substitution of sulfates by molybdate in ettringite and monosulfoaluminate were not simulated in this modeling since few thermodynamic data exist for these reactions.
- Modeling gives the concentrations of elements in the solution. This solution is assumed to be at the equilibrium and is compared to the element concentrations found in the eluates obtained experimentally after paste leaching tests. Consequently, the kinetics of the chemical reactions were not taken into account in this model, which represents only the state of equilibrium reached by the system.

Figure 5.12 presents the numerical calculations obtained from the three binders in contact with Mo. Modeling data are represented by red lines, while experimental data are represented by circles. Calcium (Ca) and molybdenum (Mo) concentrations are expressed in mg/kg of binder and they are compared with experimental results. All data are plotted as a function of the initial Mo concentrations expressed in mg/kg of binder.
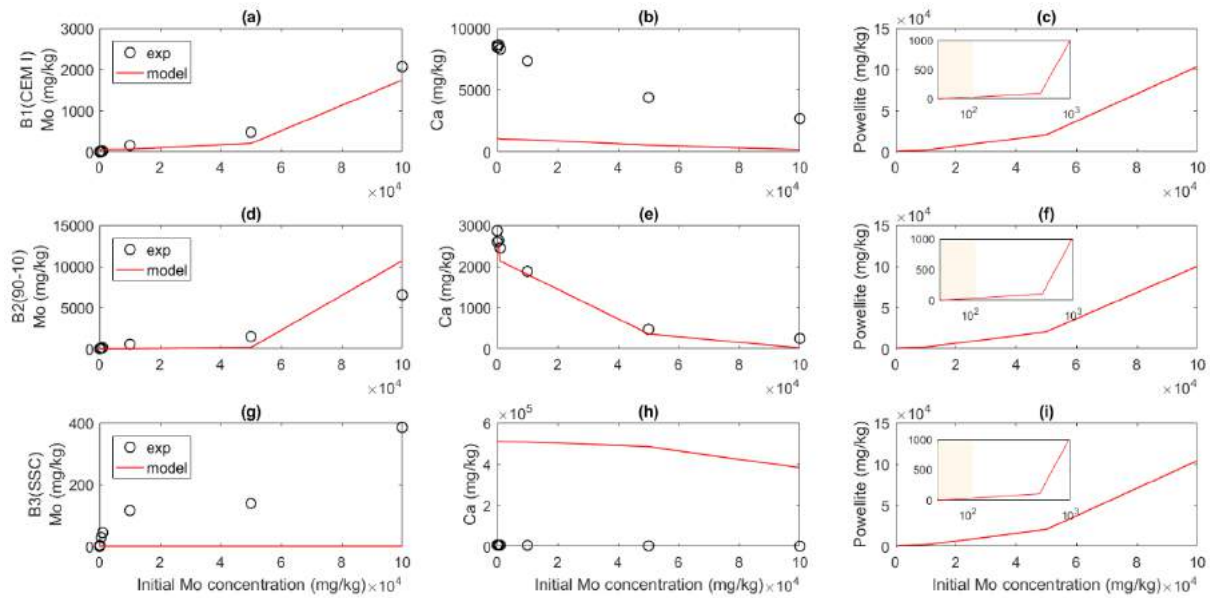
Figure 5.12 – Comparison between numerical and experimental data obtained from Mo-spiked binders. Molybdenum (Mo) and calcium (Ca) concentrations in solution and precipitation of powellite. All data are plotted as a function of the initial Mo concentration. Concentrations are expressed in mg/kg of binder. Circles: experimental data. Red lines: numerical data. (**a**), (**b**) (**c**) B1(CEM I), (**d**), (**e**), (**f**) B2(90-10), and (**g**), (**h**), (**i**) B3(SSC).

Overall, it can be observed that modeling did not fit properly the experimental data, mainly for the binder B3(SSC). However, the trends of Mo and Ca concentrations were in good agreement. Moreover, the model showed that Mo was partially immobilized in all the binders and that Ca decreased while increasing Mo concentrations. This was explained by (i) the precipitation of powellite, which was formed in all the binders and for all the Mo concentrations studied except for Mo concentrations of 50 mg/kg of binder, and (ii) the instability of ettringite at high sodium molybdate concentrations (concentrations superior to 5 wt% Mo, % by weight of dry anhydrous binder).

Regarding Ca concentrations, the discrepancies may be explained by the stability of C-S-H phases. In the model, the precipitation of C-S-H phases may be too stable with respect to the C-S-H phases that were really formed experimentally. Among all the binders, the modeling of the binder B3(SSC) showed the most important discrepancies between numerical calculations and experimental data. This model needs more adjustments in order to fit numerical and experimental data. One of them may be the stability of powellite with respect to the other phases formed in this binder. Other reason explaining the discrepancies between numerical and experimental results may be that the reaction between calcium and molybdenum to form powellite was not the only stabilization mechanism responsible for Mo immobilization. As a

reminder, EDS analyses showed that Mo interacted with sulfate-bearing phases and in this model, we did not simulate that phenomenon.

In conclusion, modeling should be adjusted in order to represent properly the behavior of the Mo-spiked binders. However, numerical calculations allowed to confirm that the precipitation of powellite was possible in all the systems in their characteristic pH values (pH 11-13), over the range of Mo concentrations studied except for concentrations equal to 50 mg_{Mo}/kg_{binder}, for which Mo was probably immobilized experimentally by other stabilization mechanisms.

In the following sections, we deal with the better understanding of Mo stabilization mechanisms by synthetic C-S-H phases and we perform a less complex model in order to predict the precipitation of powellite at low Mo concentrations.

5.2 Synthetic C-S-H phases with Mo

Justification:

One of the hypotheses taken into consideration to explain the stabilization of Mo by using the binders was the immobilization of Mo by the calcium silicate hydrates (C-S-H). In order to verify the capacity of this phase to immobilize Mo, we decided to synthesize C-S-H. Other relevant justifications of this choice are listed below:

- This phase is present as one of the main hydration products in all the three binders studied and EDS analyses showed that Mo was mixed with C-S-H.

- According to the literature, C-S-H phases present characteristics to immobilize anionic heavy metals (e.g. chromate) by co-precipitation or adsorption onto their surface [86], [127], [118].

- In the literature, ettringite (AFt) and monosulfoaluminate (Ms) have already been a topic of research to explain Mo immobilization; while only recent publications deal with the capacity of C-S-H to immobilize Mo.

Synthesis of C-S-H phases:

All the syntheses were conducted following the protocol presented in Chapter 2 – section 2.1.3.4. As a reminder, the synthesis of C-S-H phases was carried out by using three different chemical reactants: lime (CaO), amorphous silica (SiO_2) and sodium molybdate (Na_2MoO_4) and the target stoichiometric Ca/Si ratio was set at 1.6. Five different Mo concentrations were

used for the synthesis of C-S-H phases. These concentrations were chosen to observe the capacity of C-S-H to immobilize Mo at different Mo concentrations and to guarantee Mo detection. Table 2.7 recalls the concentrations of the constituents used for the synthesis of C-S-H phases.

Table 5.3 – Description of all the syntheses of C-S-H with Mo.

ID	Solid CaO (g)	SiO$_2$ (g)	Initial Mo concentration (wt%) [a]	Mo (g)	Total reactants (g)	Total water (g)[b]	Initial Mo concentration (mg/L)	Initial Mo concentration (mg/kg of dry solid) [c]
CSH			0	0	20	1000	0	0
CSH_0.25			0.25	0.05	20.11	1005.4	50	2500
CSH_1	11.98	8.02	1.0	0.2	20.43	1021.5	100	10000
CSH_2.5			2.5	0.5	21.07	1053.6	500	25000
CSH_5			5.0	1	22.15	1107.3	1000	50000

[a] % by weight of CaO+SiO$_2$
[b] Keeping a liquid to solid reactants (L/S) ratio of 50.
[c] Solid = 20 g of CaO+SiO$_2$

All the C-S-H phases were characterized by performing mineralogical and microstructural analyses. Moreover, modeling, carried out with PHREEQC, was performed in order to better understand the co-precipitation of powellite. In the following section, we present the characterization of the synthetic C-S-H phase without Mo.

5.2.1 Characterization of the synthetic C-S-H without Mo

Elements in solution after C-S-H filtration:

Synthetic C-S-H was filtrated after one month of agitation. The solution was analyzed and the remaining concentrations of Ca and Si in solution are presented in Table 5.4.

Table 5.4 – Ca and Si concentrations in solution before and after filtration of synthetic C-S-H without Mo. Final concentrations were measured twice and the values are the arithmetic averages. They are given with a confidence interval of 95%. pH of the solution is specified.

	Ca	Si	pH
Initial concentration (mg/L)	8562	3750	-
Final concentration (mg/L)	495.3 $\pm$ 10.9	12.55 $\pm$ 0.04	12.84

It can be observed that about 6% of Ca remained in solution, meaning that 94% of Ca reacted to form C-S-H. As expected, lower Si concentrations (0.34% of Si) were measured in solution.

XRD analyses:

Figure 5.13 presents the XRD pattern obtained from synthetic C-S-H without Mo where rutile (TiO_2) was present as an internal standard. The peak of rutile between 2θ 27º and 28º allowed us to confirm that the pattern was correctly positioned. Some peaks corresponding to portlandite and calcite were also identified. The eight other peaks in the XRD pattern correspond to C-S-H.
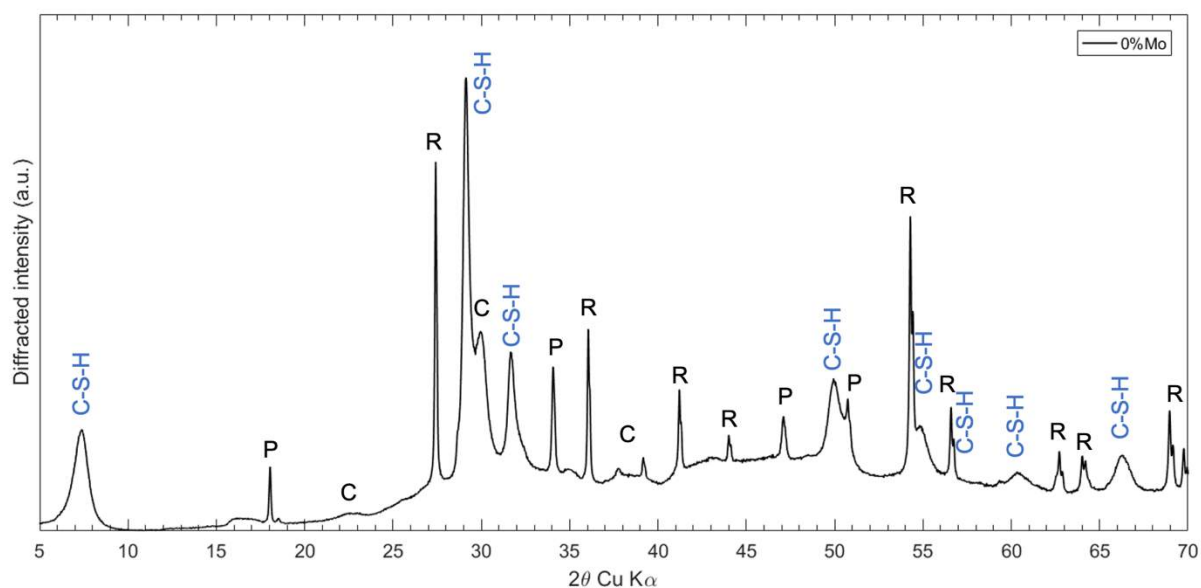
Figure 5.13 – XRD pattern obtained from the synthetic C-S-H phase without Mo. **P:** Portlandite, **C:** Calcite, **R:** Rutile.

SEM/EDS analyses:

Figure 5.14 presents the SEM/EDS observations carried out in the synthetic C-S-H phase without Mo. It can be observed the nanocrystalline framework of the C-S-H phase. Furthermore, the EDS spectrum allowed us to confirm the absence of other elements in this phase and the calcium to silicon (Ca/Si) ratio. Moreover, Figure 5.15 presents the EDS punctual analyses obtained from pure C-S-H. Figure 5.15(a) presents a chart where x-axis and y-axis represent the Ca/Si atomic ratio and the number of EDS points, respectively. The black dotted line represents the Ca/Si average value of 1.62 (from a total of 100 EDS points). Figure 5.15(b) shows a histogram of EDS punctual analyses where it can be observed that Ca/Si atomic ratio varied mainly from 1.4 to 1.8.
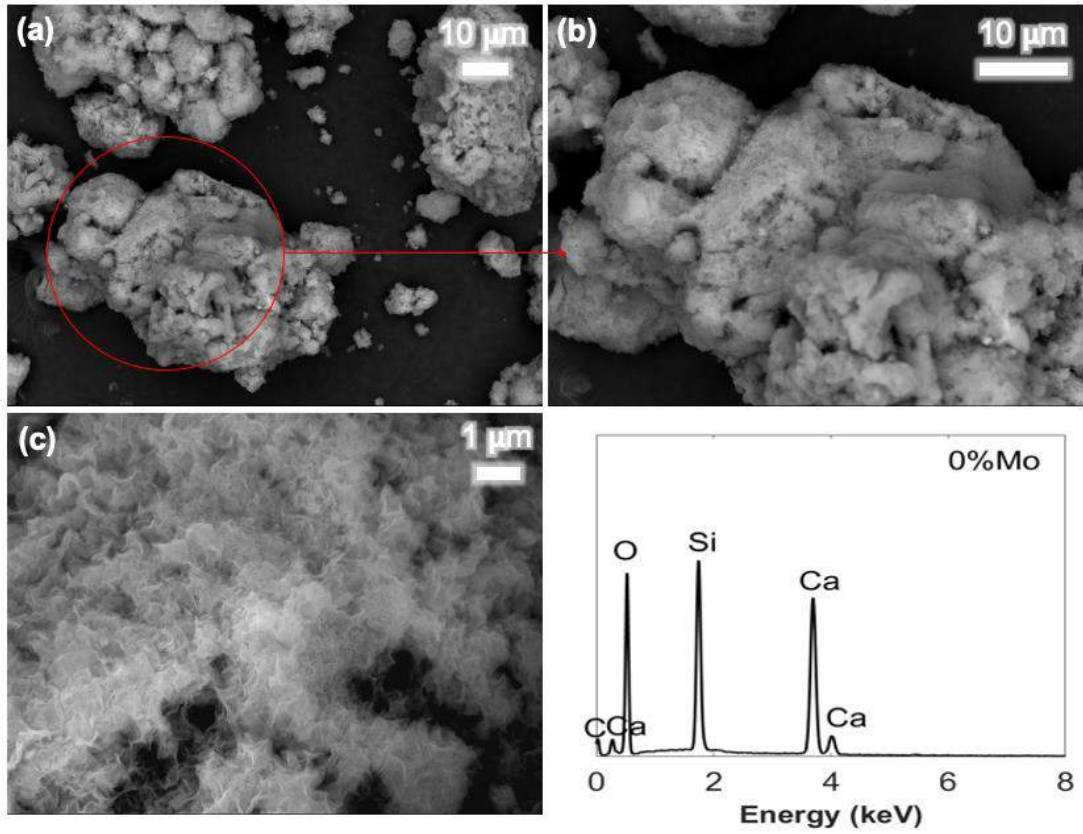
Figure 5.14 – SEM/EDS observations of synthetic C-S-H without Mo.
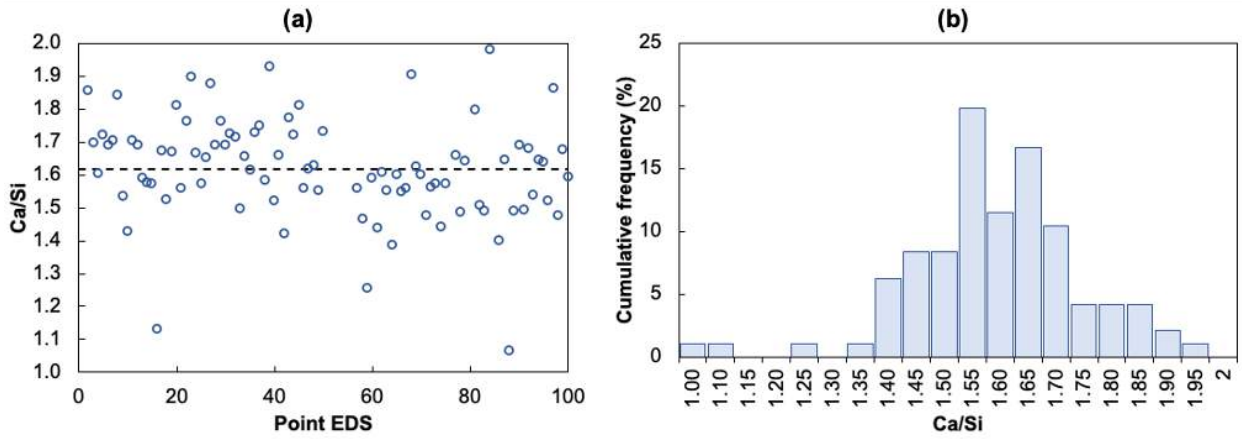
Figure 5.15 – EDS punctual analyses obtained from synthetic C-S-H without Mo. **(a)** Ca/Si vs. number of EDS points, and **(b)** histogram of EDS punctual analyses.

5.2.2 Synthetic C-S-H phases and Mo immobilization

After filtration of the synthetic C-S-H phases, solutions were chemically analyzed to measure the remaining element concentrations and therefore, to verify the retention of Mo in the solid fractions. Table 5.5 and Figure 5.16 show the pH values and concentrations in solution of molybdenum (Mo), calcium (Ca), silicon (Si) and sodium (Na). All concentrations are expressed in mg/kg of dry solid (solid = 20 g of $CaO+SiO_2$).

Table 5.5 – Element concentration in solution after synthetic C-S-H filtrations. Each point is the arithmetic average of two values. The results are presented with a confidence interval of 95%.

| Initial Mo concentration		Final element concentrations in solution (mg/kg of dry solid*)					
(wt%)	(mg/kg of dry solid)	Mo	Na	Ca	Si	pH	Mo retention (%)
0	0	0.0	0.0	49178 ± 544	628 ± 2	12.84	0
0.25	2500	114 ± 2	1756 ± 13	41885 ± 304	71 ± 19	12.88	95.5
1	10000	82 ± 0.4	5510 ± 78	39703 ± 230	52 ± 20	12.79	99.2
2.5	25000	184 ± 0.4	14390 ± 167	42840 ± 568	335 ± 29	12.73	99.3
5	50000	140 ± 5	22853 ± 299	28960 ± 265	91 ± 3	12.66	99.7

Solid = 20 g of $CaO+SiO_2$

From Figure 5.16, it can be observed that Mo concentrations in solution were relatively low compared with the initial Mo concentrations. Mo concentration in solution was about 22 times lower for the initial concentration of 0.25 wt% Mo. For the other levels, Mo concentration in solution decreased of about more than 100 times. Mo was immobilized in the solid fractions at percentages of 95 to 99%. On the other hand, sodium (Na) concentration increased in solution with increasing the initial Mo concentration. This behavior was expected due to the use of sodium molybdate (Na_2MoO_4) as the source of Mo. Additionally, the difference between the final and initial Na concentrations may indicate that Na was not adsorbed onto the C-S-H surface due to high Na concentrations and the high Ca/Si ratio of C-S-H. According to the literature, Na adsorption onto C-S-H is less for high Ca/Si values due to the high surface charge [211], [212]. As expected, the silicon (Si) concentration in solution remained very low, indicating that almost all the amorphous silica reacted to form C-S-H. Concerning the concentration of calcium (Ca) in solution, the trend of the curve remained relatively stable until the a concentration of 2.5 wt% Mo, from which, Ca concentration decreased in solution. Details about this behavior are addressed in the discussion.
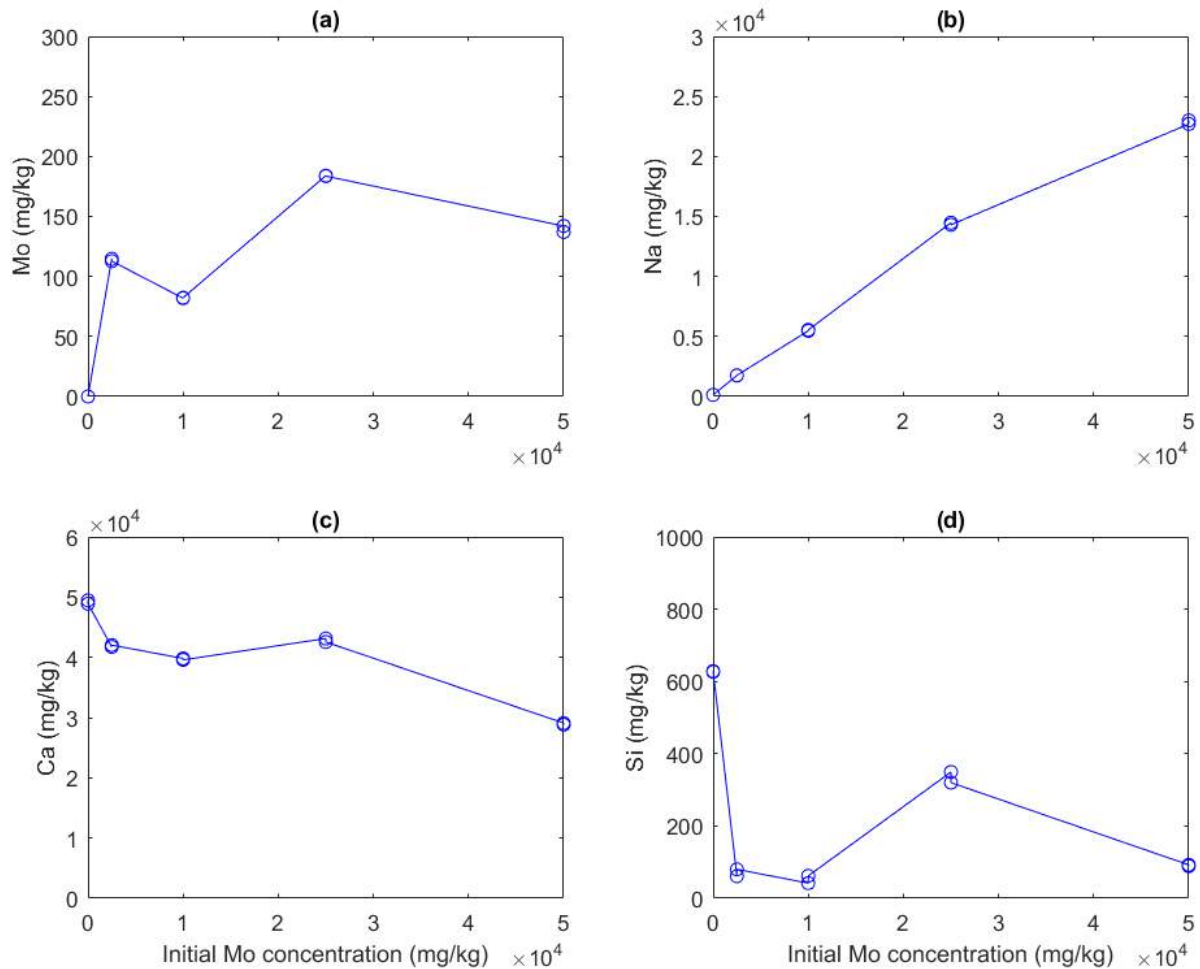
Figure 5.16 – Element concentrations in solution after filtration of synthetic C-S-H phases plotted as a function of the initial Mo concentration. Concentrations expressed in mg/kg of dry solid **(a)** Molybdenum, **(b)** sodium, **(c)** calcium, and **(d)** silicon. Solid = 20 g of $CaO+SiO_2$

As Mo was retained in the solid fractions, several hypotheses were taken into consideration in order to explain Mo immobilization in synthetic C-S-H phases:

(i)   Mo co-precipitated with free Ca^{2+} ions to form powellite ($CaMoO_4$),

(ii)   Mo was incorporated in between the C-S-H layers,

(iii) Si^{4+} was substituted by Mo^{6+}, and

(iv)   Mo was adsorbed onto the C-S-H surface.

Therefore, the characterization of synthetic C-S-H phases was carried out in order to corroborate the four hypotheses mentioned above. To this end, synthetic C-S-H phases were analyzed by using XRD, TGA, FT-IR and SEM/EDS. The approach followed is presented in

Figure 5.17. All the results will be presented by technique and they are summarized in the discussion section (cf. Table 5.10 and Figure 5.27).
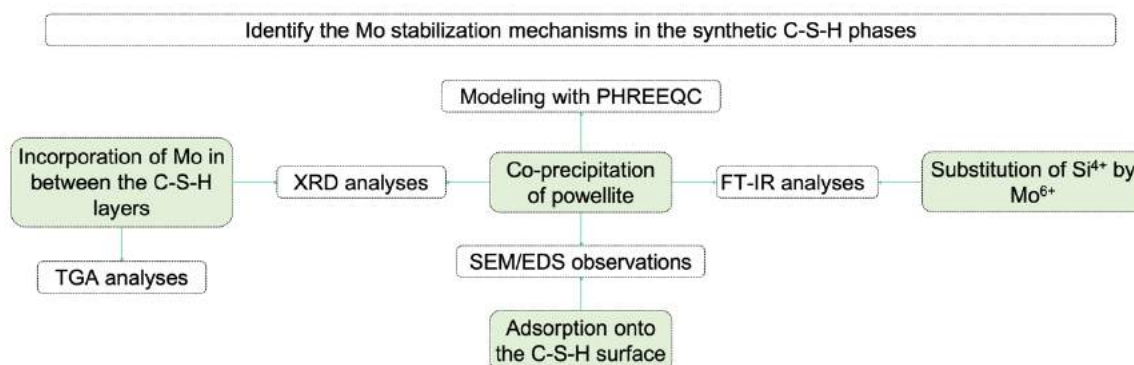
Figure 5.17 – Approach followed to identify the Mo stabilization mechanisms by synthetic C-S-H phases.

5.2.3 XRD analyses

Figure 5.18(a) presents the XRD patterns of all the synthetic C-S-H phases plotted in the range between 2θ 5⁰ and 70⁰. In this figure, the patterns were plotted shifting the y-axis and the red pattern corresponds to the synthetic C-S-H without Mo (0% Mo). Moreover, all the patterns have several peaks characteristics of rutile (TiO_2), which was the internal standard that allowed us to confirm that the patterns were correctly positioned.

It can be seen that the peak of C-S-H in between 2θ 5⁰ and 10⁰ was not shifted towards lower degrees, which may indicate that Mo was not in between C-S-H layers.

Overall, the mineral powellite ($CaMoO_4$) was identified in all the synthetic C-S-H phases containing Mo. Furthermore, it can be observed that the relative intensity of the peaks of powellite increased with increasing Mo concentrations. In order to highlight the presence of powellite, XRD patterns were plotted in Figure 5.18(b) and Figure 5.18(c) in the selected ranges from 2θ 27⁰ to 32⁰ and 2θ 57⁰ to 60⁰, respectively. All these patterns were superposed and normalized in respect to the rutile peak placed in 2θ 27⁰-28⁰. For ease of identifying powellite, the peaks were filled in different colors.
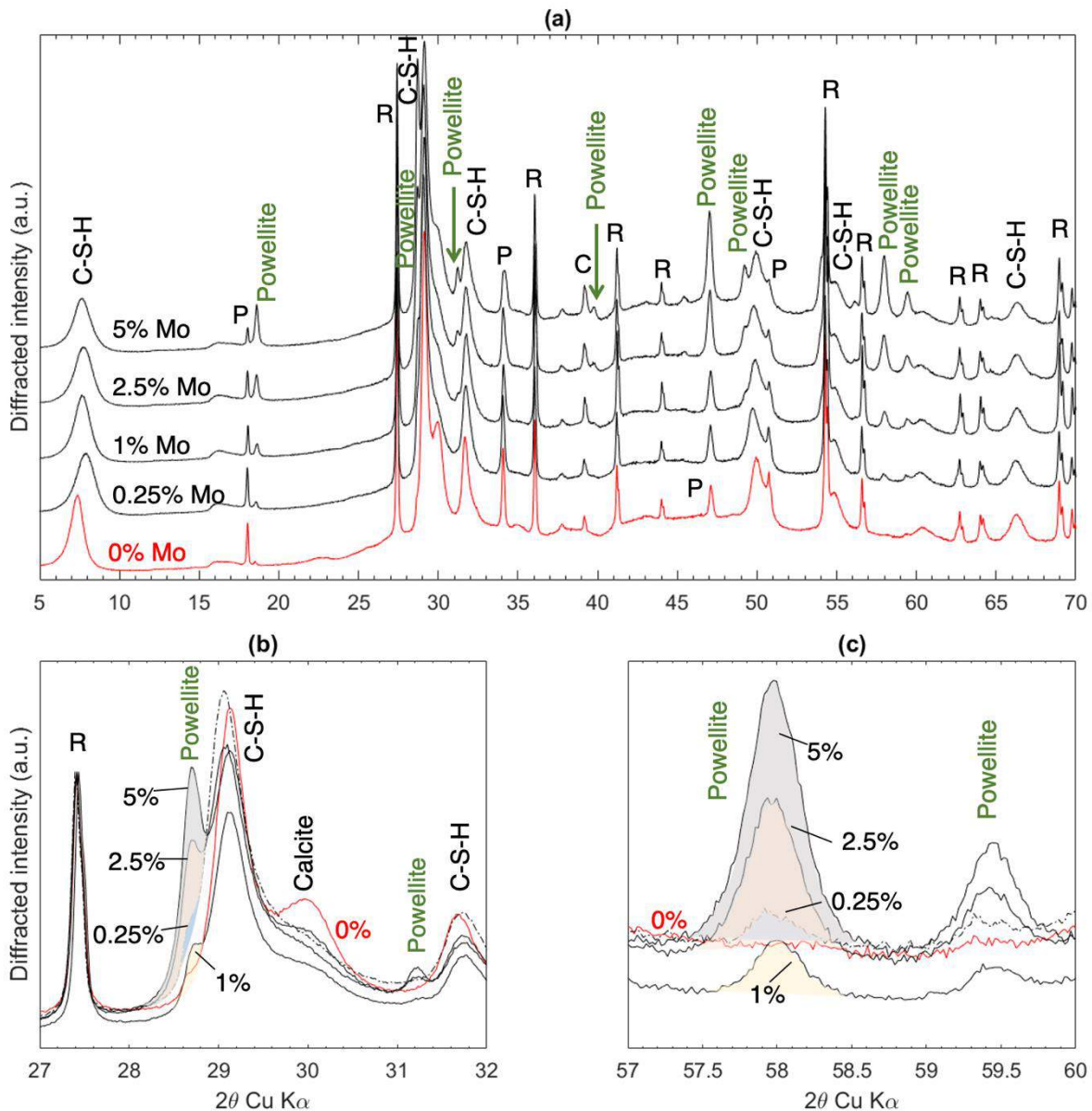
Figure 5.18 – XRD patterns of synthetic C-S-H with and without Mo using 10 wt% rutile (TiO_2) as internal standard. **(a)** from 2θ 5° to 70°, **(b)** superposed patterns from 2θ 27° and 32°, **(c)** superposed patterns from 2θ 57° and 60°. Percentages in (b) and (c) refers to initial Mo concentrations (wt%).

Estimation of the amount of powellite:

It is worth noting that we tried to estimate the quantity of powellite formed in all the solid fractions by using the XRD analyses and the Rietveld method. However, the following constraints and limitations were encountered:

(i)   C-S-H is not a standard phase; therefore, the information found in the available data base did not fit properly,

(ii)   the software did not recognize the main peak of powellite (placed in 2θ 28.5º-29º) due to the low relative intensities and because it overlapped with the main peak of C-S-H placed in 2θ 29º-29.5º.

Therefore, the amount of powellite formed during the synthesis of C-S-H was estimated by the values of the relative intensities of three peaks of powellite placed in: (i) 2θ 28.5º-29º, (ii) 2θ 57.5º-58.5º, and (iii) 2θ 59º-60º. Figure 5.19 presents the XRD pattern of pure powellite taken from RRUFF database and the position of these three peaks. The intensity of these three peaks were then compared with the relative intensity of the main peak of C-S-H (2θ 29º-29.5º). The relative intensity of this C-S-H peak was normalized to 100% and the proportions of powellite were then calculated. Table 5.6 presents the estimation of the amounts of powellite precipitated in solution. It can be seen that the relative amount of powellite increased with increasing the Mo concentrations. Moreover, it seemed that the relative amount of C-S-H decreased with increasing the amount of powellite formed. We think that this may be due to a dilution effect. More details will be presented in the following sections.

It should be noted that this method of estimation allowed us to have an idea of the amount of powellite formed in the solution. However, this method may overestimate the real concentrations of this mineral, mainly at the low Mo concentrations, where the peaks of powellite overlapped the peaks of C-S-H.
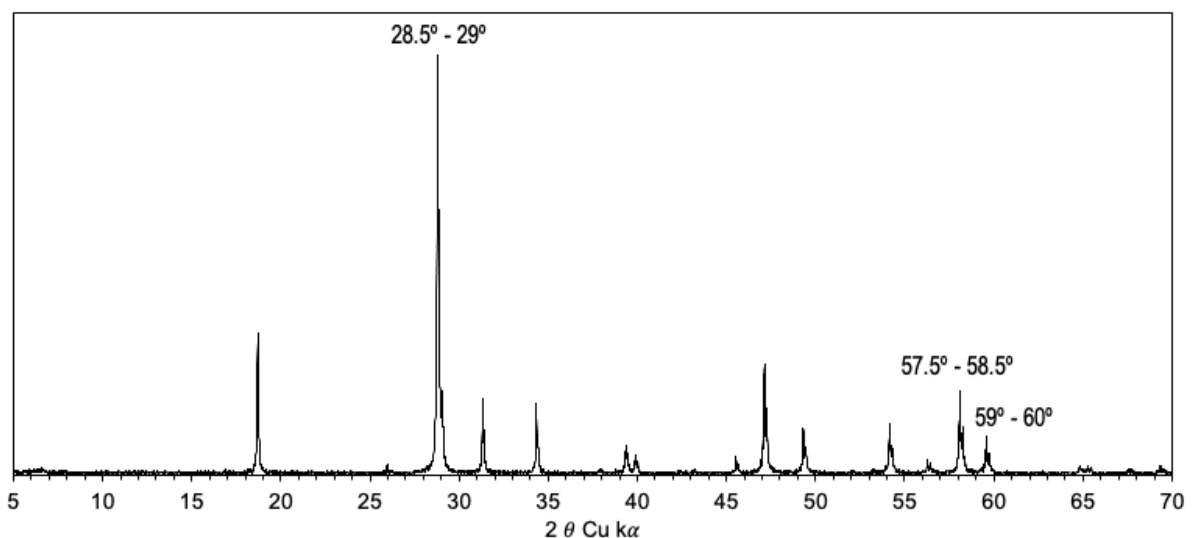
Figure 5.19 – XRD pattern of pure powellite taken from RRUFF database (ID R050355.1).

Table 5.6 – Estimation of the proportion of powellite co-precipitated in solution by using XRD patterns. Concentrations are expressed in percentage by weight (wt%).

	Position of the peaks			
	2θ 29°-29.5°	2θ 28.5°-29°	2θ 57.5°-58.5°	2θ 59°-60°
Mo (wt%)	C-S-H (wt%)	Powellite (wt%)	Powellite (wt%)	Powellite (wt%)
0	100	0	0	0
0.25	96.3	3.7	3.9	5.7
1	95.9	4.1	4.6	5.9
2.5	93.8	6.2	6.2	6.9
5	91.9	8.1	8.1	8.1

5.2.4 TGA analyses

TGA measurements were performed on synthetic C-S-H phases. We decided to humidify the synthetic phases for two days in a controlled nitrogen atmosphere using potassium sulfate (K_2SO_4) in order to have the same initial conditions before the analyses. Then, the phases were dried in an oven at 40 ºC in order to remove the bulk water [213]. Figure 5.20 presents the TGA analyses of all the synthetic C-S-H phases. Figure 5.20(a) shows the curves of differential thermogravimetry (DTG) data of weight loss expressed in wt%/ºC, and Figure 5.20(b) shows the curves of weight loss data normalized to 100 wt% of the initial weight. All data were plotted as a function of the temperature expressed in Celsius (ºC).

Table 5.7 presents the different percentages of weight loss estimated for all the synthetic C-S-H phases after TGA analyses.

Table 5.7 – Estimation of the weight loss in percentage of synthetic C-S-H phases after TGA analyses.

ID	Initial Mo concentration (wt%)	Total weight loss (%)	Weight loss between 0 and 300°C (%)	Weight loss between 300 and 550°C (%)	Weight loss between 550 and 1000°C (%)
CSH	0	21.3	16.67	3.52	1.08
CSH_0.25	0.25	21.5	16.86	3.61	0.98
CSH_1	1	19.5	14.89	3.27	1.30
CSH_2.5	2.5	19.8	14.51	3.28	2.06
CSH_5	5	18.6	13.90	3.14	1.57
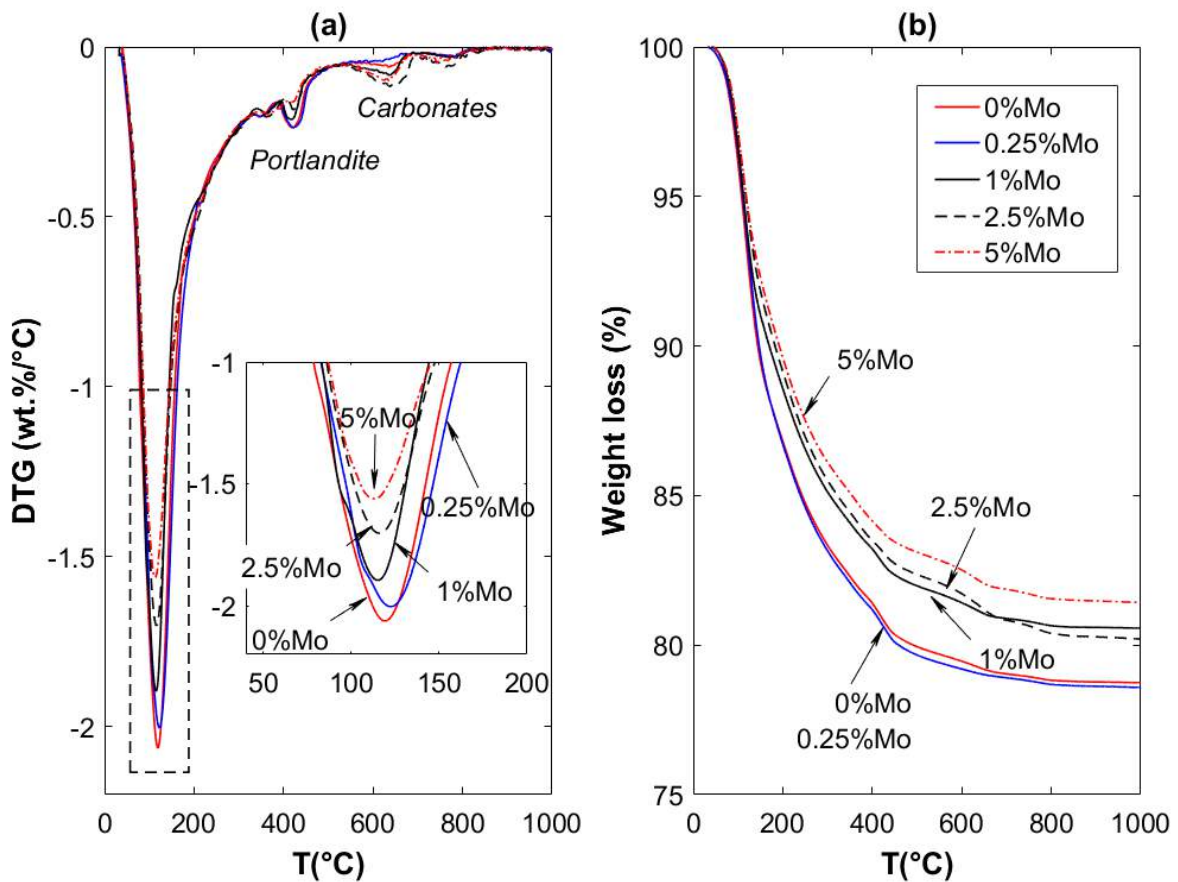
Figure 5.20 – Thermogravimetric analyses (TGA) of synthetic C-S-H phases (pre-humidified and dried at 40ºC). **(a)** Differential thermogravimetry (DTG) data of weight loss given in wt%/ºC, and **(b)** weight loss given in percentage. All data were plotted as a function of temperature from 0 to 1000ºC (heating rate 10ºC/min).

Figure 5.20(a) shows a peak placed in between 100 and 200 ºC, which corresponds to the dehydration of C-S-H. Moreover, it can be observed that the intensity of this peak decreased with increasing the initial Mo concentration. The second group of peaks were placed in between 350 and 500 ºC, and it was attributed to portlandite (CH), which was probably present due to the hydration of CaO. The third group of peaks was identified in between 600 and 800 ºC and it was mainly associated to the presence of carbonates (mainly mono- or hemicarbonates) [214] and calcite ($CaCO_3$)) due to the little carbonation of synthetic C-S-H phases during their preparation.

Figure 5.20(b) shows that the weight loss of synthetic C-S-H phases decreased with increasing Mo concentration. Moreover, it can be observed that the total weight loss of synthetic C-S-H phases was about 21% for C-S-H phases without Mo and with 0.25 wt% Mo. For the other synthetic C-S-H phases, the weight loss decreased with increasing Mo concentration.

However, it can be seen that between the C-S-H without Mo and the synthetic C-S-H phase with 5 wt% Mo, there was a little difference of total weight loss of about 2.7%.

Therefore, we can partially conclude that:

(i)   Mo co-precipitated with calcium to form powellite (cf. Figure 5.18). Therefore, less calcium was available to form C-S-H; decreasing the amount of C-S-H, which resulted in a decrease in the amount of bounded water. To confirm this, it would be then necessary to verify if Mo precipitated with free Ca ions in solution.

(ii)   The decrease in the weight loss of C-S-H can be explained by a dilution effect: the proportion of C-S-H decreased with increasing the Mo concentration because of the formation of powellite.

5.2.5 FT-IR analyses

FT-IR analyses were carried out in all the synthetic C-S-H phases in order to verify the modification of the vibration bands in the case of substitution of Si^{4+} by Mo^{6+}. If there is a substitution, the Si-O group would be modified. Figure 5.21 presents the spectra obtained from FT-IR analyses, in which x-axis and y-axis represent the wavenumber (given in cm^{-1}) and the transmittance (given in percentage), respectively. The spectra were normalized by the minimum value in order to compare the relative intensities of the different bands. Figure 5.21(a) and Figure 5.21(b) present the FT-IR spectra over the ranges from 4000 to 1100 cm^{-1} and 1100 to 600 cm^{-1}, respectively.

From Figure 5.21(a), it can be observed that the spectra feature common absorption bands with some differences in their relative intensities. The main absorption bands and corresponding assignments were: 3600-3100 cm^{-1} (OH stretching), 1700-1600 cm^{-1} (OH), 1600-1100 cm^{-1} (O-H deformation and C-O stretching), 1050-900 cm^{-1} (Si-O). In Figure 5.21(b), the spectra of sodium molybdate (Na_2MoO_4) and powellite ($CaMoO_4$) were also plotted in order to compare the position of the bands corresponding to the Mo-O group. (The powellite spectrum was obtained from the RRUFF ID R050355.2 database).
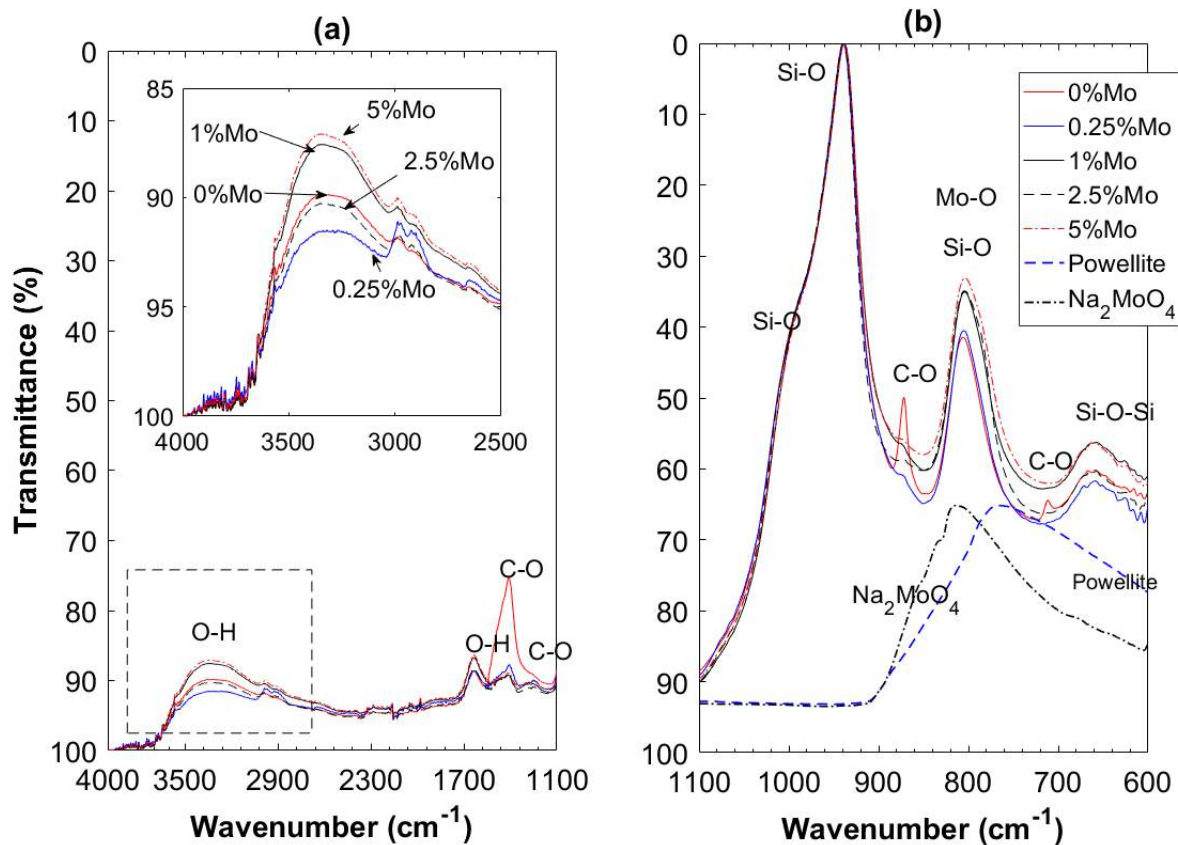
Figure 5.21 – FT-IR analyses of synthetic C-S-H phases. **(a)** In the 4000-600 cm^{-1} range, and **(b)** In the 1100-600 cm^{-1} range. Powellite spectrum obtained from RRUFF ID R050355.2.

From these analyses, it was found that:

(i)   The band of Si-O placed between 1050 and 900 cm^{-1} did not show any modification,

(ii)   The Si-O band placed between 850 and 750 cm^{-1} overlapped to Mo-O band,

(iii)   The relative intensity of the bands corresponding to Mo-O/Si-O differed among all the samples and seemed to increase with increasing Mo concentration.

In conclusion, we suggest that the increase in intensity in the band of Mo-O/Si-O corresponds to the formation of powellite. However, it is possible that at very low Mo concentrations, Mo^{6+} would replace Si^{4+} in C-S-H. To verify this, other methods with lower detection limits should be used.

5.2.6 SEM/EDS observations

<u>SEM/EDS observations:</u>

SEM observations were performed in all the synthetic C-S-H phases in order to characterize their morphology and to verify the presence of Mo. The SEM images presented provide a representative picture of the analyzed samples. EDS analyses were also carried out in powder in order to confirm the calcium to silicon (Ca/Si) atomic ratios. Figure 5.22 (at left) presents the SEM observations of synthetic C-S-H phases. Moreover, Figure 5.22 (in the middle) shows EDS spectra obtained from the samples. These spectra allowed for the verification of the presence/absence of Mo in the samples. Finally, Figure 5.22 (at right) shows the histograms of the Ca/Si atomic ratios calculated from the EDS punctual analyses.

Figure 5.22(a) shows the information about the synthetic C-S-H phase without Mo (0% Mo). The EDS spectrum confirmed the absence of Mo in this sample. EDS punctual analyses indicated that the Ca/Si atomic ratio was between 1.5 and 1.7. On the other hand, Figure 5.22(b) to Figure 5.22(e) present the information about the synthetic C-S-H phases containing Mo. Overall, the SEM images show the presence of several white points placed onto the surface of C-S-H. The amount and intensity of the white points increased with increasing the concentration of Mo. The chemical compositions of these points were obtained from the EDS spectra, which confirmed the presence of Mo (Figure 5.22 in the middle). Regarding the Ca/Si atomic ratios presented in Figure 5.22 at right, it seemed that Ca/Si ratio did not present significant changes and therefore, we think that C-S-H was not altered by the presence of Mo.
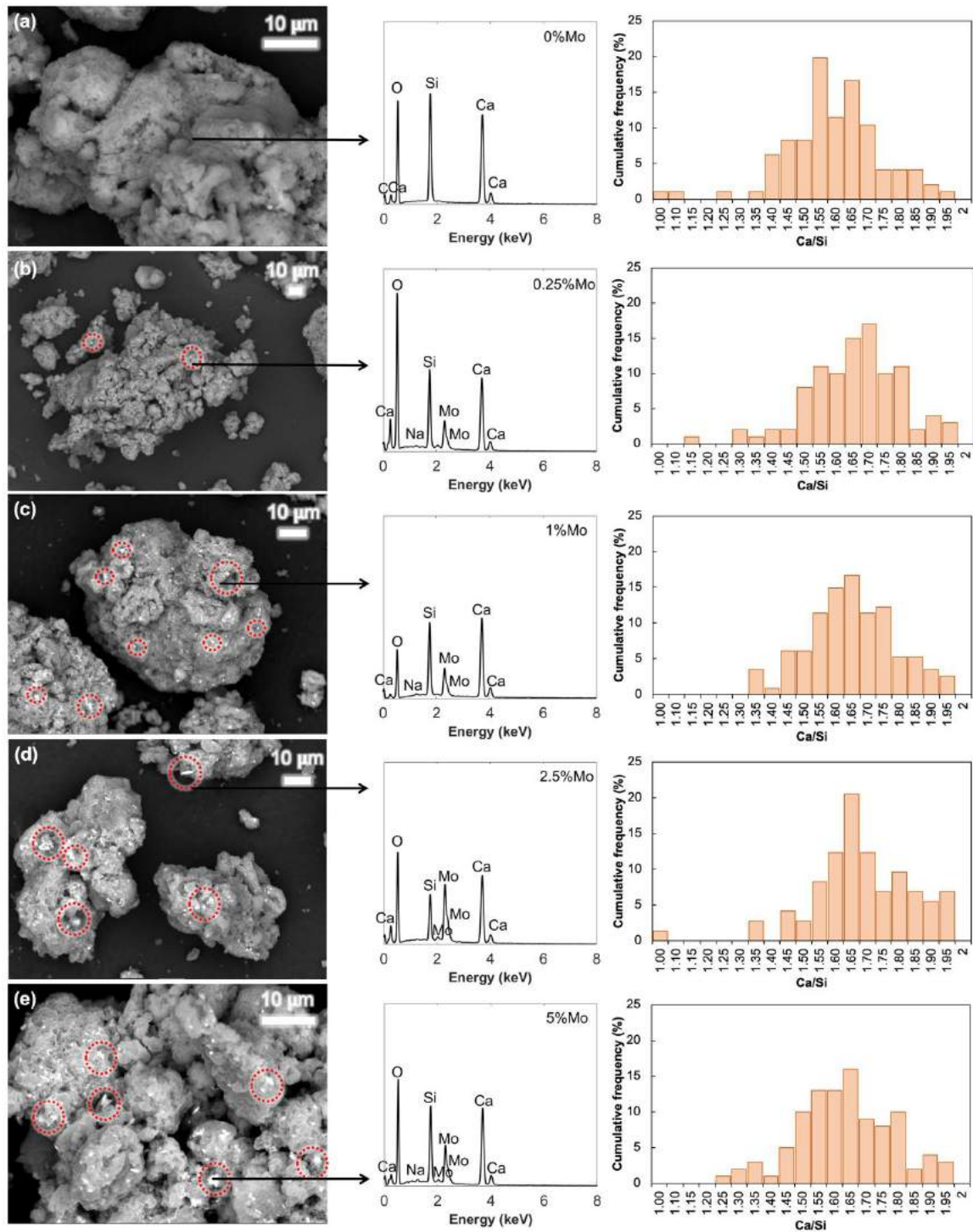
Figure 5.22 - SEM/EDS analyses of synthetic C-S-H phases. **Left:** SE images, **Middle:** EDS spectra, **Right:** Histograms of the Ca/Si ratios obtained from EDS punctual analyses. **(a)** 0 wt% Mo, **(b)** 0.25 wt% Mo, **(c)** 1 wt% Mo, **(d)** 2.5 wt% Mo, and **(e)** 5 wt% Mo. % by weight of solid (20 g of CaO+SiO$_2$).

EDS punctual analyses:

Figure 5.23 presents all the EDS plots obtained from the synthetic C-S-H phases. EDS punctual analyses were plotted in charts where x-axis and y-axis represent the Mo/Ca and Si/Ca atomic ratios, respectively. It should be noted that the number and position of EDS points were selected arbitrary in the samples (a minimum of 100 points). Figure 5.23(f) presents a schematic explanation of how to read this type of chart.
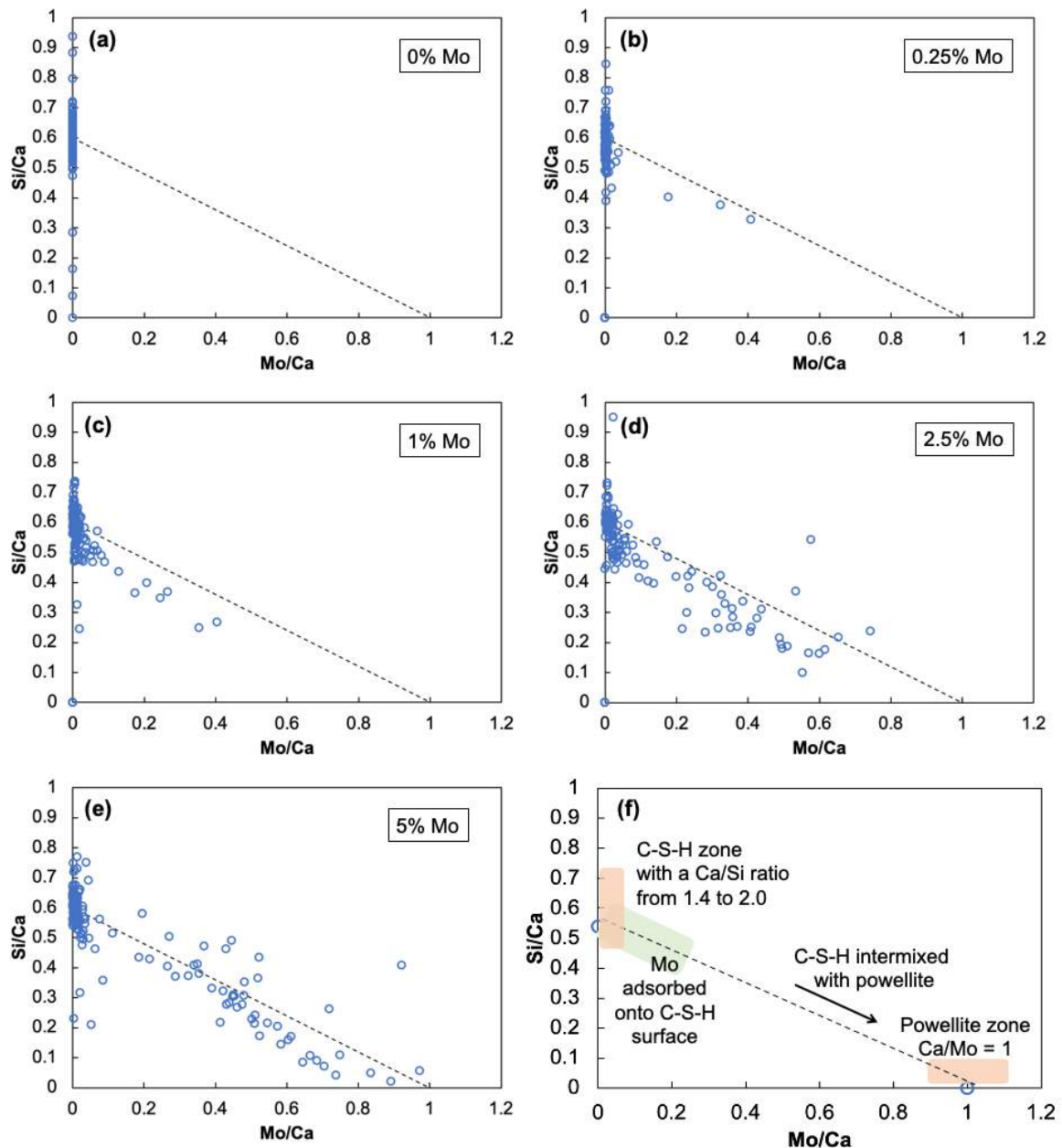
Figure 5.23 – Si/Ca vs. Mo/Ca charts from EDS punctual analyses obtained from all the synthetic C-S-H phases. **(a)** 0% Mo, **(b)** 0.25% Mo, **(c)** 1% Mo, **(d)** 2.5% Mo, **(e)** 5% Mo. (Percentages by weight of solid (20 g of CaO+SiO$_2$), and **(f)** interpretation of the chart.

Figure 5.23(a) shows the data of the synthetic C-S-H phase without Mo. It can be observed that no-point was placed in the horizontal axis due to the absence of Mo and that the Si/Ca ratio varied from 0.5 to 0.7 (Ca/Si from 2 to 1.4, respectively). On the other hand, Figure 5.23(b) shows the EDS data from the synthetic C-S-H with 0.25 wt% Mo. It can be observed that the Si/Ca atomic ratio did not change significantly and that some points appeared near the black dotted line, indicating the presence of Mo. Figure 5.23(c) shows the EDS information about the synthetic C-S-H with 1 wt% Mo, in which the Ca/Si ratio did not vary either. It can also be noted that a few more points appeared along the slope. Finally, Figure 5.23(d) and Figure 5.23(e) present the EDS analyses for synthetic C-S-H phases with 2.5 wt% and 5 wt% Mo. Similar behavior was observed in both samples; however, in these samples a bigger population of points appeared near the slope and followed the trend towards the Mo/Ca atomic ratio of 1.

These analyses indicate that:

(i)   Powellite was mixed with C-S-H.

(ii)   A proportion of Mo interacted with C-S-H surface, mainly at low Mo concentrations.

We can partially conclude that:

- The dominant stabilization mechanism of Mo was the co-precipitation of powellite,
- Mo was partially immobilized by the adsorption of Mo onto the C-S-H surface., mainly at low Mo concentrations (<1 wt%).
- Other mechanisms of Mo stabilization, such as the inclusion of Mo into the C-S-H layers and the substitution of Si^{4+} by Mo^{6+} were not identified, but they should be verified by other techniques having lower detection limits.

Numerical calculations were carried out by using a geochemical model in order to verify the co-precipitation of powellite with C-S-H. This modeling allowed us to verify the precipitation of powellite at low Mo concentrations that were not experimentally tested (<50 mg/kg of solid).

The following section presents the results obtained by modeling and compared with the experimental results.

5.2.7 Modeling

5.2.7.1 Numerical vs experimental data

Figure 5.24 presents a comparison between the numerical and experimental data obtained from the synthetic C-S-H phases. This figure gives information about the concentrations in solution of molybdenum (Mo), sodium (Na), calcium (Ca) and silicon (Si) as well as the pH values plotted as a function of the initial Mo concentration. All concentrations are given in mg/kg of solid (solid = 20 g of CaO+SiO$_2$). Experimental data are represented by circles while model calculations are given by red lines.

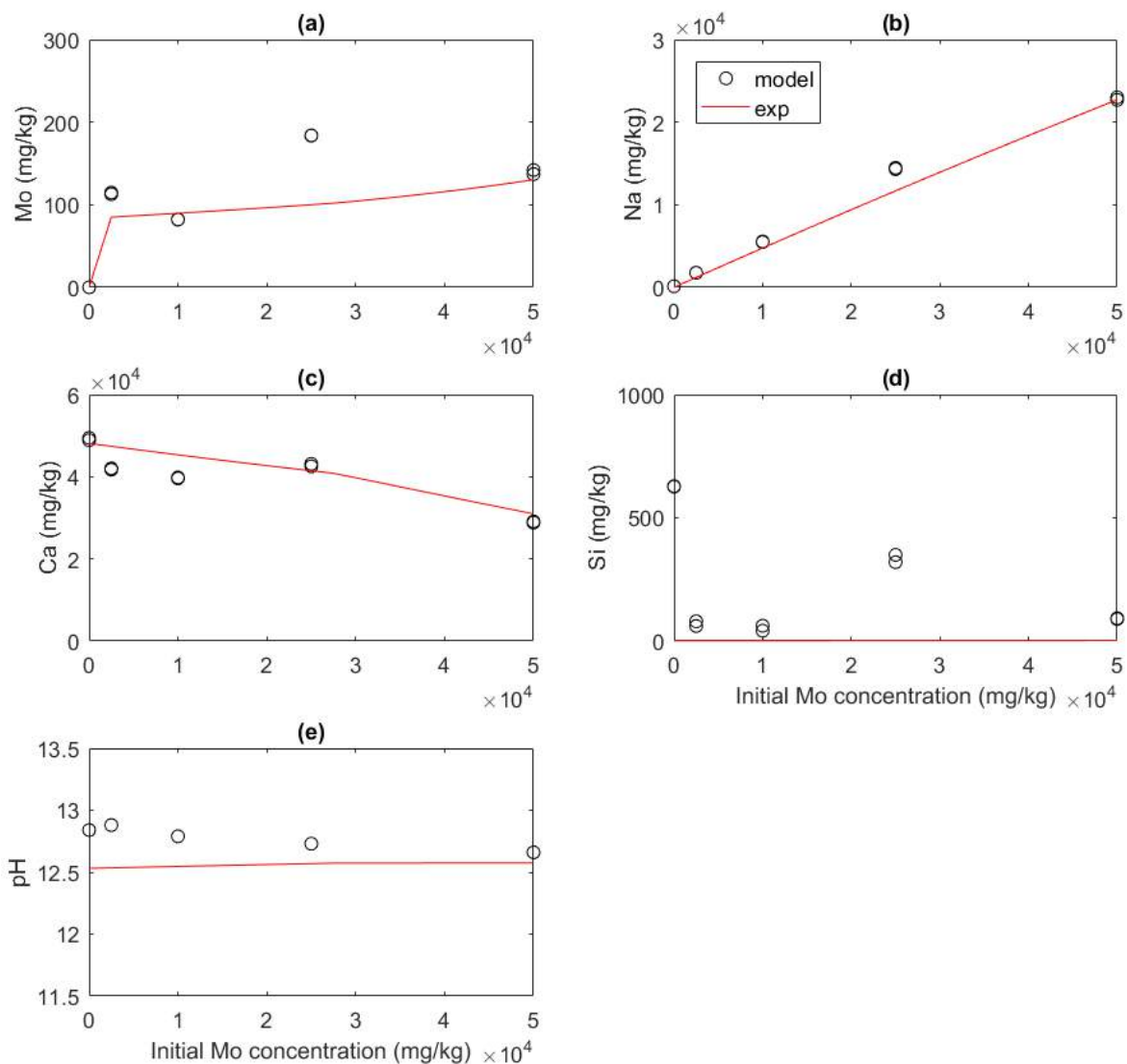**Figure 5.24** – Element concentrations in solution and pH values obtained from the synthesis of C-S-H with Mo. All the data are plotted as a function of initial Mo concentrations. All concentrations are expressed in mg/kg of dry solid. *Solid = 20 g of CaO+SiO$_2$.* Circles: experimental data. Red lines: numerical data. **(a)** molybdenum, **(b)** sodium, **(c)** calcium, **(d)** silicon, and **(e)** pH values.

Overall, experimental and numerical data were in good agreement for the general trend of element concentrations in solution. Experimental and numerical data showed that Mo concentrations in solution remained relatively constant over the initial Mo concentrations studied (cf. Figure 5.24(a)) and that Ca concentrations decreased gradually with increasing Mo concentrations in solution (cf. Figure 5.24 (c)). This indicates that free calcium ions in solution precipitated with Mo to form powellite, which seemed to be the mineral controlling Mo solubility. Figure 5.24(b) shows that sodium concentrations in solution increased with increasing Mo concentrations due to the use of sodium molybdate as source of Mo. Figure 5.24(d) indicates that silicon was present in very low concentrations in solution in both numerical and experimental calculations; however, silicon concentrations were even lower in modeling than experimentally. This was explained by the database used (Thermoddem version 1.10) for modeling, in which the thermodynamic data of C-S-H come from synthetic C-S-H phases crystallized over one year of equilibrium (meanwhile, in this study, C-S-H was obtained after one month of equilibrium). This means that, in this study, some silicon remained in solution since the solution was not yet at the equilibrium. Finally, Figure 5.24(e) presents the pH values, which remained relatively stable between the values of 12.5 and 13. It can also be observed that values obtained by the model are slightly lower than those obtained experimentally but that the trend of the values was similar.

> In order to verify if powellite precipitated at low Mo concentrations, this model was first validated by comparing the amount of powellite obtained by modeling with the amounts obtained by hand calculations.

5.2.7.2 Validation of the model – estimation the amount of powellite

In this section, we aimed to validate the information obtained by the model and therefore, we estimated the amount of powellite necessary to immobilize the total concentration of Mo used in the synthesis of C-S-H phases. To this end, we first estimated the amount of powellite by hand calculations and then, we compared these values with the ones obtained by modeling.

Hand calculations:

How many grams of Mo were initially in solution? The demonstration is made here for the highest Mo concentration: 5 wt% (% by weight of solid (20 g of $CaO+SiO_2$).

We set 20 g as the solid fraction used for the synthesis of C-S-H. Taking the highest Mo concentration → 5 wt% Mo equates to 1 g of Mo in solution.

Therefore, how many moles of powellite were necessary to immobilize 1 g of Mo?

1 mol $CaMoO_4$ contains 96 g Mo, then:

$$\frac{1 \text{ g Mo} * 1 \text{ mol } CaMoO_4}{96 \text{ g Mo}} = 0.0104 \text{ mol } CaMoO_4$$

As 1 mol $CaMoO_4$ = 200.1 g $CaMoO_4$

Then, 0.0104 mol $CaMoO_4$ = 2.084 g $CaMoO_4$

So, it is necessary to have about 2084 mg of powellite to immobilize 1 g of Mo (5 wt% Mo).

Table 5.8 presents the amounts of powellite for each of the Mo concentrations used for the different C-S-H syntheses.

Table 5.8 – Hand calculations results for the estimation of the amounts of powellite necessary to immobilize Mo concentrations used for the synthesis of C-S-H phases. Solid = 20 g of $CaO+SiO_2$

Mo (wt%)	Mo (g)	Powellite (mg)	Powellite (mg/kg of solid)
0	0	0	0
0.25	0.05	104	5200
1	0.20	417	20850
2.5	0.50	1042	52100
5	1.00	2084	104200

<u>Comparison between modeling and hand calculations:</u>

Figure 5.25(a) presents the Mo concentrations in solution obtained experimentally and by modeling. Figure 5.25(b) shows the comparison of the amounts of powellite calculated by modeling with the ones calculated by hand. Concentrations are expressed in mg/kg of solid (20 g of $CaO+SiO_2$) and are plotted as a function of the initial Mo concentrations. Experimental data are represented by circle, while model results are represented by a red line and hand calculations by asterisks.

Overall, it can be observed that the amount of powellite increased with increasing Mo concentrations in solution and that powellite precipitated in the system at concentrations between 0.25 and 5 wt% Mo (2500 and 50000 mg_{Mo}/kg_{solid}). Concerning the highest Mo concentration (5 wt% Mo), the model calculated that about 2078.6 mg/L of powellite precipitated, which was closed to the values calculated by hand (2084 mg/L~104200 mg/kg_{solid}). This means that modeling was able to predict accurately the

precipitation of powellite in the solution at concentrations between 0.25 and 5 wt% Mo (2500 and 50000 mg_{Mo}/kg_{solid}) and that powellite was the dominant stabilization mechanisms because more than 95% of Mo was immobilized by this mineral.
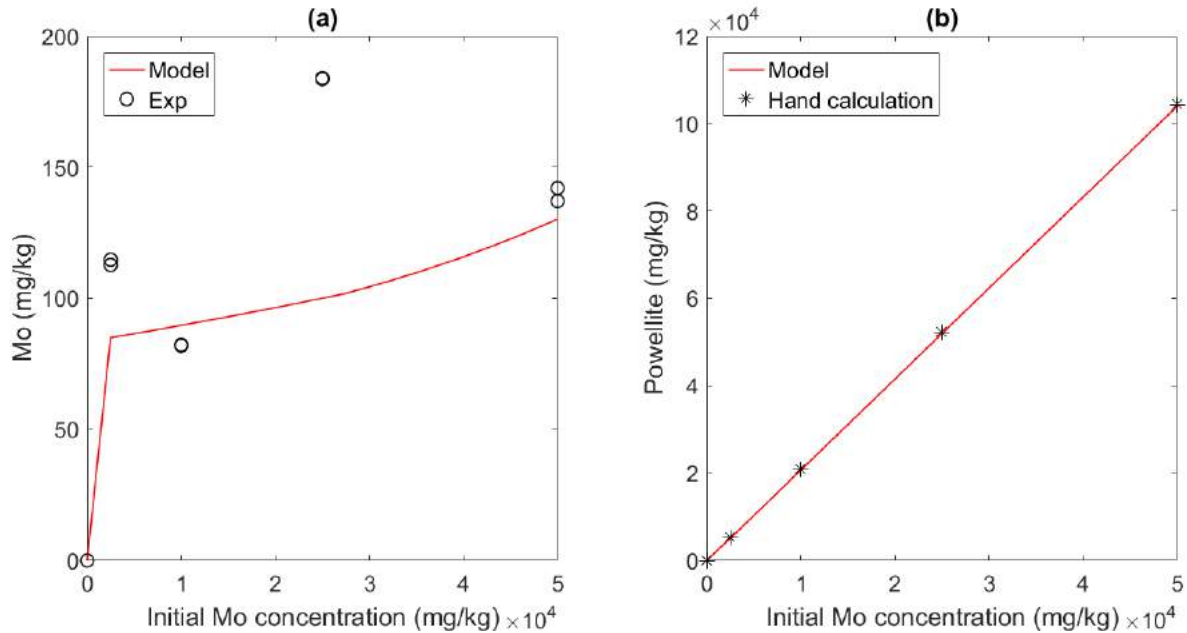
Figure 5.25 – Concentrations of molybdenum (Mo) and powellite plotted as a function of initial Mo concentration. Concentrations expressed in mg/kg of solid. **(a)** Molybdenum, **(b)** powellite. Circles: experimental data. Red lines: modeling. Asterisks: Hand calculations. *Solid = 20 g of CaO+SiO₂.*

Powellite values obtained by XRD were not used for validation of the model due to the low confidence in the values, mainly at low Mo concentrations (cf. section 5.1.2).

Since modeling was able to predict accurately the precipitation of powellite in the solution of C-S-H at Mo concentrations between 0.25 wt% and 5 wt%, we used this model to predict the precipitation of powellite at lower Mo concentrations (<0.03 wt%~ 300 mg/kg of solid).

5.2.7.3 Prediction of powellite at low Mo concentrations

The precipitation of powellite was verified at low Mo concentrations (<300 mg/kg of solid). All the concentrations used in this model are presented in Table 5.9. Moreover, Figure 5.26 presents the concentration of Mo in solution and the evolution of the precipitation of powellite.

All the data were plotted as a function of the initial Mo concentration. All concentrations are expressed in mg/kg of solid. Solid refers to the amount of CaO and SiO_2 initially used to synthetize C-S-H (20 g in total) and using liquid to solid (L/S) ratio of 50.

Table 5.9 – Initial Mo concentrations used for modeling

Waste category [a]	Initial Mo concentration			
	wt%	mg/L	mg/kg of solid [b]	mol/L
	0	0	0	0.0E+00
	1.0E-05	0.002	0.1	2.1E-08
	2.0E-05	0.004	0.2	4.2E-08
	3.0E-05	0.006	0.3	6.3E-08
	4.0E-05	0.008	0.4	8.3E-08
Inert and non-hazardous	5.0E-05	0.01	0.5	1.0E-07
	1.0E-04	0.02	1	2.1E-07
Non inert and non-hazardous	1.0E-03	0.2	10	2.1E-06
	2.0E-03	0.4	20	4.2E-06
	5.0E-03	1	50	1.0E-05
	6.0E-03	1.2	60	1.3E-05
	7.0E-03	1.4	70	1.5E-05
	8.0E-03	1.6	80	1.7E-05
	9.0E-03	1.8	90	1.9E-05
	1.0E-02	2	100	2.1E-05
	2.0E-02	4	200	4.2E-05
	3.0E-02	3	300	6.3E-05

[a] According to the French decree
[b] mg/kg were calculated for 20 g of solid (CaO+SiO_2) used for the synthesis of C-S-H and keeping a liquid to solid (L/S) ratio of 50.
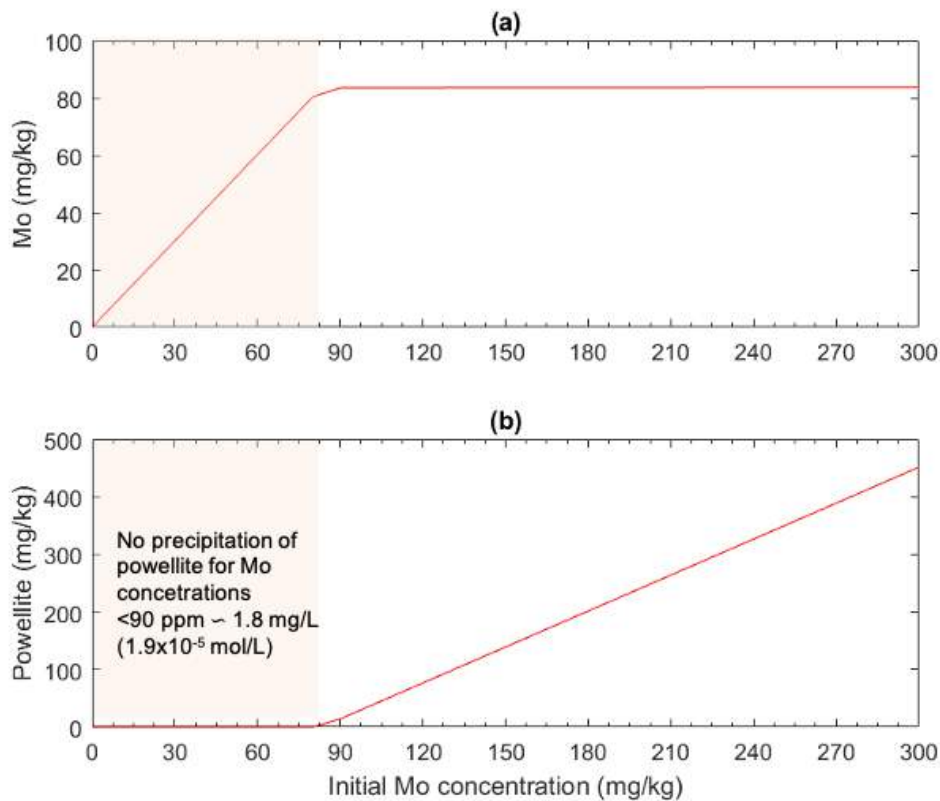
Figure 5.26 – Modeling of the precipitation of powellite at low Mo concentrations (<300 mg/mg of solid).

As observed, powellite was not able to precipitate for Mo concentrations lower than about 90 mg/kg of solid (~1.8 mg/L or ~1.9x10^{-5} mol/L). As this result was similar to the one obtained in the modeling of binders, we can partially conclude that:

(i)   with increasing Mo concentration, the precipitation of powellite become gradually the main stabilization mechanism controlling Mo solubility.

(ii)   non-precipitation of powellite at Mo concentrations lower than 90 mg/kg of solid, for these concentrations, the stabilization mechanisms controlling the solubility of Mo may be adsorption onto the surface of C-S-H, the substitution of sulfate by molybdate or the incorporation of Mo in other hydration products.

Further investigations should be carried out in order to identify the dominant stabilization mechanism at low Mo concentrations. To this end, laboratory techniques with lower detection limits have to be employed.

5.3 Summary of results

Table 5.10 summarizes the results obtained in the study of the stabilization of Mo. All the results are presented by system analyzed, Mo-spiked binders B1(CEM I), B2(90-10) and B3(SSC) and by mechanism of stabilization for which, the results obtained by different techniques are explained.

Table 5.10 – Summary of results obtained in the study of the stabilization of molybdenum

		B1 (CEM I)	B2 (90-10)	B3 (SSC)	Synthetic C-S-H
	What was done?	- Binders spiked with Mo from 0.005-10 wt% (50-100000 ppm), - Paste leaching tests at 28 days curing and chemical analyses in solution, - Mineralogical and microstructural analyses (XRD and SEM/EDS), - Modeling			- Synthesis of C-S-H phases with 0.25-5 wt% Mo, - Chemical analyses in solution, - XRD, TGA, FT-IR and SEM/EDS analyses, - Modeling
	Mo retention	74-98%	32-94%	92-99%	95-99%
Mechanism of stabilization	**Precipitation of powellite (CaMoO₄)**	**XRD:** powellite peaks appear for Mo >5 wt% (>50000 ppm)		**XRD:** powellite peaks appear for Mo >1 wt% (>10000 ppm)	**XRD:** powellite peaks appear for Mo >0.25 wt%~2500 ppm
		n/a	**SEM/EDS:** Mo/Ca atomic ratio towards 1 with increasing Mo concentration		
		n/a	n/a	n/a	**FT-IR:** the band at 850-750 cm⁻¹ (Si-O) increased in intensity due to the overlap with Mo-O band
		Modeling: not precipitation of powellite for Mo <0.005 wt%~50 ppm			**Modeling:** not precipitation of powellite for Mo <0.009 wt%~90 ppm
	Adsorption of Mo onto C-S-H surface	n/a	**SEM/EDS** (10 wt% Mo): Mo found around C-S-H		**SEM/EDS:** - Mo adsorbed onto C-S-H mainly at low Mo concentrations (<1 wt%) - White spots over all the surface of C-S-H
	Substitution of sulfate by molybdate	n/a **XRD:** absence of ettringite peak for Mo > 5 wt%	n/a: absence of sulfate bearing phases	**XRD:** shift of ettringite peak towards lower degrees with increasing Mo concentrations	n/a: absence of sulfate bearing phases
		n/a	n/a: absence of sulfate bearing phases	**SEM/EDS** (>10 wt% Mo): Mo with sulfate-bearing phases	n/a
	Redox reactions	n/a	**XRD:** no detection of MoS₂	**XRD:** no detection of MoS₂	n/a
	Inclusion of Mo in between C-S-H layers	n/a	n/a	n/a	**XRD:** peak in between 2θ 5-10° no modified
	Substitution of Si⁴⁺ by Mo⁶⁺	n/a	n/a	n/a	**FT-IR:** no modification of Si-O group (1100-900 cm⁻¹)

n/a: not applicable
ppm: mg/kg of solid

Figure 5.27 represents the main results obtained in this study. At left, this figure presents a scale of the Mo concentrations studied in this thesis:

- Experimentally a huge range of Mo concentrations were studied, varying from a few ppm (50 ppm) to several thousands of ppm (100000 ppm) (0.005 to 10 wt% Mo, respectively).

- By modeling, we studied the stabilization of Mo from 0.1 ppm to 100000 ppm.

In this figure, we also indicate some detections limits of the techniques used (ICP and XRD) as well as the different categories of waste according to the French decree. Moreover, the stabilization mechanisms that may immobilize Mo are specified, in which powellite is presented as the dominant Mo stabilization mechanisms at high Mo concentrations (>90 ppm). Thus, at low Mo concentrations (<90 ppm), the dominant stabilization mechanisms may be by the interaction of Mo with C-S-H or sulfate-bearing phases or by redox reactions. These results are more discussed in the following section.
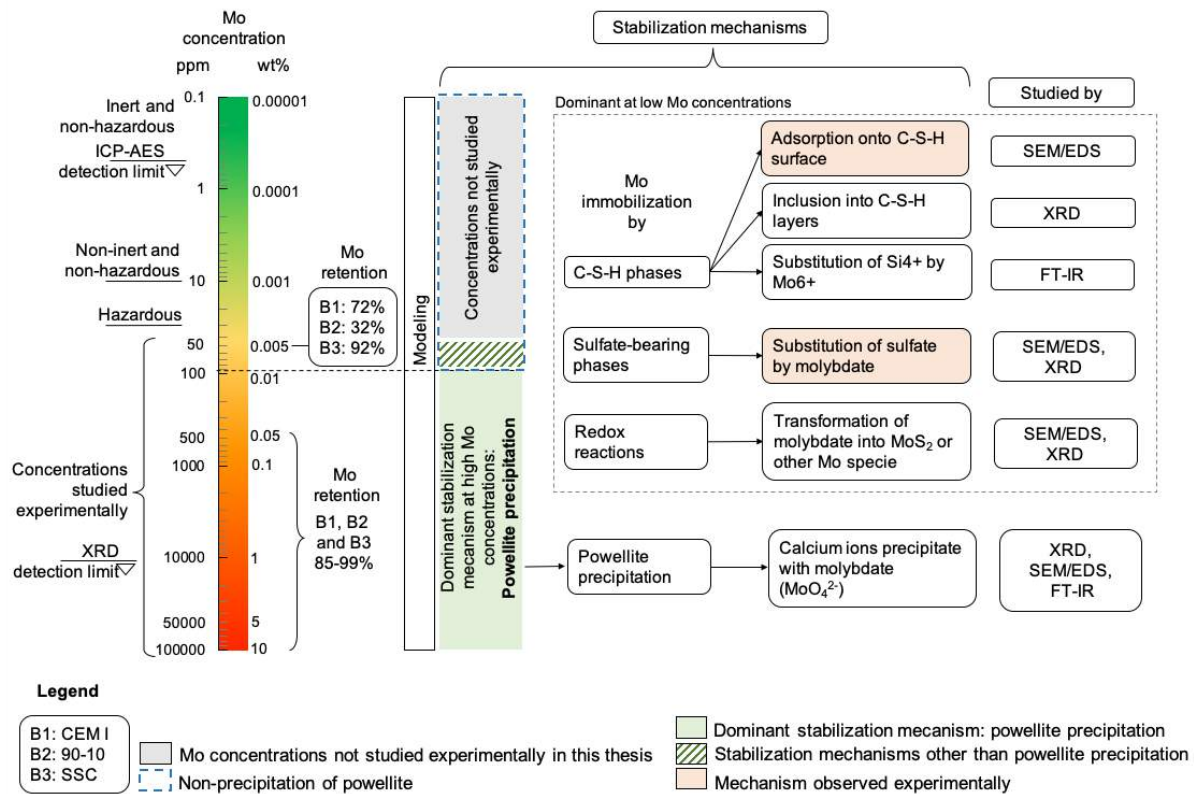

Figure 5.27 – Schematic representation of the study of the Mo stabilization.

5.4 Discussion

5.4.1 Stabilization of molybdenum by using binders

Experimental results showed that Mo was highly immobilized by all the binders tested: ordinary Portland cement -B1(CEM I), experimental binder composed of 90% ground granulated blast furnace slag (GGBS) and 10%OPC -B2(90-10), and supersulfated GGBS cement -B3(SSC). All these binders presented more or less positive characteristics to immobilize anionic heavy metals. The three binders contained high levels of calcium ions, which can precipitate with Mo. Additionally, these binders produced C-S-H at different proportions during hydration. According to the literature, C-S-H allow the physical adsorption of heavy metals onto their surface [109], [118]. Moreover, some of these binders also form ettringite (AFt) and monosulfoaluminate (Ms), in which anionic species can be present as substitutional compounds. The structure of AFt and Ms could lead to the substitution of sulfate (SO_4^{2-}) by molybdate (MoO_4^{2-}) [86], [94].

The percentage of Mo retained in the solid fractions of these hydrated binders varied from one binder to another and also depended on the initial Mo concentration. For low Mo concentrations (0.005 wt% ~50 mg_{Mo}/kg_{binder}), Mo retentions were 72%, 32% and 92% for binders B1(CEM I), B2(90-10) and B3(SSC), respectively. Whereas for high Mo concentrations (0.05-10 wt% ~500 to 100000 mg_{Mo}/kg_{binder}), Mo retentions varied from 85-99% for all the binders (cf. Figure 5.4). The Mo stabilization mechanisms are discussed as follow.

Mo stabilization mechanisms:

- Precipitation of powellite

After paste leaching tests, calcium concentrations in solution decreased with increasing Mo concentrations (cf. Figure 5.3). This behavior was similar for all the binders and was partially explained by the formation of powellite ($CaMoO_4$), a mineral containing calcium and the oxyanion molybdate (MoO_4^{2-}). Furthermore, XRD analyses corroborated the presence of powellite at high Mo concentrations (5 and 10 wt% ~50000 and 100000 mg_{Mo}/kg_{binder}). At lower Mo concentrations (<5 wt% ~50000 mg_{Mo}/kg_{binder}), the peaks of powellite were not identified in the patterns probably due to the detection limits of the XRD equipment (cf. Figure 5.27). Modeling was carried out in all the binders in order to corroborate the presence of powellite for the Mo concentrations <5 wt% ~50000 mg_{Mo}/kg_{binder}. Modeling showed that Mo was partially immobilized in all the binders by the precipitation of powellite except for binders spiked with a Mo concentration of 0.005 wt%~50 mg_{Mo}/kg_{binder}.

Therefore, we suggest that the powellite became gradually the main stabilization mechanism controlling the solubility of Mo while increasing Mo concentrations ($\geq$500 mg$_{Mo}$/kg$_{binder}$). At low Mo concentrations (<500 mg$_{Mo}$/kg$_{binder}$), Mo was partially immobilized probably by other stabilization mechanisms such as the adsorption of Mo onto C-S-H, the substitution of sulfate by molybdate in ettringite or monosulfoaluminate and redox reactions.

The identification of powellite as one of the mechanisms controlling Mo solubility was in agreement with the literature. Minocha et al. [131] studied the immobilization of Mo in an Na$_2$MoO$_4$-spiked ordinary Portland cement (OPC). They showed that Mo concentration in solution was 10 times lower than the initial Mo concentration. By performing XRD analyses, they observed that Mo precipitated with calcium ions to form powellite (CaMoO$_4$). Similarly, Kindness et al. [132] studied the immobilization of Mo in an Mo-spiked OPC and they showed that leachable Mo concentration was 40 times lower than initial Mo concentration at 12 days of curing. They explained that Mo was immobilized by the formation of powellite, which was detected by XRD analyses.

- <u>Substitution of sulfate by molybdate (MoO$_4^{2-}$)</u>

XRD analyses, obtained from binder B3(SSC), showed that ettringite (AFt) possibly suffered a structural modification at high Mo levels ($\geq$1 wt%~10000 mg$_{Mo}$/kg$_{binder}$). In fact, the peak of ettringite placed in between 2θ 9^o and 9.5^o shifted towards lower degrees, which may suggest that sulfate was partially substituted by molybdate (MoO$_4^{2-}$) and thus, the crystal lattice of the ettringite was modified due to the difference in size between these anions. According to the literature, the bond length of Mo-O is about ~1.76 Å, which is around 1.2 times bigger than sulfate (~1.49 Å) [143], [144]. Several studies have suggested that Mo was partially immobilized by sulfate-bearing phases. For example, Vollpracht et al. [144] studied the leaching of Mo in several Portland cements during hydration. After pore solution extractions, they found out that molybdate concentrations followed the opposite trend of the ettringite formation. Therefore, the authors pointed out that molybdate replaced partially to sulfate in ettringite. Similarly, Zhang and Reardon [143] studied the immobilization of Mo, Cr, B and Se by incorporation into ettringite. They showed that Mo was partially immobilized in contact with a solution containing ettringite because Mo concentrations decreased from 10 ppm to 4 ppm. However, the authors explained that Mo was the last anion preferred by ettringite due to the difference of size between molybdate and sulfate. Moreover, EDS analyses showed that Mo interacted with sulfate-bearing phases in the Mo-spiked supersulfated cement B3(SSC).

For the other two binders, B1(CEM I) and B2(90-10), there was no evidence of the substitution of sulfate by molybdate. In the case of binder B2(90-10), ettringite did not precipitate in this

binder due to the low OPC content and thus, the low sulfate concentrations. For B1(CEM I), the peaks of ettringite were identified for all the Mo concentrations except for the two highest concentrations of Mo, in which the peaks of ettringite disappeared. Several studies have shown that the presence of high content of alkalis (sodium or potassium) inhibits the formation of ettringite [187], [188]. Sodium increases the alkali conditions in the pore solution and modifies the stability of ettringite. High alkali conditions enhance the solubility of ettringite constituents, mainly sulfate, as a result, the amount of ettringite decreases in the hydrated binder [188].

- Redox reactions

According to the literature, the water-solubility of anionic heavy metals may decrease with decreasing pH values [94], [134], [204]. Eluates from leaching tests carried out in formulations containing GGBS -B2(90-10) and B3(SSC)- presented lower pH values in solution than those measured in formulation B1(CEM I). It was firstly thought that this condition could help to increase the retention of Mo in the binders. However, the binder B1(CEM I) showed higher Mo retention than B2(90-10). pH probably has an effect more important when species are immobilized only by adsorption or substitution, in which pH values modifies the behavior of anionic species as reported in the literature [95], [134].

Additionally, binders containing GGBS can help to reduce molybdate (MoO_4^{2-}) to molybdenite (MoS_2) according to the Eh-pH diagrams of Mo-O and Mo-O-S as a function of the redox conditions (cf. Chapter 1 - Figure 1.21) [124], [125]. In fact, binders containing GGBS have reducing internal environment due to the presence of sulfur in a reduced state [119], [116]. The reducing nature of the binder depends on the amount of GGBS and the degree of hydration [116]. Mancini et al. [115] showed that the treatment of a Mo-contaminated fly ash by using a ferrous sulfate-based solution may reduce molybdate to a specie with a lower Mo oxidation state. After treatment, they indicated that Mo concentrations in solution decreased with increasing the proportion of the solution used for stabilization. The authors showed that the reducing conditions should be very extreme (pH<6) in order to guarantee the immobilization of Mo. In the present study, pH values were not lower than 11 and we did not detect molybdenite (MoS_2) neither by XRD nor EDS analyses. Further investigations are needed to confirm the reduction of molybdate into other species in binders containing GGBS. To detect the transformation of oxidation states, techniques with low detection limits are required (e.g. XANES).

- <u>Adsorption of Mo onto the C-S-H surface</u>

SEM/EDS observations in binder B2(90-10) showed the presence of Mo around C-S-H phases (cf. Figure 5.7), which suggest different scenarios: (i) grains of Mo accumulated around this phase, (ii) Mo was adsorbed onto the surface of C-S-H, (iii) powellite co-precipitated in the surface of C-S-H. Similarly, for binder B3(SSC), EDS analyses showed that at low Mo concentrations, Mo seemed to interact with C-S-H. The capacity of C-S-H to immobilize Mo will be more detailed in the following section.

5.4.2 Mo stabilization by synthetic C-S-H phases

We decided to study the immobilization of Mo by synthetic C-S-H. This choice can be explained by:

- this phase is one of the main hydration products in all the three binders studied,
- EDS analyses in Mo-spiked binders pointed out that powellite was mixed with C-S-H and that Mo was probably adsorbed onto C-S-H surface.
- ettringite and monosulfoaluminate phases have already been a topic of research to explain Mo immobilization [132], [143], [215], [216]; while only a few recent papers have been published about the capacity of C-S-H to immobilize Mo. For example, two recent studies published in 2020 carried out by Lange et al. [216] and Grambow et al. [217] studied the uptake of Mo by C-S-H phases. Both studies showed a strong retention of Mo (in the form of molybdate) by synthetic C-S-H phases having Ca/Si ratios between 0.9 and 1.4. They indicated that Mo uptake increased with increasing Ca/Si ratios due to the increase of the positive surface of C-S-H.

In the present study, we performed the synthesis of five different C-S-H phases with Ca/Si ratios of 1.6 and varying the Mo concentration from 0 to 5 wt% Mo in order to guarantee Mo detection by the available laboratory techniques (XRD, SEM/EDS, FT-IR and TGA).

As presented in Table 5.5, Mo was largely immobilized (>95%) in all the synthetic C-S-H phases and over the whole range of Mo concentrations studied (0.25, 1, 2.5 and 5 wt%). Hence, four hypotheses were taken into consideration to explain Mo immobilization by C-S-H:

(i)   Mo co-precipitated with free Ca^{2+} ions to form powellite ($CaMoO_4$),

(ii)   Mo was incorporated in between the C-S-H layers,

(iii) Si^{4+} was substituted by Mo^{6+}, and

(iv)   Mo was adsorbed onto the C-S-H surface.

XRD patterns showed that powellite ($CaMoO_4$) was present in all the synthetic C-S-H phases containing Mo (cf. Figure 5.18). The characteristic peaks of powellite became more important at the highest Mo concentrations (2.5 and 5 wt%). This behavior agreed with the gradual decrease in Ca concentration in solution after the filtration of synthetic C-S-H phases (cf. Figure 5.16). On the other hand, FT-IR spectra showed an increase in intensity of the Si-O bands (850-750 cm^{-1}) with increasing Mo concentration (cf. Figure 5.21). We think that the increase in the relative intensities of the Si-O band (850-750 cm^{-1}) may not indicate a modification of the Si-O group, but the appearance of the Mo-O band due to the precipitation of powellite. In fact, the Mo-O band overlapped with the Si-O band in 850-750 cm^{-1} [218]. However, investigations with methods with lower detections limits are required to verify the substitution of Si^{4+} by Mo^{6+} at very low Mo concentrations.

Moreover, EDS punctual analyses indicated that C-S-H was mixed with powellite and that Mo was probably adsorbed onto the C-S-H surface at low Mo concentrations. SEM/EDS observations carried out in synthetic C-S-H phases showed the presence of several white spots in all the surfaces analyzed (cf. Figure 5.22). It is then possible that small amounts of Mo were adsorbed onto the surface of C-S-H phases. As mentioned previously, Lange et al. [216] indicated that molybdate uptake by C-S-H can be explained by the electrostatic sorption of Mo. High Ca/Si ratios in C-S-H increase the positive surface charge of these phases and thus, their electrostatic sorption capacity of anions. These authors studied low Mo concentrations between 5.10^{-6} and 1.10^{-7} mol/L in order to avoid supersaturation with respect to powellite.

Concerning modeling, numerical calculations showed that powellite precipitated in the system and that the amount of powellite increased with increasing Mo concentrations. For the highest Mo concentrations, the model showed that 8.1% powellite was formed immobilizing about 99% of the Mo present in solution. Furthermore, the precipitation of powellite became the dominant stabilization mechanism with increasing Mo concentrations.

In order to predict the precipitation of powellite at low concentrations, modeling was also carried at low Mo concentrations varying from 0.1 to 300 mg$_{Mo}$/kg$_{binder}$. It was found that powellite did not precipitate at Mo concentrations lower than 90 mg$_{Mo}$/kg$_{solid}$ (cf. Figure 5.26), for which other stabilization mechanisms such as adsorption onto C-S-H surface, substitution and/or inclusion may control Mo solubility. Further investigations should be carried out in order to verify the Mo concentrations and conditions necessary for these phenomena to happen. To this end, laboratory techniques with lower detection limits have to be employed.

5.5 Conclusions

The aim of this chapter was: (i) to compare the capacity of several binders to immobilize Mo in a single-step batch procedure, and (ii) to contribute to the understanding of the mechanisms associated with Mo stabilization. To this end, three different binders were studied: one Ordinary Portland cement (OPC), one experimental binder composed of 90% ground granulated blast furnace slag (GGBS) and 10% OPC, and one supersulfated GGBS cement (SSC). All the binders were spiked with sodium molybdate using six different concentrations from 0.005 to 10 wt% Mo (50 to 10000 mg_{Mo}/kg_{binder}). We also studied the capacity of calcium silicate hydrate (C-S-H) to stabilize Mo. Conclusions of this chapter are summarized in Table 5.11.

Table 5.11 – Conclusions of Chapter 5 – Stabilization of molybdenum

Mo-spiked binders	What was done?	Three different binders spiked with Na_2MoO_4 at different Mo concentrations: - one Ordinary Portland cement – B1(CEM I), - one experimental binder composed of 90% GGBS and 10%OPC – B2(90-10), - one supersulfated GGBS cement – B3(SSC). Experimental analyses: - Paste leaching tests in accordance with NF EN 12457-2 and chemical analyses in solution. - Mineralogical and microstructural characterization (XRD and SEM/EDS analyses).
	Results	- Mo was highly immobilized in all the solid fractions. - Mo retention varied from one binder to another and depended on the initial Mo concentration. - XRD and EDS showed the presence of powellite ($CaMoO_4$) at high Mo concentrations (>5 wt%). - SEM/EDS showed the presence of Mo near C-S-H phases. - Mo interacted with calcium and sulfur in B3(SSC). Probably Mo was partially immobilized by sulfate bearing phases (e.g. ettringite, monosulfoaluminate and gypsum).
Synthetic C-S-H with Mo	What was done?	- Synthesis of five different C-S-H phases over one month of equilibrium. - Chemical analyses in solution after C-S-H filtrations. - Microstructural and mineralogical characterization (XRD, TGA, FT-IR and SEM/EDS).
	Results	- Mo retention superior to 95% in all the solid fractions. - Mo stabilization mainly controlled by the co-precipitation of powellite. Immobilization of low Mo concentrations probably by the adsorption onto the C-S-H surface. - C-S-H equilibrium was not altered by the presence of Mo because Ca/Si ratios remained relatively stable at 1.6.
Modeling	code PHREEQC	**Binders:** except in binders spiked with 0.005 wt% Mo~50 ppm (% by weight of anhydrous binder). The precipitation of powellite was not the only mechanism controlling Mo solubility due to the discrepancies between experimental and numerical data. **C-S-H:** Gradual precipitation of powellite for Mo concentrations > 90 ppm ~1.9×10^{-5} mol/L.

259

Suggestions for further research:

- Stabilization of a Mo-contaminated soil

The stabilization of molybdenum was studied in Mo-spiked binders. The treatment of a natural Mo-contaminated soil would enable to corroborate the efficacy of each binder to immobilize Mo. In this case, several factors should be taken into consideration to evaluate the stabilization of Mo. We list some of them:

- o speciation of Mo,
- o ion competition,
- o harmful effect of organic matter for the hydration of the binders,
- o hydration degree of the binders due to the amount of the available water.

The experimental identification of Mo stabilization mechanisms at low concentrations (in the order of 10^{-5} mol/kg), for which powellite is expected to not precipitate, is necessary. However, understanding the stabilization mechanisms of Mo requires the accurate identification of its chemical species in the contaminated materials [219]. Mo K-edge XANES has successfully been used for identification of Mo speciation in soil (including surface adsorption and mineral precipitation) and in aqueous solutions [220], [221]. To our knowledge, however, XAS has not yet been used to study the Mo stabilization mechanisms in hydraulic binders. Thus, XAS methods (synchrotron radiation using XANES and EXAFS spectroscopy) appear to be well adapted to study the immobilization of Mo by hydraulic binders, at low Mo concentration levels typically encountered in natural materials [108], [219]. To this end, XANES and EXAFS spectra obtained from Mo-treated samples have to be compared with Mo standards in order to identify the dominant mechanisms of Mo stabilization. Mo standards are pure minerals that contain Mo. For example, the synthesis of phases such as ettringite with Mo and monosulfoaluminate with Mo would allow the identification of sulfate substitution by molybdate.

- Improving modeling for the prediction of Mo-uptake by cementitious binders

Few information is found in the literature about the solubility products of the possible reactions involved in the interaction of Mo with cementitious binders. Some thermodynamic reactions have been published concerning powellite and AFm containing Mo [138], [156]. Therefore, it would be interesting to develop a model taking into consideration, not only the precipitation of powellite, but also the formation of other Mo-bearing phases such as the substitution of sulfate by molybdate in ettringite. However, it is also important to verify the coherence of the database before predicting Mo behavior in such complex systems.

C-S-H phases are known to have high sorption capacity due to their high specific surface; therefore, a model of surface adsorption of C-S-H and Mo should be carried out in order to better evaluate the capacity of C-S-H to immobilize Mo. This type of modeling should focus mainly on very low Mo concentrations (in the order of 10^{-5} mol/kg) for which powellite is expected to not precipitate.

GENERAL CONCLUSIONS

General conclusions

Excavation operations produce several tons of soil generally contaminated by the presence of pollutants. Excavated soil is considered as waste and it can be either sent to landfill or destined for reuse depending on the level of pollution. In any case, soil should be properly treated in order to: (i) decrease the release of pollutants into the environment, and (ii) minimize the problems involved in civil engineering applications due to the reactions between cementitious phases and pollutants. In the context of this thesis, we focused on sulfates and molybdenum (Mo). Concerning sulfates, we considered two main issues: (i) external sulfate attack of concrete structures, which are in direct contact with sulfate-rich soils (e.g. dams, foundations), and (ii) the release of sulfates into solution in addition to the swelling and mechanical strength loss in sulfate-rich soil intended for valorization (e.g. reuse in road construction). In the case of Mo, its release into solution is also a serious concern as it can lead to significant risks for the environment.

Therefore, this study aimed to investigate the reaction of concrete in contact with sulfates, and the stabilization of sulfates by using cementitious and alternative binders for pollution reduction and for reuse of soil. Additionally, the interaction of Mo with cementitious binders was also studied in order to better understand the stabilization of Mo-contaminated materials. The main conclusions of this research were grouped in three parts and are summarized below. Perspectives for future research are also suggested.

Concrete under external sulfate attack

This part of the study aimed to: (i) realize a benchmark of several binders by testing their capacity to resist external sulfate attack under similar experimental conditions, and (ii) contribute to the understanding of the mechanisms associated with the expansion or non-expansion of the binders by using microstructural and mineralogical analyses and thermodynamic calculations.

Therefore, we studied the capacity of seven different concretes to resist external sulfate attack (ESA) under similar experimental conditions. Concretes were made of three different Portland cements (ordinary Portland cement, sulfate-resisting Portland cement and blast furnace slag cement) and four alternative binders grouped into two categories: (i) ettringite binders (supersulfated cement and calcium sulfoaluminate cement), and alkali-activated binders (alkali-activated slag and metakaolin-based geopolymer).

The resistance to external sulfate attack was studied by measuring the longitudinal expansion of concrete samples according to the Swiss Standard SIA 262/1:2013 Appendix D. This test consists of accelerating the sulfate attack on concrete by exposure of samples to 4 cycles of drying/submersion followed by a consecutive submersion in a solution containing 50 g/L of sodium sulfate. This standard sets the maximum guideline value of longitudinal expansion to 0.1%. Mineralogical and microstructural characterizations and thermodynamic calculations carried out before and after ESA contributed to the better understanding of the absence/presence of expansion in the binders.

It was found that ordinary Portland cement had the maximal expansion (0.4%) and noticeable cracking due to the reaction between aluminates and sulfates. In fact, dense amounts of ettringite were observed in all the analyzed surface of this concrete at the end of the test. In contrast, Portland cement without C_3A presented lower expansions (0.07%) and no cracking. However, visual inspections allowed for the identification of cracking after 550 days of immersion. This cracking was explained by the precipitation of gypsum. In this type of material, calcium and aluminum ions are available from C_4AF; however, this aluminate phase reacts with a lower kinetics compared to C_3A and thus, ettringite forms at a very slow rate and in minor quantities.

On the other hand, no visual damage was observed in blast furnace slag Portland cement-based concretes and it was found that the magnitude of the final expansion depended on the curing time before sulfate exposure. Concretes cured for 90 days presented 40% less expansion than those cured for 28 days. This behavior can be explained probably by the difference in their porosity. Furthermore, low expansion in these concretes was explained by the formation of ettringite in minor extent than in ordinary Portland cement and developed in air voids. Moreover, the important proportion of slag (82%) and the low content of clinker (15%) reduced the C_3A content and thus, the availability of rapidly soluble aluminum to react with sulfates. In addition to this, clinker was consumed by the GGBS to be activated, and the amount of clinker can be considered insufficient to enable the precipitation of large amounts of expansive phases. Furthermore, the unavailability of aluminum for reaction with sulfates can also be explained by the formation of C-A-S-H and hydrotalcite phases.

Concerning the alternative binders (ettringite binders and alkali-activated binders), they had low expansions in the range of 0.01-0.03% and no visual damages were observed during and after ESA. Low expansions in these binders were explained by the uptake of water and the absence of reactions between the constituents of the hardened matrices with the sulfates in solution. In the case of the ettringite binders (calcium sulfoaluminate-belite cement and supersulfated GGBS cement), their low expansions were explained by the absence of C_3A and portlandite in addition to the formation of ettringite during hydration. In the case of alkali-activated binders (alkali-activated slag (AAS) binder and metakaolin-based geopolymer), the absence of C_3A and portlandite also explained their low expansions. Furthermore, the unavailability of aluminum for reaction with sulfates due to the formation of C-A-S-H and hydrotalcite phases during hydration of the AAS binder also explained the low expansion reactions. In addition, in the absence of calcium (case of the metakaolin-based geopolymer), expansive phases such as ettringite and gypsum cannot be formed.

Perspectives:

Detailed perspectives were presented at the end of Chapter 3 (cf. section 3.6). Here, we recall the main perspectives.

In this part of the study, we calculated the saturation indices of ettringite, monosulfoaluminate and gypsum by using PHREEQC and the element concentrations of poral solutions. It was assumed that these saturation indices were the result of the state of equilibrium of the poral solution. It would be also interesting to estimate the equilibrium states of the reaction products of the hardened binders at the different steps by varying the concentration of sulfates. These results could be compared with experimental data if the quantification of phases was carried out.

In this thesis, we studied the capacity of binders to resist external sulfate attack by measuring longitudinal expansions. However, other parameters can be also evaluated in order to ensure their capacity to resist external sulfate attack. For example, it would be interesting to measure their mechanical properties (e.g. compressive strength) during the period of sulfate exposure.

Stabilization of sulfates

This part of the thesis aimed to: (i) compare the capacity of several alternative binders to immobilize sulfates in a sulfate-spiked soil, (ii) contribute to the understanding of the sulfate stabilization mechanisms, and (iii) evaluate the swelling potential and the mechanical properties of all the treatments.

Therefore, we compared the capacity of four different binders to stabilize sulfates in a sulfate-spiked soil. To this end, the soil was treated with one ordinary Portland cement (OPC), one alternative clinker (composed of ye'elimite and belite), one blast furnace slag Portland cement (CEM III/C), and one experimental binder composed of 90% ground granulated blast furnace slag (GGBS) and 10% OPC. Treatment of sulfate-rich soil was assessed in accordance with the French Standard NF P 94-100 in which the maximum guideline value of volume expansion is set to 5% and the minimum tensile strength is 0.2 MPa. Furthermore, sulfate immobilization was studied by leaching tests carried out in accordance with the European Standard NF EN 12457-5, using a single step batch procedure at natural pH condition by using distilled water as a leachate. Mechanisms of sulfate stabilization were studied by carrying out mineralogical and microstructural characterization and modeling. Modeling was performed by using a geochemical model using the code PHREEQC.

After leaching tests, it was observed that all the treatments led to a decrease in sulfate concentration in solution to values lower than 1000 mg/kg of dry soil, which is the guideline value established for the French Decree of 12 December 2014, for inert and non-hazardous waste. However, treatments with only OPC and clinker released heavy metals into solution in excess (mainly chromium) due to their high clinker content. Moreover, these binders led to high volume expansions (>5%) caused by the formation of ettringite in excess. In contrast, binders containing GGBS led to low volume expansions (<2%), a sulfate retention of about 89% and low heavy metals contents were detected in solution (inferior to the guideline values established by the French Decree). Sulfate solubility was controlled by ettringite, which did not lead to expansion probably due to the low kinetics of precipitation in addition to the absence of portlandite, which is often related to expansive ettringite.

Among all the treatments, the use of the experimental binder gave the better performance in terms of sulfate leaching, swelling and tensile strength. Therefore, this formulation was deeply studied at medium and long-term by performing leaching tests at 6 months in order to ensure the sulfate stabilization. Moreover, as the treatment of sulfate-rich soil concerns the reuse of soil for engineering works (e.g. road construction), this formulation was also evaluated by performing different geotechnical experiments (workability, compressive strength tests, swelling and mechanical class performance). It was found that stabilization of sulfates remained stable in time and geotechnical properties of the treated soil were found to be acceptable for being used in civil engineering projects. Moreover, the model performed in this binder showed that numerical calculations were in good agreement with experimental results

when the hydration degree of GGBS was assumed to be 30%. The geochemical model was then able to predict correctly the sulfate concentrations in solution as a function of the binder dosage used in the treatment. Modeling showed that ettringite was indeed the main stabilization mechanism controlling the solubility of sulfates and that sulfates were partially immobilized at concentrations near 1000 mg/kg from a proportion of 7% of binder added to the sulfate-spiked soil.

Perspectives:

Detailed perspectives were presented at the end of Chapter 4 (cf. section 4.6).

The stabilization of sulfates was evaluated in a sulfate-spiked soil, it would be then interesting to treat a natural sulfate-rich soil with the same formulations used in this study and thus, corroborate their capacity to immobilize sulfates.

On the other hand, the stabilization of sulfates in this study was satisfactory by using binders containing GGBS. In the modeling, the hydration degree of GGBS was assumed to be 30%. This hydration degree should be confirmed experimentally in a system composed of "soil+binder+sulfate" and by taking into account several factors such as the dilution effect of the binder, the amount of water available to hydrate the binder and consumed by the soil and the amount of clay containing magnesium, which is also present in GGBS.

Stabilization of molybdenum (Mo)

In this part of the thesis, we aimed to: (i) compare the capacity of several binders to immobilize molybdenum, and (ii) contribute to the understanding of the mechanisms associated with molybdenum stabilization.

Hence, we studied the interaction of Mo with three different binders and their capacity to stabilize Mo. To this end, three binders were artificially spiked with different Mo concentrations using sodium molybdate. The binders studied were: one ordinary Portland cement (OPC) - B1(CEM I), one experimental binder composed of 90% GGBS and 10%OPC -B2(90-10), and one supersulfated GGBS cement -B3(SSC). Immobilization of Mo was assessed by carrying out paste leaching tests in accordance with the European Standard NF EN 12457-5 using a single step batch procedure at natural pH condition. Moreover, stabilization mechanisms were studied by using mineralogical and microstructural analyses and a geochemical model by using the code PHREEQC. The synthesis of calcium silicate hydrate (C-S-H) with Mo was also carried out in order to study its capacity to immobilize Mo; In this case, all the phases were also characterized by mineralogical and microstructural analyses and studied by modeling.

Paste leaching tests showed that Mo was retained in all the solid fractions at high Mo concentrations. The percentage of Mo retained in the solid fractions of these hydrated binders varied from one binder to another and also depended on the initial Mo concentration. For low Mo concentrations (0.005 wt% ~50 mg/kg of binder), Mo retentions were 72%, 32% and 92% for binders B1(CEM I), B2(90-10) and B3(SSC), respectively. Meanwhile for high Mo concentrations varying from 0.05 to 10 wt% Mo (~500-100000 mg_{Mo}/kg_{binder}), Mo retentions varied from 85-99% for all the binders. The order of Mo retention in terms of binder was B3>B1>B2.

Overall, the precipitation of powellite ($CaMoO_4$) was found to be the main mechanism controlling Mo solubility in all the Mo-spiked binders, except for binders spiked with a Mo concentration of 0.005 wt%~50 mg_{Mo}/kg_{binder}. For which, Mo was partially immobilized probably by other stabilization mechanisms such as the adsorption of Mo onto C-S-H, the substitution of sulfate by molybdate in ettringite or monosulfoaluminate and by redox reactions.

Experimental observations showed that Mo was also mixed with calcium and sulfates probably due to the substitution or adsorption in sulfate-bearing phases. Moreover, Mo was related to calcium silicate hydrates (C-S-H) probably due to the co-precipitation of powellite in the C-S-H surface or due to the adsorption of Mo onto the C-S-H surface. The synthesis of C-S-H and the modeling showed that powellite precipitated only for Mo concentrations higher than 90 mg_{Mo}/kg_{solid} (~$1.9x10^{-5}$ mol/L).

Perspectives:

Detailed perspectives were presented at the end of Chapter 5 (cf. section 5.5).

The stabilization of molybdenum was studied in Mo-spiked binders. The treatment of a real Mo-contaminated material would enable to corroborate the efficacy of each binder to immobilize Mo. In this case, several factors may be taken into consideration to evaluate the stabilization of Mo (e.g. ion competition, harmful effect of organic matter in the hydration of the binders). However, the experimental identification of Mo stabilization mechanisms at low Mo concentrations (in the order of 10^{-5} mol/kg), for which powellite is expected to not precipitate, is necessary. To this end, the accurate identification of Mo chemical species is necessary and therefore, the use of methods with low detection limits such as XAS methods (synchrotron radiation using XANES and EXAFS spectroscopy) and MET.

On the other hand, few information is found in the literature about the solubility products of the possible reactions involved in the interaction of Mo with cementitious binders. Therefore, the development of a geochemical model that takes into account, not only the precipitation of powellite, but also the formation of other Mo-bearing phases such as the substitution of sulfate by molybdate in ettringite, would allow for better understanding of the Mo stabilization mechanisms. Moreover, C-S-H phases are known to have high sorption capacity due to their high specific surface; therefore, a model of surface adsorption of C-S-H and Mo should be carried out in order to better evaluate the capacity of C-S-H to immobilize low Mo concentrations (in the order of 10^{-5} mol/kg) for which powellite is expected to not precipitate.

Conclusions générales

Les opérations d'excavation produisent plusieurs tonnes de sols généralement contaminés par la présence de polluants. Les sols excavés sont considérés comme des déchets et sont, soit envoyés en décharge, soit destinés à être réutilisés en fonction du niveau de pollution. Dans tous les cas, les sols doivent être correctement traités afin de : (i) diminuer le relargage de polluants dans l'environnement, et (ii) minimiser les problèmes entrainés dans les projets de génie civil liés aux réactions entre les phases cimentaires et les polluants. Dans cette thèse, nous nous sommes concentrés sur les sulfates et le molybdène (Mo). Concernant les sulfates, nous avons considéré deux problématiques principales : (i) l'attaque sulfatique externe des structures en béton qui sont en contact direct avec des sols sulfatés (ex : barrages, fondations), et (ii) le relargage de sulfates en solution, en plus du gonflement et de la perte de résistance mécanique dans des sols sulfatés destinés à la valorisation (ex : réutilisation dans la construction de routes). Dans le cas du Mo, il peut se retrouver en solution, entraînant alors des risques importants pour l'environnement.

Par conséquent, dans cette thèse, nous avons étudié la réaction du béton au contact des sulfates et la stabilisation des sulfates en utilisant des liants cimentaires et alternatifs afin de réduire la pollution des sols et aussi envisager leur réutilisation dans des projets de génie civil. De plus, nous avons étudié l'interaction du Mo avec les liants cimentaires afin de mieux comprendre la stabilisation des sols contaminés au Mo. Les principales conclusions de cette recherche ont été regroupées en trois parties et sont résumées ci-dessous. Des perspectives de recherche sont également suggérées.

Béton sous attaque sulfatique externe

Cette partie visait à : (i) réaliser un « benchmark » ou une étude comparative de plusieurs liants vis-à-vis de leur capacité à résister à l'attaque sulfatique externe dans des conditions expérimentales similaires, et (ii) contribuer à la compréhension des mécanismes associés à l'expansion ou non-expansion des liants en utilisant des analyses microstructurales et minéralogiques ainsi que des calculs thermodynamiques.

Par conséquent, nous avons étudié la capacité de sept bétons à résister à l'attaque sulfatique externe dans les mêmes conditions expérimentales. Trois ciments Portland et quatre liants alternatifs ont été utilisés pour fabriquer ces bétons. Les liants alternatifs ont été regroupés en deux catégories : (i) liants alcali-activés avec ou sans oxydes de calcium (laitier alcali-activé et un géopolymère à base de métakaolin) et (ii) liants ettringitiques (ciment sursulfaté et ciment sulfoalumineux).

La résistance à l'attaque sulfate externe a été étudiée en mesurant l'expansion longitudinale d'échantillons en béton selon la norme suisse SIA 262/1 : 2013 Annexe D. Ce test consiste à accélérer l'attaque par l'exposition des échantillons à 4 cycles de séchage/immersion suivie d'une immersion consécutive dans une solution contenant 50 g/L de sulfate de sodium. Cette norme fixe à 0,1% la valeur maximale de l'expansion longitudinale. De plus, des analyses minéralogiques et microstructurales et des calculs thermodynamiques avant et après attaque ont été réalisés afin de mettre en évidence les mécanismes d'expansion et de non-expansion des liants.

Nous avons trouvé que, parmi tous les bétons, l'expansion maximale (0,4%) a été obtenue avec le ciment Portland classique. Celui-ci a, par ailleurs, présenté des fissurations en raison de la formation d'ettringite en excès provoquée par la réaction entre les aluminates et les sulfates. En effet, une quantité d'ettringite importante a été observée dans toute la surface analysée de ce béton à la fin de l'essai. En revanche, le ciment Portland sans C_3A a présenté des expansions plus faibles (0,07%) et aucune fissuration à la fin du test. Cependant, des inspections visuelles à plus long terme ont permis d'identifier des fissures après 550 jours d'immersion. Cette fissuration peut s'expliquer par la précipitation du gypse. Dans ce type de matériau, les ions calcium et aluminium proviennent du

C_4AF. Cependant, cette phase d'aluminate réagit avec une cinétique inférieure à celle du C_3A et ainsi, l'ettringite se forme à une vitesse très lente et en quantités mineures.

D'autre part, aucun dommage visuel n'a été observé dans les bétons à base de ciment Portland de laitier de haut fourneau et il a été constaté que l'amplitude de l'expansion finale dépendait du temps de durcissement avant l'exposition aux sulfates. Les bétons durcis pendant 90 jours ont présenté une expansion 40% inférieure à celle obtenue après 28 jours de durcissement. Ce comportement s'explique probablement par la différence de porosité. De plus, la faible expansion de ces bétons s'explique par la formation d'ettringite moins importante que dans le cas du ciment Portland ordinaire et développée dans les vides d'air. Par ailleurs, la forte proportion de laitier (82%) et la faible teneur en clinker (15%) conduisent à une réduction de la teneur en C_3A et donc de l'indisponibilité d'aluminium rapidement soluble pour réagir avec les sulfates. L'indisponibilité de l'aluminium pour la réaction avec les sulfates peut également s'expliquer par la formation de phases C-A-S-H et d'hydrotalcite. En plus de cela, le clinker a été consommé par le GGBS pour être activé, et donc sa quantité peut être considérée comme insuffisante pour permettre la précipitation de phases expansives en proportion importante.

Concernant les liants alternatifs (liants d'ettringite et liants activés par les alcalis), ils ont présenté de faibles expansions, de l'ordre de 0,01 à 0,03%, et aucun dommage visuel n'a été observé pendant et après l'attaque sulfatique externe. Les faibles expansions de ces liants sont expliquées par la prise d'eau et l'absence de réactions entre les constituants des matrices durcies et les sulfates en solution. Dans le cas des liants ettringitiques (ciment sulfoaluminate-bélite de calcium et ciment GGBS supersulfaté), leurs faibles expansions s'expliquent par l'absence de C_3A et de portlandite en plus de la formation d'ettringite lors de l'hydratation. Dans le cas des liants alcali-activés (laitier alcali-activé et géopolymère à base de métakaolin), l'absence de C_3A et de portlandite justifient leurs faibles expansions. De plus, l'indisponibilité de l'aluminium pour la réaction avec les sulfates en raison de la formation de phases C-A-S-H et hydrotalcite lors de l'hydratation du laitier alcali-activé peut être également à l'origine de faibles expansions. Par ailleurs, en cas d'absence d'oxydes de calcium (cas du métakaolin à base de géopolymère), les phases expansives telles que l'ettringite et le gypse ne peuvent pas se former.

Perspectives :

Les perspectives détaillées sont présentées à la fin du Chapitre 3 (cf. section 3.6). Ici, nous présentons un résumé de ces perspectives.

Dans cette étude, nous avons calculé les indices de saturation de l'ettringite, du monosulfoaluminate et du gypse en utilisant le code PHREEQC et les concentrations en éléments mesurées dans les solutions porales. On a supposé que ces indices de saturation étaient le résultat de l'état d'équilibre de la solution porale. Cependant, il serait également intéressant d'estimer les états d'équilibre des produits de réaction des liants durcis aux différentes étapes en faisant varier la concentration en sulfates. Ces résultats pourraient être comparés à des données expérimentales si la quantification des phases était effectuée.

D'un autre côté, dans cette thèse, nous avons étudié la capacité des liants à résister à l'attaque sulfatique externe en mesurant les expansions longitudinales. Cependant, d'autres paramètres peuvent également être évalués afin de garantir la capacité de ces liants à résister à cette attaque. Par exemple, il serait intéressant de mesurer leurs propriétés mécaniques (ex. résistance à la compression) pendant la période d'exposition aux sulfates.

Stabilisation des sulfates

Cette partie visait à : (i) comparer la capacité de plusieurs liants alternatifs à immobiliser les sulfates dans un sol sulfaté, (ii) comprendre les mécanismes d'immobilisation des sulfates, et (iii) évaluer le potentiel de gonflement et les propriétés mécaniques des traitements du sol sulfaté.

Nous avons donc étudié l'immobilisation des sulfates, le gonflement et les propriétés mécaniques de différents traitements. Un sol artificiellement sulfaté a été traité par quatre liants différents : un OPC, un clinker alternatif (composé de ye'elimite et de bélite), un ciment au laitier de haut fourneau (de type CEM III) et un liant expérimental (90% laitier et 10% OPC).

Les traitements du sol sulfaté ont été évalués conformément à la norme française NF P 94-100 dans laquelle la valeur guide maximale de l'expansion volumique est fixée à 5% et la résistance minimale à la traction est de 0,2 MPa. Par ailleurs, l'immobilisation des sulfates a été étudiée par des tests de lixiviation réalisés conformément à la norme européenne NF EN 12457-5. Les mécanismes de stabilisation des sulfates ont été étudiés en effectuant une caractérisation minéralogique et microstructurale ainsi qu'une modélisation géochimique en utilisant le code PHREEQC.

Après des tests de lixiviation, il a été observé que tous les traitements conduisaient à une diminution de la concentration des sulfates en solution à des valeurs inférieures à 1000 mg/kg de sol sec (valeur maximale établie par l'arrêté français du 12 décembre 2014, pour la catégorie des déchets inertes et non-dangereux). Cependant, les traitements avec l'OPC et le clinker ont conduit au relargage de métaux lourds en solution, notamment du chrome, du fait de leur teneur élevée en clinker. De plus, ces liants ont également entrainé des expansions élevées (>5%) à cause de la formation d'ettringite en excès. En revanche, les liants contenant du laitier ont conduit à de faibles expansions (<2%), la rétention des sulfates a été d'environ 89%, avec un relargage limité de métaux lourds. La solubilité des sulfates a été contrôlée par l'ettringite, qui n'a pas conduit à une expansion, peut-être en raison de la faible cinétique de précipitation et de l'absence de portlandite, souvent liée à l'ettringite expansive.

Parmi tous les traitements, l'utilisation du liant expérimental contentant 90% laitier et 10% OPC a donné les meilleures performances en termes de lixiviation aux sulfates, de gonflement et de résistance à la traction. Par conséquent, cette formulation a été étudiée à moyen et long termes en réalisant des tests de lixiviation à des âges ultérieurs (6 mois) afin de vérifier la stabilisation des sulfates. De plus, comme le traitement des sols sulfatés concerne la réutilisation des sols pour des travaux d'ingénierie (ex : construction de routes), cette formulation a également été évaluée en réalisant différents essais géotechniques (maniabilité, essais de résistance à la compression, gonflement et performances de classe mécanique). Nous avons constaté que la stabilisation des sulfates est restée stable dans le temps et que les propriétés géotechniques du sol traité étaient satisfaisantes pour envisager une utilisation dans des projets de génie civil. De plus, la modélisation réalisée avec ce liant a montré que les résultats numériques étaient en accord avec les résultats expérimentaux lorsque le degré d'hydratation du laitier était supposé être de 30%. Le modèle géochimique a alors pu prédire correctement les concentrations de sulfates en solution en fonction du dosage de liant utilisé dans le traitement. La modélisation a montré que l'ettringite était en effet le principal mécanisme de stabilisation contrôlant la solubilité des sulfates et que les sulfates étaient partiellement immobilisés à des concentrations proches de 1000 mg/kg à partir de 7% de liant ajouté au sol sulfaté.

Perspectives :

Les perspectives détaillées sont présentées à la fin du Chapitre 4 (cf. section 4.6). Ici, nous présentons un résumé de ces perspectives.

La stabilisation des sulfates a été évaluée ici dans un sol sulfaté. Il serait alors intéressant de traiter un sol naturel riche en sulfates avec les mêmes formulations utilisées dans cette étude afin de vérifier leur capacité à immobiliser les sulfates et ne pas produire de gonflement.

De plus, la stabilisation des sulfates par des liants contenant du laitier s'est révélée être satisfaisante. Pour la modélisation, un degré d'hydratation du laitier de 30% a été supposé. Ce degré d'hydratation devrait être confirmé expérimentalement dans un système constitué de « sol + liant + sulfates ». Dans ce cas, plusieurs facteurs devront être pris en compte, tels que l'effet de dilution du liant, la quantité d'eau disponible pour hydrater le liant et celle

consommée par le sol, ainsi que la quantité d'argile contenant du magnésium qui est également présente dans le laitier.

Stabilisation du molybdène (Mo)

Cette partie visait à : (i) comparer la capacité de plusieurs liants à immobiliser du molybdène, et (ii) contribuer à la compréhension des mécanismes associés à sa stabilisation.

Nous avons alors étudié l'interaction du Mo avec plusieurs liants et évalué leur capacité à stabiliser le Mo. Nous nous sommes concentrés sur l'interaction du Mo avec trois liants différents : un OPC (B1), un liant expérimental composé de 90% laitier et 10% OPC (B2) et un ciment sur-sulfaté (B3). Ainsi, ces trois liants ont été artificiellement dopés avec différentes concentrations de Mo. La stabilisation du Mo a été aussi étudiée par la synthèse du silicate de calcium hydraté (C-S-H) en utilisant cinq teneurs différentes en Mo.

L'immobilisation du Mo a été évaluée en effectuant des tests de lixiviation sur pâte réalisés conformément à la norme européenne NF EN 12457-5 à des conditions de pH neutre. De plus, les mécanismes de stabilisation ont été étudiés en utilisant des analyses minéralogiques et microstructurales et la modélisation géochimique.

Les tests de lixiviation sur pâte ont montré que le Mo a été largement fixé dans toutes les fractions solides, notamment à des teneurs élevées de Mo. Nous avons observé que la rétention du Mo augmentait avec la concentration initiale de Mo dans les liants. L'ordre suivant a été obtenu pour la rétention du Mo par les liants : B3> B1> B2.

Dans l'ensemble, la précipitation de powellite ($CaMoO_4$) s'est avérée être le principal mécanisme de stabilisation du Mo pour les concentrations étudiées sauf pour des concentrations inferieurs à 500 mg/kg of binder. De plus, le Mo a été mélangé avec du calcium et des sulfates, probablement en raison de la substitution ou de l'adsorption dans les phases sulfatées. Le Mo a été également lié aux hydrates de silicate de calcium (C-S-H) probablement en raison de la co-précipitation de powellite à la surface des C-S-H ou en raison de l'adsorption de Mo sur la surface des C-S-H. Concernant la synthèse de C-S-H, les données expérimentales et celles issues de la modélisation ont montré que la powellite avait co-précipité pour des teneurs en Mo supérieures à 90 ppm ($1,9x10^{-5}$ mol/L). Nous suggérons qu'à faibles concentrations, le Mo est plutôt immobilisé par l'adsorption sur les surfaces de C-S-H, comme indiqué expérimentalement.

Perspectives :

Les perspectives détaillées sont présentées à la fin du Chapitre 5 (cf. section 5.5). Ici, nous présentons un résumé de ces perspectives.

La stabilisation du Mo a été étudiée dans des liants dopés en Mo. Le traitement d'un matériau naturellement contaminé en Mo permettrait de vérifier l'efficacité de chaque liant à immobiliser le Mo. Dans ce cas, plusieurs facteurs devront être pris en compte pour évaluer la stabilisation du Mo, tels que la compétition ionique et l'effet de la matière organique sur l'hydratation du liant.

L'identification expérimentale des mécanismes de stabilisation du Mo à de faibles concentrations (de l'ordre de 10^{-5} mol/kg), pour lesquels la powellite ne devrait pas précipiter, est nécessaire. Cependant, la compréhension des mécanismes de stabilisation du Mo nécessite l'identification précise de ses espèces chimiques dans les matériaux contaminés [10]. Mo K-edge XANES a été utilisé avec succès pour l'identification de la spéciation du Mo dans le sol (y compris l'adsorption de surface et la précipitation minérale) et dans les solutions aqueuses [11], [12]. A notre connaissance, la technique XAS n'a cependant pas encore été utilisée pour étudier les mécanismes de stabilisation du Mo dans les liants hydrauliques. Ainsi, les méthodes XAS (rayonnement synchrotron par spectroscopie XANES et EXAFS) semblent être bien adaptées pour étudier l'immobilisation du Mo par des liants hydrauliques, à de faibles

concentrations de Mo typiquement rencontrées dans les matériaux naturels [10], [13]. Pour ce faire, les spectres XANES et EXAFS obtenus à partir d'échantillons traités doivent être comparés aux standards du Mo afin d'identifier les mécanismes de stabilisation dominants. Les standards du Mo sont des minéraux purs qui contiennent du Mo. Par exemple, la synthèse de phases telles que l'ettringite avec Mo et le monosulfoaluminate avec Mo permettrait l'identification de la substitution du sulfate par le molybdate.

D'un autre côté, peu d'informations sont disponibles dans la littérature sur les produits de solubilité des possibles réactions impliquées dans l'interaction du Mo avec les liants cimentaires. Certaines réactions thermodynamiques ont été publiées concernant la powellite et l'AFm contenant du Mo. Par conséquent, il serait intéressant de développer un modèle géochimique prenant en compte non seulement la précipitation de powellite, mais aussi la formation d'autres phases contenant du Mo comme la substitution du sulfate par le molybdate dans l'ettringite, afin d'améliorer la compréhension des mécanismes d'immobilisation du Mo.

Comme les phases C-S-H sont connues pour avoir une capacité de sorption élevée en raison de leur surface spécifique importante, le fait de développer un modèle d'adsorption de surface avec le C-S-H et le Mo permettrait de mieux comprendre la capacité du C-S-H à immobiliser le Mo. Ce type de modélisation devrait se focaliser principalement sur de très faibles concentrations de Mo (de l'ordre de 10^{-5} mol/kg) pour lesquelles la powellite ne devrait pas précipiter.

REFERENCES

References

[1]   A. Le Roux and S. Orsetti, "Les réactions sulfatiques : Conditions de formation, structure et expansion des minéraux secondaires sulfatés," *Bulletin des Laboratoires des Ponts et Chaussees*, no. 225, pp. 41–50, 2000.

[2]   N. Talluri, A. Puppala, B. Chittoori, A. Gaily, and P. Harris, "Stabilization of high-sulfate soils by extended mellowing," *Transportation Research Record*, vol. 2363, no. 2363, pp. 96–104, 2013.

[3]   G. Escadeillas and H. Hornain, "La durabilité des bétons vis-a-vis des environnements chimiquement agressifs," in *La Durabilité Des Bétons*, 2008, pp. 613–705.

[4]   N. N. Greenwood and A. Earnshaw, *Chemistry of the Elements*. Elsevier, 1997.

[5]   Société Française de Chimie, "Exploitation du gypse," 2016. [Online]. Available: http://www.societechimiquedefrance.fr/extras/Donnees/espace_travail/mine/caso/texc aso.htm.

[6]   M. Alexander, A. Bertron, and N. De Belie, *Performance of Cement-Based Materials in Aggressive Aqueous Environments*, vol. 10. 2013.

[7]   A. Klimchouk, "The dissolution and conversion of gypsum and anhydrite," *International Journal of Speleology*, vol. 25, no. 3/4, pp. 21–36, 1996.

[8]   W. Müllauer, R. E. Beddoe, and D. Heinz, "Sulfate attack expansion mechanisms," *Cement and Concrete Research*, vol. 52, pp. 208–215, 2013.

[9]   M. Komljenović, N. Džunuzović, and V. Nikolić, "Resistance to external sulfate attack - Comparison of two alkali-activated binders," *MATEC Web of Conferences*, vol. 163, p. 6001, 2018.

[10]   N. Bur, "Étude Des Caractéristiques Physico-Chimiques De Nouveaux Bétons Éco-Respectueux Pour Leur Résistance À L'Environnement Dans Le Cadre Du Développement Durable," p. 225, 2012.

[11]   A. Nonat, "L'hydratation des ciments," in *La durabilité des bétons*, 2008, pp. 25–50.

[12]   M. Santhanam, M. D. Cohen, and J. Olek, "Mechanism of sulfate attack: A fresh look - Part 1; Summary of experimental results," *Cement and Concrete Research*, vol. 32, no. 6, pp. 915–921, 2002.

[13]   T. Schmidt, B. Lothenbach, M. Romer, J. Neuenschwander, and K. Scrivener, "Physical and microstructural aspects of sulfate attack on ordinary and limestone blended Portland cements," *Cement and Concrete Research*, vol. 39, no. 12, pp. 1111–1121, 2009.

[14]   B. Tian and M. D. Cohen, "Does gypsum formation during sulfate attack on concrete lead to expansion?," *Cement and Concrete Research*, vol. 30, no. 1, pp. 117–123, Jan. 2000.

[15]   G. W. Scherer, "Stress from crystallization of salt," *Cement and Concrete Research*, vol. 34, no. 9, pp. 1613–1624, 2004.

[16]   G. W. Scherer, "Crystallization in pores," *Cement and Concrete Research*, vol. 29, no. 8, pp. 1347–1358, 1999.

[17]   P. K. Mehta, "Mechanism of expansion associated with ettringite formation," *Cement and Concrete Research*, vol. 3, no. 1, pp. 1–6, 1973.

[18]   A. E. Idiart, C. M. López, and I. Carol, "Chemo-mechanical analysis of concrete cracking and degradation due to external sulfate attack: A meso-scale model," *Cement and*

Concrete Composites, vol. 33, no. 3, pp. 411–423, 2011.

[19] M. C. G. Juenger, F. Winnefeld, J. L. Provis, and J. H. Ideker, "Advances in alternative cementitious binders," *Cement and Concrete Research*, vol. 41, no. 12, pp. 1232–1243, 2011.

[20] C. Ouyang, A. Nanni, and W. F. Chang, "Internal and external sources of sulfate ions in portland cement mortar: two types of chemical attack," *Cement and Concrete Research*, vol. 18, no. 5, pp. 699–709, 1988.

[21] R. S. Gollop and H. F. W. Taylor, "Microstructural and microanalytical studies of sulfate attack III. Sulfate-resisting portland cement: Reactions with sodium and magnesium sulfate solutions," *Cement and Concrete Research*, vol. 25, no. 7, pp. 1581–1590, 1995.

[22] L. Heller and M. Ben-Yair, "Effect of sulphate solutions on normal and sulphate-resisting portland cement," *Journal of Applied Chemistry*, vol. 14, no. 1, pp. 20–30, 2007.

[23] S. N. Ghosh, Ed., *Advances in Cement Technology*, 1st ed. 1983.

[24] J. Trägårdh and F. Bellmann, "Sulphate attack," in *Structural Survey*, vol. 19, no. 2, 2001, pp. 89–118.

[25] M. Michel, "Accélération de ciment au laitier par du ciment sulfo-alumineux," Institut National des Sciences Appliquées de Lyon, 2009.

[26] T. Bakharev, J. G. Sanjayan, and Y. B. Cheng, "Sulfate attack on alkali-activated slag concrete," *Cement and Concrete Research*, vol. 32, no. 2, pp. 211–216, 2002.

[27] O. Al-Amoudi, "Attack on plain and blended cements exposed to aggressive sulfate environments," *Cement and Concrete Composites*, vol. 24, pp. 305–316, 2002.

[28] G. Blanc, "Développement de nouveaux composites cimentaires à bas module d'élasticité : propriétés mécaniques et durabilité vis-à-vis des sollicitations environnementales," Université de Toulouse, 2017.

[29] J. Colas, "Etude de la valorisation des déblais de chantiers de tunnels en granulats à béton," Université Paris-Est, 2012.

[30] C. Yu, W. Sun, and K. Scrivener, "Degradation mechanism of slag blended mortars immersed in sodium sulfate solution," *Cement and Concrete Research*, vol. 72, pp. 37–47, Jun. 2015.

[31] N. Džunuzović, M. Komljenović, V. Nikolić, and T. Ivanović, "External sulfate attack on alkali-activated fly ash-blast furnace slag composite," *Construction and Building Materials*, vol. 157, pp. 737–747, 2017.

[32] P. Duan, C. Yan, and W. Zhou, "Influence of partial replacement of fly ash by metakaolin on mechanical properties and microstructure of fly ash geopolymer paste exposed to sulfate attack," *Ceramics International*, vol. 42, no. 2, pp. 3504–3517, 2016.

[33] M. B. Karakoç, I. Türkmen, M. M. Maraş, F. Kantarci, and R. Demirboła, "Sulfate resistance of ferrochrome slag based geopolymer concrete," *Ceramics International*, vol. 42, no. 1, pp. 1254–1260, 2016.

[34] H. E. Elyamany, A. E. M. Abd Elmoaty, and A. M. Elshaboury, "Magnesium sulfate resistance of geopolymer mortar," *Construction and Building Materials*, vol. 184, pp. 111–127, 2018.

[35] V. Sata, A. Sathonsaowaphak, and P. Chindaprasirt, "Resistance of lignite bottom ash geopolymer mortar to sulfate and sulfuric acid attack," *Cement and Concrete Composites*, vol. 34, no. 5, pp. 700–708, 2012.

[36] P. Duxson and J. L. Provis, "Designing precursors for geopolymer cements," *Journal of*

the American Ceramic Society, vol. 91, no. 12, pp. 3864–3869, 2008.

[37]   J. L. Provis, "Activating solution chemistry for geopolymers," *Geopolymers: Structures, Processing, Properties and Industrial Applications*, pp. 50–71, 2009.

[38]   P. Duxson, A. Fernández-Jiménez, J. L. Provis, G. C. Lukey, A. Palomo, and J. S. J. Van Deventer, "Geopolymer technology: The current state of the art," *Journal of Materials Science*, vol. 42, no. 9, pp. 2917–2933, 2007.

[39]   R. Pouhet, "Formulation and durability of metakaolin-based geopolymers," Université de Toulouse III - Paul Sabatier, 2015.

[40]   M. Komljenović, Z. Baščarević, N. Marjanović, and V. Nikolić, "External sulfate attack on alkali-activated slag," *Construction and Building Materials*, vol. 49, pp. 31–39, 2013.

[41]   A. Allahverdi, H. Hashemi, and M. Mahinroosta, "Resistance of Alkali-activated Slag Cement Against Sodium Sulfate," *Iranian Journal of Materials Science & Engineering*, vol. 17, no. 1, 2020.

[42]   H. Ye, Z. Chen, and L. Huang, "Mechanism of sulfate attack on alkali-activated slag: The role of activator composition," *Cement and Concrete Research*, vol. 125, p. 105868, Nov. 2019.

[43]   I. Ismail, S. A. Bernal, J. L. Provis, S. Hamdan, and J. S. J. Van Deventer, "Microstructural changes in alkali activated fly ash/slag geopolymers with sulfate exposure," *Materials and Structures/Materiaux et Constructions*, vol. 46, no. 3, pp. 361–373, 2013.

[44]   P. Chindaprasirt, U. Rattanasak, and S. Taebuanhuad, "Resistance to acid and sulfate solutions of microwave-assisted high calcium fly ash geopolymer," *Materials and Structures*, vol. 46, no. 3, pp. 375–381, Mar. 2013.

[45]   H. A. Alcamand, P. H. R. Borges, F. A. Silva, and A. C. C. Trindade, "The effect of matrix composition and calcium content on the sulfate durability of metakaolin and metakaolin/slag alkali-activated mortars," *Ceramics International*, vol. 44, no. 5, pp. 5037–5044, Apr. 2018.

[46]   I. A. Chen, C. W. Hargis, and M. C. G. Juenger, "Understanding expansion in calcium sulfoaluminate-belite cements," *Cement and Concrete Research*, vol. 42, no. 1, pp. 51–60, 2012.

[47]   C. W. Hargis, B. Lothenbach, C. J. Müller, and F. Winnefeld, "Further insights into calcium sulfoaluminate cement expansion," *Advances in Cement Research*, vol. 31, no. 4, pp. 160–177, Apr. 2019.

[48]   K. Ogawa and D. M. Roy, "C4A3S̄ hydration, ettringite formation, and its expansion mechanism: III. Effect of CaO, NaOH and NaCl; conclusions," *Cement and Concrete Research*, vol. 12, no. 2, pp. 247–256, Mar. 1982.

[49]   J. Beretka, M. Marroccoli, N. Sherman, and G. L. Valenti, "The influence of C4A3S̄ content and WS ratio on the performance of calcium sulfoaluminate-based cements," *Cement and Concrete Research*, vol. 26, no. 11, pp. 1673–1681, Nov. 1996.

[50]   W. Kurdowski and A. Thiel, "On the role of free calcium oxide in expansive cements," *Cement and Concrete Research*, vol. 11, no. 1, pp. 29–40, Jan. 1981.

[51]   F. P. Glasser and L. Zhang, "High-performance cement matrices based on calcium sulfoaluminate-belite compositions," *Cement and Concrete Research*, vol. 31, no. 12, pp. 1881–1886, 2001.

[52]   E. Bescher, E. K. Rice, C. Ramseyer, and S. Roswurm, "Sulfate resistance of calcium sulphoaluminate cement," *Journal of Structural Integrity and Maintenance*, vol. 1, no. 3,

pp. 131–139, Jul. 2016.

[53] T. Grounds, D. V. Nowell, and F. W. Wilburn, "Resistance of supersulfated cement to strong sulfate solutions," *Journal of Thermal Analysis and Calorimetry*, vol. 72, no. 1, pp. 181–190, 2003.

[54] Q. Niu and R. Zhang, "Effect of supersulphated cement on sulfate attack of cement mortar," in *Proceedings of the 3rd International Conference on Advances in Energy and Environmental Science 2015*, 2015.

[55] F. Winnefeld and B. Lothenbach, "Hydration of calcium sulfoaluminate cements - Experimental findings and thermodynamic modelling," *Cement and Concrete Research*, vol. 40, no. 8, pp. 1239–1247, 2010.

[56] J. Péra and J. Ambroise, "New applications of calcium sulfoaluminate cement," *Cement and Concrete Research*, vol. 34, no. 4, pp. 671–676, 2004.

[57] R. Trauchessec, "Mélanges de ciments sulfoalumineux et Portland," Université de Lorraine, 2013.

[58] G. Bernardo, A. Telesca, and G. L. Valenti, "A porosimetric study of calcium sulfoaluminate cement pastes cured at early ages," *Cement and Concrete Research*, vol. 36, no. 6, pp. 1042–1047, Jun. 2006.

[59] K. Ndiaye, M. Cyr, and S. Ginestet, "Development of a cementitious material for thermal energy storage at low temperature," *Construction and Building Materials*, vol. 242, p. 118130, May 2020.

[60] P. C. Hewlett and M. Liska, Eds., *Lea's Chemistry of Cement and Concrete*, vol. 58, no. 10. Elsevier, 2019.

[61] T. Matschei, F. Bellmann, and J. Stark, "Hydration behaviour of sulphate-activated slag cements," *Advances in Cement Research*, vol. 17, no. 4, pp. 167–178, 2005.

[62] A. Gruskovnjak *et al.*, "Hydration mechanisms of super sulphated slag cement," *Cement and Concrete Research*, vol. 38, no. 7, pp. 983–992, 2008.

[63] T. Cerulli, C. Pistolesi, C. Maltese, and D. Salvioni, "Durability of traditional plasters with respect to blast furnace slag-based plaster," *Cement and Concrete Research*, vol. 33, no. 9, pp. 1375–1383, 2003.

[64] M. Singh and M. Garg, "Calcium sulfate hemihydrate activated low heat sulfate resistant cement," *Construction and Building Materials*, vol. 16, no. 3, pp. 181–186, 2002.

[65] LCPC-SETRA, *Guide Technique: Réalisation des remblais et des couches de forme*, 2nd ed. 2000.

[66] LCPC-SETRA, *Guide technique: Traitement des sols à la chaux et/ou aux liants hydrauliques Application à la réalisation*. 2000.

[67] T. Le Borgne, "Caractérisation et quantification des éléments perturbateurs de prise lors du traitement des sols," Institut National Polytechnique De Lorraine, 2010.

[68] D. Hunter, "Lime-induced heave in sulfate-bearing clay soils," *Journal of Geotechnical Engineering*, vol. 114, no. 2, pp. 150–167, 1988.

[69] N. Cabane, "Sols traités à la chaux et aux liants hydrauliques : Contribution à l'identification et à l'analyse des élèments perturbateurs de la stabilisation," Université Jean Monnet - Saint-Etienne, 2004.

[70] E. Celik and Z. Nalbantoglu, "Effects of ground granulated blastfurnace slag (GGBS) on the swelling properties of lime-stabilized sulfate-bearing soils," *Engineering Geology*, vol. 163, pp. 20–25, 2013.

[71] P. Harris, J. von Holdt, S. Sebesta, and T. Scullion, "Part 3: Cementitious, Chemical, and Mechanical Stabilization: Recommendations for Stabilization of High-Sulfate Soils in Texas," *Transportation Research Record: Journal of the Transportation Research Board*, vol. 1952, pp. 71–79, 2006.

[72] B. Kolani, L. Buffo-Lacarrière, A. Sellier, G. Escadeillas, L. Boutillon, and L. Linger, "Hydration of slag-blended cements," *Cement and Concrete Composites*, vol. 34, no. 9, pp. 1009–1018, 2012.

[73] A. J. Puppala, E. Wattanasanticharoen, and K. Punthutaecha, "Experimental evaluations of stabilisation methods for sulphate-rich expansive soils," *Ground Improvement*, vol. 9, no. 2, pp. 89–90, 2005.

[74] W. Wang, A. Roy, R. K. Seals, and J. B. Metcalf, "Stabilization of Sulfate-Containing Soil by Cementitious Mixtures Mechanical Properties," *Transportation Research Record*, vol. 1837, no. 1837, pp. 12–19, 2003.

[75] D. Dermatas, "Ettringite-Induced Swelling in Soils: State-of-the-Art," *Applied Mechanics Reviews*, vol. 48, no. 10, pp. 659–673, Oct. 1995.

[76] A. J. Puppala, J. A. Griffin, L. R. Hoyos, and S. Chomtid, "Studies on sulfate-resistant cement stabilization methods to address sulfate-induced soil heave," *Journal of Geotechnical and Geoenvironmental Engineering*, vol. 130, no. 4, pp. 391–402, 2004.

[77] P. B. V. S. Kota, D. Hazlett, and L. Perrin, "Sulfate-bearing soils: Problems with calcium-based stabilizers," *Transportation Research Record*, no. 1546, pp. 62–69, 1996.

[78] M. Mahedi, B. Cetin, and D. J. White, *Performance Evaluation of Cement and Slag Stabilized Expansive Soils*, vol. 2672, no. 52. 2018.

[79] S. Wild, J. M. Kinuthia, G. I. Jones, and D. D. Higgins, "Effects of partial substitution of lime with ground granulated blast furnace slag (GGBS) on the strength properties of lime-stabilised sulphate-bearing clay soils," *Engineering Geology*, vol. 51, no. 1, pp. 37–53, 1998.

[80] J. M. Kinuthia, S. Wild, and G. I. Jones, "Effects of monovalent and divalent metal sulphates on consistency and compaction of lime-stabilised kaolinite," *Applied Clay Science*, vol. 14, no. 1–3, pp. 27–45, 1999.

[81] S. Wild and W. A. Tasong, "Influence of ground granulated blastfurnace slag on the sulphate resistance of lime-stabilized kaolinite," *Magazine of Concrete Research*, vol. 51, no. 4, pp. 247–254, 1999.

[82] W. A. Tasong, S. Wild, and R. J. D. Tilley, "Mechanisms by which ground granulated blastfurnace slag prevents sulphate attack of lime-stabilized kaolinite," *Cement and Concrete Research*, vol. 29, no. 7, pp. 975–982, 1999.

[83] S. Wild, J. M. Kinuthia, G. I. Jones, and D. D. Higgins, "Suppression of swelling associated with ettringite formation in lime stabilized sulphate bearing clay soils by partial substitution of lime with ground granulated blastfurnace slag," *Engineering Geology*, vol. 51, no. 4, pp. 257–277, 1999.

[84] V. Trincal, V. Thiéry, Y. Mamindy-Pajany, and S. Hillier, "Use of hydraulic binders for reducing sulphate leaching: application to gypsiferous soil sampled in Ile-de-France region (France)," *Environmental Science and Pollution Research*, vol. 25, no. 23, pp. 22977–22997, 2018.

[85] S. Peysson, "Contribution à l'étude de la stabilisation de déchets par du ciment sulfo-alumineux," Institut National des Sciences Appliquées de Lyon, 2005.

[86] Q. Y. Chen, M. Tyrer, C. D. Hills, X. M. Yang, and P. Carey, "Immobilisation of heavy metal in cement-based solidification/stabilisation: A review," *Waste Management*, vol.

29, no. 1, pp. 390–403, 2009.

[87] Wordl Health Organization, "Guidelines for Drinking-water Quality," Geneva, 2004.

[88] Legifrance, *Arrêté du 12 décembre 2014 relatif aux conditions d'admission des déchets inertes dans les installations relevant des rubriques 2515, 2516, 2517 et dans les installations de stockage de déchets inertes relevant de la rubrique 2760 de la nomenclature des i.* France, 2014, pp. 3–7.

[89] "Décision n ° 2003/33/CE du 19/12/02 établissant des critères et des procédures d'admission des déchets dans les décharges, conformément à l'article 16 et à l'annexe II de la directive 1999/ 31/CE," 2003, no. 6, pp. 1–33.

[90] J. Bergmans, P. Nielsen, R. Snellings, and K. Broos, "Recycling of autoclaved aerated concrete in floor screeds: Sulfate leaching reduction by ettringite formation," *Construction and Building Materials*, vol. 111, pp. 9–14, 2016.

[91] S. A. Leonard and J. A. Stegemann, "Contaminant leaching from stabilized/solidified acid tars," *Journal of Environmental Engineering*, vol. 136, no. 12, pp. 1369–1378, 2010.

[92] E. Galán Huertos and A. Romero Baena, "Contaminación de Suelos por Metales Pesados," in *Revista de la sociedad española de mineralogía*, 2009, pp. 48–60.

[93] M. E. Watson, *The Handbook of Trace Elements*, vol. 27, no. 4. 1998.

[94] W. W. Wenzel and B. J. Alloway, *Heavy Metals in Soils*, 3rd ed., vol. 22. Dordrecht: Springer Netherlands, 2013.

[95] N. T. Basta, J. A. Ryan, and R. L. Chaney, "Trace element chemistry in residual-treated soil: Key concepts and metal bioavailability," *Journal of Environmental Quality*, vol. 34, no. 1, pp. 49–63, 2005.

[96] J. Sirven, "Détéction de Métaux lourds dans les sols par spectroscopie d'émission sur plasma induit par laser (LIBS)," Université de Bordeaux 1, 2006.

[97] G. PLAISANCE, "Bibliographic des Sols de France," 1957.

[98] Agence de l'Environnement et de la Maîtrise de l'Energie (ADEME) -SOGREAH, "Bilan qualitatif de la contamination par les éléments tracés métalliques et les composés tracés organiques et application quantitative pour les éléments tracés métalliques," 2007.

[99] U. C. Gupta, *Molybdenum in agriculture*, vol. 35, no. 01. Cambridge University Press, 1997.

[100] C. Siebert, J. C. Pett-Ridge, S. Opfergelt, R. A. Guicharnaud, A. N. Halliday, and K. W. Burton, "Molybdenum isotope fractionation in soils: Influence of redox conditions, organic matter, and atmospheric inputs," *Geochimica et Cosmochimica Acta*, vol. 162, pp. 1–24, 2015.

[101] B. A. Averill, "Fe-S and Mo-Fe-S clusters as models for the active site of nitrogenase," in *Copper, Molybdenum, and Vanadium in Biological Systems*, Springer-Verlag, 2007, pp. 59–103.

[102] B. C. Bostick, S. Fendorf, and G. R. Helz, "Differential adsorption of molybdate and tetrathiomolybdate on pyrite (FeS2)," *Environmental Science and Technology*, vol. 37, no. 2, pp. 285–291, 2003.

[103] J. A. Erdman, R. J. Ebens, and A. A. Case, "Molybdenosis: A Potential Problem in Ruminants Grazing on Coal Mine Spoils," *Journal of Range Management*, vol. 31, no. 1, p. 34, 1978.

[104] C. A. M. Van Gestel *et al.*, "Effect of long-term equilibration on the toxicity of molybdenum to soil organisms," *Environmental Pollution*, vol. 162, pp. 1–7, 2012.

[105] P. C. H. Mitchell, "Coordination compounds of molybdenum," *Coordination Chemistry Reviews*, vol. 1, no. 3, pp. 315–350, 1966.

[106] P. L. Smedley and D. G. Kinniburgh, "Molybdenum in natural waters: A review of occurrence, distributions and controls," *Applied Geochemistry*, vol. 84, pp. 387–432, Sep. 2017.

[107] A. Cabrerizo, D. Bulteel, J. Waligora, G. Landrot, E. Fonda, and F. Olard, "Chemical, mineralogical, and environmental characterization of tunnel boring muds for their valorization in road construction: a focus on molybdenum characterization," *Environmental Science and Pollution Research*, no. Melt 2000, 2020.

[108] T. A. Kirpichtchikova, A. Manceau, L. Spadini, F. Panfili, M. A. Marcus, and T. Jacquet, "Speciation and solubility of heavy metals in contaminated soil using X-ray microfluorescence, EXAFS spectroscopy, chemical extraction, and thermodynamic modeling," *Geochimica et Cosmochimica Acta*, vol. 70, no. 9, pp. 2163–2190, 2006.

[109] F. P. Glasser, "Fundamental aspects of cement solidification and stabilisation," *Journal of Hazardous Materials*, vol. 52, no. 2–3, pp. 151–170, 1997.

[110] Q. Zhou, N. B. Milestone, and M. Hayes, "An alternative to Portland Cement for waste encapsulation-The calcium sulfoaluminate cement system," *Journal of Hazardous Materials*, vol. 136, no. 1 SPEC. ISS., pp. 120–129, 2006.

[111] G. E. Voglar and D. Leštan, "Equilibrium leaching of toxic elements from cement stabilized soil," *Journal of Hazardous Materials*, vol. 246–247, pp. 18–25, 2013.

[112] R. D. Spence and C. Shi, *Stabilization and solidification of hazardous, radioactive, and mixed wastes*. CRC Press, 2004.

[113] C. Cau-dit-Coumes, "Alternative Binders to Ordinary Portland Cement for Radwaste Solidification and Stabilization," in *Cement-Based Materials for Nuclear Waste Storage*, New York, NY: Springer New York, 2013, pp. 171–191.

[114] B. Batchelor, "Overview of waste stabilization with cement," *Waste Management*, vol. 26, no. 7, pp. 689–698, Jan. 2006.

[115] G. Mancini, F. Palmeri, A. Luciano, P. Viotti, and D. Fino, "Partial Stabilization of Mo-Containing Hazardous Wastes Using a Ferrous Sulfate-Based Additive as a Redox Agent," *Waste and Biomass Valorization*, no. 0123456789, 2020.

[116] S. Mundra *et al.*, "Steel corrosion in reinforced alkali-activated materials," *RILEM Technical Letters*, vol. 2, pp. 33–39, 2017.

[117] C. Napia, T. Sinsiri, C. Jaturapitakkul, and P. Chindaprasirt, "Leaching of heavy metals from solidified waste using Portland cement and zeolite as a binder," *Waste Management*, vol. 32, no. 7, pp. 1459–1467, 2012.

[118] C. K. Park, "Hydration and solidification of hazardous wastes containing heavy metals using modified cementitious materials," *Cement and Concrete Research*, vol. 30, no. 3, pp. 429–435, 2000.

[119] Y. Bai, N. C. Collier, N. B. Milestone, and C. H. Yang, "The potential for using slags activated with near neutral salts as immobilisation matrices for nuclear wastes containing reactive metals," *Journal of Nuclear Materials*, vol. 413, no. 3, pp. 183–192, 2011.

[120] J. Deja, "Immobilization of Cr6+, Cd2+, Zn2+ and Pb2+ in alkali-activated slag binders," *Cement and Concrete Research*, vol. 32, no. 12, pp. 1971–1979, Dec. 2002.

[121] R. B. Kogbara and A. Al-Tabbaa, "Mechanical and leaching behaviour of slag-cement and lime-activated slag stabilised/solidified contaminated soil," *Science of the Total*

Environment, vol. 409, no. 11, pp. 2325–2335, 2011.

[122] Z. Giergiczny and A. Król, "Immobilization of heavy metals (Pb, Cu, Cr, Zn, Cd, Mn) in the mineral additions containing concrete composites," *Journal of Hazardous Materials*, vol. 160, no. 2–3, pp. 247–255, 2008.

[123] M. L. Allan and L. E. Kukacka, "Blast furnace slag-modified grouts for in situ stabilization of chromium-contaminated soil," *Waste Management*, vol. 15, no. 3, pp. 193–202, 1995.

[124] N. Takeno, "Atlas of Eh-pH diagrams Intercomparison of thermodynamic databases," 2005.

[125] S. E. Kesler, *Eh-pH diagrams for geochemistry*, vol. 53, no. 3. 1989.

[126] C. D. Hills, C. J. Sollars, and R. Perry, "A calorimetric and microstructural study of solidified toxic wastes -Part 2: A model for poisoning of OPC hydration," *Waste Management*, vol. 14, no. 7, pp. 601–612, 1994.

[127] M. L. D. Gougar, B. E. Scheetz, and D. M. Roy, "Ettringite and C-S-H portland cement phases for waste ion immobilization: A review," *Waste Management*, vol. 16, no. 4, pp. 295–303, 1996.

[128] D. H. Moon, D. G. Grubb, and T. L. Reilly, "Stabilization/solidification of selenium-impacted soils using Portland cement and cement kiln dust," *Journal of Hazardous Materials*, vol. 168, no. 2–3, pp. 944–951, 2009.

[129] I. Baur and C. A. Johnson, "The solubility of selenate-AFt ($3CaO \cdot Al_2O_3 \cdot 3CaSeO_4 \cdot 37.5H_2O$) and selenate-AFm ($3CaO \cdot Al_2O_3 \cdot CaSeO_4 \cdot xH_2O$)," *Cement and Concrete Research*, vol. 33, no. 11, pp. 1741–1748, 2003.

[130] A. Palomo and M. Palacios, "Alkali-activated cementitious materials: Alternative matrices for the immobilisation of hazardous wastes - Part II. Stabilisation of chromium and lead," *Cement and Concrete Research*, vol. 33, no. 2, pp. 289–295, 2003.

[131] A. Minocha and M. H. Goyal, "Immobilization of Molybdenum in Ordinary Portland Cement," *Journal of Chemical Engineering & Process Technology*, vol. 04, no. 05, pp. 5–10, 2013.

[132] A. Kindness, E. E. Lachowski, A. K. Minocha, and F. P. Glasser, "Immobilisation and fixation of molybdenum (VI) by Portland cement," *Waste Management*, vol. 14, no. 2, pp. 97–102, 1994.

[133] "Futura Sciences." [Online]. Available: https://www.futura-sciences.com/sciences/definitions/chimie-substitution-1625/.

[134] A. C. M. Bourg and J. P. G. Loch, "Mobilization of Heavy Metals as Affected by pH and Redox Conditions," in *Biogeodynamics of Pollutants in Soils and Sediments*, no. March 2016, Berlin, Heidelberg: Springer Berlin Heidelberg, 1995, pp. 87–102.

[135] S. Berger, "Etude des potentialités des ciments sulfo-alumineux bélitique pour le conditionnement du zinc : de l'hydratation à la durabilité," Université de Lille 1, 2009.

[136] M. Chrysochoou and D. Dermatas, "Evaluation of ettringite and hydrocalumite formation for heavy metal immobilization: Literature review and experimental study," *Journal of Hazardous Materials*, vol. 136, no. 1 SPEC. ISS., pp. 20–33, 2006.

[137] F. Goetz-Neunhoeffer and J. Neubauer, "Refined ettringite ($Ca_6Al_2(SO_4)_3(OH)_{12} \cdot 26H_2O$) structure for quantitative X-ray diffraction analysis," *Powder Diffraction*, vol. 21, no. 1, pp. 4–11, 2006.

[138] G. Cornelis, C. A. Johnson, T. Van Gerven, and C. Vandecasteele, "Leaching mechanisms of oxyanionic metalloid and metal species in alkaline solid wastes: A review," *Applied Geochemistry*, vol. 23, no. 5, pp. 955–976, May 2008.

[139] J.-B. Champenois *et al.*, "Crystal structures of Boro-AFm and sBoro-AFt phases," *Cement and Concrete Research*, vol. 42, no. 10, pp. 1362–1370, Oct. 2012.

[140] S. C. B. Myneni, S. J. Traina, T. J. Logan, and G. A. Waychunas, "Oxyanion Behavior in Alkaline Environments: Sorption and Desorption of Arsenate in Ettringite," *Environmental Science & Technology*, vol. 31, no. 6, pp. 1761–1768, Jun. 1997.

[141] D. J. Hassett, G. J. McCarthy, P. Kumarathasan, and D. Pflughoeft-Hassett, "Synthesis and characterization of selenate and sulfate-selenate ettringite structure phases," *Materials Research Bulletin*, vol. 25, no. 11, pp. 1347–1354, 1990.

[142] G. J. McCarthy, D. J. Hassett, and J. A. Bender, "Synthesis, Crystal Chemistry and Stability of Ettringite, A Material with Potential Applications in Hazardous Waste Immobilization," *MRS Proceedings*, vol. 245, pp. 129–140, 1991.

[143] M. Zhang and E. J. Reardon, "Removal of B, Cr, Mo, and Se from Wastewater by Incorporation into Hydrocalumite and Ettringite," *Environmental Science & Technology*, vol. 37, no. 13, pp. 2947–2952, Jul. 2003.

[144] A. Vollpracht and W. Brameshuber, "Binding and leaching of trace elements in Portland cement pastes," *Cement and Concrete Research*, vol. 79, pp. 76–92, Jan. 2016.

[145] E. Wiberg and N. Wiberg, *Lehrbuch der anorganischen Chemie*. Berlin; New York: Walter de Gruyter, 2007.

[146] J. Plant, D. Smith, B. Smith, and L. Williams, "Environmental geochemistry at the global scale," *Applied Geochemistry*, vol. 16, no. 11–12, pp. 1291–1308, 2001.

[147] A. C. M. Bourg, "Speciation of Heavy Metals in Soils and Groundwater and Implications for Their Natural and Provoked Mobility," in *Heavy Metals*, 1995, pp. 19–31.

[148] J. Duchesne and G. Laforest, "Evaluation of the degree of Cr ions immobilization by different binders," *Cement and Concrete Research*, vol. 34, no. 7, pp. 1173–1177, 2004.

[149] C. Zhu and G. Anderson, *Environmental Applications of Geochemical Modeling*. Cambridge University Press, 2002.

[150] S. Goldberg, "Geochemistry, Groundwater and Pollution," *Vadose Zone Journal*, vol. 5, no. 1, pp. 510–510, Jan. 2006.

[151] D. L. Parkhurst and C. A. J. Appelo, "PHREEQC (Version 3)-A Computer Program for Speciation, Batch-Reaction, One-Dimensional Transport, and Inverse Geochemical Calculations," 2013.

[152] W. Sun and H. M. Selim, "Molybdenum-phosphate retention and transport in soils," *Geoderma*, vol. 308, pp. 60–68, Dec. 2017.

[153] K. C. Carroll, J. F. Artiola, and M. L. Brusseau, "Transport of molybdenum in a biosolid-amended alkaline soil," *Chemosphere*, vol. 65, no. 5, pp. 778–785, Oct. 2006.

[154] K. J. Reddy and S. P. Gloss, "Geochemical speciation as related to the mobility of F, Mo and Se in soil leachates," *Applied Geochemistry*, vol. 8, pp. 159–163, Jan. 1993.

[155] L. Wang, K. J. Reddy, and L. C. Munn, "Geochemical modeling for predicting potential solid phases controlling the dissolved molybdenum in coal overburden, Powder River Basin, WY, U.S.A.," *Applied Geochemistry*, vol. 9, no. 1, pp. 37–43, Jan. 1994.

[156] J. Hyks, T. Astrup, and T. H. Christensen, "Long-term leaching from MSWI air-pollution-control residues: Leaching characterization and modeling," *Journal of Hazardous Materials*, vol. 162, no. 1, pp. 80–91, 2009.

[157] W. Chen and H. J. H. Brouwers, "The hydration of slag, part 2: Reaction models for blended cement," *Journal of Materials Science*, vol. 42, no. 2, pp. 444–464, 2007.

[158] R. Pouhet and M. Cyr, "Formulation and performance of flash metakaolin geopolymer concretes," *Construction and Building Materials*, vol. 120, pp. 150–160, 2016.

[159] D. Hardjito, S. E. Wallah, D. M. J. Sumajouw, and B. V. Rangan, "Factors influencing the compressive strength of fly ash-based geopolymer concrete," *Civil Engineering Dimension*, vol. 6, no. 2, pp. 88–93, 2004.

[160] C. de recherches Routières, "Code de bonne pratique pour les revêtements industrr," Bruxelles, 2004.

[161] B. Burkart, G. C. Goss, and J. P. Kern, "The role of gypsum in production of sulfate-induced deformation of lime-stabilized soils," *Environmental and Engineering Geoscience*, vol. 5, no. 2, pp. 173–187, Jan. 1999.

[162] H. Eswaran and Gong Zi-Tong, "Properties, genesis, classification, and distribution of soils with gypsum," in *Occurrence, characteristics, and genesis of carbonate, gypsum, and silica accumulations in soils. Proc. symposium, Anaheim, CA, 1988*, Madison, WI: Soil Science Society of America, 1991, pp. 89–119.

[163] C. Roosz *et al.*, "Distribution of Water in Synthetic Calcium Silicate Hydrates," *Langmuir*, vol. 32, no. 27, pp. 6794–6805, Jul. 2016.

[164] S. Petit and J. Madejova, "Fourier Transform Infrared Spectroscopy," 2013, pp. 213–231.

[165] M. Cyr, P. Rivard, F. Labrecque, and A. Daidié, "High-pressure device for fluid extraction from porous materials: Application to cement-based materials," *Journal of the American Ceramic Society*, vol. 91, no. 8, pp. 2653–2658, 2008.

[166] P. Blanc *et al.*, "Thermoddem: A geochemical database focused on low temperature water/rock interactions and waste materials," *Applied Geochemistry*, vol. 27, no. 10, pp. 2107–2116, Oct. 2012.

[167] B. Lothenbach *et al.*, "Cemdata18: A chemical thermodynamic database for hydrated Portland cements and alkali-activated materials," *Cement and Concrete Research*, vol. 115, no. October 2017, pp. 472–506, 2019.

[168] M. E. Essington, "Calcium molybdate solubility in spent oil shale and a preliminary evaluation of the association constants for the formation of CaMoO40(aq), KMoO4-(aq), and NaMoO4-(aq)," *Environmental Science & Technology*, vol. 24, no. 2, pp. 214–220, Feb. 1990.

[169] B. Lothenbach, G. Le Saout, M. Ben Haha, R. Figi, and E. Wieland, "Hydration of a low-alkali CEM III/B-SiO2 cement (LAC)," *Cement and Concrete Research*, vol. 42, no. 2, pp. 410–423, 2012.

[170] R. Taylor, I. G. Richardson, and R. M. D. Brydson, "Composition and microstructure of 20-year-old ordinary Portland cement-ground granulated blast-furnace slag blends containing 0 to 100% slag," *Cement and Concrete Research*, vol. 40, no. 7, pp. 971–983, 2010.

[171] F. Winnefeld, L. H. J. Martin, C. J. Müller, and B. Lothenbach, "Using gypsum to control hydration kinetics of CSA cements," *Construction and Building Materials*, vol. 155, pp. 154–163, 2017.

[172] A. Berrio, C. Rodriguez, and J. I. Tobón, "Effect of Al2O3/SiO2 ratio on ye'elimite production on CSA cement," *Construction and Building Materials*, vol. 168, pp. 512–521, 2018.

[173] M. García-Maté, I. Santacruz, Á. G. De La Torre, L. León-Reina, and M. A. G. Aranda, "Rheological and hydration characterization of calcium sulfoaluminate cement pastes," *Cement and Concrete Composites*, vol. 34, no. 5, pp. 684–691, 2012.

[174] C. Baux, A. Phelipot-Mardelé, C. Lanos, and A. Pierre, "Mechanical Performances of Super Sulfated Cements," *Key Engineering Materials*, vol. 617, pp. 32–35, Jun. 2014.

[175] M. Kovtun, E. P. Kearsley, and J. Shekhovtsova, "Chemical acceleration of a neutral granulated blast-furnace slag activated by sodium carbonate," *Cement and Concrete Research*, vol. 72, pp. 1–9, Jun. 2015.

[176] H. Zhang and S. Luo, "Modeling the leaching behavior of simulated HLW-glass using PHREEQC," *Nuclear Science and Techniques/Hewuli*, vol. 18, no. 3, pp. 150–153, 2007.

[177] D. Benavente, P. Brimblecombe, and C. M. Grossi, "Thermodynamic calculations for the salt crystallisation damage in porous built heritage using PHREEQC," *Environmental Earth Sciences*, vol. 74, no. 3, pp. 2297–2313, 2015.

[178] P. J. Stuyfzand, "An accurate, relatively simple calculation of the saturation index of calcite for fresh to salt water," *Journal of Hydrology*, vol. 105, no. 1–2, pp. 95–107, 1989.

[179] P. Feng, E. J. Garboczi, C. Miao, and J. W. Bullard, "Microstructural origins of cement paste degradation by external sulfate attack," *Construction and Building Materials*, vol. 96, pp. 391–403, Oct. 2015.

[180] I. Pajares, S. Martínez-Ramírez, and M. . Blanco-Varela, "Evolution of ettringite in presence of carbonate, and silicate ions," *Cement and Concrete Composites*, vol. 25, no. 8, pp. 861–865, Dec. 2003.

[181] K. Ogawa and D. M. Roy, "C4A3S hydration, ettringite formation, and its expansion mechanism: II. Microstructural observation of expansion," *Cement and Concrete Research*, vol. 12, no. 1, pp. 101–109, Jan. 1982.

[182] M. Whittaker and L. Black, "Current knowledge of external sulfate attack," *Advances in Cement Research*, vol. 27, no. 9, pp. 532–545, Oct. 2015.

[183] L. Diaz Caselles, J. Hot, C. Roosz, and M. Cyr, "Stabilization of soils containing sulfates by using alternative hydraulic binders," *Applied Geochemistry*, vol. 113, p. 104494, Feb. 2020.

[184] I. Kharchenco and V. Alekseev, "Effect of ettringite morphology on the properties of expanding cement systems," *E3S Web of Conferences*, vol. 110, p. 01037, Aug. 2019.

[185] J. Yu, J. Qian, J. Tang, Z. Ji, and Y. Fan, "Effect of ettringite seed crystals on the properties of calcium sulphoaluminate cement," *Construction and Building Materials*, vol. 207, pp. 249–257, May 2019.

[186] K. Tosun and B. Baradan, "Effect of ettringite morphology on DEF-related expansion," *Cement and Concrete Composites*, vol. 32, no. 4, pp. 271–280, Apr. 2010.

[187] P. W. Brown and J. V. Bothe, "The stability of ettringite," *Advances in Cement Research*, vol. 5, no. 18, pp. 47–63, 1993.

[188] F. P. Glasser, "The stability of ettringite," in *International RILEM Workshop on Internal Sulfate Attack and Delayed Ettringite Formation*, 2004, pp. 43–64.

[189] Y. Elakneswaran, C. Li, T. Kajio, E. Owaki, M. Ogino, and T. Nawa, "Durability of slag-blended cement due to U-phase instability in sulphate environment," *Materials and Structures*, vol. 53, no. 6, p. 146, Dec. 2020.

[190] M. Ben Haha, B. Lothenbach, G. Le Saout, and F. Winnefeld, "Influence of slag chemistry on the hydration of alkali-activated blast-furnace slag — Part II: Effect of Al2O3," *Cement and Concrete Research*, vol. 42, no. 1, pp. 74–83, Jan. 2012.

[191] H. G. Midgley and P. Bhaskara Rao, "Formation of stratlingite, 2CaO.SiO2.Al2O3.8H2O, in relation to the hydration of high alumina cement," *Cement*

and Concrete Research, vol. 8, no. 2, pp. 169–172, 1978.

[192] P. V. Brady and J. V. Walther, "Kinetics of quartz dissolution at low temperatures," *Chemical Geology*, vol. 82, no. C, pp. 253–264, 1990.

[193] U. Schwertmann, "Solubility and dissolution of iron oxides," *Plant and Soil*, vol. 130, no. 1–2, pp. 1–25, 1991.

[194] P. M. Dove and D. A. Crerar, "Kinetics of quartz dissolution in electrolyte solutions using a hydrothermal mixed flow reactor," *Geochimica et Cosmochimica Acta*, vol. 54, no. 4, pp. 955–969, 1990.

[195] C. J. Warren and E. J. Reardon, "The solubility of ettringite at 25°C," *Cement and Concrete Research*, vol. 24, no. 8, pp. 1515–1524, 1994.

[196] A. M. Cody, H. Lee, R. D. Cody, and P. G. Spry, "The effects of chemical environment on the nucleation, growth, and stability of ettringite [Ca3Al(OH)6]2(SO4)3·26H2O," *Cement and Concrete Research*, vol. 34, no. 5, pp. 869–881, 2004.

[197] P. Feng, C. Miao, and J. W. Bullard, "Factors Influencing the Stability of AFm and AFt in the Ca-Al-S-O-H System at 25°C," *Journal of the American Ceramic Society*, vol. 99, no. 3, pp. 1031–1041, 2016.

[198] S. Sinyoung, P. Songsiriritthigul, S. Asavapisit, and P. Kajitvichyanukul, "Chromium behavior during cement-production processes: A clinkerization, hydration, and leaching study," *Journal of Hazardous Materials*, vol. 191, no. 1–3, pp. 296–305, 2011.

[199] F. Sorrentino, "Chemistry and engineering of the production process: State of the art," *Cement and Concrete Research*, vol. 41, no. 7, pp. 616–623, 2011.

[200] A. Eštoková, L. Palaščáková, E. Singovszká, and M. Holub, "Analysis of the chromium concentrations in cement materials," *Procedia Engineering*, vol. 42, no. August, pp. 123–130, 2012.

[201] A. Kindness, A. Macias, and F. P. Glasser, "Immobilization of chromium in cement matrices," *Waste Management*, vol. 14, no. 1, pp. 3–11, 1994.

[202] P. K. Mehta, "Mechanism of sulfate attack on portland cement concrete - Another look," *Cement and Concrete Research*, vol. 13, no. 3, pp. 401–406, 1983.

[203] M. Chaouche, X. X. Gao, M. Cyr, M. Cotte, and L. Frouin, "On the origin of the blue/green color of blast-furnace slag-based materials: Sulfur K-edge XANES investigation," *Journal of the American Ceramic Society*, vol. 100, no. 4, pp. 1707–1716, 2017.

[204] S. M. Leisinger, A. Bhatnagar, B. Lothenbach, and C. A. Johnson, "Solubility of chromate in a hydrated OPC," *Applied Geochemistry*, vol. 48, pp. 132–140, 2014.

[205] L. De Windt, P. Chaurand, and J. Rose, "Kinetics of steel slag leaching: Batch tests and modeling," *Waste Management*, vol. 31, no. 2, pp. 225–235, Feb. 2011.

[206] S. Wild, M. R. Abdi, and G. Leng-Ward, "Sulphate Expansion of Lime-Stabilized Kaolinite: II. Reaction Products and Expansion," *Clay Minerals*, vol. 28, no. 4, pp. 569–583, 1993.

[207] A. Attari, C. McNally, and M. G. Richardson, "A combined SEM–Calorimetric approach for assessing hydration and porosity development in GGBS concrete," *Cement and Concrete Composites*, vol. 68, pp. 46–56, Apr. 2016.

[208] M. Vítková, V. Ettler, M. Mihaljevič, and O. Šebek, *Effect of sample preparation on contaminant leaching from copper smelting slag*, vol. 197. 2011.

[209] J. A. Lackovic, N. P. Nikolaidis, P. Chheda, R. J. Carley, and E. Patton, "Evaluation of

batch leaching procedures for estimating metal mobility in glaciated soils," *Ground Water Monitoring and Remediation*, vol. 17, no. 3, pp. 231–240, Aug. 1997.

[210] M. Zandi, N. V. Russell, R. G. J. Edyvean, R. J. Hand, and P. Ward, *Interpretation of standard leaching test BS en 12457-2: Is your sample hazardous or inert?*, vol. 9, no. 12. 2007.

[211] C. Labbez, I. Pochard, B. Jönsson, and A. Nonat, "C-S-H/solution interface: Experimental and Monte Carlo studies," *Cement and Concrete Research*, vol. 41, no. 2, pp. 161–168, Feb. 2011.

[212] S.-Y. Hong and F. P. Glasser, "Alkali binding in cement pastes," *Cement and Concrete Research*, vol. 29, no. 12, pp. 1893–1903, Dec. 1999.

[213] S. Gaboreau *et al.*, "Hydration Properties and Interlayer Organization in Synthetic C-S-H," *Langmuir*, vol. 36, no. 32, pp. 9449–9464, Aug. 2020.

[214] K. Scrivener, R. Snellings, and B. Lothenbach, *A Practical Guide to Microstructural Analysis of Cementitious Materials*. 2015.

[215] N. C. M. Marty, S. Grangeon, E. Elkaïm, C. Tournassat, C. Fauchet, and F. Claret, "Thermodynamic and crystallographic model for anion uptake by hydrated calcium aluminate (AFm): An example of molybdenum," *Scientific Reports*, vol. 8, no. 1, pp. 1–13, 2018.

[216] S. Lange, M. Klinkenberg, J. Barthel, D. Bosbach, and G. Deissmann, "Uptake and retention of molybdenum in cementitious systems," *Applied Geochemistry*, vol. 119, no. May, p. 104630, 2020.

[217] B. Grambow *et al.*, "Retention and diffusion of radioactive and toxic species on cementitious systems: Main outcome of the CEBAMA project," *Applied Geochemistry*, vol. 112, no. December, 2020.

[218] O. Ponta, R. Ciceo-Lucacel, A. Vulpoi, T. Radu, V. Simon, and S. Simon, "Synthesis and characterisation of nanostructured silica-powellite-HAP composites," *Journal of Materials Science*, vol. 50, no. 2, pp. 577–586, 2014.

[219] G. Landrot and S. Khaokaew, "Lead Speciation and Association with Organic Matter in Various Particle-Size Fractions of Contaminated Soils," *Environmental Science and Technology*, vol. 52, no. 12, pp. 6780–6788, 2018.

[220] J. P. Gustafsson and C. Tiberg, "Molybdenum binding to soil constituents in acid soils: An XAS and modelling study," *Chemical Geology*, vol. 417, pp. 279–288, 2015.

[221] W. Sun and H. M. Selim, "Kinetics of molybdenum adsorption and desorption in soils," *Journal of Environmental Quality*, vol. 47, no. 3, pp. 504–512, 2018.